Magnetic Induction Tomography Spectroscopy (MITS): Tomograph Optimization for Biomedical Application

PhD Thesis

Conducted by

Sinan Issa, Dipl.-Ing. BSc

at

Institute of Medical Engineering

Faculty of Computer Science and Biomedical Engineering

Graz University of Technology

Supervisor

Ao.Univ.-Prof. Dipl.-Ing. Dr.techn. Hermann Scharfetter

Graz, Austria, 2020

Affidavit

I declare that I have authored this thesis independently, that I have not used other than the declared sources/resources, and that I have explicitly indicated all material which has been quoted either literally or by content from the sources used. The text document uploaded to TUGRAZonline is identical to the present doctoral thesis.

Graz, Austria,

Date   Signature

Acknowledgements

Abstract

Magnetic Induction Tomography Spectroscopy (MITS):

Tomograph Optimization for Biomedical Application

Magnetic induction tomography spectroscopy (MITS) is a contactless, noninvasive near-field imaging modality aiming at the reconstruction of the passive electromagnetic properties of different materials or media. If any material or medium should be a biological one, such as living tissue, then speaking of biomedical MITS, the core theme of this thesis.

It is much to be hoped to find MITS in some routine medical applications in the future. However, answering such hopes certainly involves a great deal of arduous research work because living tissues are necessarily expected to be under investigation, and dealing with such complex biological structures as which is definitely most challenging. Therefore, the different problematic issues regarding the measuring and imaging processes have to be comprehensively analyzed and carefully tackled in order to hopefully ultimately activate biomedical MITS in routine clinical use. Furthermore, as far as possible and practicable, it is of prime importance to address these issues experimentally rather than only by simulation because many of the problems to be confronted with during the technical implementation of the MITS modality are unpredictable, extremely difficult to simulate or cannot be simulated, the reason why this work is completely based on experimental research. A probably most appropriate starting point in this regard would be the MITS tomograph itself being responsible for the measuring and imaging processes, the reason why this study is completely concerned with tomograph optimization in biomedical MITS.

For these purposes, the proposed general optimization approaches were applied to a prototype MITS tomograph. The performed optimization covered the tomograph's hardware, software and measurement environments, and is naturally not to be considered as to be specific to this prototype tomograph, but to any MITS tomograph in general to be optimized to meet the technical requirements for biomedical applications.

❖ As regards hardware environment, the optimization essentially concerned its core module, namely, the transceiver system, and hence the relevant subsystems: mechanics, electrics and electronics. In this respect, a novel dual-plane elliptical transceiver system was constructed. As its geometric layout approximates the shape of the human body, especially the truncal regions, it is particularly appropriate for thoracic, abdominal and pelvic applications.

❖ As regards software environment, the optimization essentially concerned its core module, namely, the imaging program, and hence the relevant subprograms: data postprocessing, sensitivity calculation and image reconstruction. In this respect, a novel hybrid dynamic-parametric imaging concept was developed. The addressed application example of this concept was hybrid state-frequency-differential imaging wherein simultaneous local and spectroscopic conductivity changes in the biological target medium were reconstructed together into one and the same image, gained from one and the same measurement.

❖ As regards measurement environment, the optimization essentially concerned the detection of unintentional patient movements during measurement and the elimination of their consequences prior to image reconstruction. In this respect, a novel detection and elimination technique (D&E) was originated. It allows detecting and eliminating any motion-induced signal errors whatsoever, whether those caused by the patient, the transceiver system or both together, hence, eliminating any motion artefacts in the images to be reconstructed without any need to repeat the time-consuming measurement and imaging processes.

The applicability of the introduced tomograph optimization approaches in biomedical MITS was assessed through multifrequency measurements in the β-dispersion frequency range on different biological targets located within background media of physiological conductivity, and through image reconstruction performed on the gained real measurement data. The qualitatively and quantitatively analyzed measurement and image reconstruction results verify the biomedical applicability of the optimized MITS tomograph and support the proposed aspects.

Keywords

Kurzfassung

Magnetische Induktions-Tomographie-Spektroskopie (MITS): Tomograph-Optimierung für biomedizinische Anwendung

Magnetische Induktions-Tomographie-Spektroskopie (MITS) ist eine kontaktlose, nicht-invasive Nahfeld-Bildgebungsmodalität zur Rekonstruktion der passiven elektromagnetischen Eigenschaften verschiedener Materialien oder Medien. Wenn es sich bei einem Material oder Medium um ein biologisches handelt, beispielsweise um lebendes Gewebe, dann spricht man von biomedizinischer MITS, dem Kernthema dieser Dissertation.

Es ist sehr zu hoffen, dass MITS in Zukunft in einigen routinemäßigen medizinischen Anwendungen zum Einsatz kommt. Die Erfüllung solcher Hoffnungen ist jedoch sicherlich mit einem erheblichen Forschungsaufwand verbunden, da davon auszugehen ist, dass lebende Gewebe untersucht werden und der Umgang mit derart komplexen biologischen Strukturen bestimmt die größte Herausforderung darstellt. Daher müssen die verschiedenen problematischen Themen bezüglich der Mess- und Bildgebungsprozesse umfassend analysiert und sorgfältig angegangen werden, um biomedizinische MITS hoffentlich letztendlich im klinischen Routineeinsatz zu aktivieren. Darüber hinaus ist es von größter Wichtigkeit, diese Themen, soweit dies möglich und praktikabel ist, eher experimentell als nur durch Simulation anzugehen. Das liegt daran, dass viele der auftretenden Probleme bei der technischen Implementierung der MITS-Modalität unvorhersehbar sind, extrem schwierig zu simulieren sind oder nicht simuliert werden können. Dies ist der Grund, weshalb diese Arbeit vollständig auf experimenteller Forschung basiert. Ein wahrscheinlich am besten geeigneter Ausgangspunkt in diesem Zusammenhang wäre der MITS-Tomograph selbst, da er für die Mess- und Bildgebungsprozesse verantwortlich ist. Aus diesem Grund befasst sich diese Studie ausschließlich mit Tomographoptimierung in biomedizinischer MITS.
Zu diesem Zweck wurden die vorgeschlagenen allgemeinen Optimierungsansätze auf einen Prototyp-MITS-Tomographen angewandt. Die durchgeführte Optimierung deckte die Hardware-, Software- und Messumgebungen des Tomographen ab und ist natürlich nicht als spezifisch für diesen Prototyp-Tomographen anzusehen, sondern für jeden MITS-Tomographen im Allgemeinen, der zur Erfüllung der technischen Anforderungen für biomedizinische Anwendungen zu optimieren ist.

❖ In puncto Hardwareumgebung betraf die Optimierung im Wesentlichen das Kernmodul, nämlich das Transceiversystem, und somit die dazugehörigen Teilsysteme: Mechanik, Elektrik und Elektronik. In dieser Hinsicht wurde ein neuartiges elliptisches Zweiebenen-Transceiversystem konstruiert. Da seine geometrische Anordnung der Form des menschlichen Körpers, insbesondere der trunkalen Bereiche, nahekommt, eignet es sich besonders für thorakale, abdominale und pelvine Anwendungen.

❖ In puncto Softwareumgebung betraf die Optimierung im Wesentlichen das Kernmodul, nämlich das Bildgebungsprogramm, und somit die dazugehörigen Unterprogramme: Datennachverarbeitung, Sensitivitätsberechnung und Bildrekonstruktion. In dieser Hinsicht wurde ein neuartiges hybrides dynamisch-parametrisches Bildgebungskonzept entwickelt. Das behandelte Anwendungsbeispiel für dieses Konzept war hybride zustands-frequenz-differentielle Bildgebung, wobei simultane lokale und spektroskopische Leitfähigkeitsänderungen im biologischen Zielmedium zusammen in ein und dasselbe Bild rekonstruiert wurden, das aus ein und derselben Messung gewonnen wurde.

❖ In puncto Messumgebung betraf die Optimierung im Wesentlichen die Erkennung unbeabsichtigter Bewegungen des Patienten während der Messung und die Beseitigung ihrer Konsequenzen vor der Bildrekonstruktion. In dieser Hinsicht wurde eine neuartige Detektions- und Eliminationstechnik (D&E) geschaffen. Sie ermöglicht die Detektion und Elimination jeglicher bewegungsbedingten Signalfehler, unabhängig davon, ob diese vom Patienten, dem Transceiversystem oder beiden zusammen verursacht werden. Dadurch werden jegliche Bewegungsartefakte in den zu rekonstruierenden Bildern eliminiert, ohne dass die zeitaufwändigen Mess- und Bildgebungsprozesse wiederholt werden müssen.

Durch Multifrequenzmessungen im β-Dispersionsfrequenzbereich an verschiedenen biologischen, innerhalb Hintergrundmedien mit physiologischer Leitfähigkeit gelegenen Zielobjekten, und durch Bildrekonstruktion basierend auf den gewonnenen realen Messdaten wurde die Anwendbarkeit der eingeführten Tomograph-Optimierungsansätze in biomedizinischer MITS beurteilt. Die qualitativ und quantitativ analysierten Mess- und Bildrekonstruktionsergebnisse verifizieren die biomedizinische Anwendbarkeit des optimierten MITS-Tomographen und unterstützen die vorgeschlagenen Aspekte.

Schlüsselwörter

Magnetische Induktions-Tomographie-Spektroskopie (MITS); biomedizinische MITS; Tomographoptimierung; Transceiversystem; dynamische, parametrische und hybride dynamisch-parametrische Bildgebung; zustands-, frequenz- und hybride zustands-frequenz-differentielle Bildgebung; Detektions- und Eliminationstechnik (D&E).

_____

Contents

Chapter 1

Bioelectrical Spectroscopy

This chapter provides a brief basic background about bioelectrical spectroscopy, particularly with regard to the passive electrical properties. It is a fully introductory chapter thought relevant for understanding the basic rationale behind this thesis.

1.1 Definitions

❖   Passive Electromagnetic Properties

The dielectric, electrical and magnetic properties of a non-isolated physical system, such as the dielectric permittivity, electrical resistivity, electrical conductivity and magnetic permeability, will be termed in this study *passive electromagnetic properties (PEP)*.

The in-depth investigation of the PEP of biological tissue can be of biomedical usefulness, particularly in analyzing its heterogeneous structure and developing diagnostic and therapeutic applications.

❖   Polarization

The induction of a net electric dipole moment in a non-isolated physical system through the spatial rearrangement of its electric charge distribution in response to an external excitation signal will be termed in this study *polarization*.

Biological tissue is polarizable. If it undergoes excitation by an alternating electric field, it shall undergo polarization due to the net electric dipole moment to be induced, mainly, through the translational displacement of electric charges forming non-permanent electric dipoles and/or the rotational orientation of inherent permanent electric dipoles.
The polarization of biological tissue can be of biomedical relevance, particularly in characterizing biological tissue regarding its PEP dielectrically.

❖   Relaxation

The transition of a non-isolated physical system exposed to an external excitation signal from its initial stationary equilibrium state before excitation into a new stationary equilibrium state after excitation will be termed in this study *relaxation*.

Biological tissue is relaxable. If it undergoes polarization, it shall undergo relaxation due to its ability to attain and retain a new stationary equilibrium state with its new electric charge distribution after polarization.
The relaxation of biological tissue can be of biomedical significance, particularly in characterizing biological tissue regarding its PEP electrochemically.

❖   Dispersion

The variation of a non-isolated physical system regarding one or more of its parameters with the frequency of an external excitation signal will be termed in this study *dispersion*.

Biological tissue is dispersive. If it undergoes polarization and relaxation, it shall undergo dispersion due to the variation of its PEP with the applied excitation frequency.

The dispersion of biological tissue can be of biomedical importance, particularly in characterizing biological tissue regarding its PEP spectroscopically.

Remarks

For the sake of simplicity and convenience, depending on the context, the abbreviation PEP may also refer to one single passive electric or magnetic property. In addition, all PEP of biological tissue may be prefixed with *bio* in an analogous manner to *bioimpedance*, e.g., the *electrical admittance, admittivity* and *conductivity of biological tissue* become *bioadmittance, bioadmittivity* and *bioconductivity*, respectively, etc.

1.2   Basics

With regard to its PEP, biological tissue exhibits dispersion in consequence of an external alternating electric field. [Schwan 1957] studied this dispersion by measuring some PEP of biological tissue and cell suspensions over a broad frequency range. Figure (1.1) illustrates an example of the dispersive behaviour of biological tissue regarding its specific electrical impedance (impedivity, complex resistivity), specific electrical admittance (admittivity, complex conductivity) and complex relative dielectric permittivity (adapted, modified and redrawn from [Schwan 1994]). It can be clearly seen how characteristically the bioimpedivity and biopermittivity descend with ascending frequency within three successive approximate frequency ranges marked with the Greek letters α, β and γ, respectively. Predictably, this characteristic decrease in both PEP is inherent to a characteristic increase in the bioadmittivity, the reciprocal of the bioimpedivity. This characteristic behaviour of the PEP of biological tissues within these three frequency ranges will be termed according to [Schwan 1957] *α-, β-* and *γ-dispersion*, respectively.
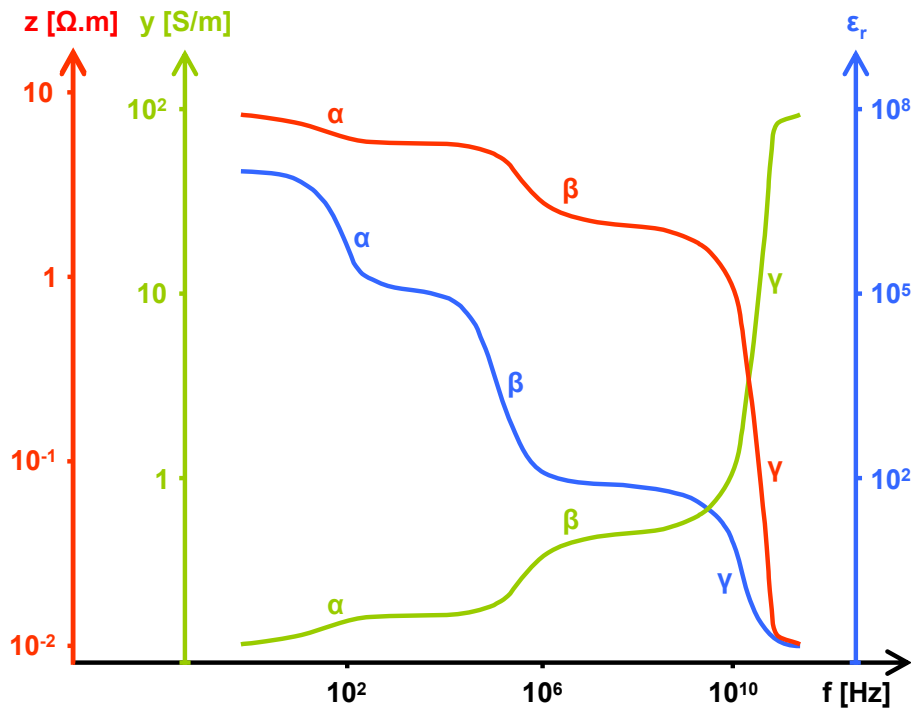
Figure (1.1): Dispersion of the bioimpedivity (z), bioadmittivity (y) and relative bio-permittivity (ε_r). α, β and γ figuratively mark three dispersion regions within which the three PEP exhibit a characteristic behaviour. While the spectra of z and ε_r undergo a negative slope throughout these regions, the spectrum of y undergoes a positive one.

Figure (1.1) shows that the frequency ranges of these dispersions may differ more or less when observing different PEP of the same tissue, respectively. In addition, these frequency ranges may differ more or less when observing the same PEP of different tissues, respectively. In other words, the α-, β- and γ-dispersion frequency ranges are PEP- and tissue-dependent or -specific, as is exactly the case with the so-called *relaxation frequency* and the corresponding *relaxation time constant*, the reason why they are also called *characteristic frequency* and *characteristic time constant*. The latter two parameters can be demonstrated, better understood and even graphically estimated by plotting the spectrum of a given PEP for a given tissue -other than in figure (1.1)- in the complex plane, i.e., by plotting the PEP locus in the Nyquist diagram, to be closely examined at the end of this chapter.

1.3   Biological Tissue Characterization and Classification

In order to characterize biological tissues based on the dispersion of their PEP, and to classify them accordingly regarding the different bioelectrical aspects, e.g., dielectrically, electrochemically, spectroscopically, etc., it is very important to look into the individual dispersions and to ascertain their exact reasons. Generally, it can be stated that the dispersion of biological tissue arises from the cooccurrence of polarization and relaxation. More specifically, the whole process is directly related to the concomitant electrochemical processes in the different frequency ranges which are in turn strongly related to many relevant factors, such as the chemical content, its (in)homogeneity, (an)isotropy, temperature and (path)physiological status. Therefore, the relevant research has usually subdivided the individual PEP spectra (dispersions) into multiple sub-spectra (sub-dispersions) depending on the governing bioelectrical mechanisms in the different frequency ranges; put it another way, each whole PEP dispersion curve has been divided into multiple dispersion regions, as is the case in the previous PEP dispersion examples with three regions each: α, β and γ (usually referred to in the literature as *dispersions* rather than *dispersion regions*). In this context, it can be inferred that there can often be more or less partial overlapping between the different dispersion regions, and that such a distinct separation between them as in the previous example representation in figure (1.1) does not necessarily reflect the general case of the various living tissues. On all these grounds, in the following paragraph, only the most addressed dispersions in the literature will be recalled and briefly explained; in addition, only an approximate frequency range will be assigned to each dispersion, and only its main cause will be stated.

1.3.1   Dispersions

❖   α-Dispersion

It mainly occurs in the frequency range between *extremely low frequencies (ELF)* and *very low frequencies (VLF)* of the electromagnetic spectrum, usually between a few *[Hz]* and a few *[kHz]*. The α-dispersion is mainly caused by the relaxation of non-permanent electric dipoles which induce their net dipole moment through a translational displacement polarization process. In this process, the counterions, which are trapped at the charged surfaces of cell membranes and large molecules

in consequence of an intrinsic charge build-up process, are translationally displaced by the applied electric field along these charged surfaces creating surface current densities.

❖   β-Dispersion

It mainly occurs in the frequency range between *low frequencies (LF)* and *very high frequencies (VHF)* of the electromagnetic spectrum, usually between several tens of *[kHz]* and several tens of *[MHz]*. Principally, the β-dispersion shares the same main cause of the α-dispersion, i.e., relaxation of a translational displacement polarization process. However, the underlying polarization process mainly obeys another different mechanism, namely, the *Maxwell-Wagner* interfacial mechanism presented in [Wagner 1914]. The Maxwell-Wagner type of polarization occurs in those materials containing interfaces between different dielectric media, as is the case in biological tissues where the cell membranes separate between the *intracellular space (ICS)* and the *extracellular space (ECS)*. As already mentioned, charge intrinsically builds up at the charged cell membranes' surfaces; however, in contrast to the α-dispersion, the translational charge displacement by the applied electric field does not occur along the membranes but across them, i.e., the induced currents try to flow from the ECS through the cell membranes into the ICS. The intensity of this flow is tuneable by the applied field frequency, as will be demonstrated in the next paragraph.

❖   γ-Dispersion

It mainly occurs in the frequency range between *ultra high frequencies (UHF)* and *extremely high frequencies (EHF)* of the electromagnetic spectrum, usually between several hundreds of *[MHz]* and several tens of *[GHz]*. The γ-dispersion is mainly caused by the relaxation of intrinsic permanent electric dipoles -in a mostly aqueous polar medium- which induce their net dipole moment through a rotational orientation (dipolar, molecular) polarization process. In this process, the free polar water molecules, also others such as salts and proteins, which are randomly oriented, are rotationally reoriented by the applied electric field towards the field direction.

❖   δ-Dispersion

The -usually called- *δ-dispersion* mainly occurs in the VHF range of the electro-

magnetic spectrum, usually within several tens of *[MHz]*. Principally, the δ-dispersion shares the exact main cause of the γ-dispersion, i.e., relaxation of a rotational orientation polarization process in a mostly aqueous polar medium. However, the underlying polar medium not only contains free water molecules, but also more or less strongly bound ones. This bound water results from an intrinsic electrostatic dipole-dipole attractive interaction process. This process leads to the formation of strong hydrogen bridge bonds between the water molecules themselves on the one hand, and between them and other polar molecules, such as salts and proteins, building hydration shells therearound on the other hand. These bound water molecules and thus other water-bound molecules are rotationally not as orientable by the applied electric field as the free ones. In terms of polarization and relaxation, this hindered rotational orientability causes them to be not as polarizable and relaxable as the free ones because it takes them longer to be rotationally reoriented towards the field direction, i.e., longer to produce their own net dipole moment and hence to polarize. Consequently, it takes them longer to relax involving thereby lower relaxation frequencies than in case of the free polar molecules.

The δ-dispersion has been less addressed in the literature than the other afore-stated major three ones. Actually, when considering the underlying main frequency range, the δ-dispersion may rather be regarded as a minor or side β-dispersion, but also much rather as a minor or side γ-dispersion when considering the underlying main polarization mechanism. On this account, the δ-dispersion might be observed as a quasi-γ-dispersion occurring mainly in the upper β-dispersion frequency range.

1.3.2   Models

Several models have been developed so far trying to explain the polarization, relaxation and the consequent dispersion of biological tissues regarding their PEP. A comprehensive discussion on many of these models can be found in [Grimnes and Martinsen 2000]. The major α, β and γ dispersions and other minor ones derived therefrom have been theoretically and experimentally extensively retreated and broadly covered in the literature in order to determine their causes and develop respective models, e.g., [Hanai 1960; Pethig 1979; Pethig and Kell 1987; Gheorghiu 1993, 1994; Martinsen et al. 2002]. In this regard, the focus of the research has been usually laid on the analysis of various types of homogeneous and inhomogeneous biological cell suspensions as well as healthy and unhealthy biological tissues. An introduction on the structural modelling of PEP-based diagnostic meth-

ods with references to many of these research studies on the different dispersion models can be found in [Scharfetter 1999]; for interested readers, hereunder are a select few of these studies:

- Different biological cell suspensions: spheroidal cells [Fricke 1924, 1925], cylindrical cells [Fricke 1955], spherical cells [Fricke 1955; Pauly and Schwan 1959; Gheorghiu 1994], ellipsoidal cells [Asami et al. 1980; Gheorghiu 1999].
- Different biological tissues: tumorous breast [Fricke and Morse 1926], ischaemic liver and kidney [Schäfer 1991], liver [Gersing et al. 1995], normal and pathological breast [Jossinet 1996], lung [Nopp et al. 1996, 1997], freshly excised breast [Jossinet 1998], red blood [Gheorghiu 1999], ischaemic skeletal muscle [Schäfer et al. 1999], breast [Jossinet and Schmitt 1999].

Hereof, only three of the most well-known relaxation and dispersion models treated in the literature will be recalled and briefly discussed, namely, the *Cole bioimpedance model* [Cole 1940] and the subsequent *Cole-Cole general dielectric model* [Cole and Cole 1941] together with the precedent *Debye ideal dielectric model* [Debye 1913], all published before presenting the characteristic α, β and γ dispersions in [Schwan 1957]. Actually, as will be discussed at the end of this paragraph, the Cole-Cole general dielectric relaxation model represents the principal outcome of an empirical reanalysis of the Debye ideal one. Even though the latter model turned out later to be not that appropriate to describe the relaxation of biological tissues, it has still been very appropriate to be applied, on the one hand, as a specific relaxation model to many homogeneous dielectrics, on the other hand, as a helping introductory relaxation model to many inhomogeneous dielectrics including biological tissues in order to begin a -mostly theoretical- research therewith.

The human body is composed of many tissues of different chemical structures. The consequence of such complex composition is that all of the afore-stated main dispersions along with other side ones can be observed, whether individually, more than one or even all together depending on the exact chemical content of the tissue in question and the observed frequency range. Among all these dispersions, as will be more evident in the next chapters, the β-dispersion represents the most relevant one to this study. As explained hereinbefore, the main polarization process accounting for the emergence of the β-dispersion is of the Maxwell-Wagner type which occurs in those systems where externally induced currents try to pass interfaces between different dielectric media. Due to their heterogeneous structure, biological tissues match a multi-dielectric milieu comprising many of such

systems. Therefore, most tissues undergo an explicit interfacial polarization process and shall hence exhibit a distinct β-dispersion within the underlying frequency range. In their most simplest case, biological tissues can be considered as a composition of many different suspensions of cells, each containing two different dielectric media, the *intracellular fluid (ICF)* and the *extracellular fluid (ECF)*, separated by resistive interfaces, the *cell membranes (CM)*.

Observing a biological cell within a cell suspension electrically and replacing each of its main biological components, the ICF and the CM, together with the thin-film ECF therearound by one or more equivalent passive electrical elements, thus, some equivalent electrical circuit diagrams representing the biological cell can be generated, such as the simplified ones depicted in figure (1.2), whereby the β-dispersion according to the models of Cole and Cole can be more easily understood.
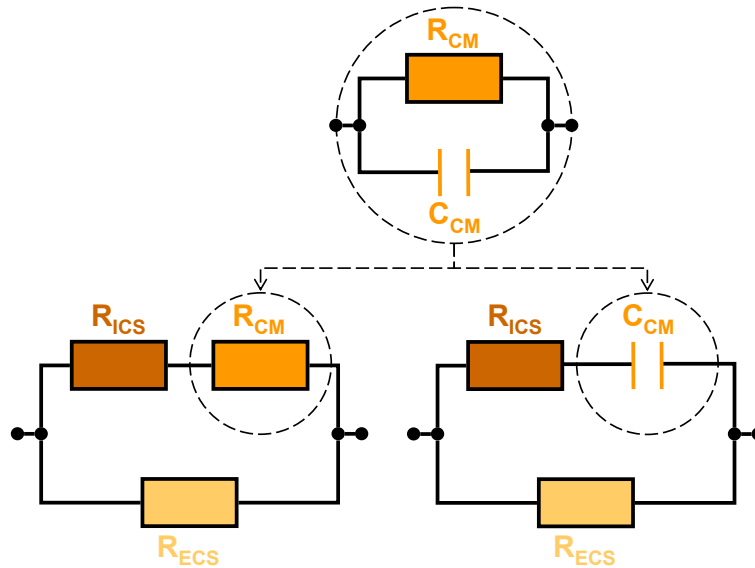
Figure (1.2): Equivalent electrical circuit of one biological cell within the surrounding extracellular space. Left: at low frequencies, right: at high frequencies. R_{ECS}: resistance of the ECS around the cell, R_{ICS}: resistance of the ICS, R_{CM}: resistance of the CM, C_{CM}: capacitance of the CM. On one side, C_{CM} is omitted from the left circuit due to the dominance of its reactance (X_{CM}) over the parallel-connected R_{CM} at relatively very low frequencies (f_0, explained hereinbelow), i.e., due to $\{|X_{CM}|_{f0} = 1 / (2\pi f_0 \, C_{CM}) \gg R_{CM}\}$; on the other side, R_{CM} is omitted from the right circuit due to its dominance over X_{CM} at relatively very high frequencies (f_∞, explained hereinbelow), i.e., due to $\{|X_{CM}|_{f\infty} = 1 / (2\pi f_\infty \, C_{CM}) \ll R_{CM}\}$. Accordingly, biological tissue might electrically be observed as a series connection of numerous of such individual cells, i.e., of their equivalent impedances.

Applying an alternating electric field to a suspension of such cells shown in figure (1.2), thus, at low frequencies, as low as the lowest frequencies in the β-dispersion frequency range, the induced current can almost exclusively flow within the ECS around the cells but not through the CM into the ICS due to the quasi-infinite CM capacitive reactance which causes the CM equivalent impedance to be almost equal to the CM high resistance. Consequently, the cellular medium still holds high impedance, high permittivity and low admittance values. In contrast, at high frequencies, as high as the highest frequencies in the β-dispersion frequency range, the current can easily flow through the CM into the ICS due to the quasi-zero CM capacitive reactance which causes the CM high resistance to be almost short-circuited. Consequently, the impedance and permittivity of the cellular medium decrease, whereas its admittance increases.

At first, the relaxation and dispersion model will be expressed by the following famous phenomenological *Cole equation* for biological tissues with regard to their electrical impedance (rewritten from [Cole 1940]):

$$Z(\omega) = |Z(\omega)| * e^{-j\theta(\omega)} = R(\omega) - jX(\omega) = R_{f\infty} + \{(R_{f0} - R_{f\infty}) / (1 + (j\omega\tau_c)^{\alpha})\} \quad (1.1)$$

with $\{\omega = 2\pi f\}$ and $\{\tau_c = 1 / 2\pi f_c = 1 / \omega_c\}$

where, for the sake of convenience, the terminology of this and other model equations (1.2-1.6) stated hereinbelow is gathered after equation (1.6).

This empirical Cole equation may be considered as not to be necessarily restricted to the impedance, biological tissues or the impedance of biological tissues. In other words, it may also be applied to other dielectrics than biological tissues on the one hand; on the other hand, it may also be reformulated to describe other PEP than the impedance and then to be applied to biological tissues and other dielectrics as well. In addition, this reformulation can be managed to treat extrinsic PEP as well as their corresponding intrinsic versions, i.e., the PEP can be expressed nonspecifically similar to equation (1.1) as in equations (1.2) and (1.6) as well as specifically as in equations (1.3-1.5). However, in all these cases, as mentioned hereinbefore, different relaxation time constants and hence relaxation frequencies must be taken into account depending on the PEP and the tissue or other dielectric being observed; the same applies to the Cole exponent α.

All the above remarks considered, with respect to the impedance's reciprocal, the electrical admittance, the Cole model may alternatively be expressed in the following equivalent way (rewritten from [Grimnes and Martinsen 2000]):

$$Y(\omega) = |Y(\omega)| * e^{j\theta(\omega)} = G(\omega) + jB(\omega) = G_{f0} + \{(G_{f\infty} - G_{f0}) / (1 + (j\omega\tau_c)^{-\alpha})\} \quad (1.2)$$

In an analogous manner, the corresponding specific electrical impedance and its reciprocal, the specific electrical admittance, may be expressed as follows, respectively:

$$z(\omega) = |z(\omega)| * e^{-j\theta(\omega)} = \rho(\omega) - jx(\omega) = \rho_{f\infty} + \{(\rho_{f0} - \rho_{f\infty}) / (1 + (j\omega\tau_c)^{\alpha})\} \quad (1.3)$$

$$y(\omega) = |y(\omega)| * e^{j\theta(\omega)} = \sigma(\omega) + jb(\omega) = \sigma_{f0} + \{(\sigma_{f\infty} - \sigma_{f0}) / (1 + (j\omega\tau_c)^{-\alpha})\} \quad (1.4)$$

And finally, there exists another famous phenomenological expression for the relaxation and dispersion model, namely, the following *Cole-Cole equation* for dielectric materials with regard to their complex dielectric permittivity (rewritten from [Cole and Cole 1941]):

$$\varepsilon(\omega) = |\varepsilon(\omega)| * e^{-j\theta(\omega)} = \varepsilon'(\omega) - j\varepsilon''(\omega) = \varepsilon_{f\infty} + \{(\varepsilon_{f0} - \varepsilon_{f\infty}) / (1 + (j\omega\tau_c)^{1-\alpha})\} \quad (1.5)$$

Or alternatively, with respect to the corresponding complex dielectric capacitance, the Cole-Cole model may be expressed in the following equivalent way (rewritten from [Grimnes and Martinsen 2000]):

$$C(\omega) = |C(\omega)| * e^{-j\theta(\omega)} = C'(\omega) - jC''(\omega) = C_{f\infty} + \{(C_{f0} - C_{f\infty}) / (1 + (j\omega\tau_c)^{1-\alpha})\} \quad (1.6)$$

Z, Y, z, y, ε, C: impedance, admittance, impedivity, admittivity, permittivity and capacitance, respectively.
ω, f: angular frequency and temporal frequency, respectively.
j: imaginary unit ($\sqrt{-1}$).
θ: phase angle.
R, G, ρ, σ, ε', C': resistance, conductance, resistivity, conductivity, real part of the permittivity and real part of the capacitance, respectively.
X, B, x, b, ε'', C'': reactance, susceptance, reactivity, susceptivity, imaginary part of the permittivity and imaginary part of the capacitance, respectively.
τ_c, f_c, ω_c: characteristic or relaxation time constant, characteristic or relaxation fre-

quency and characteristic or relaxation angular frequency, respectively.

R_{f0}, G_{f0}, ρ_{f0}, σ_{f0}, ε_{f0}, C_{f0}: *resistance, conductance, resistivity, conductivity, permittivity and capacitance at frequency f_0 far lower than f_c, respectively.*

$R_{f\infty}$, $G_{f\infty}$, $\rho_{f\infty}$, $\sigma_{f\infty}$, $\varepsilon_{f\infty}$, $C_{f\infty}$: *resistance, conductance, resistivity, conductivity, permittivity and capacitance at frequency f_∞ far higher than f_c, respectively.*

α: Cole exponent.
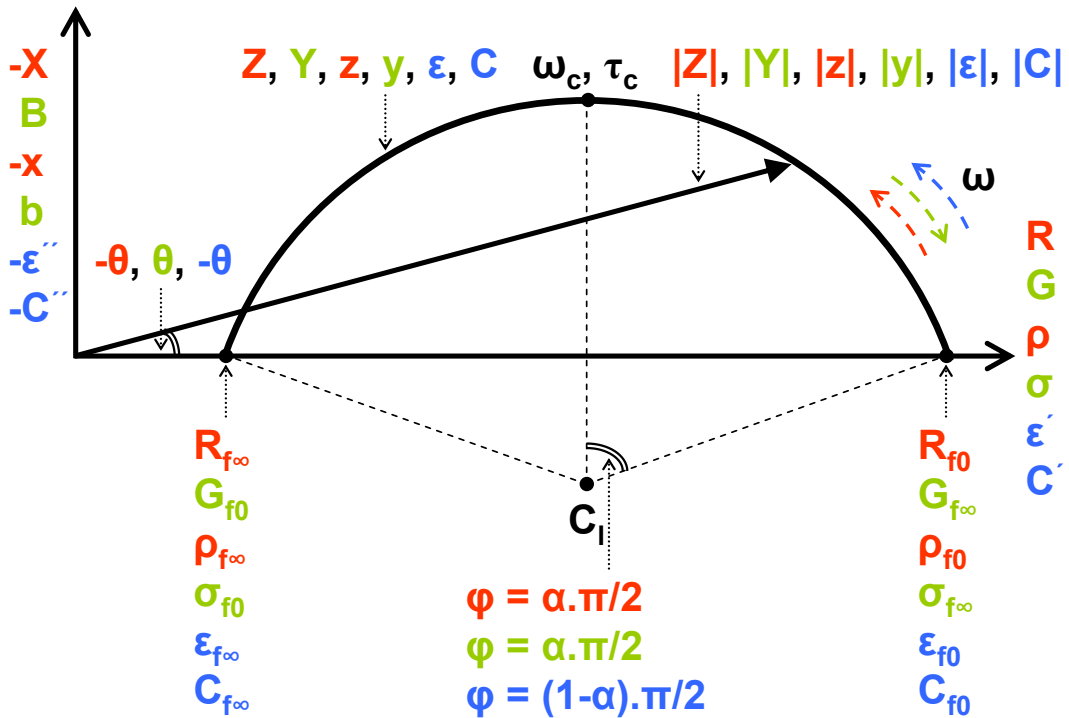
Figure (1.3): General example representation of the relaxation and dispersion model according to Cole and Cole. With reference to their respective equations (1.1-1.6), the imaginary parts of Z, z, ε and C are negative, whereas those ones of Y and y are positive; for the sake of consistency, in order to have a common locus for all of them, the sign of the imaginary part of the former group is retained and both groups are plotted on the same positive part of the imaginary axis; otherwise, the plot of the former group has to be vertically mirrored (with respect to the real axis). C_l: centre of the circular-arc locus, φ: depression angle. The coloured, curved arrows denote the direction of increasing ω. f_0 and f_∞ correspond to min(Re(PEP)) and max(Re(PEP)), respectively, in case of Y and y or to max(Re(PEP)) and min(Re(PEP)), respectively, in case of Z, z, ε and C at the lowest and the highest applied frequency $\{f_0 \ll f_c\}$ and $\{f_\infty \gg f_c\}$, respectively, where f_c and thus ω_c and τ_c correspond to max(|Im(PEP)|).

By means of a unified (generalized) locus for all of the PEP treated in equations (1.1-1.6), figure (1.3) graphically summarizes the discussion in this paragraph on relaxation and dispersion in accordance with the models of Cole and Cole. Such kind of PEP graphical representation is usually referred to as *Cole plot* when demonstrating *Z* according to equation (1.1) and as *Cole-Cole plot* when demonstrating *ε* according to equation (1.5) (recall that any dispersion -together with the related τ_c, ω_c and *α*- is PEP- and tissue-specific; for the sake of simplicity, the different PEP loci are represented in figure (1.3) by means of a global locus).

As can be seen in figure (1.3), the characteristic frequency corresponds to the local minimum or maximum of the PEP locus depending on the observed PEP and can thus be mathematically defined as the frequency whereat the locus' imaginary part reaches its maximum absolute value, and the corresponding characteristic time constant can then be simply defined as the reciprocal of the relaxation angular frequency as additionally given in equation (1.1).

In contrast to the non-constant, frequency-dependent phase angle *{θ = f(ω)}*, the depression angle *φ* remains constant, i.e., frequency-independent for a given Cole exponent *α* as it is only linked thereto, i.e., *{φ = f(α)}*. *α* itself is an empirically determined parameter which depends on the nature of the observed dielectric medium, herein biological tissue, and takes a value *[0 ≤ α ≤ 1]*. This parameter may have more than one physical interpretation, but it is generally agreed that it essentially stems from the distribution of multiple characteristic time constants in case of materials exhibiting multiple dispersions, as is the case of biological tissues. In this case, τ_c can be considered as a mean characteristic (relaxation) time constant, and *α* can thus allow distinguishing between different spectral shapes. When *(α = 0)*, the general dielectric dispersion model in the previous Cole-Cole equation (1.5) reduces to the original ideal one in the following *Debye equation* with one single relaxation time constant, i.e., one single dispersion (rewritten from [Debye 1929]):

$$\varepsilon(\omega) = |\varepsilon(\omega)| * e^{-j\theta(\omega)} = \varepsilon^{'}(\omega) - j\varepsilon^{''}(\omega) = \varepsilon_{f\infty} + \{(\varepsilon_{f0} - \varepsilon_{f\infty}) / (1 + j\omega\tau_c)\} \qquad (1.7)$$

In this case, in contrast to the circular-arc locus of *ε* in figure (1.3) with its centre C_l *depressed* beneath the real axis due to *(φ < π/2)* (whence the name *depression angle*), the locus of *ε* is a complete semi-circle with its centre located exactly on the real axis halfway between ε_{f0} and $\varepsilon_{f\infty}$ due to *(φ = π/2)*.

The Debye ideal dielectric relaxation model was published many years before the Cole-Cole general one. Originally, it describes the relaxation of polar gases and dilute solutions of polar liquids, all exhibiting single dispersions. Therefore, it may better be used as a specific model to describe the relaxation of homogeneous polar dielectrics undergoing an explicit dipolar (orientation) polarization process in the microwave frequency range and thus exhibiting a distinct γ-dispersion, rather than to describe the relaxation of such highly inhomogeneous, highly anisotropic dielectrics exhibiting multiple dispersions as living tissues. In other words, the Cole-Cole model with its phenomenological factor α is physiologically more realistic, and its validity in this regard has generally been well recognized thus far.

Still discussing the Cole-Cole general dielectric model in equation (1.5), when α increases within the range *[0 < α ≤ 1]* corresponding to *(φ < π/2)* in figure (1.3), the Cole-Cole dispersion will extend over a wider frequency range than the Debye dispersion with *(α = 0)* and *(φ = π/2)*. This broadening of the Cole-Cole dispersion over the Debye dispersion can graphically be best demonstrated by plotting both spectra for a given dielectric -as in figure (1.1)- on a logarithmic frequency scale where the Cole-Cole spectrum will morphologically look more stretched with respect to the frequency axis than the Debye spectrum.

The whole above discussion on α with regard to ε in equation (1.5) holds true with regard to C in equation (1.6) as the exponent *(1-α)* and thus the depression angle *{φ = (1−α) π/2}* agree in both equations. In contrast, with regard to Z, Y, z and y in their respective equations (1.1-1.4), aside from its sign, the exponent to be considered is α, and the corresponding depression angle is *{φ = α π/2}*. In this case, a Debye dispersion occurs when *(α = 1)* yielding *(φ = π/2)*, and a Cole-Cole dispersion, i.e., a broader one than the former, occurs when α decreases within the range *[1 > α ≥ 0]* yielding *(φ < π/2)*.

Chapter 2

Magnetic Induction Tomography Spectroscopy (MITS)

This chapter introduces the MITS modality and discusses some of its several sides and relevant issues, particularly from the biomedical point of view. It is a half-introductory, half-methodological chapter thought relevant before going into the concrete technical realization of the methodology and the experimental implementation of the aimed measurement and imaging applications. The information provided at different stations throughout this chapter on different MITS development aspects, especially with regard to the underlying thesis' goals, forms in its entirety a multi-sided review on MITS progress thus far. The last subchapter underlines and discusses the motivations for and objectives of this thesis.

2.1   Methodology

2.1.1   Definition

Magnetic induction tomography spectroscopy (MITS), the combination of *magnetic induction tomography (MIT)* and *magnetic induction spectroscopy (MIS)*, is a contactless, noninvasive near-field imaging modality aiming at the reconstruction of the PEP of different materials or media. If any material or medium should be a biological one, such as living tissue, then speaking of *biomedical MITS*, the core theme of this thesis.

2.1.2   Principle

MITS requires multifrequency *excitation (primary) magnetic fields* to be coupled to the medium under investigation. These fields are generated by means of multifrequency currents circulating through a transmitting coil array, usually, surrounding the medium region. As a direct consequence, eddy currents, conduction and displacement ones, will be induced in the medium where their distribution and intensity, i.e., local density, are proportional to the strength and frequency of the applied excitation field on the one hand, and to the conductivity and permittivity of the medium on the other hand, thus, inversely proportional to the medium's resistivity. Eddy currents interfere with (perturb) the excitation fields and proportionally induce in turn *perturbation (secondary, response) magnetic fields*. However, this does not necessarily mean that the induced conduction and displacement currents in the medium are the only cause of the perturbation field. As will be seen at several stations throughout this study, depending on the nature and thus magnetic behaviour of the investigated medium or a certain *region of interest (ROI)* therein, the magnetization of the medium by the excitation field can also contribute to a greater or lesser extent to the induction of the perturbation field; thus, in addition to the conductivity and permittivity distributions, the perturbation field also reflects the permeability distribution in the medium. The primary and secondary fields are then sensed together in form of *primary (carrier)* and *secondary (perturbation, response) voltages*, respectively, by means of a receiving coil array, usually, surrounding the medium region.

Figure (2.1) shows a simple illustration describing the foregoing cycle of the MITS measurement process.
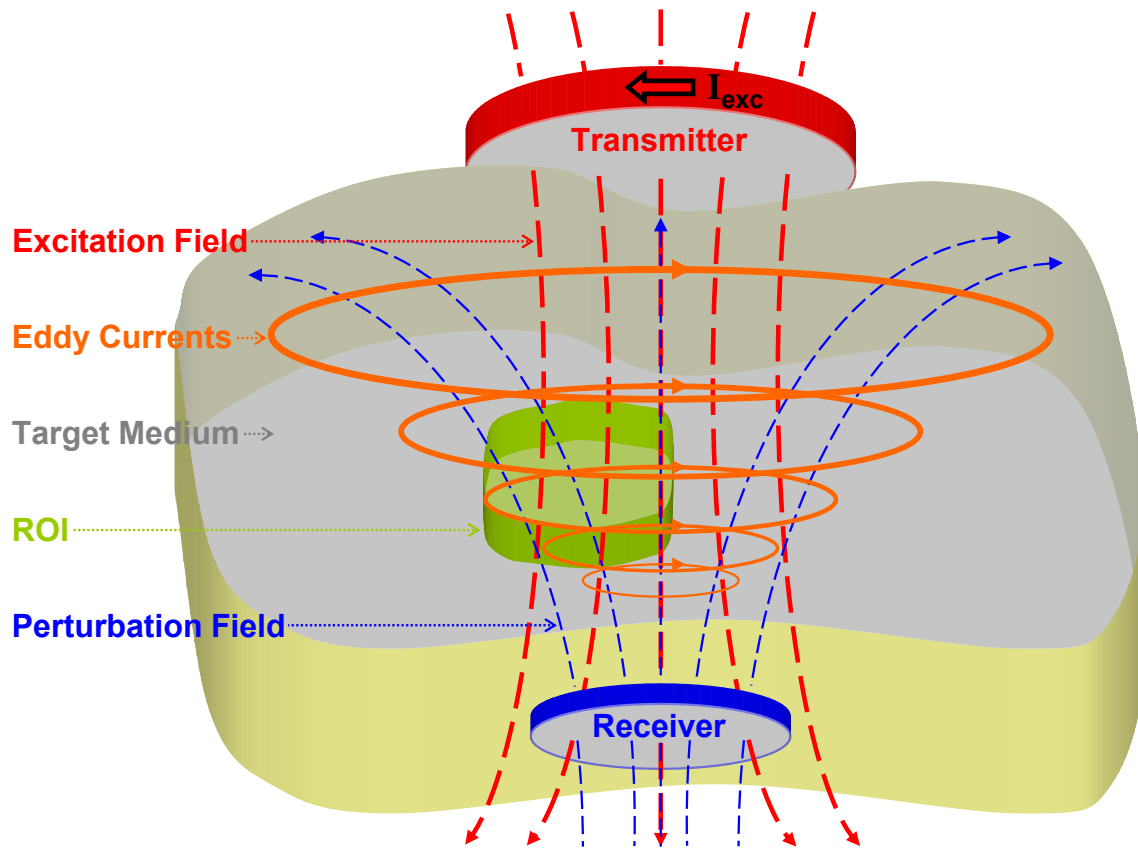
Figure (2.1): Functional concept of MITS. The orange loops symbolize eddy currents distributed in a target medium containing a ROI where the length and thickness of the loops denote the density of the currents. The circulating multifrequency excitation current (I_{exc}) in the transmitter is the cause of the multifrequency excitation field, and the latter is the cause of the eddy currents. The measured perturbation field at the receiver is the carrier of the desired information about the internal PEP distributions at the different frequencies.

The received signals are then fed into the processing stage where they will be preconditioned, i.e., filtered and amplified, and finally precisely decomposed into real and imaginary components by means of an appropriate demodulation method, thus, providing their magnitude and phase information at the applied excitation frequencies. Being directly linked to the perturbation field and hence to the PEP distributions in the target medium, the perturbation voltage represents the actual signal of interest in MITS, i.e., the true MITS signal. Within the mathematical context of the MITS problem, this signal will be treated in terms of its functional relationship to the PEP in order to retrieve their distributions by means of an appropriate image reconstruction algorithm.

2.1.3 Determinants

The following definitions will be used in this chapter:

- B and ΔB are the generated *primary magnetic field* and the induced *perturbation magnetic field*, respectively.
- V and ΔV are the consequently induced *carrier* and *perturbation voltages* in an open receiver coil circuit (voltage mode).
- Equivalently, I and ΔI are the consequently induced *carrier* and *perturbation currents* in a shorted receiver coil circuit (current mode: assuming that these currents do not additionally perturb the primary field B when flowing through the short-circuited receiver coil).
- Δy is the *admittivity change* of the target material (assuming a nonmagnetic target material and hence no change in its permeability μ, i.e. *($\Delta\mu = 0$)*).

Thus, following this terminology and the two bracketed assumptions, some of the most relevant key parameters in MITS can generally be stated as follows:

❖ Signal to Carrier Ratio

The ratio of the *perturbation signal ΔV* to the *carrier signal V*. Equivalently, it can be expressed as the ratio between the corresponding *perturbation* and *primary fields ΔB* and B or *perturbation* and *carrier currents ΔI* and I:

$$SCR = \Delta V / V = \Delta B / B = \Delta I / I \qquad (2.1)$$

❖ Absolute Sensitivity

The ratio of the *perturbation signal ΔV* to the *admittivity change Δy* at a unit excitation current *($I_{exc} = 1\ A$)*:

$$S_{abs} = \Delta V / \Delta y \qquad (2.2)$$

❖ Relative Sensitivity

The ratio of the *absolute sensitivity S_{abs}* to the *carrier signal V*. Equivalently, it can be expressed as the ratio of the *signal-to-carrier ratio SCR* to the *admittivity change Δy*:

$$S_{rel} = S_{abs} / V = SCR / \Delta y \qquad (2.3)$$

The reliable calculation of the above-stated ratios is strongly dependent on the precise extraction of the perturbation signal ΔV -shared between them all- from the total received signal in MITS consisting of the carrier, perturbation and noise signals. In biomedical MITS, the accompanying various types of noise might be of the same order of magnitude as ΔV itself or even larger depending on many direct and indirect factors influencing ΔV, e.g., the measurement object, system, setup, process, settings, environment, etc. Thus, the sum of all experimental (measurement and human) errors might heavily affect ΔV. On these grounds, the overall effect of all kinds of noise on ΔV has to be adequately minimized; otherwise, ΔV could be totally hidden in the noise.

2.2 History

This subchapter only gives a brief general history about MITS; further specific information on the progress of MITS so far regarding different aspects will be provided throughout the study whenever contextually needed or relevant. For a comprehensive historical review on MITS up to the beginning of 2004, the reader is referred to [Griffiths 2001, 2005]; a recent brief review can be found in [Ma and Soleimani 2017].

MIT [Korzhenevskii and Cherepenin 1997; Griffiths et al. 1999; Korjenevsky et al. 2000] and MIS [Scharfetter et al. 2001 (a), 2002 (b), 2003], combined together as MITS, have been a regular field of research since the early 1990s. The MITS research has not only considered the various required hardware for the technical realization of the method, but also the various required software, the relevant mathematical and physical backgrounds, and the limitations of the method regarding all these aspects. Besides its applicability in the industrial field, the research has also concentrated on the applicability of MITS in the biomedical field, which is why biological samples or similar ones regarding their PEP have usually been under investigation. Most of the biomedical MITS research has in turn concentrated on the electrical conductivity among other PEP, not only due to its importance in biomedicine, but also due to the ability to exploit the key feature of MITS, namely, imaging, on the conductivity, whereas due to different difficulties and restrictions, to be discussed in detail in the next subchapter, all trials so far to image the dielectric permittivity or magnetic permeability have been without success, and both PEP have been under estimation of their average values or changes based on their (real) contributions to the total received MITS signal (more precisely, to the *SCR*) without

involving tomography, or even spectroscopy, i.e., without actual reconstruction of their distributions within the investigated samples (some example studies thereon are cited in the following lines; of course, still only speaking of biomedical MITS as industrial MITS has expectedly achieved success in imaging ferromagnetic materials due to their high relative permeability unlike the nonmagnetic biological materials, e.g., [Peyton et al. 1996; Borges et al. 1999; Ma and Soleimani 2018]). Although the permittivity and permeability are more difficult to deal with in biomedical MITS, i.e., to measure or reconstruct, some studies have addressed the sensitivity of the technique to both PEP. The single-frequency MIT measurements in [Watson et al. 2003, 2008; Griffiths et al. 2007] on the permittivity of different media including biological ones delivered some reasonable results; however, the derived estimator of the permittivity was only applicable within a particular context regarding the conductivity of the measured media and the penetration depth of the applied electromagnetic field therethrough, to be explained in the next subchapter. Also the problematic measurement of the permeability of biological media was extensively tackled in [Casañas et al. 2001 (a), 2001 (b), 2003, 2004; Scharfetter et al. 2003] in order to experimentally prove the sensitivity of MITS to the magnetic properties of biological tissues.

Becoming an interesting field for many researchers, the trend of the MITS development research has been oriented by some research groups towards the synthesis of multichannel and/or multifrequency measurement and imaging systems which have served as prototypes for experimental purposes. Due to the many transmit-receive combinations available thereby, the multichannel implementation increases the number of the independent measurements and consequently the image resolution on the one hand, and it reduces the measurement time and consequently the experimental errors on the other hand. Moreover, the multifrequency implementation also offers the latter advantage due to the possibility of simultaneous excitation at multiple frequencies required for spectroscopic applications. The first multichannel systems appeared in the 1990s. They were equipped with single-frequency hardware (MIT) and intended for the industrial research, e.g., [Yu et al. 1993, 1994; Williams and Beck 1995; Peyton et al. 1996, 1999]. Proposed versions for the biomedical research have been later introduced since the beginning of the current century, e.g., [Korjenevsky et al. 2000; Watson et al. 2002 (b); Vauhkonen et al. 2008; Xu et al. 2009; Wei and Soleimani 2012 (a); Xiang et al. 2019], again, without involving spectroscopy technically (MIT), i.e., without implementing multifrequency hardware. Later industrial multichannel systems, e.g., [Ma et al. 2012 (a), 2017 (a)], have still used single-frequency hardware (MIT). [Scharfetter

et al. 2001 (a), 2002 (b); Barai et al. 2012] performed spectroscopic measurements on different biological samples using single-channel, multifrequency systems without involving tomography (MIS). [Rosell-Ferrer et al. 2006] reported a multichannel, multifrequency tomograph (MITS) for biomedical applications. Having only one single transmitter but many receivers, an effective multichannel configuration of their system for imaging purposes was actually only accomplished at the expense of measurement time and quality due to software-controlled stepwise rotation of the measurement object in front of the receivers in order to increase the number of the transmit-receive combinations and hence independent signals. [Scharfetter et al. 2007] introduced a quasi-fully synchronized multichannel, multifrequency tomograph (MITS) for biomedical applications having the ability to quasi-single-shot imaging. The respective hardware for the generation of the multifrequency excitation signal was thereafter effectively modified into a high-speed version in [Scharfetter et al. 2008] which has been definitely required for such an important advancement of the MITS technique as the implementation of multichannel, multifrequency single-shot imaging systems.

2.3   Applicability

2.3.1   The Biomedical MITS Signal

As mentioned hereinbefore, the perturbation signal ΔV corresponding to the secondary field ΔB represents the actual desired MITS signal that will be inversely mapped onto the aimed PEP to be reconstructed during the imaging process. Usually, ΔV can be expressed in relation to the carrier signal V corresponding to the primary field B, i.e., in terms of the SCR as shown in equation (2.4) (restated from [Scharfetter et al. 2003]). Although it represents a ratio, many studies have actually treated the SCR rather than ΔV as the true MITS signal, and the whole outcome of these studies (calculations, reconstructions, conclusions, etc.) was based on the SCR, most often on its imaginary part for certain reasons to be discussed later in this paragraph. Figure (2.2) shows a simple *magnetic-induction (MI)* measurement setup from which equation (2.4) can be derived. Before analyzing this equation, it is relevant to refer to another two ones, equations (2.5) and (2.6), stating the electrical conductivity of the measurement object and the skin depth therein, respectively, in case of time-harmonic electromagnetic excitation. In this case, the conductivity is usually expressed as a complex quantity (admittivity) by equation (2.5),

and the skin depth is usually approximated by equation (2.6).

$$SCR = \Delta V / V = \Delta B / B = \Delta I / I = G_1\, \omega\mu_0\, (\omega\varepsilon_0\varepsilon_r - j\sigma) + G_2\, \chi_m \qquad (2.4)$$

with $\{G_1 = ahr^4 / (2\, (a^2 + r^2)^2)\}$, $\{G_2 = a^3hr^2\, (8a^2 - r^2) / (2\, (a^2 + r^2)^4)\}$ and $\{\chi_m = \mu_r - 1\}$.

$$y = \sigma + j\omega\varepsilon = \sigma + j\omega\varepsilon_0\varepsilon_r \qquad (2.5)$$

$$\delta = \sqrt{(2 / \omega\mu\sigma)} = \sqrt{(2 / \omega\mu_0\mu_r\sigma)} \qquad (2.6)$$

G_1, G_2: geometric constants.

a, h, r: distance between the transmitter or the receiver and the measurement object (half of the distance between the transmitter and the receiver), height (thickness) and radius of the measurement object, respectively.

j, ω: imaginary unit ($\sqrt{-1}$) and angular frequency, respectively.

ε_0, μ_0: *vacuum permittivity and permeability, respectively.*

ε_r, μ_r: *relative permittivity and permeability of the measurement object, respectively.*

ε, μ: absolute permittivity and permeability of the measurement object, respectively.

χ_m: *magnetic susceptibility of the measurement object.*

y, σ: admittivity and conductivity of the measurement object, respectively.

δ: skin depth in the measurement object.

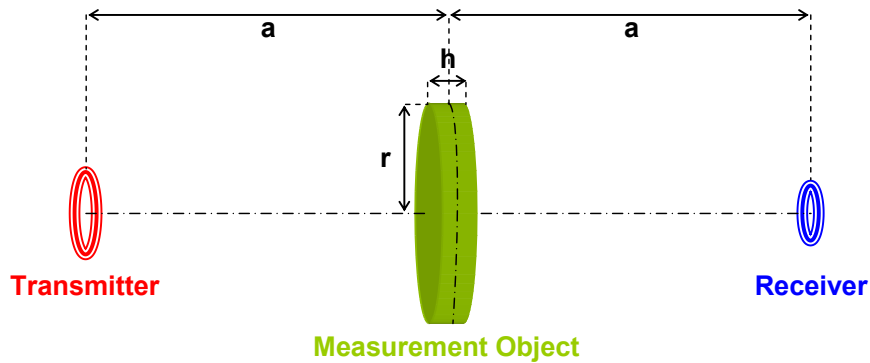**Transmitter** **Receiver**
Measurement Object

Figure (2.2): Illustration of a single-transceiver MI measurement arrangement with the presupposed geometry for equation (2.4). Due to the assumed small radii of the transmitter and receiver in comparison to the distance therebetween, they can be modelled as two magnetic dipoles.

Equation (2.4) will be discussed and considered to be valid under the following conditions [Scharfetter et al. 2003; Casañas et al. 2004; Griffiths 2005]:

- As can be seen in figure (2.2), the measurement object is a cylindrical (disc-shaped) sample of known geometry, centred coaxially between the transmitting and receiving coils. The radii of both coils are considerably small with respect to the distance between them. The sample's thickness is also very small in comparison to this distance *{h « 2a}*.
- The secondary field caused by the sample is much less than the primary one *{|ΔB| « |B|}* (weak primary field perturbations).
- The penetration depth of the primary field through the sample, i.e., the skin depth, is greater than its thickness *{δ > h}*.

Biological tissue fulfills the last two preconditions regarding the measurement object within a wide part of the β-dispersion frequency range, i.e., it represents an appropriate case example of a sample that weakly perturbs the primary field as long as the applied field frequency does not contradict the last precondition concerning the skin or penetration depth. If the measurement setup is properly configured to fulfill the geometric prerequisites on the excitation and sensing coils regarding their dimensions and positions, then equation (2.4) may well be applied to biological tissue.

The first right-hand-side term in equation (2.4) is caused by the induced eddy currents in the sample; while the contribution of the conduction eddy currents to the induction of ΔB is proportional to σ and ω, the contribution of the displacement eddy currents is proportional to ε_r and ω^2; while the former contribution is imaginary, negative and lags *B* by *90°*, the latter one is real, positive and in phase with *B*. [Griffiths et al. 2007; Watson et al. 2008] replaced the relative permittivity of the sample ε_r in equation (2.4) by the quantity *(ε_r − 1)* in order to ensure that *(SCR = 0)* when there is no sample present, i.e., when *(σ = 0 S/m)* and *(ε_r = 1)*; otherwise, equation (2.4) yields a residual *SCR* due to the unit relative permittivity of the air in the measured space between the transmitter and the receiver. The second right-hand-side term in equation (2.4) is caused by the induced magnetic dipoles in the sample; it is proportional to μ_r, independent of ω, real and in phase with *B*; while it is positive in case of a paramagnetic sample *(μ_r > 1, χ_m > 0)*, it is negative in case of a diamagnetic one *(μ_r < 1, χ_m < 0)*. If the sample exhibits neither a paramagnetic nor a diamagnetic behaviour, i.e., if it is nonmagnetic *(μ_r = 1, χ_m = 0)*, then equation (2.4) can be reduced to its first right-hand-side term. In other words, equation (2.4)

may be approximated by the following version if the sample is almost neutral magnetically $(\mu_r \approx 1, \chi_m \approx 0)$, as is usually the case of biological tissue:

$$SCR = \Delta V / V = \Delta B / B = \Delta I / I \approx G_1\, \omega\mu_0\, (\omega\varepsilon_0\varepsilon_r - j\sigma) \qquad (2.7)$$

Summarizing all previous notes on equation (2.4), it can generally be stated that the true MITS signal consists of two main components: a first real one representing the permittivity as well as the permeability (susceptibility) signals, and a second imaginary one representing the conductivity signal. However, the individual contributions of these signals to the total one vary depending on the nature of the material under measurement and the applied excitation frequency. This variation makes it difficult to extract them from the total signal individually, especially in case of biological tissue where the measured signals are of too small magnitudes. Although the recent high-resolution, high-precision hardware generation for high-phase-sensitive demodulation can help to precisely separate the real and imaginary parts of the MITS signal, it cannot help to separate the permittivity and permeability signals, both contained in the real part. Moreover, the systematic errors are expected to appear in the real part [Scharfetter et al. 2001 (b), 2003], making this separation even more difficult. Employing wideband multifrequency hardware and conducting synchronous measurements within properly selected frequency bands based on the nature of the measured material may ease the separation problems being discussed, yet still not sufficient in biomedical MITS when measuring the diverse biological tissues in the low frequency range. As will be seen later in this paragraph, under certain conditions, the conductivity signal of biological tissue, i.e., its imaginary signal, dominates the true MITS signal within the lower β-dispersion frequency range covering the whole *medium frequency (MF)* range and a good part of the *high frequency (HF)* range of the electromagnetic spectrum. At low frequencies, however, the sharp changes in the permittivity of biological tissue make the separation of the different contributions a more complex issue. As shown in equation (2.4), on one side, the dielectric contribution to the MITS signal is proportional to ω^2; on the other side, ε_r may decrease dramatically with increasing frequency which counteracts and can neutralize this proportionality to ω^2. Furthermore, the magnetic contribution, which shares the real part of the MITS signal with the dielectric one, is independent of frequency. [Scharfetter et al. 2003] conducted MI measurements at *50 kHz* on water (diamagnetic: $\mu_r < 1, \chi_m < 0$). They found that the real part of the water signal can be comparable in magnitude to the imaginary part of a signal produced by a sample of physiological conductivity on the one hand, and the diamagnetic contribution to the real part of the water signal is con-

siderably larger than the dielectric one on the other hand. [Casañas et al. 2004] performed in-silico and in-vivo MI measurements at *28 kHz* on the hepatic region of test subjects with different diamagnetic and paramagnetic liver iron concentrations. Their preliminary results showed that at *28 kHz*, the dielectric contribution to the real part of the hepatic-region signal is larger than the diamagnetic one or even dominant, being in marked contrast to water at *50 kHz* shown in [Scharfetter et al. 2003]. The latter even referred to a special case under certain conditions wherein the real-valued permeability signal might entirely dominate the total signal, namely, at low frequencies, a few *[kHz]*, if the permittivity of the measured material is not that large so that the real-valued permittivity signal can be neglected on the one hand, and if the imaginary conductivity signal falls below the noise level on the other hand.

Due to the low sensitivity of biomedical MITS in the low frequency range covering the whole α-dispersion up to the lower limit of the β-dispersion, and due to physical limitations, [Scharfetter et al. 2001 (a), 2003] expected that the reasonable measurement frequency range in biomedical MITS may extend from several tens of *[kHz]* to several tens of *[MHz]*. Their point of view was supported by previous investigations on bioimpedance measurement methods, e.g., [Scharfetter et al. 1999], and by the fact that the β-dispersion of almost all biological tissues occurs within this frequency range where many (patho)physiological changes can be observed and diagnostically valuable information can be obtained. In terms of equation (2.4), the upper limit of the applicable frequency range, i.e., the highest allowable frequency, is determined by the smallest required penetration depth of the applied excitation field through the measured biological medium. In other words, the highest allowed frequency must not exceed a certain threshold level, higher than which the skin depth in the sample (equation (2.6)) becomes less than its thickness; otherwise, the afore-stated last two applicability preconditions for equation (2.4) are violated and the presumed case of weak primary field perturbations is no longer satisfied.

The case of *weak primary field perturbations* caused by biological materials and its consequences has already been addressed in many papers, e.g., [Griffiths et al. 1999; Korjenevsky and Cherepenin 1999; Scharfetter et al. 2001 (a), 2003]. It implies weak interactions between B and ΔB, i.e., $\{|\Delta B| \ll |B|\}$, leading to $\{|\Delta V| \ll |V|\}$, whence the very low *SCR* in biomedical MITS. In case of weak perturbations in the lower β-dispersion frequency range, i.e., between a few or several tens of *[kHz]* and a few or several *[MHz]*, the *SCR* of the almost nonmagnetic biological tissue

(equation (2.7)) is dominated by its imaginary part corresponding to the contribution of the conduction eddy currents, i.e., to the conductivity σ. This statement means actually no more than that in this frequency range, the admittivity y of biological tissue (equation (2.5)) is dominated by its real part, the conductivity term σ, because the *SCR* in equation (2.7) is no more than -aside from the geometric constant G_1- a multiplication of y in equation (2.5) by *(-j$\omega\mu_0$)*, or put it another way, because the *SCR* is proportional to y, and if y is dominated by σ, then the *SCR* is consequently dominated by its contribution. Combining these two conclusions regarding *SCR* and y in biomedical MITS together leads to the inference that the imaginary part of the *SCR* for a weakly perturbing material as biological tissue reflects in good approximation the real part σ of its admittivity y, again, within the frequency range mentioned above. Accordingly, if $\Delta\sigma$ represents the change in the bioconductivity σ, and $\Delta\Phi$ the corresponding change in the *phase angle Φ* between *V, B, I* and *(V+ΔV), (B+ΔB), (I+ΔI)*, respectively, then the previous equations (2.1-2.5) and (2.7) stating y, *SCR*, S_{abs} and S_{rel} may be reformulated into approximated biomedical versions as shown hereunder, where the subscript *BM* stands for *biomedical* or *biological material*:

$$y_{BM} \approx Re(y) \approx \sigma \qquad\qquad (2.8)$$

$$SCR_{BM} \approx Im(SCR) \approx Im(\Delta V) \,/\, |V| \approx Im(\Delta B) \,/\, |B| \approx Im(\Delta I) \,/\, |I| \approx \Delta\Phi$$

$$\approx -G_1 \, j\omega\mu_0 \sigma \qquad\qquad (2.9)$$

$$S_{abs\text{-}BM} \approx Im(\Delta V) \,/\, \Delta\sigma \qquad\qquad (2.10)$$

$$S_{rel\text{-}BM} \approx S_{abs\text{-}BM} \,/\, V \approx SCR_{BM} \,/\, \Delta\sigma \approx \Delta\Phi \,/\, \Delta\sigma \qquad\qquad (2.11)$$

In contrast to biological materials and the induced weak primary field perturbations, electrically high-conductive or magnetically high-permeable materials cannot fulfill the applicability conditions for equation (2.4) as they induce strong primary field perturbations due to their high conductivity or high permeability, respectively, and hence the very small skin depth therein (see equation (2.6)). Consequently, equation (2.4) and the derived ones therefrom (2.7) and (2.9) cannot be applied to such materials. In case of *strong primary field perturbations*, the true MITS signal is an almost entirely real signal which, depending on the physical nature of the measured material and the applied excitation frequency, may mainly represent a conductivity signal, a permeability signal or both together. As regards the former

case, wherein the measured material is of high conductivity and negligible permeability, the previous ratios defining the absolute and relative sensitivity, S_{abs} and S_{rel} in equations (2.2) and (2.3), respectively, or even their constrained biomedical versions S_{abs-BM} and S_{rel-BM} in equations (2.10) and (2.11) (ignoring the subscript BM), respectively, are still applicable because the sensitivity only depends on Δy. In contrast, in the latter two cases, where the measured material is mainly of high permeability or both of high permeability and high conductivity, respectively, all four previous definitions of the sensitivity are no more applicable because the sensitivity also depends on $\Delta \mu$, the change in the permeability μ of the measured material. Naturally, in all three cases, equation (2.8), which approximates the admittivity y in equation (2.5) by the real conductivity σ, is still considered to be applicable as the contribution of the displacement eddy currents in such materials to the induction of the MITS signal may be neglected over a wide frequency range due to $\{\omega \varepsilon_0 \varepsilon_r \ll \sigma\}$.

Even though the bioconductivity signal is relatively small, it is still -within the frequency range of interest discussed in this paragraph- much larger than the biopermittivity signal, the biopermeability signal or both together. In conclusion, when considering these three PEP within the scope of biomedical MITS, it can be stated that the conductivity is, beyond doubt, the easiest one to observe within the most useful part of the β-dispersion frequency range.

2.3.2   Advantages and Applications

Most advantages of MITS are related to its contactless measurement manner. This manner enables the technique to avoid any direct electric (conductive, galvanic) coupling between the tomograph and the patient, hence, avoiding all the related problems, especially those arising when electrode-based measurement methods are in use, e.g.:

- Problematic skin-electrode interface.
- Electrode polarization.
- Restricted ion mobility in electrolytes.
- Temperature dependence.
- The use of contact agents (coupling gels and pastes).
- Boundary effect, i.e., distortion of the streamlines of the applied electric field at the edges of the skin-surface electrodes.

- Parasitic effects due to various stray capacitances, especially those arising between the current-injecting and the voltage-sensing electrodes in the four-wire technique which may heavily affect the bioimpedance spectrum.
- Restricted flow of the injected currents through those body tissues that are completely or partly covered with high-impedance bone tissue, such as the brain tissue under the calvarium. The worst case may be the deeply keratinized and often chapped skin tissue which acts electrically as an insulating layer.

Moreover, the complete galvanic decoupling between the imaging unit and the patient in MITS allows for:

- Optimal non-invasiveness and safety conditions. There can be no leakage currents flowing through the patient. The eddy currents induced within the body are the required operating currents which have not caused any undesirable side effects so far.
- Hygienic usage.
- Feeding the image reconstruction algorithm with the required exact positions of the exciting and sensing coils as they can be well fixed at the desired positions around the measurement space independent of the patient.

Furthermore, MITS might offer many other features than its non-contact nature and the related benefits, e.g.:

- Cost-effective implementation.
- Bedside applicability.
- Continuous monitoring of some vital functions.

There has been no imaging modality that fulfills all these desirable properties or clinical needs together.

Studying the dispersive behaviour of biological tissues regarding their PEP allows for a better understanding of their complex structure and can hence play an important role in the characterization and thus classification of biological tissues regarding different relevant aspects. In this respect, the MITS technique can in turn play an important part in achieving these purposes, not only due to its sensitivity to the different PEP, but also due to its spectroscopic applicability. Obtaining information about ICF, ECF and their proportions for the different tissues can help to draw conclusions about their composition and hydration status which are of particular

importance in the structural analysis of biological tissues and thus in the diagnostic analysis of various clinical conditions. In this regard, the MITS technique may help to obtain the different PEP plots of Cole and Cole (equations (1.1-1.6)) for the different biological tissues and thus to evaluate their structure and fluid balance as these plots allow observing their PEP dispersions and thus their ICF and ECF behaviours in the different frequency ranges. Moreover, besides the PEP, some other tissue-specific parameters can be gained from the plots of Cole and Cole, such as the Cole exponent and the characteristic (relaxation) frequency and therewith its reciprocal, the characteristic time constant; these parameters would complement the aimed characterization and classification of biological tissues. Thus, MITS can be of considerable biomedical usefulness, particularly in the β-dispersion frequency range where many differences between healthy and diseased tissues can be observed, especially in case of pathological accumulations, shifts or whatever changes of watery fluids which can induce considerable PEP changes.

On all these grounds, it looks promising to take advantage of biomedical MITS to monitor several pathological processes and to facilitate different clinical applications, especially those associated with marked conductivity changes. One of the most proposed MITS diagnostic applications with regard to the bioconductivity is imaging of the human brain through the reconstruction of the conductivity distribution within the brain tissue. Such an application might allow for the detection of those cerebral diseases involving concomitant local conductivity changes. A very common research example in this respect has been the detection of brain oedema as suggested in, e.g., [Netz et al. 1993; Gonzáles and Rubinsky 2006; Gonzáles et al. 2010; Jin et al. 2011; Li et al. 2017 (a), 2017 (b), 2019; Zhao et al. 2019] based on MI measurements on different media including living tissues. Such suggestions have been supported by the imaging results of many MIT simulation studies, e.g., [Merwa et al. 2004; Merwa and Scharfetter 2007 (b)]. Another dominating research example in this regard is the detection of brain haemorrhage as suggested in, e.g., [Gonzáles et al. 2013; Sun et al. 2014; Jin et al. 2014; Pan et al. 2015] based on MI measurements on living tissues. Such suggestions have also been supported by the imaging results of many MIT simulation studies, e.g., [Zolgharni et al. 2009 (a), 2009 (b), 2010; Dekdouk et al. 2010; Chen et al. 2010; Xiao et al. 2017, 2018, 2019]. Expectedly, the detection of brain ischaemia has also been addressed parallel to the foregoing two applications as suggested in, e.g., [Gonzáles et al. 2009; Yan et al. 2017] based on MI measurements on living tissues.
Besides the brain or the head, the MITS research has also addressed other body regions, such as cardiac, thoracic ones and the limbs, which has broadened the

biomedical applicability spectrum of MITS towards the investigation of other relevant pathological changes, such as cardiac, pulmonary, extremities oedemata and respiratory disorders. Already in the late 1960s, [Tarjan and McFee 1968] performed MI measurements on the effective resistivity of the human torso and head. Some other in-vivo research examples are: the MIT state-differential (inhalation-exhalation) imaging experiments in [Korzhenevsky and Sapetsky 2001] on the thoracic region; the MIT measurements in [Watson et al. 2003, 2008] on the average conductivity of human thighs; the MIT absolute imaging experiments in [Watson et al. 2008] on the conductivity distribution within a human thigh; the MIT measurements in [Liebold et al. 2008] on the acquisition of heartbeat and breath signals. The same principles applied in all these studies cited above might also be exploited in the examination of water balance in dialysis patients and in the diagnosis of different ischaemic strokes. Some other suggested applications based on the bioconductivity changes are: imaging of teeth caries [Matoorian et al. 1995]; examination of wound healing [Riedel et al. 2002]; measurement of body composition [Goss et al. 2003 (b); Tapp et al. 2003]; monitoring of cryosurgical treatments [Ma et al. 2012 (b), 2016; Ma and Soleimani 2017].

Besides the conductivity, the possibility of including the permittivity and permeability in the MITS biomedical applicability spectrum has also been considered. As for the biopermittivity, [Watson et al. 2003, 2008] used *Re(SCR)* for the estimation of the average permittivity of living human thighs. In the latter study, [Watson et al. 2008], again, using *Re(SCR)*, an absolute image showing the permittivity distribution within a living human thigh was believed to be reconstructed. As for the biopermeability, [Casañas et al. 2001 (a); Scharfetter et al. 2003] emphasized the sensitivity of MITS to low-contrast permeability changes in biological media and suggested exploiting this finding in the noninvasive measurement of physiological and pathophysiological changes of iron concentrations in the human body. Their finding and suggestion could be supported by the preliminary in-vitro and in-vivo results of their MI measurements on hepatic iron overload in [Casañas et al. 2001 (b), 2003, 2004]. Such trials might form a basis for feasible MITS diagnostic applications with regard to the permittivity and permeability.

Generally speaking, the industrial applicability spectrum of MITS differs from the biomedical one; however, there is a material- or application-dependent intersection area between both applicability fields, namely, when biological materials or similar ones regarding their PEP are involved in industrial processes, e.g., in agricultural, food and pharmaceutical industry. In this area, biomedical and industrial MITS

may share one and the same common ground regarding all methodological, technical, mathematical and physical details including the case of weak perturbations and its consequences explained in the previous paragraph, implying that the previous approximation equations (2.8-2.11) for the biomedical case may still be applicable in this area if the involved conditions are satisfied. Even the low-conductive multiphase flow industry is included in this area. [Watson et al. 2008; Wei and Soleimani 2012 (b); Ma et al. 2015] used their biomedical MIT systems to reconstruct images from low-conductive static multiphase phantoms simulating different multiphase flow regimes (in the latter study, [Ma et al. 2015], also an experiment with a quasi-static saline water was conducted). Interestingly, but not unexpectedly, they unusually applied those same relatively high frequencies they usually applied in their biomedical experiments, namely, *10 MHz* in the former study and *13 MHz* in the latter two ones, whereas no frequencies higher than a few hundreds of *[kHz]* have usually been applied in the industrial MITS research. This is, however, comprehensible as no conducting phase of higher than *12.64 S/m* was used in their experiments.

It is a matter of course that electrically high-conductive or magnetically high-permeable materials are extremely far from this interfacial application area between biomedical and industrial MITS. Dealing with such materials represents one of the most typical application examples suggested in the industrial MITS research, especially for the metal industry, including the *non-destructive testing (NDT)* of metals for defect-free production and operation. Actually, aside from its biomedical applicability, MITS was originally mainly intended for industrial purposes. In this respect, many industrial applications have been proposed, some whereof have already been experimentally tried. More information on the industrial aspect of MITS can be found in [Griffiths 2001, 2005; Tapp and Peyton 2003; Ma and Soleimani 2017].

A recent interesting -but rather complex- use of MITS is to employ MITS in combination with another tomographic modality in order to take advantage of both modalities in certain applications where the use of either modality alone does not necessarily deliver all the desired information, thus, forming some kind of *dual-* or *hybrid-modality tomography*. [Zhang et al. 2014] combined MIT and *electrical capacitance tomography (ECT)* in order to image a sample of high conductivity, iron, together with another one of low permittivity, wood. Unexpectedly, the high permeability of iron was completely excluded from the discussion, analysis and image reconstruction algorithm; however, expectedly, its high conductivity allowed for

some reasonable preliminary results. In a subsequent study, [Zhang et al. 2015] applied the same dual modality (using another MIT system and a modified ECT system), however, to static multiphase phantoms comprising oil, water and gas (air), a typical three-phase flow regime in the petroleum industry in the usual continuous-flow case. In a first experiment, their objective was to image a phase of low permittivity (silicone oil: $\varepsilon_r \approx 2.5$) together with another one of relatively much higher permittivity (water: $\varepsilon_r \approx 80$) within a gas background (air: $\varepsilon_r \approx 1$), where saline water of different conductivities as well as non-conductive (deionized) water was tried; in a second experiment, the objective was to image the oil together with the air within a water background, where, again, saline water of different conductivities as well as deionized water was tried. Whether used as a background or a main phase, their experiments delivered reasonable results in case of conductive water (tap or saline water: $\sigma \geq 0.0586 \ S/m$), in marked contrast to non-conductive water (deionized water: $\sigma = 0.0003 \ S/m$) or even very low-conductive water $(\sigma \leq 0.02 \ S/m)$. Also in case of free-space (air) background, reasonable results could be obtained. The main idea underlying both studies was to gain a priori information on the conductivity distribution within the multimedia phantom by means of MIT, i.e., to reconstruct an image of the conductive medium (iron in the former study; saline water in the latter study), and then to use this information to update the forward solution of ECT and hence to use ECT to reconstruct the permittivity distribution within the phantom excluding the conductive medium, i.e., to gain an image of the dielectric medium (wood in the former study; oil and air in the latter study). Afterwards, both images may be merged (fused) into a final complete one showing both conductive and dielectric media together (iron with wood in the former study; saline water with oil and air in the latter study). Another example of a dual-modality application was experimented in [Ma et al. 2017 (b)] where MIT was combined with the -differently called in the literature- *electromagnetic velocity tomography (EVT)* in order to calculate the volumetric flow rate of water in a multiphase flow phantom comprising a continuous conductive phase (saline water: $\sigma \approx 3.5 \ S/m$) and a discontinuous non-conductive one (silicone oil: $\sigma \approx 0 \ S/m$), a typical two-phase flow regime in the oil industry in the usual wholly continuous case. Also this hybrid modality yielded reasonable results. While MIT provided the volumetric fraction of water based on the reconstructed conductivity distribution within the observed flow, EVT provided its local velocity based on the reconstructed velocity distribution. Afterwards, both parameters were used to calculate the aimed water volumetric flow rate.

The previous three examples involve ECT or EVT which are counted among industrial imaging modalities; therefore, these examples do not necessarily imply

prospective biomedical dual-modality application employing MITS. However, combining MITS with another biomedical tomographic modality will allow for such application and might improve the imaging outcomes. An example of such combination was simulated in [Schober 2011] where MIT was used in conjunction with *electrical impedance tomography (EIT)*, however, not the conventional EIT, but its *induced-current* version *(ICEIT)* wherein the required alternating operating currents were coupled to the simulated object under test inductively by means of the MIT transmitting coils rather than galvanically by means of current-injecting electrodes. Generally, the reconstructed MIT images were better than those reconstructed by ICEIT or the hybrid modality (MIT-ICEIT); however, no explicit conclusions about these results were drawn because further analysis and comparison regarding many other different aspects than only the used regularization matrix would have been needed. Expectably, due to the double number of the simulated independent signals in MIT-ICEIT in comparison to MIT or ICEIT, the calculated radial resolution in MIT-ICEIT was, yet only slightly, higher than in MIT or ICEIT. As a matter of course, such combination of MIT and ICEIT into MIT-ICEIT requires an appropriate adaptation of both solution algorithms into a consistent hybrid algorithm.

In this regard, a somewhat similar concept to the hybrid-modality tomography arises when replacing the receiving subsystem of the MITS system, i.e., the receiving circuitry including the receivers, by another subsystem obeying a different methodology. Examples of such tomographic modalities with prospective biomedical applications may be *magneto-acoustic tomography with magnetic induction (MAT-MI)*, e.g., [Hu et al. 2010, 2011] and *magnetic induction tomography with optical atomic magnetometers (OAM)* or simply *optical MIT* (no agreed abbreviation in the literature), e.g., [Marmugi and Renzoni 2016; Deans et al. 2016]. While MAT-MI employs ultrasonic transducers instead of the conventional MIT receivers, OAM-based MIT employs optically pumped *radio-frequency OAMs (RF-OAM)*. Of course, a corresponding modification of the image reconstruction algorithm is to be considered.

2.4   Motivations and Objectives

It is much to be hoped to find MITS in some routine medical applications in the future. However, answering such hopes certainly involves a great deal of arduous research work because living tissues are necessarily expected to be under inves-

tigation, and dealing with such complex biological structures as which is definitely most challenging. Therefore, the different problematic issues regarding the measuring and imaging processes have to be comprehensively analyzed and carefully tackled in order to hopefully ultimately activate biomedical MITS in routine clinical use. Furthermore, as far as possible and practicable, it is of prime importance to address these issues experimentally rather than only by simulation because many of the problems to be confronted with during the technical implementation of the MITS modality are unpredictable, extremely difficult to simulate or cannot be simulated (detailed examples will be presented in chapters (5) and (6)), the reason why this study is completely based on experimental research. A probably most appropriate starting point in this regard would be the MITS tomograph itself being responsible for the measuring and imaging processes, the reason why this thesis is completely concerned with tomograph optimization in biomedical MITS.

For these purposes, the proposed general optimization approaches to be introduced in this subchapter were applied to a prototype MITS tomograph already existing at Institute of Medical Engineering (IMT), Graz University of Technology (TUG) [Issa 2007; Scharfetter et al. 2007]. The performed optimization covered the tomograph's hardware, software and measurement environments, and is naturally not to be considered as to be specific to this prototype tomograph, but to any MITS tomograph in general to be optimized to meet the technical requirements for biomedical applications:

❖   Hardware

The optimization essentially concerned the core module of the hardware environment, namely, the transceiver system, and hence the relevant subsystems: mechanics, electrics and electronics.

❖   Software

The optimization essentially concerned the core module of the software environment, namely, the imaging program, and hence the relevant subprograms: data postprocessing, sensitivity calculation and image reconstruction.

❖   Measurement

The optimization essentially concerned the detection of unintentional patient movements during measurement and the elimination of their consequences prior to image reconstruction.

2.4.1   Hardware Optimization

2.4.1.1   Mechanical Structure and Transceiver System

As mentioned previously, the construction of multichannel systems has become an indispensable requirement in MITS. It allows, above all, for a sufficient dataset of independent signals required for image reconstruction to be acquired. For the purpose of practical simulation of a multichannel arrangement using one single transceiver, the idea of stepwise mechanical scanning has already been employed since the 1990s, e.g., [Al-Zeibak and Saunders 1993; Griffiths et al. 1999]. Since then, mechanical scanning has been performed in more or less different ways. [Űlker and Gencer 2002; Riedel et al. 2002; Riedel and Dössel 2003; Karbeyaz and Gencer 2003; Xu et al. 2008] translated a single transceiver over the object to be measured. [Trakic et al. 2012] rotated a single large transmit-receive coil around the measurement object, and called this setup *rotational* or *rotating MIT (RMIT)*. In a simple preliminary way, [Wei and Soleimani 2012 (c)] tried to evaluate the RMIT idea in the industrial application field by manually rotating a tiny circular array of *1 cm* radius and *8* off-the-shelf tiny ferrite-core transmit-receive coils around metallic objects. [Igney et al. 2005] applied the mechanical scanning principle conversely, i.e., they translated a tank including a sample over a planar array of *4-8* transmitters-receivers rather than the array itself. By some contrast, [Rosell-Ferrer et al. 2006] rotated the sample within -but without- the tank in front of a circular array of *14* receivers exposed to a single excitation field, announcing therewith, actually, the principle of rotational mechanical scanning, i.e., RMIT, prior to the two above-mentioned examples in 2012. Again, having only one single transmitter, [Liu et al. 2008, 2014] rotated a sample placed on a circular plate in front of an array of *15* receivers.

As the reduction of measurement time and consequently experimental errors affecting the already too small signal in biomedical MITS is of fundamental importance, it is far better to increase the number of the transmit-receive combinations (independent signals) by constructing true multichannel MITS transceiver systems with a fair number of transmitters and receivers rather than by conducting multiple separate measurements with different transmitters-receivers arrangements or by scanning the measurement object mechanically (whether through moving it itself or the transmitters and/or receivers) because the latter methods increase the experimental errors due to worsening one or more of their preexisting sources as well as involving one or more new sources in the measurement process.

Except in simulation MITS studies, multiplane (multilayer) transceiver systems have rarely been implemented. Depending on the layout of the coil array and the dimensions of the target medium, the additional main advantage of this design is that it can largely or even entirely cover or enclose the desired imaging region. [Scharfetter et al. 2008] presented a two-plane circular transceiver array surrounding a cylindrical measurement space, an upper and a lower plane with *8* transceivers each. The same two-plane arrangement was configured in [Wei et al. 2012], but with *8* transmit-receive coils in each plane rather than *8-8* transmitters-receivers. By some contrast, [Xu et al. 2009] arranged a two-plane transceiver array in two circular layers of different radii, respectively, on the outer surface of a hemispherical glass bowl simulating the human brain, an upper and a lower layer with *9* and *6* transceivers, respectively.

If vertical cross-sectional imaging should be performed on the human body or models thereof, especially on its long parts such as the extremities and torso, then adapting a multiplane configuration to the MITS transceiver system is more appropriate than a single-plane one to longitudinally scan such parts.

Most of the MITS transceiver systems constructed so far have had a circular or annular layout. This circular configuration has been adapted to the transmitters and receivers in case of multiple of both, e.g., [Korjenevsky et al. 2000; Watson et al. 2008; Scharfetter et al. 2008; Vauhkonen et al. 2008; Xiang et al. 2019] or only to the receivers in case of one single transmitter, e.g., [Rosell-Ferrer et al. 2006; Liu et al. 2008]. The circular coil system has also been preferred in industrial MITS, e.g., [Peyton et al. 1996, 1999; Ma et al. 2012 (a); Wei and Soleimani 2013]. The simplicity and radial symmetry of the circular configuration make it very attractive; it can be very appropriate, on the one hand, for the suppression of the carrier signal if certain arrangements are taken into account, on the other hand, for the step-wise rotation of the coil system (whether partially or entirely) or the measurement object in order to increase the number of the independent measurements as exemplified hereinabove. Moreover, the circular geometry has been preferred in MITS simulation work, whether in pure simulation studies, e.g., [Merwa at al. 2005 (a), 2006; Scharfetter et al. 2006 (b); Merwa and Scharfetter 2007 (a), 2008; Liu et al. 2019] or in mixed studies, e.g., [Merwa at al. 2005 (b); Scharfetter et al. 2006 (a); Brunner et al. 2006]. The circular configuration has proved to be very convenient to apply a simple mathematical model simulating a cylindrical imaging space containing the target medium.

If horizontal cross-sectional imaging should be performed on the human body or models thereof, especially on its wide parts such as the thorax, abdomen and pel-

vis, then adapting an elliptical configuration to the MITS transceiver system is more appropriate than a circular one to approximate the shapes of such parts.

In biomedical MITS, the primary (carrier) signal is many orders of magnitude larger than the secondary (biological) signal. If the former can be considerably suppressed or possibly eliminated, then a wide or maximal dynamic range can be reserved for the latter and thereby higher measurement precision and resolution can be reached because this will result in higher SCR and as a direct consequence higher S_{rel} (see equations (2.1) and (2.3)). One of the most suggested approaches for carrier signal suppression or cancellation has been based on the use of different types of gradiometers (GRAD), each consisting of two contrarily wound (counter-phase), serially connected coils, such as the axial GRAD with its two coils facing each other coaxially and the planar GRAD (PGRAD) with its two coils lying next to each other in the same plane, where the coils have usually been etched on *printed circuit boards (PCB)* rather than conventionally wound on plastic formers. Such GRADs have been first adapted to single-channel systems, e.g., [Rosell et al. 2001; Scharfetter et al. 2001 (a); Riedel et al. 2002] and later to multi-channel systems, e.g., [Riedel et al. 2004; Scharfetter et al. 2008; Xu et al. 2009; Xiang et al. 2019]. A second approach in this regard has been the electronic cancellation of the primary signal through subtracting it in a proper way in a later electronic stage after the receiving stage as applied in [Griffiths et al. 1999; Scharfetter et al. 2002 (a)] to single-channel arrangements and in [Yu et al. 1994, 1998] to multi-channel industrial prototypes. For better suppression results, [Scharfetter et al. 2001 (a); Űlker and Gencer 2002; Karbeyaz and Gencer 2003] combined the gradiometer concept with the electronic one in single-channel systems. Another approach in this respect was presented in [Watson et al. 2004, 2005] where they suggested compensating or minimizing the primary signal in planar-array MIT through special receiver coil alignment. The practical implementation of this suggestion in a planar-array system was presented in [Igney et al. 2005] using an array of *4-8* transmitters-receivers. [Scharfetter et al. 2004, 2005] experimented with the new aligned receiver and called it *SC90* and *zero flow coil (ZFC)*, respectively, where SC90 denotes a *solenoid coil (SC)*, the face or axis whereof is *perpendicular (90)* to the face or axis of the transmitting coil, respectively; thus, the former receives no primary magnetic flux from the latter, as is exactly the case with the ZFC, whence the name. Prior to that, a related idea was adapted in [Yu and Peyton 1998; Peyton et al. 1999] to industrial multichannel systems through certain overlapping of the transmitting and receiving coils; however, their alignment method was only adequate for the suppression of those two carrier signals induced in each

receiver by the two adjacent transmitters, but not those carrier signals induced by the non-adjacent transmitters. To benefit from both concepts, [Scharfetter et al. 2005; Huang et al. 2007] combined the gradiometer concept with the alignment one obtaining a *zero flow/flux GRAD (ZFGRAD)* and an *alignment GRAD*, respectively, where, again, *zero flow/flux* indicates that no primary magnetic flux flows through the GRAD, as is exactly the case with the alignment GRAD. [Scharfetter et al. 2004, 2005] studied many types of receivers: horizontally oriented solenoids aligned as ZFCs (SC90), horizontally oriented PGRADs aligned as ZFGRADs and vertically oriented PGRADs aligned face to face with the transmitting coils. They found that the ZFC would significantly simplify the measurement setup and was the best of all analyzed receiver versions regarding sensitivity. While the ZFC suffered more from external electromagnetic interferences, the ZFGRAD and PGRAD were more prone to systematic errors as discussed in detail in [Scharfetter et al. 2003; Scharfetter 2005, 2007]. Due to their electrical realization as a series connection of two counter-phase coils, it is never easy to ensure that no mismatch between the two coils in any parameter whatsoever already exists, e.g., electrical parameters and mechanical adjustment, or will exist, e.g., parasitic effects and temperature. [Griffiths 2005] reemphasized the applicability of the electronic cancellation concept to multichannel systems; however, small amplitude and phase drifts of the compensation signal might falsify the cancellation process dramatically.

Considering all these concepts for the suppression of the primary signal, while the gradiometer concept would require high mechanical and thermal stability, the electronic concept would require high electronic stability. In contrast, the alignment concept with the ZFC is very simple to implement and can be, if the ZFC is properly shielded, the best compromise between them all to be adapted to the MITS transceiver system.

In this work, an adjustable multichannel, dual-plane elliptical transceiver system with a two-layer array of *2x8* air-core solenoids acting as transmitters and a two-layer array of *2x8* PCB *planar ZFCs (PZFC)* acting as receivers shall be constructed and adapted to the existing MITS tomograph.

Relevant hardware optimization tasks required to accomplish the functions of the new mechanical structure and transceiver system shall be:

- Adequate, uncomplicated adjustment mechanism for an effective suppression of the carrier signal.

- Solid, metal-free (non-conductive and non-permeable) mechanical construction with an easy-to-handle opening mechanism in order to allow positioning a test person or a large test model into the transceiver system.
- Immunity against internal and external noise sources without the need for any kind of inconvenient electromagnetic or electrostatic shielding enclosures or cages which might complicate the mechanical body of the transceiver system and thus the measurement setup.

2.4.1.2   Signal Generation and Intermediate Amplification

The generation of the carrier signal in the prototype tomograph was realized by means of *8 digital-to-analog converters (DAC)*, each with a full-scale output voltage range of *±10 V*. In spite of the satisfying resolution of *16 bit* of this *8*-channel DAC card, its maximum multichannel update rate of *1.25 MS/s* was quite low for an MITS tomograph. Therefore, [Pamperl 2008] implemented a new high-speed *8*-channel DAC card with a multichannel update rate of up to *150 MS/s*. As these new *8* DACs have a full-scale output voltage range of only *±1 V* which is as low as *10%* of the allowed input voltage of the *8* subsequent *power amplifiers (PA)*, an additional *8*-channel non-power amplification stage between the *8* DACs and the *8* PAs is required, where an amplification factor of *10* should completely compensate for the loss in the excitation signal amplitude consequent on the replacement of the low-speed DAC card.

In this work, an *8*-channel, high-level preamplification circuit for the multifrequency excitation signal shall be implemented and adapted to the existing MITS tomograph.

The new preamplification PCB shall ensure:

- A flat frequency response over a frequency range far wider than the tomograph's operating frequency range for possible future extension of the latter.
- Stable integration into the tomograph's circuitry system without any parasitic effects on any other circuits thereof and vice versa.

2.4.1.3 Control Experiments

Measurement errors caused by hardware inaccuracies may propagate to image reconstruction and hence affect the aimed images, especially in biomedical MITS where the useful signals are of too small magnitudes. On this account, different test measurements have to be conducted in order to check the functionality of the optimized hardware components and evaluate their appropriateness accordingly.

In this work, through various control measurements with uniform settings, the overall performance of the MITS tomograph with regard to the optimized hardware shall be assessed.

The assessment shall consider the different relevant aspects in this regard:

- Experimental sensitivity.
- Measurement noise.
- Parasitic coupling.
- Carrier signal suppression.
- Frequency response.

2.4.2 Software Optimization

2.4.2.1 Data Processing and Image Reconstruction

The measurement phase comprises signal transmitting, receiving, preprocessing, acquisition and postprocessing, all occurring during measurement, i.e., online. Afterwards, the gained data undergo a further extensive offline data analysis and preprocessing phase comprising data correction, evaluation, inspection and preparation. This phase is managed by means of a dedicated, already existing *graphical user interface (GUI)* at IMT-TUG. Being the measurement (forward) data to be dealt with in image reconstruction in order to reconstruct the corresponding imaging (inverse) data, the output data of this GUI need to be furthermore processed (prepared) in various ways in accordance with the various image reconstruction schemes to be carried through, listed hereinbelow. Therefore, another comprehensive program dedicated to the subsequent phase of the data analysis and preprocessing phase, i.e., to the data postprocessing and image reconstruction phase, is required.

In this work, a stand-alone data postprocessing and image reconstruction GUI shall be programmed and adapted to the existing MITS tomograph.

The new GUI shall allow for:

- Various imaging types:
  - Static imaging (absolute imaging).
  - Dynamic, parametric and dynamic-parametric imaging (differential imaging), namely, respectively:
    - State-differential imaging.
    - Frequency-differential imaging.
    - State-frequency-differential imaging.
- Various regularized solutions:
  - Maximum a posteriori solution.
  - Tikhonov solution.
  - Truncated singular value decomposition solution.
- Preparing and outputting the reconstructed imaging data for tomographic visualization.

Relevant software optimization tasks required to accomplish the functions of the new GUI shall be:

- Adaptation of the existing algorithms responsible for the solution of the MITS forward problem and the calculation of the sensitivity matrix.
- Preparing and outputting the calculated sensitivity matrix for the solution of the MITS inverse problem by means of the new GUI.

The above-mentioned *hybrid dynamic-parametric imaging* represents a new imaging approach in MITS to be addressed and experimentally tried for the very first time thus far in this study, i.e., in biomedical MITS. As its name implies, this approach combines the functions or properties of both dynamic and parametric imaging together. When choosing the frequency as the influencing parameter regarding parametric imaging, the new concept yields the above-mentioned *hybrid state-frequency-differential imaging*. When, as is the case in this work, an actual MITS tomograph with multifrequency hardware is available, no more than one single measurement is required to attain the corresponding hybrid state-frequency-differential images, namely, a combined state-frequency-differential measurement.

Accordingly, the proposed hybrid imaging concept allows benefiting from the advantages of both dynamic and parametric imaging together and thus gathering the information provided by the corresponding state-differential and frequency-differential images in one and the same image gained from one and the same measurement.

2.4.2.2   Imaging Experiments

Imaging represents the principal objective of biomedical MITS. On this account, the overall performance of the MITS tomograph with regard to the accomplished optimization in its entirety has to be assessed through imaging experiments.

In this work, through multifrequency measurements in the β-dispersion frequency range on different biological targets located within background media of physiological conductivity, and through image reconstruction performed on the resulting real measurement data, the biomedical applicability of the optimized MITS tomograph shall be ascertained.

The imaging process shall be conducted according to different types:

- Dynamically: state-differentially.
- Parametrically: frequency-differentially.
- Dynamically-parametrically: state-frequency-differentially.

where the images of each type shall be reconstructed according to different intended regularization schemes in the context of different implemented inverse solvers, respectively:

- Maximum a posteriori regularization based on the data covariance matrix.
- Tikhonov regularization based on the identity matrix.
- Truncated singular value decomposition.

Parallelly, based on the performed measurement and image reconstruction tasks, the applicability of the new hybrid dynamic-parametric (state-frequency-differential) imaging approach in biomedical MITS shall be assessed.

2.4.3 Measurement Optimization

2.4.3.1 Motion Detection and Artefact Elimination

In biomedical MITS, experimental errors might affect the useful signal to such an extent that no usable images at all can be hoped for. Experimental errors in biomedical MITS can generally be classified into measurement and human errors; more specifically, the former class can in turn be subclassified into systematic and unsystematic (random) errors, and the latter one into examiner and patient errors. Measurement errors can be reduced or corrected if appropriate procedures are undertaken before, during and after measurement. A common simple approach is averaging of multiple signal frames during a stationary phase of the measurement in order to increase the *signal-to-noise ratio (SNR)* in case of unsystematic errors. Additional data-detrending prior to averaging can also be effective in removing the systematic slow, linear drifts. Both error correction procedures were applied to all measurements performed throughout this work without exception. Naturally, systematic errors may be greatly reduced or even eliminated if their reasons can be exactly identified. As regards human errors, whether examiner- or patient-related ones, they can be avoided if good care is taken before and during measurement; however, they can sometimes be unavoidable in biomedical MITS as in case of unintentional movements of the patient during measurement which might induce an unwanted signal change as large as the biological signal itself or even larger. Therefore, it would be highly desirable to be able to deal with the consequences of such human errors (unintentional patient movements) -as in case of measurement errors- after measurement prior to image reconstruction in order to cancel out the motion-induced signal errors and hence motion artefacts in the images to be reconstructed without any need to repeat the time-consuming measuring and imaging processes. Highly desirable would be also to be able to filter out similar motion artefacts caused by other unwanted movements during measurement than those unintentional ones of the patient, such as unexpected movements of the transceiver system, whether its transmitters, receivers or both together, whether one, some or all of them. In addition, it is of particular importance that any proposed motion detection and artefact elimination methodology would not require complex implementation or complicate the measurement setup or the measurement process.

Heretofore, specific MITS studies on detection of unwanted movements of the target or transceiver system and elimination of the resulting signal errors have rarely

been published. [Lanfermann et al. 2008; Scharfetter et al. 2010] suggested tracking the target through mounting small coils thereon and reconstructing their positions. The gained tracking information, i.e., the reconstructed positions of the coils, might then be used in a proper way to filter out the movement artefacts. Although interesting, such a tracking idea requires, on the one hand, the reconstruction of the exact positions of the coils on the target which might be achieved by means of an appropriate image reconstruction algorithm for the nonlinear MITS problem, on the other hand, another appropriate algorithm for the elimination of the movement artefacts in the reconstructed target images based on the reconstructed coils' positions. While the former requirement is computationally very time-consuming due to the iterative nature of such algorithms, the latter one is a much more complex issue to address and hence to implement such an unproblematically applicable algorithm based just only on a few possibly changing reference points in the *four-dimensional (4D)* target space during measurement.

In this work, an uncomplicated measurement optimization technique in biomedical MITS allowing the detection and elimination of motion-induced signal errors prior to image reconstruction shall be developed and adapted to the existing MITS tomograph [Issa and Scharfetter 2018]. This technique will be termed *detection and elimination* and abbreviated as *D&E*. Based on the possible use of two kinds of electromagnetic markers within two contexts of motion detection, respectively, the flexible choice between two types of D&E, respectively, each with its own advantages, shall be offered. These two kinds, contexts and types will be termed, pairwise respectively: *active marker* and *passive marker*; *active detection* and *passive detection*; *active D&E* and *passive D&E*.

Relevant software optimization tasks required to accomplish the functions of the new D&E technique shall be:

- Adaptation of the measurement control and synchronization suite of the measurement software package.
- Adaptation of the data processing and image reconstruction suites of the imaging software package.

2.4.3.2 Control and Imaging Experiments

The validation of the D&E methodology must consider two intuitive facts. First, the induced signal errors due to any unwanted movements, whether of the target or transceiver system, propagate to image reconstruction resulting in motion artefacts; second, the D&E approach requires a precise separation of the target and marker signals, both contained in the total received MITS signal. Therefore, the correct evaluation of the D&E technique requires measuring a moved marked target as well as an unmoved unmarked one along with subsequent imaging. Afterwards, the resulting erroneous and error-free signals and images have to be compared with each other on the one hand, and with those signals and images obtained after applying the D&E technique to the erroneous signals on the other hand.

In this work, through multifrequency measurements in the β-dispersion frequency range on an electromagnetically marked background medium of physiological conductivity containing a biological phantom, and through image reconstruction performed on the resulting real measurement data, the applicability of the developed D&E measurement optimization technique in biomedical MITS in case of active and passive D&E shall be ascertained.

The D&E technique shall be applied using a variety of markers:

- A switchable coil used as a non-permanent active marker.
- A ferromagnetic plate used as a permanent passive marker.
- A closed coil used as a permanent passive marker.

For the sake of good order, the discussed thesis goals will be handled in the following three chapters in the same manner; first, the methods complete with the experimental setup and performed measurements will be explained, then the results will be presented and discussed. In addition, normal and common characters and symbols will be used to represent all mathematical terms whatsoever; however, whenever contextually necessary, bold lower- and upper-case letters will be used for compact vector and matrix notation, respectively.

Chapter 3

Hardware Optimization

This chapter introduces the prototype MITS tomograph to be optimized for biomedical application and used in the experimental part of this thesis. It discusses the performed hardware optimization stage in conjunction with control experiments qualifying the overall performance of the MITS tomograph with regard to the optimized hardware.

3.1   Prototype versus Optimized MITS Tomograph

Figure (3.1) shows both the preliminary and the enhanced version of the MITS tomograph developed at IMT-TUG.
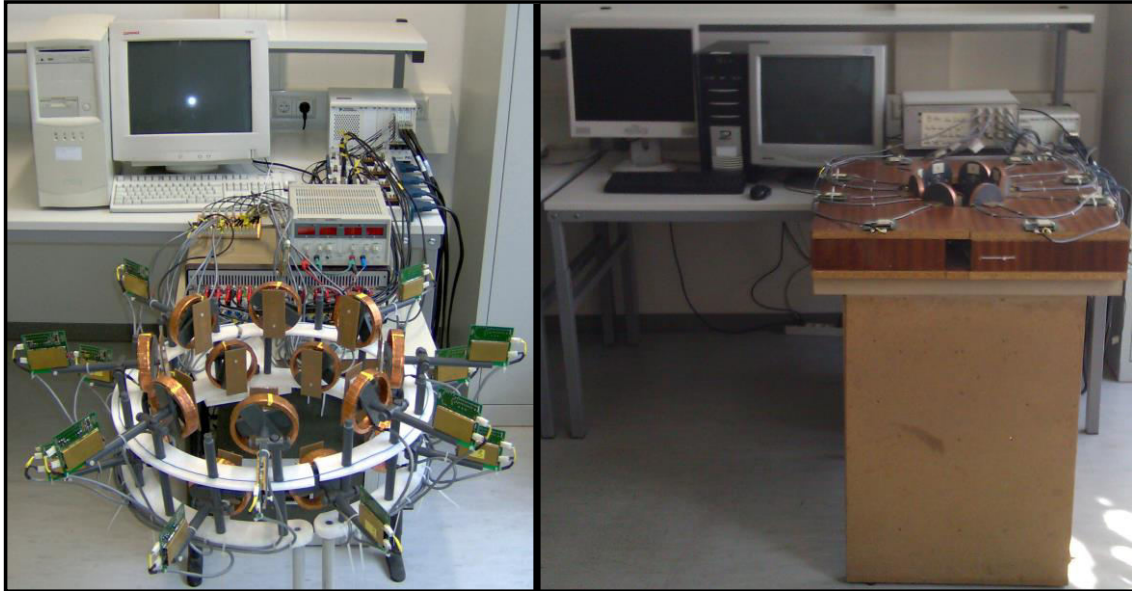

Figure (3.1): Prototype and optimized MITS tomographs. Left: prototype tomograph, right: optimized tomograph. Obvious is the difference in the configuration of the coil system and the construction of its supporting body. While the prototype coil array is circular and held by a plastic framework, the optimized one is elliptical and fitted in a custom-designed, robust wooden table. The prototype coil system is made up of a two-layer array of 2x8 air-core solenoids acting as transmitters and another one of 2x8 vertically oriented PGRADs acting as receivers; the optimized coil system will be described in every detail hereinafter.

Various experiments were performed using the prototype version in the early stage of this work, but most of the research was conducted after upgrading it to the optimized version. During the course of the optimization process, some subsystems of the prototype system were completely redesigned and newly created, e.g., mechanics, transceiver array, and data processing and image reconstruction software; other subsystems were partially modified, e.g., electrics, electronics, and measurement control and synchronization software. In this chapter, only the most significant new hardware implementations will be detailed; for detailed information about all unmodified implementations, the reader is referred to [Issa 2007].

3.2 Measurement Chain

Figure (3.2) shows a simplified block and flow diagram for the optimized MITS to-mograph describing the signal flow path in the order explained thereunder.

Transceiver System & Measurement Object
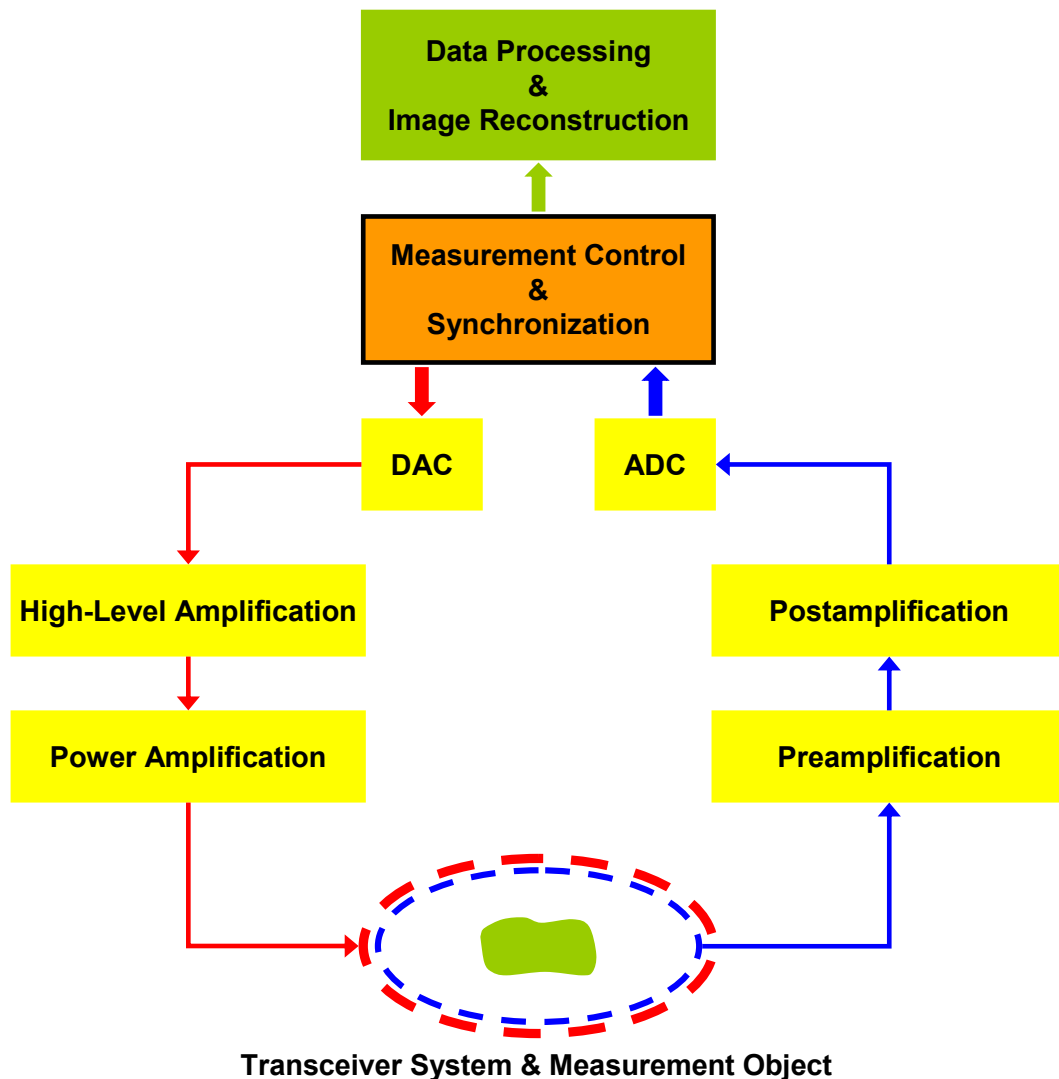
Figure (3.2): Measurement chain of the optimized MITS tomograph. The host computer (orange-coloured block) controls the whole measurement process. In a first step, the generated multifrequency signals by the 8 available DACs will be high-level-, power-amplified and 8-to-16 demultiplexed in order to excite all 16 transmitters of the coil system. In a second step, the 16 received signals will be pre-, post-amplified and 16-to-8 multiplexed in order to acquire them all by the 8 available ADCs. In the final step, the acquired multifrequency data will be processed, and the images will be reconstructed.

❖   Measurement Control and Synchronization

The central computer controls all subprocesses of the measurement process and regulates their chronological order through predefined triggering and synchronization protocols. These tasks are managed by means of the programming system-control environment *LabVIEW™* from *National Instruments™ (NI™)*.

❖   DAC

The DAC channels are responsible for the generation of the multifrequency carrier signals.

❖   High-Level Amplification and Power Amplification

The generated carrier signals will be high-level- and power-amplified before feeding them into the transmitters.

❖   Transceiver System and Measurement Object

The transmitted excitation signals interact with the target object, and the induced perturbation signals will be picked up at the receivers.

❖   Preamplification and Postamplification

The received signals will be pre- and post-amplified before feeding them into the *analog-to-digital converters (ADC)*.

❖   ADC

The ADC channels are responsible for the acquisition of the conditioned received signals.

❖   Data Processing and Image Reconstruction

The acquired data at the different frequencies will be analyzed and processed, the MITS forward and inverse problems will be solved, and the reconstructed imaging data will be prepared for tomographic visualization. These tasks are managed by means of the programming numerical-computation environment *MATLAB*® from *The MathWorks™* in conjunction with the automatic mesh-generation environment *NETGEN* [Schöberl 1997]. Finally, the prepared imaging data will be tomographically visualized by means of the interactive parallel-visualization environment *ParaView* from *Kitware et al*.

3.3   Mechanics and Transceiver System

3.3.1   Transceiver

Figures (3.3) and (3.4) show the geometry and configuration of a *transmitter (TX)* and a *receiver (RX)* forming together the centrepiece of the developed MITS coil system, the *transceiver (TRX)*.
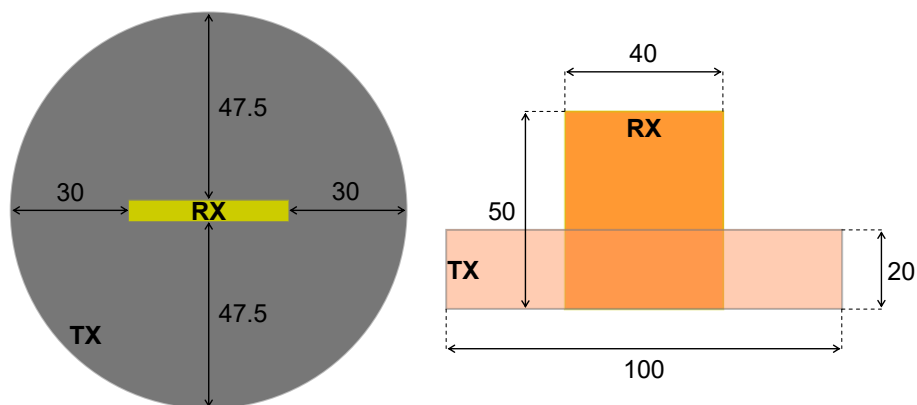
Figure (3.3): Geometry of the MITS transceiver. Left: front view, right: top view. All dimensions are given in [mm].
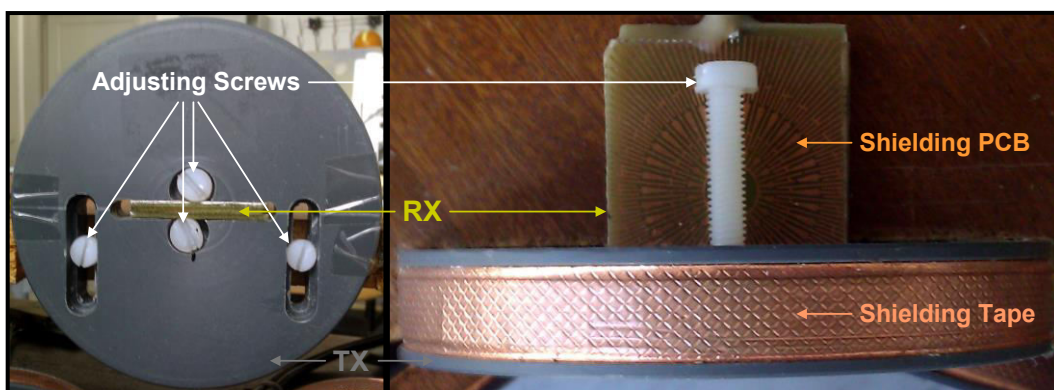

Figure (3.4): Configuration of the MITS transceiver. Left: front view, right: top view. The white plastic screws form together some kind of adjustment mechanism where, in contrast to the four front screws in the left photograph, the rear long one in the right photograph is usually not mounted unless necessity arises.

❖   Transmitter

A single-layer air-core solenoid wound on a circular massive hard-plastic former acts as a transmitting coil. This TX is mounted onto a supporting wooden table with its face perpendicular to the table's surface (see additionally figures (3.6) and (3.7)). The parameters of the TX are listed in table (3.1).

Parameter	Value	Unit
DC resistance	0.43	Ω
Inductance	11.81	µH
Resonance frequency	2.88	MHz
Number of windings	16	1
Copper wire radius	0.25	mm
Copper shield width	10	mm
Copper shield thickness	0.1	mm

Table (3.1): Transmitter specifications.

❖   Receiver

A double-layer rectangular spiral etched on a double-sided PCB, respectively, acts as a receiving coil. This RX is mounted in the horizontal median plane of the TX in such a way that the RX face is perpendicular to the TX face, and it lies symmetrically centrically with respect to the TX for a particular purpose clarified hereinbelow. The parameters of the RX are listed in table (3.2).

Parameter	Value	Unit
DC resistance	17.98	Ω
Inductance	40.14	µH
Resonance frequency	3.25	MHz
Number of windings	36	1
Copper layer width	0.35	mm
Copper layer thickness	0.035	mm
Copper shield layer thickness	0.035	mm

Table (3.2): Receiver specifications.

❖   Shielding

All coils were properly shielded in order to increase the electromagnetic and electrostatic immunity of the transceiver array against the different internal and external interferences, especially parasitic capacitive coupling between the different TXs and RXs. The TX was shielded by means of a conductive, self-adhesive copper tape stretched on both sides around the windings. As eddy currents in the shield affect the quality factor and consequently the sensitivity, the shielding copper strip was slotted opposite to the cable connections of the TX [Issa 2005]. In this way, a closed conductor loop through the shield and consequently excessive circulation of eddy currents therein can be avoided. The RX was shielded by means of two single-sided PCBs, one on each side. On each shielding PCB, a special copper ground plane in the shape of a radial grid was etched (see the right photograph in figure (3.4) and the last row in table (3.2)). In order to reduce parasitic coupling between the electronics and the TRX as well as external electromagnetic interferences, double-shielded connection cables were used everywhere.

❖   Adjustment

The symmetric centric position of the RX with respect to the TX shown in figures (3.3) and (3.4) represents the basic setup of the TRX. In this setup, the unperturbed primary magnetic flux flowing through the RX is theoretically zero; thus, the RX will be called *planar zero flux coil (PZFC)*. Practically, this condition can be almost fulfilled in case of a single-TRX arrangement, but is not that straightforward in case of a multi-TRX arrangement like the one shown in figures (3.5) and (3.6) because each RX must be not only adjusted with respect to the inbuilt TX, but also with respect to all other TXs together. In such multi-TRX setups, slight misalignments of one or more RXs and/or TXs might complicate the mutual adjustment between the individual TRXs so that the PZFC no more fulfills its purpose. For this reason, each TRX was additionally equipped with a multidirectional adjustment mechanism consisting merely of some plastic screws as shown in figure (3.4).

3.3.2   Transceiver Array

The new transceiver array is demonstrated in figures (3.5) and (3.6) in this paragraph and figure (3.7) in the second following paragraph. It has an elliptical cross section, and consists of an upper and a lower plane with *8* TRXs each.
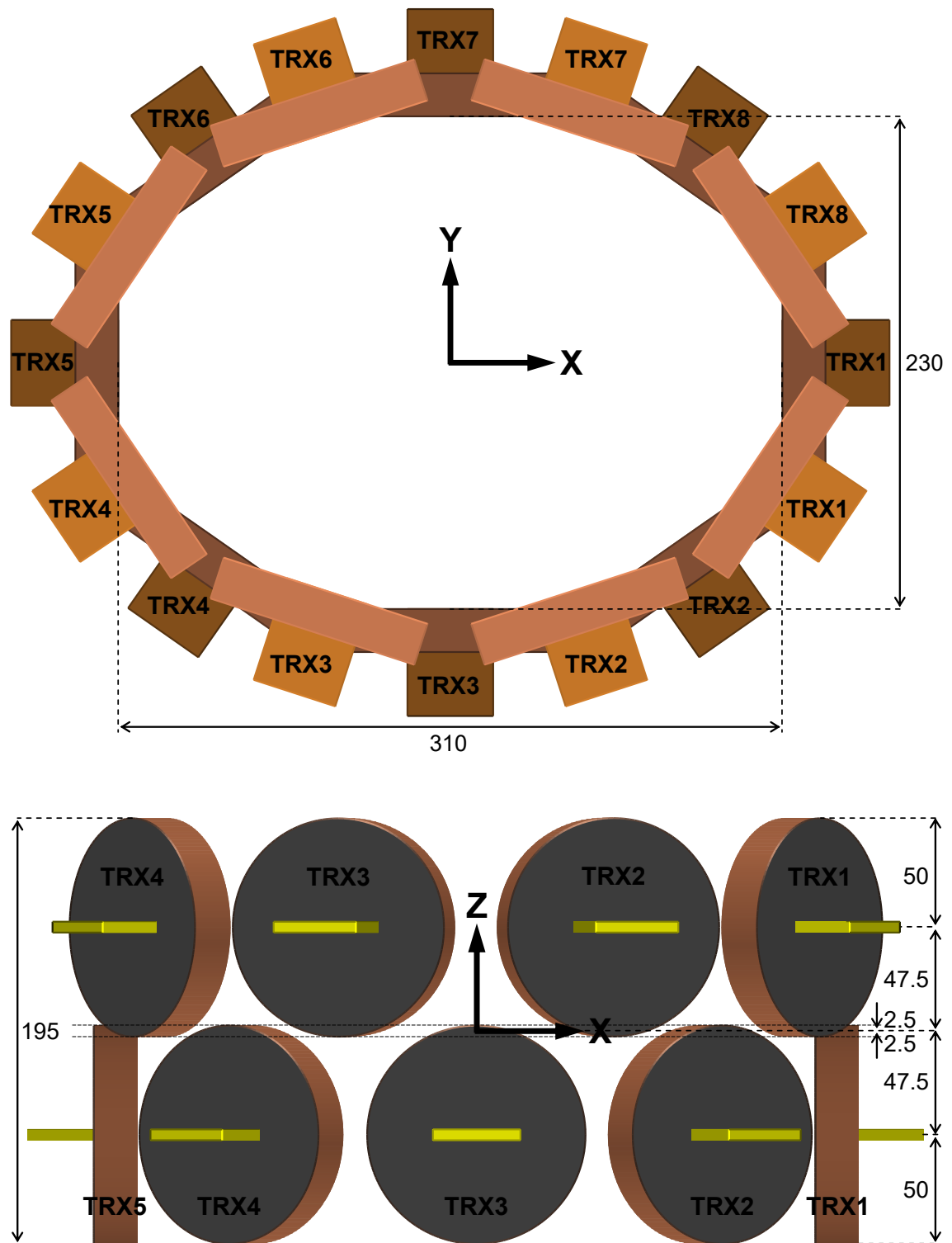
Figure (3.5): Geometry of the MITS transceiver array. Top: top view, bottom: long-side view. All dimensions are given in [mm]; detailed dimensions of the TRX can be taken from figure (3.3).

Figure (3.6): Configuration of the MITS transceiver array. Left: top view, right: three-dimensional (3D) view. A close-up view of the TRX is provided in figure (3.4).

As discussed previously, several advantages are combined in such transceiver array:

- Having *16* TXs and *16* RXs, it offers a fair number of independent signals and thereby an acceptable spatial resolution on the one hand, and it reduces measurement time and thereby experimental errors on the other hand, e.g., when compared to single-TRX systems utilizing mechanical scanning.
- Having a dual-plane design, it can cover and hence scan extended regions of the human body much better than the most frequently designed single-plane coil systems.
- Having an elliptical configuration, it can approximate the shape of the human body, particularly its truncal (thoracic, abdominal and pelvic) regions due to their morphology, much better than the most frequently configured circular or planar coil systems.

3.3.3   Carrier Signal Cancellation

Before starting a series of measurements, the transceiver array must be checked for the correctness of its adjustment. If any readjustment shall be necessary, then it can best be performed in two successive steps by means of the previously described adjusting mechanism. In the first step, each of the *8* TRXs in each plane is to be adjusted individually; in the second step, all *8* TRXs are to be adjusted with respect to each other. This two-step *check-and-adjust* procedure should ensure

minimum mutual coupling between the TXs and RXs in each plane and hence minimum residual carrier signal, thus, providing sufficient dynamic range for the perturbation signal.

3.3.4   Mechanical Structure

Figure (3.7) shows a robustly constructed, custom-made table building the supporting mechanical body of the new MITS transceiver system.
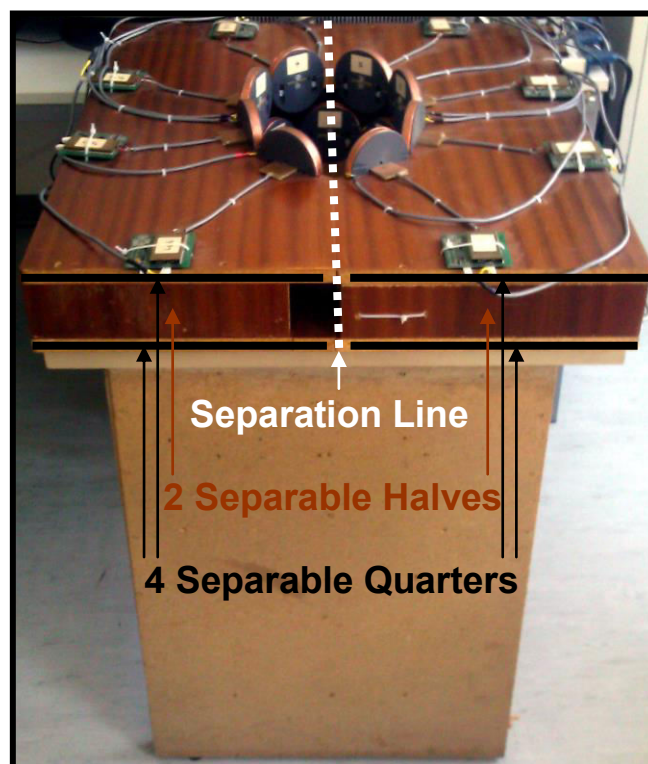
Figure (3.7): Mechanical structure of the MITS transceiver system. The 8 electronic boards on the edges of the table surface are the preamplifiers for the received signal (another 8 ones are hidden between the two layers of the table surface). They occupy a compromise position, i.e., not too close to the TRXs as otherwise they could contaminate the signal, and not too far from them in order to avoid long signal transmission cables and the related problems, especially phase errors. The latter measure was also taken for the cables between the pre- and post-amplifiers, which were laid just only as long as necessary.

The supporting table is completely made of solid wood in order to ensure mechanical stability and hence avoid related signal drifts on the one hand, and to avoid

additional parasitic contributions to the useful signal as might be expected when using metallic materials in the mechanical construction on the other hand. This table is manufactured in the form of a double-layer surface borne by a firmly fixed base framework. The double-layer surface is assembled from *4* detachable parts, each bearing *4* TRXs. On the one hand, these parts together form some kind of opening mechanism that allows positioning a subject or a large test phantom into the transceiver array; on the other hand, the transceiver array can be separated into either *2* halves with *8* TRXs each or *4* quarters with *4* TRXs each, which can be freely placed so that measurements on test persons or objects with dimensions greater than those basic (default) ones of the transceiver array in figure (3.5) become possible.

3.4   High-Level Excitation Signal Preamplification

Figure (3.8) shows the new *8*-channel amplification circuit required between the *8* DAC channels and the *8* PA channels, where the high-performance, wideband video *operational amplifier (Op-Amp) AD811* from *Analog Devices* represents the key electronic component in this circuit.
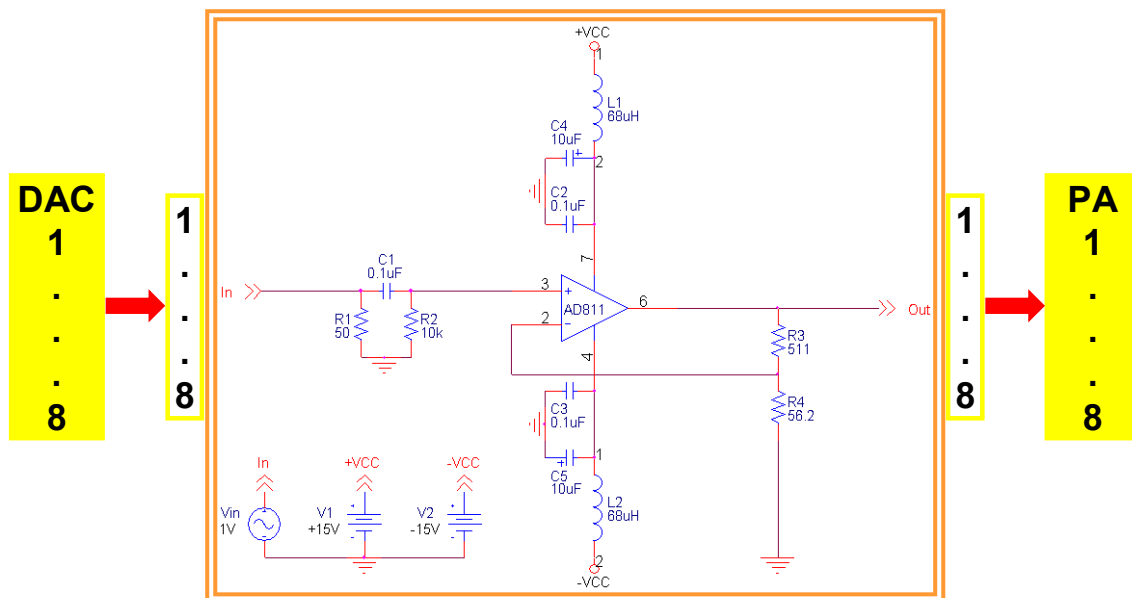

Figure (3.8): Single channel of the 8-channel high-level preamplification circuit of the MITS excitation signal. This circuit is the driver for the subsequent PA. As the PA allows for an input signal up to 10 V, and the DAC can maximally deliver 10% thereof, a gain of 10 is needed.

❖ Supply

The Op-Amp was externally supplied from a bipolar power supply unit with operating voltages $\pm V_{cc}$ of *±15 V* (leads *4* and *7*) in order to attain a sufficient output voltage swing as well as a large closed-loop bandwidth. Stabilization measures were taken in order to increase the immunity against noise and avoid oscillations, namely, the high-frequency bypass capacitors C_2 and C_3, the low-frequency bypass capacitors C_4 and C_5, and the decoupling and filtering inductors L_1 and L_2. These arrangements provide better settling time and lower distortion on the one hand; on the other hand, they help to avoid possible resonance effects caused by parasitic power supply leads' inductances, which can end in peaks in the Op-Amp response at high frequencies.

❖ Input

The Op-Amp is configured in the noninverting mode. Thus, the DAC device feeds its noninverting input (lead *3*) with the generated multifrequency sinusoidal *input signal (V_{in})*. The *50 Ω* input resistor R_1 is responsible for impedance matching in order to minimize reflections in the signal transmission coaxial cable. The *0.1 μF* capacitor C_1 and the *10 kΩ* resistor R_2 form together a passive analog first-order high-pass filter in order to get rid of undesirable low-frequency signal components. As its *time constant* is $\{\tau = R_2\,C_1 = 1\ ms\}$, it has a *cutoff frequency* of $\{f_c = 1\,/\,2\pi\tau \approx 160\ Hz\}$.

❖ Output

The feedback loop of the Op-Amp between its output (lead *6*) and its inverting input (lead *2*) is controlled by the resistor R_3 which can herein be also considered as the load resistance because the latter is not of necessity for the underlying application. Due to its current-feedback-based modus operandi, the closed-loop bandwidth of the Op-Amp is mainly determined by the feedback resistor R_3. In addition, its closed-loop bandwidth depends on the chosen operating supply voltages $\pm V_{cc}$. The *511 Ω* feedback resistor R_3 and the *56.2 Ω* gain resistor R_4 provide together with the noninverting implementation of the Op-Amp the aimed *closed-loop amplification factor*, i.e., gain, of $\{A_{CL} = 1 + (R_3\,/\,R_4) \approx 10\}$. The resulting multifrequency *output signal* $\{V_{out} = A_{CL}\,V_{in} = 10\,V_{in}\}$ is fed into the subsequent PA circuit through a *50 Ω* matching resistor (not shown in figure (3.8)) for reflectionless signal transmission.

❖   Board

The PCB layout was designed by means of the electronic layout-design environment *EAGLE* from *CadSoft*. Relevant PCB layout design measures were adopted and their corresponding criteria were considered in order to assure a stable operation. The high-frequency bypass capacitors C_2 and C_3 were chosen as ceramic ones and mounted close to the power supply pins in order to minimize parasitic traces' inductances and resistances, whereas the low-frequency bypass capacitors C_4 and C_5 were chosen as aluminium electrolytic ones and mounted far from the power supply pins. All used resistors were selected as metal film ones with a low tolerance of *1%* as well as low parasitic inductance and capacitance. The signal traces of the output voltage divider R_3-R_4 were routed as short as possible in order to avoid possible gain errors at high frequencies caused by their parasitic inductances. A ground plane was etched on the PCB in order to reduce noise and avoid too many traces. In order to further minimize the parasitic coupling, especially stray capacitances at the nodes of the output and inverting input, the ground plane was printed opposite to the PCB side on which all signal traces were printed. More PCB layout and design details can be found in appendix (A).

3.5   Measurements

Various control measurements were conducted in order to qualify the overall performance of the MITS tomograph after accomplishing the hardware optimization stage. For the sake of consistency and comparability, the same measurement protocol was applied in all experiments performed throughout this work; this protocol consisted of the following three sub-protocols:

❖   Measurement Data Correction Subprotocol

In order to increase the reliability of the measurement data and to check their reproducibility, the measurements were repeatedly performed in a multiframe manner, i.e., multiple successive signal frames were acquired during one and the same measurement at an acquisition speed of *1 frame/s*. Signal prefiltering, such as detrending and averaging, was then applied to the acquired signal frames. The phase correction of the acquired signals was performed according to the approach described in detail in [Scharfetter and Issa 2008; Scharfetter et al. 2009]. Briefly, the phase correction algorithm requires stochastic mechanical vibration of the coil

array during a real-time calibration period (calibration frames) in the beginning of the measurement prior to the actual measurement period (measurement frames) in order to get a sufficient variance -only- in the calibration frames. Afterwards, for each transmit-receive measurement combination, the correction angle compensating for all phase errors will be calculated from the calibration frames and applied to the measurement frames, i.e., to the needed data. This calculation is based on a certain finding in [Scharfetter et al. 2001 (b), 2003], namely: in biomedical MITS, signal variations caused by mechanical transmitter and/or receiver vibrations mainly affect the real part of the useful signal, whereas its imaginary part remains almost unaffected. Accordingly, the phase correction angle is obtained as the one which minimizes the variance of the imaginary signal. After phase correction, mechanical noise of the imaginary signal is suppressed as much as possible.

❖   Measurement Settings Subprotocol

The excitation signal was applied at *500 kHz* representing the middle frequency of the operating frequency range of the MITS tomograph. At this frequency, the TXs were driven by an excitation current of about *0.5 A*. The DAC channels generated the carrier signals at an update rate of *75 MS/s* and a resolution of *12 bit*. The ADC channels acquired the received signals at a sampling rate of *7.5 MS/s* and a resolution of *12 bit*; thus, with a frame (window) length of *20 ms*, the ADCs had to acquire *150 kS/frame* at an acquisition speed of *50 frame/s*. However, besides the data acquisition task, the host computer, a normal *personal computer (PC)*, was also responsible for all measurement control and synchronization tasks as well as signal demodulation and processing tasks. Therefore, unfortunately, this theoretical acquisition speed of *50 frame/s* reduced to the above-mentioned practical one of *1 frame/s*. For the same reason and due to the large volumes of different data involved, the applicable high update and sampling rates of the DACs and ADCs of *150 MS/s* and *60 MS/s*, respectively, were practically not utilizable.

❖   Measurement Cycle and Timing Subprotocol

This subroutine was programmed in order to predefine the number and type of the consecutive frames to be acquired on the one hand, and the time intervals between them to be set on the other hand. Two types of frames are being distinguished, namely, calibration frames and measurement frames. The desired number of frames was only restricted to the desired duration of measurement; a calibration cycle of *15 frames* and a measurement cycle of *30 frames* were found to be reasonably adequate. As regards the time intervals between the individual

frames, the general rule was to set them all to *zero*, i.e. to acquire all frames instantly after each other without any pause between them, except in the following two special cases:

- In all measurements whatever, there was always a time interval of few seconds to be set between the last calibration frame and the first measurement frame in order to get the coil system steady again after the mechanical vibration, i.e., before starting the actual measurement.
- In state-differential measurements, a second pause was always required between the last frame of the first state and the first frame of the second state in order to perform a certain action, e.g., moving a target object inside the coil system or taking it out. The length of this pause depended on the action to be performed, yet no pause longer than several seconds was needed in this work.

Additional settings and measurement-specific details that are not mentioned above will be provided in the experiments.

3.5.1   Experimental Sensitivity

The aim of this experiment was neither to determine the absolute sensitivity S_{abs} nor the relative sensitivity S_{rel} stated in the previous equations (2.2) and (2.3), respectively, but only to investigate the general shape of the sensitivity curve produced by the new MITS transceiver system. The sensitivity curve to be obtained can serve as a reference for choosing nonarbitrary positions for the ROI within the imaging space enclosed by the transceiver array, as will be seen in the imaging experiments of the next two chapters.

For this control experiment, the measurement setup demonstrated in figure (3.9) was arranged. During one and the same multiframe measurement at *500 kHz*, a brass sphere of *14 mm* diameter was displaced stepwise within the transceiver array shown in figure (3.5) along the z-axis. This displacement occurred in *12* successive steps, each with *1 cm* length, along the vertical median plane of TRX1 of the lower layer from the point *(0, 0, -60)* to the point *(0, 0, 60)* with reference to the origin of the local coordinate system shown in figure (3.9). Thus, including the initial and end positions, there were *13* positions whereat the brazen sphere was measured; at each of these positions, *5 frames* were acquired and averaged. The corresponding *13* signals received at RX1 of the lower plane were used to plot the MITS sensitivity curve.
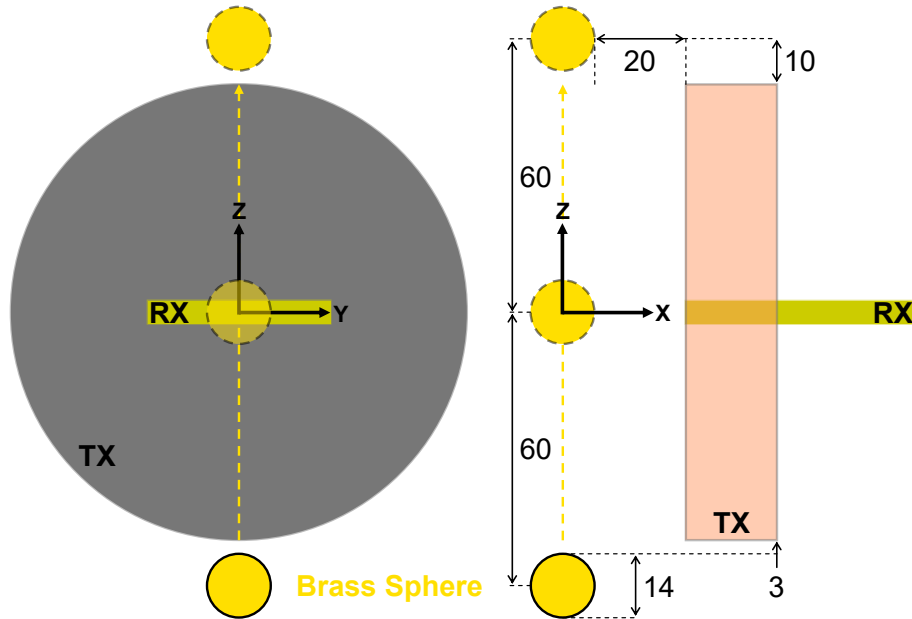
Figure (3.9): Measurement setup for the investigation of the experimental sensitivity of the MITS transceiver system. Left: front view, right: side view. The dashed brazen-yellow arrows denote the displacement path and direction of the brass sphere. For the sake of clarity, only the TRX facing the sphere in the transceiver array is shown (TRX1, bottom plane); therefore, the coordinate axes in the figure are only auxiliary, illustrative ones and not identical with those original ones of the whole transceiver array shown in figure (3.5); with reference to the origin of the original coordinate system, the displacement of the sphere occurred from the point (128, 0, -107.5) to the point (128, 0, 12.5). All dimensions are given in [mm]; detailed dimensions of the TRX can be taken from figure (3.3).

As discussed previously, a highly conductive material like brass ($\sigma \approx 1.5 \times 10^7$ S/m) produces a quasi-pure real signal. Indeed, the modulus of the measured sphere signal proved to be quasi-equal to its real part due to the comparatively negligible imaginary part. For this reason, the sensitivity curve was plotted from the real frames of the acquired sphere signal.

3.5.2 Measurement Noise

In biomedical MITS, the different types of noise can sometimes contaminate the desired signal to such an extent that no useful information at all can be attained.

Some types of noise can be directly or indirectly estimated through performing certain measurements and/or making certain calculations, while some other types are difficult to estimate. In many measurement applications, it is usual to present or define the measurement noise as the sum of those different types of noise caused by the electronics of the system's measuring hardware, and to calculate it according to the following equation:

$$N_{s\text{-}in} = N_{rms\text{-}out} / (A \sqrt{N_{bw}}) \tag{3.1}$$

where $N_{s\text{-}in}$, $N_{rms\text{-}out}$, A and N_{bw} represent the *total equivalent spectral input noise voltage density*, *total root mean square output noise voltage*, *total amplification factor* and *equivalent noise bandwidth*, respectively.

For the estimation of the measurement noise of the optimized MITS tomograph and thereby the effectiveness of the implemented electromagnetic shielding, the following equation was used:

$$N = STD / A \tag{3.2}$$

where N and STD represent the *measurement noise* and the *standard deviation of the acquired signal frames*, respectively, calculated after detrending, phase and consequently amplitude correction.

In this control experiment, the previous figure (3.5) can be regarded as the corresponding measurement setup, i.e., empty-space measurements were carried out for the evaluation of N. Equation (3.2) was applied to the real and imaginary parts of all independent signals acquired at *500 kHz* from the upper and lower layer of the coil array, and STD was calculated from the *30 frames* of a typical measurement cycle.

In addition, the *average noise mean(N)* and the *relative percent difference $\Delta_{\%}(N)$* between the imaginary and real noise *Im(N)* and *Re(N)* will be used to assess to which extent the signal's real and imaginary parts are affected by noise including systematic errors and thereby to assess the underlying phase correction approach described previously.

$$\Delta_{\%}(N) = 100\% \, |Im(N) - Re(N)| \, / \, |Im(N)| \tag{3.3}$$

3.5.3   Parasitic Capacitive Coupling

Parasitic capacitive coupling is an important source of errors in MITS. Ideally, the transmitter and the receiver should only be coupled by the secondary magnetic field caused by the eddy currents in the body. However, due to imperfections, they are also directly coupled by a residual mutual inductance as well as parasitic capacitances which allow for dielectric currents between them. Both pathways can cause a considerable offset which superimposes on the useful signal. This offset, in principle, would still not be a major problem if it was sufficiently small so as not to reduce the dynamic range of the ADC on the one hand, and if it had a significantly different spectral content than the useful signal so as to allow for easy filtering on the other hand. Both conditions are usually not easily fulfilled; a certain residual capacitive coupling is unavoidable, even with electrostatic shielding. [Griffiths 2001, 2005] argued that due to insufficient screening in [Al-Zeibak and Saunders 1993], their reconstructed images were highly questionable. The capacitive coupling between the transmitter and the receiver was most likely so large that actually their measurement system performed ECT rather than MIT. Therefore, effective electrostatic shielding is an issue of prime importance in an MITS system.

The effectiveness of the implemented electrostatic shielding of the optimized MITS tomograph was assessed by means of the measurement setup depicted in figure (3.10). The used tank therein was made of plastic and manufactured to dimensions in the shape of an elliptical cylinder. This custom-made tank was filled with saline solutions of physiological conductivity *(0.15 or 0.2 S/m)* and used as a conducting background medium containing a test phantom (ROI) in all imaging experiments throughout this work. In this control experiment, the tank was only filled with distilled water and served as the test phantom itself, providing a strong dielectric pathway between the TXs and RXs, to be addressed hereinafter. The measurement was performed in two successive, dielectrically different states of the measurement space surrounded by the transceiver array; in each state, *15 frames* were acquired and averaged. In the first state, the tank with distilled water was in situ as shown in figure (3.10); in the second state, the tank was removed (empty-space measurement). The parasitic capacitive coupling was assessed based on the real and imaginary state-differential signals acquired at *500 kHz* from all independent TX-RX measurement channels of the upper and lower layer of the coil array according to the following equation:

$$V_{dw\text{-}es} = V_{dw} - V_{es} \qquad\qquad (3.4)$$

where $V_{dw\text{-}es}$ represents the *state-differential signal*, i.e., the difference between the *signals* V_{dw} and V_{es} received in the first state, *distilled-water*, and second state, *empty space*, respectively.

Although [Goss et al. 2003 (a)] believed that this will not always be the case, [Griffiths 1999] found that the parasitic capacitive coupling mainly affects the real signal. This meets the finding in [Scharfetter et al. 2001 (b), 2003] that systematic errors predominately appear in the real part of the biomedical MITS signal, whereas its imaginary part remains almost unaffected. In this regard, the *average signal mean($V_{dw\text{-}es}$)* and the *relative percent difference $\Delta_\%(V_{dw\text{-}es})$* between the real and imaginary parts *Re($V_{dw\text{-}es}$)* and *Im($V_{dw\text{-}es}$)* can be used as quantitative measures to ascertain this point, i.e., to check whether capacitive noise mainly affects the real signal.

$$\Delta_\%(V_{dw\text{-}es}) = 100\% \; |Im(V_{dw\text{-}es}) - Re(V_{dw\text{-}es})| \; / \; |Im(V_{dw\text{-}es})| \qquad (3.5)$$

Usually, in case of macroscopic (conventional) dielectric capacitors, the capacitance scales with the relative permittivity of the insulator. Taking into account the relative permittivity of water at room temperature and *500 kHz*, i.e., *($\varepsilon_r = 80$)*, the container with distilled water increases the stray capacitances between the different coils to a large extent compared to empty space. Accordingly, if $V_{dw\text{-}es}$ had any magnitude higher than the usual noise level N, then this value of $V_{dw\text{-}es}$ would mainly represent a parasitic capacitive signal as the contribution of the susceptibility *($\mu_r \approx 1$, $\chi_m \approx 0$)* and conductivity *($\sigma \approx 0.001$ S/m)* of distilled water to the induction of $V_{dw\text{-}es}$ can be neglected. Thus, the *relative percent difference $\Delta_\%(N, V_{dw\text{-}es})$* between N and $V_{dw\text{-}es}$ can be used as a quantitative measure to comment on and clear up this issue.

$$\Delta_\%(N, V_{dw\text{-}es}) = 100\% \; |N - V_{dw\text{-}es}| \; / \; |N| \qquad (3.6)$$

where both the real and imaginary parts of N and $V_{dw\text{-}es}$ need to be considered in the assessment based on this equation.

Remark

The conductivity of whatever liquid (water or ionic solution) used for whatever purpose in this work was measured or adjusted by means of the conductivity meter *digimeter L 21* from *AQUALYTIC®*.
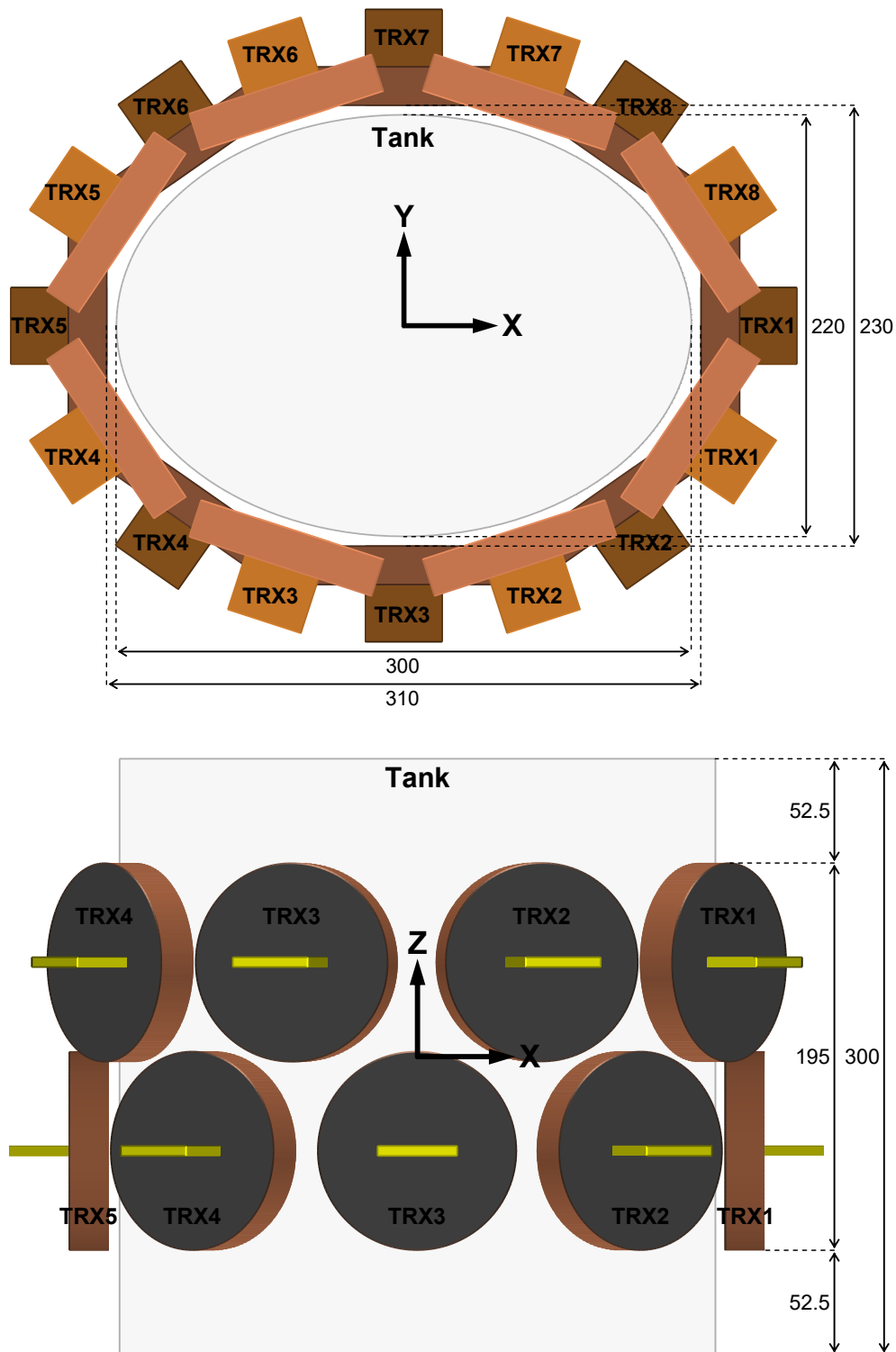
Figure (3.10): Measurement setup for the estimation of the parasitic capacitive coupling in the MITS transceiver system. Top: top view, bottom: long-side view. All dimensions are given in [mm]; detailed dimensions of the TRX and the whole array can be taken from figures (3.3) and (3.5), respectively.

3.5.4   Carrier Signal Reduction

In MITS, one of the most commonly implemented configurations of the transceiver has been the one wherein the transmitter and receiver lie coaxially face to face. This classic configuration has been applied to both single- and multi-transceiver systems regardless of the construction type of the transmitters or receivers, whether solenoid or PCB ones, and independent of the implementation type of the receivers, whether conventional ones or gradiometers of different types. The coaxial design of the transceiver has also been particularly preferred in MITS simulation studies.

In order to assess the performance of the developed MITS transceiver system and its adjustment mechanism regarding the reduction of the carrier signal, the new perpendicular TRX shown in figure (3.3) was compared to a coaxial version thereof configured for this purpose shown in figure (3.11).
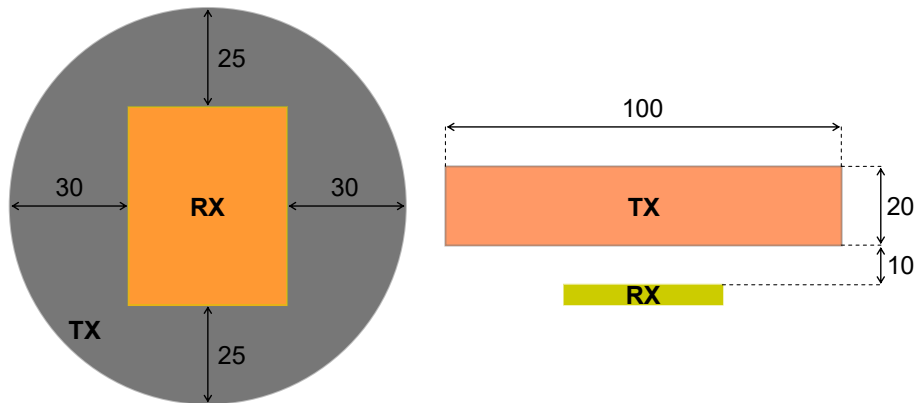
Figure (3.11): Geometry of the coaxial version of the MITS transceiver for the evaluation of the carrier signal reduction ratio. Left: front view, right: top view. All dimensions are given in [mm].

The comparison between the two TRXs was made through involving both of them in the following logarithmic relation:

$$CSRR = 20 \, log(V_p \, / \, V_c) \hspace{3cm} (3.7)$$

where *CSRR* represents the *carrier signal reduction ratio*; V_p and V_c represent the *residual carrier signals* measured in the *perpendicular* and *coaxial* transceiver configurations, respectively, after best possible adjustment.

For the evaluation of the *CSRR*, empty-space measurements *at 500 kHz* were performed. The *CSRR* was calculated, and hence V_p and V_c were measured, in case of both single- and multi-TRX setups. In the single-TRX setup, only one of the *16* TRXs at a time was in operation, i.e., the RX of a certain TRX received the residual carrier signal from the inbuilt TX only. In the multi-TRX setup, the whole upper or lower *8*-TRX plane was in operation, i.e., each of the *8* RXs in an activated plane simultaneously received the residual carrier signal from all *8* TXs in this plane. As the measurement results of V_p expectedly showed only slight, insignificant differences between the *16* registered values in the single-TRX setup on the one hand, and between the *16* registered values in the multi-TRX setup on the other hand, mean values of V_p were used in the calculation of the *CSRR*, i.e., the average V_p of each plane in each setup over the *8* values involved was inserted in equation (3.7). For the same reason, it was not necessary in the measurements of V_c to reconfigure the whole transceiver array coaxially; therefore, only top and bottom TRX3 were arbitrarily chosen to be reconfigured, and thus the corresponding V_c results were considered in the calculation of the *CSRR* according to equation (3.7).

3.5.5   Excitation Signal Preamplification Circuit

The functionality of the implemented high-level amplification circuit was evaluated through observing its frequency response (Bode plot) to a sinusoidal input signal V_{in} over a frequency range far wider than the measurement frequency range of the MITS tomograph. V_{in} was fed into the circuit from the stand-alone function generator *HP 33120A* from *Hewlett Packard* with an amplitude of *1 V* representing the full-scale output signal of the built-in function generator (DAC) of the tomograph.

The maximally applicable frequency of the *HP 33120A* was *15 MHz*, and no malfunction or any kind of instability whatsoever could be observed in the circuit's frequency response up to this frequency; the test frequency range was virtually extended to *100 MHz* by means of the electronic-circuit simulation tool *PSpice*® of the electronic-design automation environment *OrCAD*® from *Cadence Design Systems*. While the gain frequency response (Bode magnitude plot) provided a window for the inspection of the closed-loop amplification behaviour of the circuit, the phase frequency response (Bode phase plot) provided another window for the parallel inspection of its closed-loop phase behaviour.

3.6   Results and Discussion

3.6.1   Experimental Sensitivity

Figure (3.12) shows a line graph containing the sensitivity curve produced by the new MITS transceiver system as a result of the brass sphere measurement at *500 kHz* conducted according to figure (3.9).

As can be seen in figure (3.12), the course of the MITS sensitivity curve is morphologically similar to the antisymmetric course of a non-phase-shifted whole-period sine wave. However, in contrast to the latter, the former does not exhibit an absolute zero-crossing at *(z = 0)*, being theoretically the point of zero sensitivity of the PZFC (see figure (3.9)). This is most probably due to a small misplacement of the sphere and/or a small misadjustment of the lower TRX1. Also at its initial and end positions, *(z = -6 cm)* and *(z = 6 cm)*, respectively, the sphere still lies, but to a much lesser extent, in the sensitive region of the PZFC; therefore, again, a non-zero sensitivity is to be expected thereat.
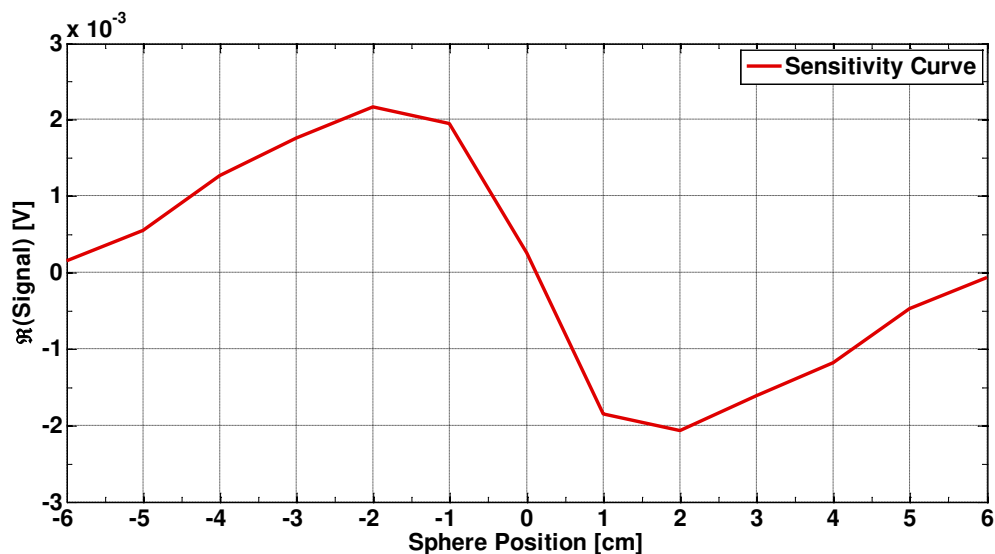
Figure (3.12): Experimental sensitivity of the MITS transceiver system. The sensitivity is represented as the real-part response of the PZFC to a multistep displacement of a brazen sphere parallel to the z-axis of the original coordinate system of the transceiver array shown in figure (3.5). The graph's x-axis with its label "Sphere Position [cm]" describes the multistep displacement of the sphere along the z-axis of the local coordinate system of the lower TRX1 according to figure (3.9).

In conclusion, it can be stated that the obtained sensitivity curve represents a useful tool for finding positions of certain sensitivities for the ROI in imaging tasks. In this work, it served as a reference for choosing two high-sensitive positions for the imaged organic potato in the next chapter as well as a low-sensitive position for the imaged low-conductive saline phantom in the chapter after next.

3.6.2   Measurement Noise

Figure (3.13) presents four colour maps quantifying *Re(N)* and *Im(N)* at *500 kHz* according to equation (3.2) for all possible TX-RX measurement combinations of the upper and lower plane of the new MITS transceiver array. Table (3.3) provides *mean(N)* for each of these maps together with $\Delta_\%(N)$ calculated according to equation (3.3).

As evident in figure (3.13), *Re(N)* is considerably greater than *Im(N)* for all TX-RX combinations, *66.45%* on average (*$\Delta_\%(N)$* in table (3.3)), implying that the phase correction of the acquired signal frames was successfully accomplished based on the variance minimization of the imaginary signal. This represents a good indicator regarding conductivity imaging in biomedical MITS, i.e., in the physiological conductivity range, as the conductivity signal is an imaginary one. Of course, an ideal phase correction in an empty-space measurement means that the received signal is purely real having the same phase of the transmitted carrier signal (assuming that the carrier signal is being already defined as the reference real signal of the underlying phasor diagram with phase angle *($\Phi = 0°$)*). However, in view of the long electronic measurement chain, a slight phase shift and consequently a small imaginary signal might practically be unavoidable.

The general observation in each noise map of figure (3.13) is that the noise values of the different TX-RX combinations differ from each other. This can be attributed to the different vibration dynamics of the different coils due to the stochastic nature of the previously mentioned mechanical vibration applied to the coil array for the purpose of phase correction. Nevertheless, there are only a few TX-RX combinations with a relatively considerable noise difference recognized by the black and white squares in the noise maps. Another observation is that when observing a certain TX, then more often than not, the noise of the two RXs adjacent to it or the RX encircled by it is higher than that of the other RXs. This is already expected because these three RXs usually have higher magnetic coupling with the TX in question and thus exhibit more sensitivity to mechanical noise like vibration.
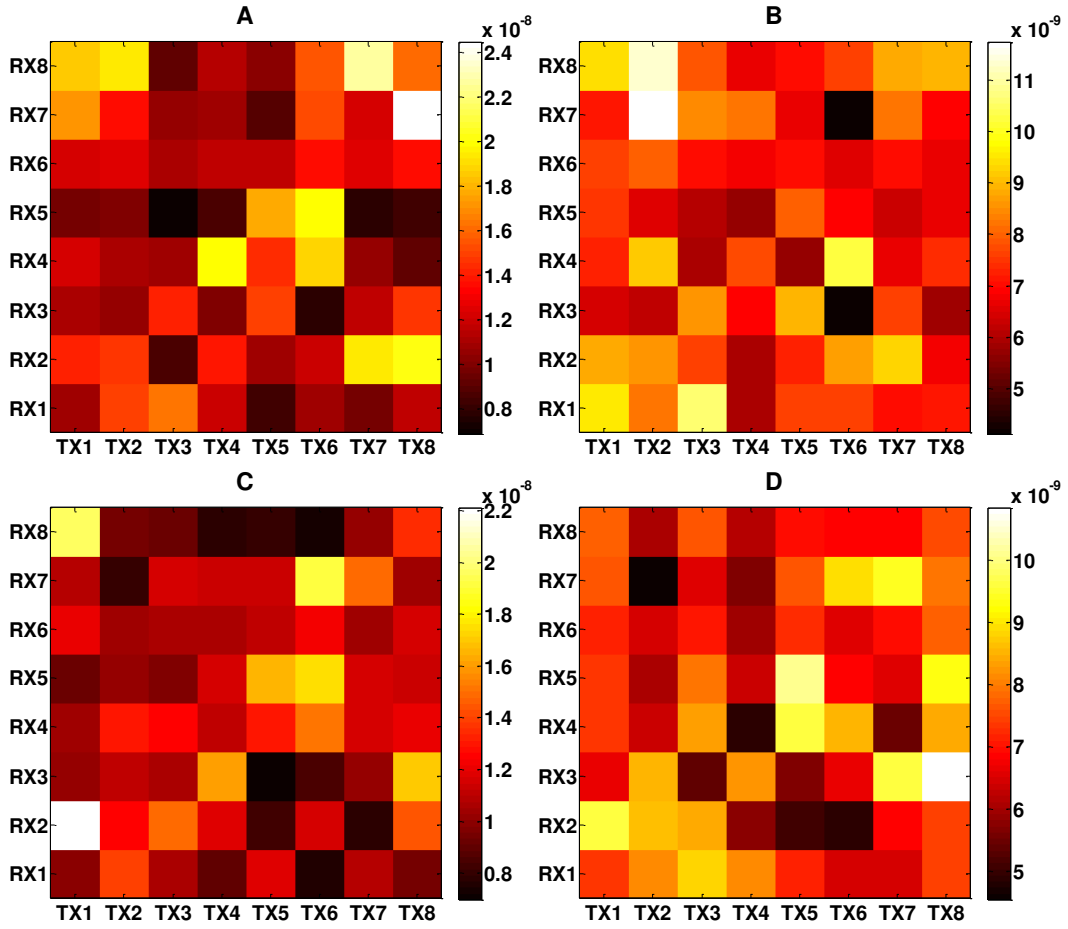
Figure (3.13): Measurement noise of the optimized MITS tomograph. A: Re(N), top TRX plane; B: Im(N), top TRX plane; C: Re(N), bottom TRX plane; D: Im(N), bottom TRX plane. All scales are given in [V]. The difference between real and imaginary noise can be clearly seen on the corresponding differently scaled colour bars.

Noise Map	mean(N) [nV]	$\Delta_\%(N)$
A	13.05	73.31
B	7.53	
C	11.65	59.59
D	7.30	

Table (3.3): Additional data on the noise maps in figure (3.13).

In case of improper electromagnetic shielding, the noise can be of the order of *[μV]* or even higher so that the biomedical MITS signal will be entirely hidden in the noise. Considering all maps of *N* in figure (3.13) as a whole together with the corresponding mean values in table (3.3), it may be concluded that *N* smoothly varies within a relatively narrow range of ca. *4-24 nV* (ca. half an order of magnitude), or on average within ca. *7-13 nV* (less than a fifth order of magnitude). This doubtlessly indicates the effectiveness of the implemented electromagnetic shielding against external noise.

In conclusion, it can be stated that the measurement noise can certainly be classified as low-level noise in biomedical MITS, especially the imaginary noise. As will be seen in the next two chapters, the overall performance of the optimized MITS tomograph regarding noise allows for an *SNR* pretty sufficient for low-contrast conductivity imaging, e.g., up to *68 dB* in the physiological conductivity range and in the lower β-dispersion frequency range.

3.6.3   Parasitic Capacitive Coupling

Figure (3.14) presents four colour maps quantifying $Re(V_{dw\text{-}es})$ and $Im(V_{dw\text{-}es})$ at *500 kHz* according to equation (3.4) for all possible TX-RX measurement combinations of the upper and lower plane of the new MITS transceiver array. Table (3.4) provides *mean*$(V_{dw\text{-}es})$ for each of these maps together with $\Delta_{\%}(V_{dw\text{-}es})$ and $\Delta_{\%}(N,V_{dw\text{-}es})$ calculated according to equations (3.5) and (3.6), respectively.

Comparing the signal maps in figure (3.14) to the noise maps in figure (3.13) reveals that $\{Re(V_{dw\text{-}es}) < Re(N)\}$ and $\{Im(V_{dw\text{-}es}) < Im(N)\}$ for almost all TX-RX combinations, *26.62%* on average $(\Delta_{\%}(N,V_{dw\text{-}es})$ in table (3.4)). Accordingly, even if $V_{dw\text{-}es}$ was entirely caused by residual capacitive coupling, it is fairly lower than the already low noise level, indicating thereby the effectiveness of the implemented electrostatic shielding. Moreover, figure (3.14) clearly shows the expected dominance of $Re(V_{dw\text{-}es})$ over $Im(V_{dw\text{-}es})$ for all TX-RX combinations without exception, *75.29%* on average $(\Delta_{\%}(V_{dw\text{-}es})$ in table (3.4)). Thus, the imaginary conductivity signal will be much less affected by capacitive noise.

It may be additionally mentioned that (as referred to in, e.g., [Watson et al. 2001; Scharfetter et al. 2003; Griffiths et al. 2007]) capacitively coupled signals to the RXs may have been further reduced through the subsequent differential preamplification circuitry with a high *common mode rejection ratio (CMRR)* of *97 dB* at *500 kHz*.
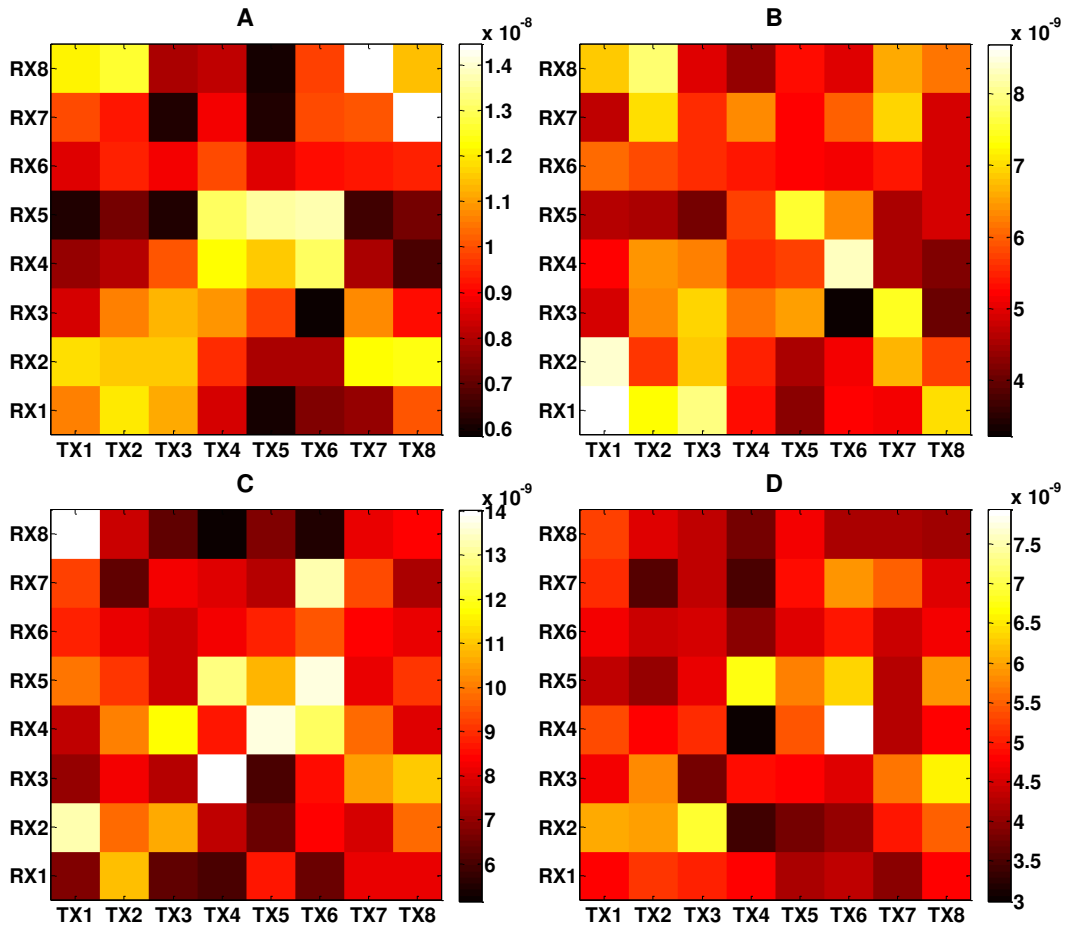
Figure (3.14): State-differential signal between a distilled-water and an empty-space measurement phase. A: Re($V_{dw\text{-}es}$), top TRX plane; B: Im($V_{dw\text{-}es}$), top TRX plane; C: Re($V_{dw\text{-}es}$), bottom TRX plane; D: Im($V_{dw\text{-}es}$), bottom TRX plane. All scales are given in [V]. The difference between the real and imaginary signals can be clearly seen on the corresponding differently scaled colour bars.

Signal Map	mean($V_{dw\text{-}es}$) [nV]	$\Delta_\%(V_{dw\text{-}es})$	$\Delta_\%(N, V_{dw\text{-}es})$
A	9.64		26.13
B	5.79	66.49	23.11
C	8.91		23.52
D	4.84	84.09	33.70

Table (3.4): Additional data on the signal maps in figure (3.14).

In conclusion, it can be stated that the capacitive noise is of no consequence on the overall performance of the optimized MITS tomograph. In addition, the presented results indicate that the applied phase-sensitive demodulation and precise phase correction are able to efficiently suppress most of the spurious effects in the imaginary signal. This is of particular importance in biomedical MITS as the imaginary conductivity signal is usually the one of interest.

3.6.4 Carrier Signal Reduction

Table (3.5) summarizes the residual carrier signals V_p and V_c acquired at *500 kHz* after best possible adjustment of the perpendicular and coaxial TRXs, respectively, together with the carrier signal reduction ratio *CSRR* calculated therefrom according to equation (3.7) for the single- and multi-TRX setups of the upper and lower plane of the new MITS transceiver array.

Measurement Setup	V_p [mV]	V_c [mV]	CSRR [dB]
Single-TRX − Top plane	0.13	1750	-82.58
Single-TRX − Bottom plane	0.12	1760	-83.33
Multi-TRX − Top plane	0.52	2730	-74.40
Multi-TRX − Bottom plane	0.49	2750	-74.98

Table (3.5): Residual carrier signals and carrier signal reduction ratio.

Table (3.5) shows that the perpendicular TRX greatly reduced the carrier signal in the single- and multi-TRX setups, up to ca. *83* and *75 dB*, respectively. The effectiveness of such high *CSRR* will be substantiated in the next chapter when detecting (imaging) a small biological target which induced an imaginary perturbation signal of *6.89 µV* at *500 kHz* in the opposing PZFC. Considering the average multi-TRX residual carrier voltage of *505 µV* in table (3.5), an SCR_{BM} of *(0.0136 ≡ 1.36%)* can be attained (equation (2.9)). When receiving such *6.89-µV* perturbation signal at the coaxial RX, the average carrier voltage of *2740 mV* in table (3.5) would lead to an SCR_{BM} as low as *2.51 x 10^{-6}* which is out of detectability, even with an ADC resolution of *16 bit*.

In conclusion, it can be stated that the new transceiver system allows for a satisfy-ing suppression of the carrier signal and hence for an adequate *SCR* in biomedical applications.

3.6.5 Excitation Signal Preamplification Circuit

The frequency response of the implemented high-level amplification PCB is shown in figure (3.15), both phase and magnitude responses.
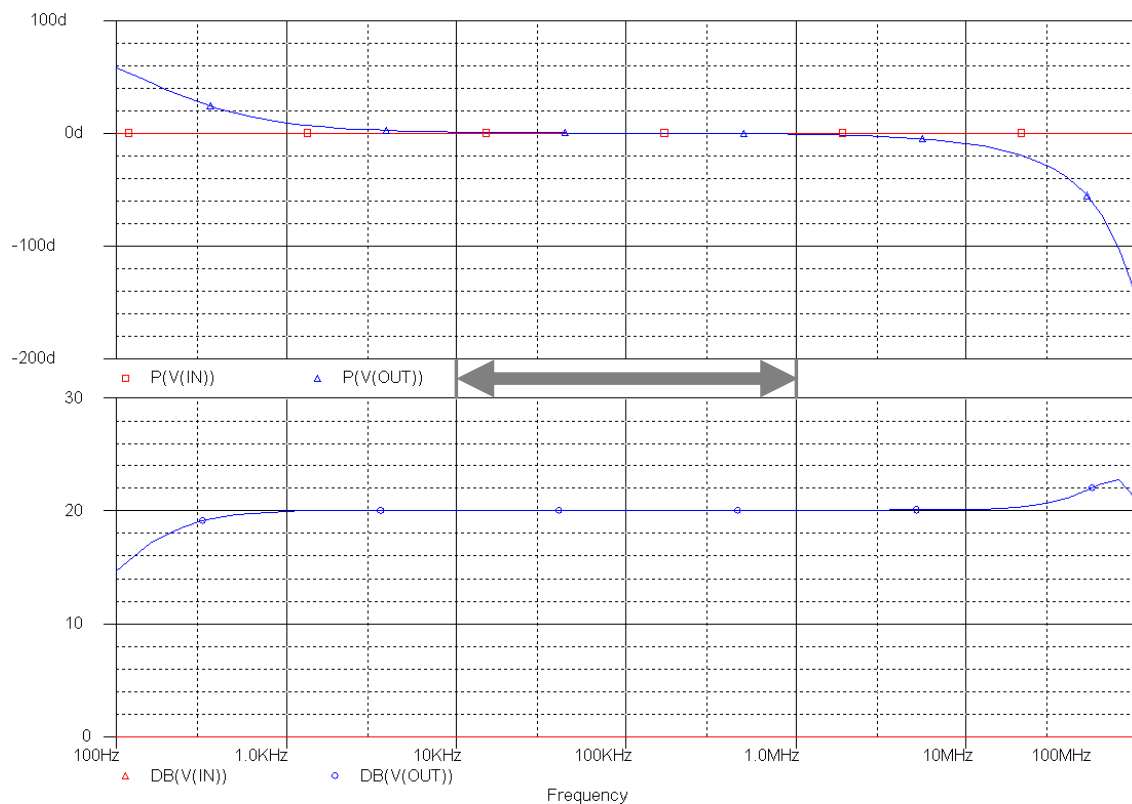
Figure (3.15): Frequency response of the high-level preamplification circuit of the MITS excitation signal. Top: phase response P in [°] where the red line P(V(IN)) and the blue curve P(V(OUT)) denote the input and output signal phase, respec-tively; bottom: magnitude response DB in [dB] where the red line DB(V(IN)) and the blue curve DB(V(OUT)) denote the input and output signal magnitude, respec-tively. The grey double arrow between the two Bode graphs marks the measure-ment frequency range of the MITS tomograph.

A sinusoidal signal V_{in} of *1 V* amplitude, equivalent to *0 dB* in the Bode magnitude plot, was fed into the noninverting input of the Op-Amp. This V_{in} of *1 V* at the Op-Amp's input appeared as a V_{out} of *10 V* at its output up to a few tens of *[MHz]*, equivalent to the aimed gain of *20 dB* in the magnitude response and hence ascertaining the required closed-loop amplification factor of $\{A_{CL} = V_{out} / V_{in} = 10\}$.

The operating frequency range of the MITS tomograph extends from *10 kHz* to *1 MHz*. As can be seen in figure (3.15), this range is entirely included in the flattest region of the gain frequency response on the one hand, and no significant phase shift can be observed therein on the other hand.

The applied V_{in} of *1 V* represents the maximum output signal of the preceding generation stage. Accordingly, the obtained V_{out} of *10 V* represents the maximum output signal of this driver amplifier, which is sufficient for exploiting the full output dynamic range of the succeeding PA.

According to the Op-Amp dynamic performance from the AD811's datasheet, the *slew rate (SR)* has a typical value of *2500 V/µs* at a V_{out} of *10 V*. At such typical SR and such -herein maximal- V_{out}, the *full power bandwidth (FPBW)* reaches a typical value as high as $\{FPBW = SR / 2\pi V_{out} \approx 40\ MHz\}$.

As can be seen in the Bode diagram, there are only two effects at the beginning and at the end of the observed *100 Hz-100 MHz* frequency response, respectively. While the first low-frequency one is caused by the high-pass filter R_2-C_1 at the input of the Op-Amp (see figure (3.8)), the second high-frequency one arises due to the high-level V_{out} of *10 V* whereat linearity begins to degrade.

In conclusion, it can be stated that the implemented multichannel amplification unit proved its functionality in the optimized MITS tomograph. It ensures a proper operation with the required high-level preamplification of the excitation signal on the one hand, and a stable integration into the electronic flow path of the excitation signal on the other hand.

Chapter 4

Software Optimization

This chapter explains the biomedical MITS forward and inverse problems and therewith the imaging process to be schematized, implemented and undergone in this thesis. It discusses the performed software optimization stage in conjunction with imaging experiments qualifying the overall performance of the MITS tomograph with regard to the optimized hardware and software. In addition, it introduces the new hybrid dynamic-parametric (state-frequency-differential) imaging concept in biomedical MITS to be integrated into the imaging process.

4.1   Imaging Process

Figure (4.1) schematically outlines the main steps to be performed in this work in order to accomplish an imaging process, i.e., to reconstruct images.
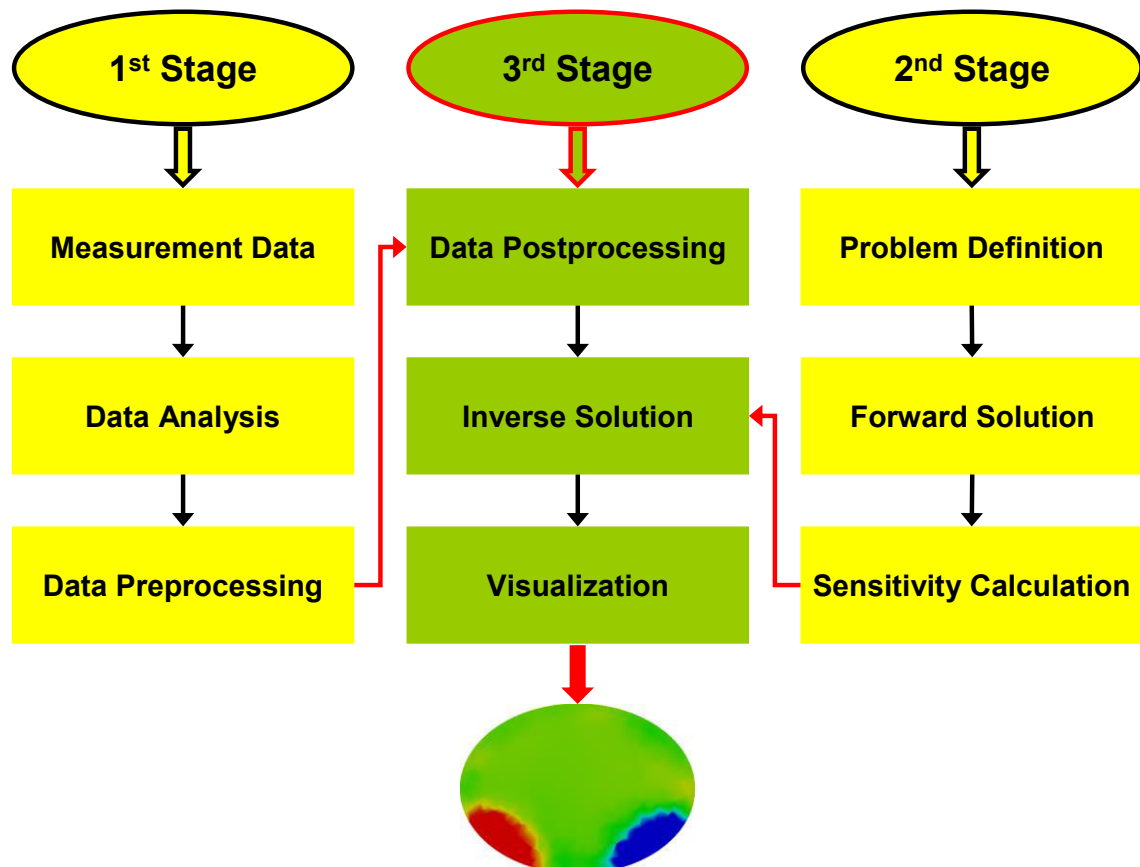

Figure (4.1): Imaging process of MITS. The processed measurement data and the calculated sensitivity matrix are, above all, the required inputs for the solution of the inverse problem, i.e., for image reconstruction.

According to figure (4.1), the following three stages have to be successfully accomplished in order to carry the MITS imaging process through:

❖   1st Stage: Data Analysis and Preprocessing

For these purposes, the dedicated, already existing GUI at IMT-TUG was used. This data correction GUI provides the third stage with, above all, its first main input, the corrected voltage data.

❖   **2nd Stage: Forward Solution and Sensitivity Calculation**

For these purposes, some of the dedicated, already existing algorithms were modified, ending up with an adapted forward algorithm. This forward solver provides the third stage with, above all, its second main input, the sensitivity matrix.

❖   **3rd Stage: Data Postprocessing and Inverse Solution**

For these purposes, a new stand-alone GUI was programmed. This image reconstruction GUI receives the required input data from the first two stages and feeds the reconstructed, tomographically visualizable output data into the responsible application program.

4.2 Data Analysis

Figure (4.2) schematically summarizes the main steps throughout the data analysis and preprocessing stage of the MITS imaging process.

Besides data correction, having its own GUI, this initial stage allows for the assessment of the quality of the acquired data before going through the data postprocessing and inverse solution stage. If the data are not satisfying, then the reasons can be easily investigated and remeasurements can be performed. As detailed in figure (4.2), the output data structure of this stage contains -besides other helpful information- the phase- and amplitude-corrected signals along with some statistical details thereof, to be used in the final data postprocessing and inverse solution stage of the imaging process in equations (4.43), (4.44) and (4.48-4.53).

4.3 The Biomedical MITS Problem

A general formulation of the MITS problem is:

$$v = s(PEP) = s(\sigma, \varepsilon, \mu) \qquad\qquad (4.1)$$

$$PEP = (\sigma, \varepsilon, \mu) = s^{-1}(v) \qquad\qquad (4.2)$$

stating the forward and inverse mappings, respectively, where *v* is the *measured voltage* representing the true MITS signal, and *s* is a *nonlinear forward mapping function* representing the physical relationship between *v* and the PEP *(σ, ε, μ)*.
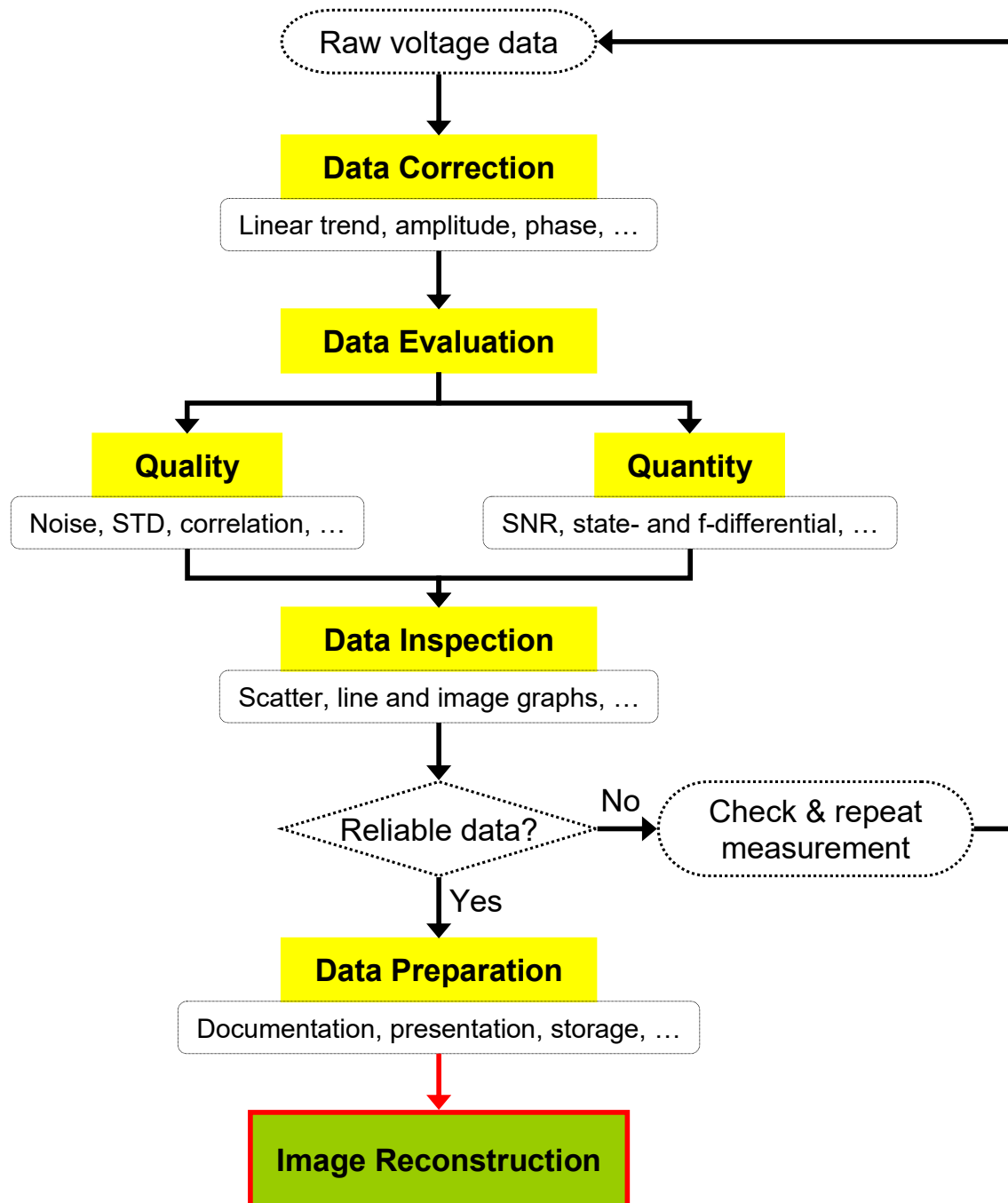
Figure (4.2): Data analysis and preprocessing sequence. This sequence represents the first stage of the MITS imaging process prior to image reconstruction. All data gathered from this sequence will be outputted into one single data structure from which the required data for the image reconstruction GUI can be obtained, above all, the corrected signals and their standard deviations.

Thus, the MITS forward problem is to calculate the voltages induced in the receivers according to the PEP distributions in the medium under investigation and, just the reverse case, the MITS inverse problem is to reconstruct the PEP distributions from the measured voltages. As a matter of course, dealing with and thus solving both problems requires knowledge of the underlying physics that relates the measured voltages and the various PEP to each other.

Recalling the extensive discussion on the biomedical MITS signal together with the related equations (2.8-2.11) from the previous paragraph (2.3.1) describing the case of weak perturbations caused by biological tissues and its consequences regarding the individual contributions of σ, ε and μ to the induction of the true perturbation signal, accordingly, particularly in the lower β-dispersion frequency range, the contributions of ε and μ are usually negligible in comparison to that of σ because the permittivity (imaginary) term *($\omega\varepsilon$)* of the complex conductivity *{y = σ + $j\omega\varepsilon$}* is usually negligible in comparison to the conductivity (real) term σ and biological tissues are almost nonmagnetic *($\mu_r \approx 1$, $\chi_m \approx 0$)*. Based thereon, the biomedical MITS problem represents an almost pure conduction eddy-current problem. Thus, the general formulation of the MITS problem in equations (4.1) and (4.2) can be restated in an approximate form as follows, respectively:

$$v = s(\sigma) \qquad\qquad (4.3)$$

$$\sigma = s^{-1}(v) \qquad\qquad (4.4)$$

In this context, the derivative of v with respect to σ represents a measure of the change in v in the receiving coils in consequence of a change in σ in the investigated medium:

$$S = \partial v / \partial \sigma = \partial s(\sigma) / \partial \sigma \qquad\qquad (4.5)$$

where this measure will still be termed as usual *sensitivity* and abbreviated as *S*.

Remarks

As will be seen later during the linearization and solution of the biomedical MITS problem, *S* will be approximated by the respective ratio between the absolute changes in the linearized system:

$$S = \Delta v / \Delta \sigma \qquad\qquad (4.6)$$

This formula is no more than the previously explained approximated biomedical version $\{S_{abs\text{-}BM} \approx Im(\Delta V) / \Delta\sigma\}$ of the absolute sensitivity $\{S_{abs} = \Delta V / \Delta y\}$ in case of nonmagnetic materials including biological tissues; however, as $Im(\Delta v)$ needs to be written hundreds of times in this and the next chapter, it would be more convenient to write Δv rather than $Im(\Delta v)$, and to recall the dominance of the imaginary part or to write it explicitly whenever contextually necessity arises.

4.4   Forward Problem and Sensitivity

Algorithms responsible for the solution of the MITS forward problem and calculation of the sensitivity matrix have been continually developed at IMT-TUG and by external researchers. Expectedly, these algorithms share some features with those previously developed for EIT; some routines have even been completely developed from their respective EIT versions. The developed algorithms have been mostly investigated in simulations, but also in some experimental settings. Although all programmed algorithms share some essential solution strategies, they differ in some handling routines. As for examples of common basic solution approaches, not to mention the well-known *Maxwell equations (ME)* and the corresponding potential formulation of the governing field equations, the calculation of the *eddy-current field (E)* in the conducting target medium and of the *sensitivity matrix (S)* was based on the powerful *finite element method (FEM)* through the application of the iterative preconditioned *Galerkin weighted residual method* with tetrahedral *finite elements (FE)*; in addition, the derivation of the analytical formula of the sensitivity for the calculation of *S* was based on the efficient *reciprocity theorem* through the generalization of the static/quasi-static mutual-impedance formula in [Geselowitz 1971] to the non-quasi-static (time-harmonic) electromagnetic case in [Mortarelli 1980] applicable to the MITS eddy-current problem (a detailed example thereof can be found in [Hollaus et al. 2004 (a)]). As for examples of different handling procedures, an existing algorithm was reprogrammed to use a *Coulomb-gauged* quasi-static version of MEs due to its computational convenience in low-frequency applications. The corresponding auxiliary potentials for the calculation of *E* were calculated differently; while a combined analytical-numerical procedure (without involving FEM) was applied for the calculation of the *magnetic vector potential (A)*, tetrahedral FEs of first order together with the iterative *quasi-minimal residual method (QMR)* preconditioned by inverse-based multi-level *incomplete lower-upper factorization (ILU)* after [Bollhöfer and Saad 2006] were applied for the calculation of the *electric scalar potential (Φ)*. In contrast, an ungauged time-

harmonic version of MEs was used in [Hollaus et al. 2004 (b)] due to its accuracy in high-frequency applications. The corresponding *reduced magnetic vector potential (A_r)* and *electric scalar potential (V)* for the calculation of E were both calculated by means of tetrahedral FEs of second order together with the iterative *conjugate gradient method (CG)* preconditioned by *incomplete Cholesky factorization*. The choice not to gauge the A_r-V formulation originated in [Biró 1999] where various formulations of eddy-current problems in terms of scalar and vector potentials were reviewed. It was found out that a well-thought-out iterative solution of the ungauged potential equations yields consistent results which are numerically as robust as those obtained by the corresponding Coulomb-gauged solution schemes. From own and others' experience, [Merwa et al. 2003] supported the latter finding and exploited it in order to achieve stable solutions.

For this study, as detailed in figure (4.3), the different required subroutines for forward solution and sensitivity calculation were gathered from the available main routines at IMT-TUG and reassembled into an adapted forward solver after carrying out the required modifications, above all:

❖   Alteration of the preconfigured circular geometry of the previous coil system into the elliptical geometry of the new one (figure (3.5)). The main geometric information of the new configuration to be fed into the forward solver is, inter alia, the coordinates and dimensions of the TXs and RXs, and their respective orientation vectors in the 3D elliptical-cylindrical measurement space. All these entries must accurately match the true geometry of the developed dual-layer transceiver array due to their crucial role in the reliable calculation of the electric field E and hence the sensitivity matrix S.

❖   Alteration of the predefined structure of S into the new specific structure required for the inverse solution and hence the reconstruction of the vector of the conductivity distribution σ in the real target medium. S must be rearranged in the forward solver in accordance with the structure of the vector of the measured voltages v to be acquired in the real experimental setup. More precisely, stated component-wise in equation (4.7) of the linearized MITS problem described later, S must be preconfigured according to the preplanned transmit-receive measurement sequence to be performed during the real-time measuring task where each row of S corresponds to the ith TX-RX measuring pair of the sequence and each column of S corresponds to the jth FE of the discretized target medium to be imaged.

Problem Definition

Weak perturbations ➜ Biomedical problem ➜ $v = s(\sigma)$

Problem Solution

MEs ➜ A-Φ potential formulation ➜ Coulomb gauge ➜ Quasi-stationarity

E

Reciprocity theorem

v_{sim}   **S**

Calculation

A: analytical-numerical method
Φ: FEM ➜ Galerkin weighted residual method ➜
Preconditioned CG ➜ First order tetrahedral FEs

Forward mesh ➜ Piecewise constant conductivity distribution

Inverse mesh ➜ Constant conductivity distribution

E   **v_{sim}**   **S**   **E**
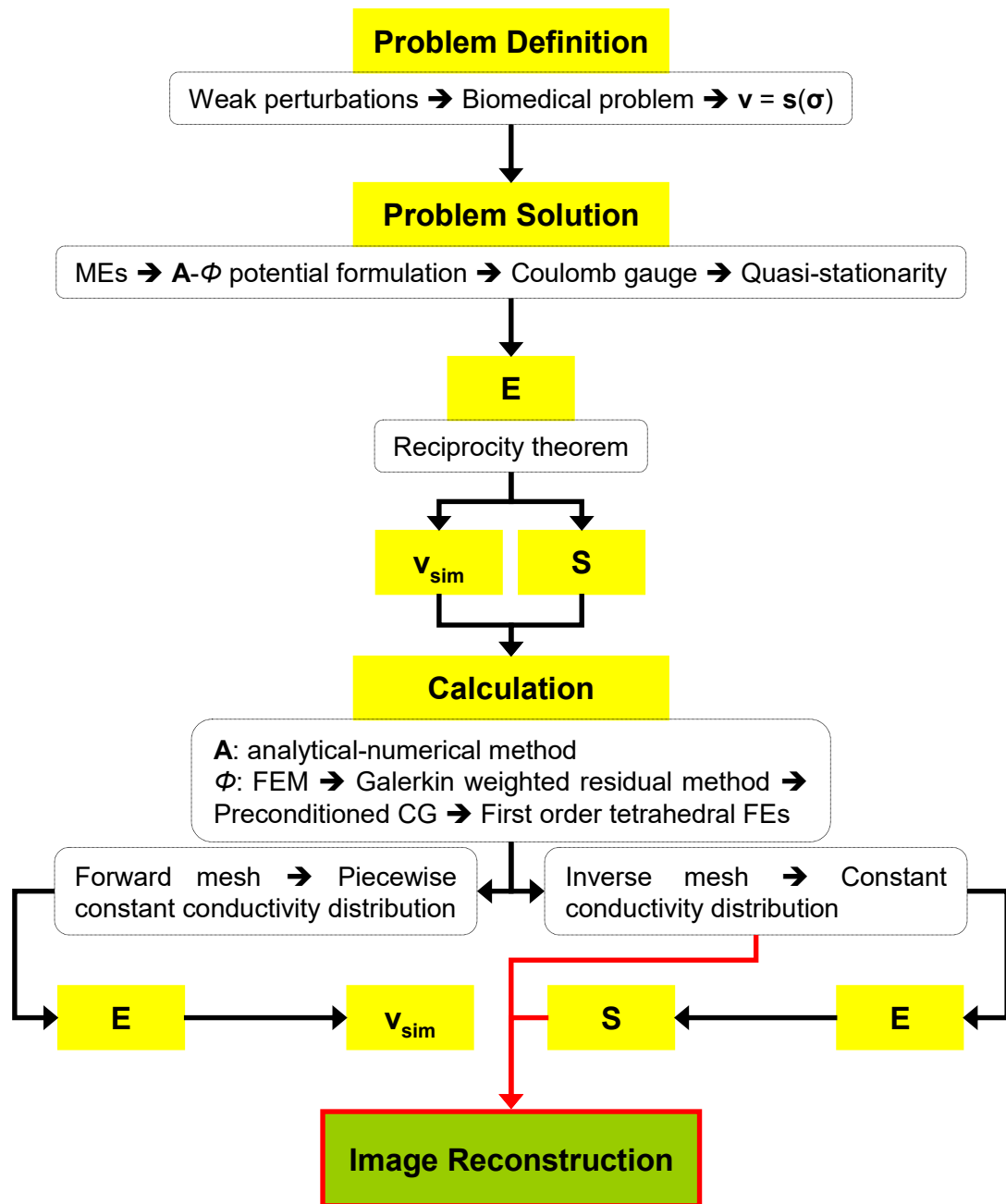
Image Reconstruction

*Figure (4.3): Forward solution and sensitivity calculation sequence. This sequence represents the second stage of the MITS imaging process prior to image reconstruction. **v_{sim}**: forward solution of the modelled (simulated) biomedical MITS problem representing the vector of the calculated voltages; it is not to be confused with the vector of the real measurement data **v** to be gained from the actual measurements conducted in this work. All data gathered from this sequence will be outputted into several data structures from which the required data for the image reconstruction GUI can be obtained, namely, the sensitivity matrix **S** and the corresponding inverse mesh of the FE model.*

$$S_{ij} = \Delta v_i \,/\, \Delta \sigma_j \qquad\qquad (4.7)$$

with *(i = 1, …, m)* and *(j = 1, …, n)*.

Thus, *m* represents the number of the available TX-RX measurement combinations (independent measurements, measured voltages) equal to the number of the TXs multiplied by the number of the RXs, and *n* represents the predetermined number of the FEs (tetrahedrons, voxels) in the conducting region discretized by FEM.

❖   Replacement of the previously used commercial FE-model generation and visualization program by two new open-source programs. Unfortunately, the multifunctional high-performance mesh-generation and tomographic-visualization environment *HyperMesh*® from *Altair Engineering* was no longer on hand at IMT-TUG. Therefore, on the one hand, the new program *NETGEN* has to be integrated into the forward solver for mesh generation; on the other hand, the new stand-alone program *ParaView* has to be used for tomographic visualization.

Figure (4.3) schematically summarizes the main steps throughout the forward solution and sensitivity calculation stage of the MITS imaging process, performed by the adapted forward solver.
The principal output of this intermediate stage to be fed into the final image reconstruction stage is the sensitivity matrix **S** which will be inputted to the inverse solution step. **S** is calculated according to the predetermined constant conductivity distribution assigned to the inverse FE model (inverse mesh). The latter will in turn be inputted to the visualization step of the final stage for converting the vector of the distributed conductivities **σ** within the FEM-discretized target medium into tomographically visualizable data.

4.5   Inverse Problem and Image Reconstruction

4.5.1   Problem Considerations

Recalling the previous equations (4.3-4.5) stating the forward and inverse eddy-current problems, and the corresponding sensitivity formula, respectively, i.e., in contextual notation:

$$v_i = s_i(\boldsymbol{\sigma}) \qquad (4.8)$$

$$\sigma_j = s_j^{-1}(\boldsymbol{v}) \qquad (4.9)$$

$$S_{ij} = \partial v_i / \partial \sigma_j = \partial s_i(\boldsymbol{\sigma}) / \partial \sigma_j \qquad (4.10)$$

with *(i = 1, …, m)* and *(j = 1, …, n)*, i.e., *v = (v₁, …, vₘ)* and *σ = (σ₁, …, σₙ)*

with $(i = 1, \ldots, m)$ and $(j = 1, \ldots, n)$, i.e., $v = (v_1, \ldots, v_m)$ and $\sigma = (\sigma_1, \ldots, \sigma_n)$

where **s** is the *nonlinear forward operator* which maps the vector of the *distributed conductivities* **σ** in the FEM-discretized target medium with *n* FEs onto the vector of the *induced voltages* **v** in the receivers with *m* independent voltages.

In this work, *(m = 256)* is less than *1%* of *(n = 30000)*, i.e., the available voltages **v** are much less than the sought conductivities **σ**. Thus, besides nonlinearity, the underlying MITS problem to be treated is extremely underdetermined and has hence no unique solution, i.e., it is severely ill-posed. This ill-posedness may lead to a drastic numerical instability. In terms of ill-conditioning, the sensitivity matrix **S** may contain several very small singular values and have hence a very large condition number, to be hereinafter closely examined. Consequently, low levels of noise or errors whatsoever affecting **v** to be measured may be inversely mapped through the ill-conditioned **S** into considerably high levels thereof onto **σ** to be reconstructed. Therefore, all these inherent problems have to be carefully tackled throughout the solution process in order to attain a stable inverse solution. For this purpose, the implemented solution strategy in this study comprises three main procedures, namely, linearization, optimization and regularization.

4.5.2   Problem Linearization

One of the most commonly used methods for the linear approximation of nonlinear systems is based on the well-known Taylor formulation. When applied to the biomedical MITS forward problem (4.8), this problem can then be expressed by the first-order term of its Taylor-series expansion about some initial conductivity distribution **σ₀**, i.e., by the sum of the first two terms in the series as shown in the following formulation:

$$v_i = s_i(\boldsymbol{\sigma}) \approx s_i(\boldsymbol{\sigma}_0) + \sum_{j=1}^{n} [(\partial s_i(\boldsymbol{\sigma}) / \partial \sigma_j)|_{\sigma=\sigma_0} \ (\sigma_j - \sigma_{0j})] \qquad (4.11)$$

or explicitly arranged as:

$$\Delta v_i = s_i(\boldsymbol{\sigma}) - s_i(\boldsymbol{\sigma_0}) \approx \sum_{j=1}^{n} [(\partial s_i(\boldsymbol{\sigma}) / \partial \sigma_j)|_{\sigma=\sigma_0} \Delta \sigma_j] \qquad (4.12)$$

with $(i = 1, ..., m)$ and $(j = 1, ..., n)$, i.e., $\boldsymbol{v} = (v_1, ..., v_m)$, $\boldsymbol{\sigma} = (\sigma_1, ..., \sigma_n)$ and $\boldsymbol{\sigma_0} = (\sigma_{01}, ..., \sigma_{0n})$.

As can be clearly seen in equation (4.12), the right-hand-side term contains the sensitivity formula (4.10) evaluated at $\boldsymbol{\sigma_0}$:

$$S_{ij} = (\partial s_i(\boldsymbol{\sigma}) / \partial \sigma_j)|_{\sigma=\sigma_0} \qquad (4.13)$$

Thus, the combination of both equations (4.12) and (4.13) may be stated as follows:

$$\Delta v_i = \sum_{j=1}^{n} S_{ij} \Delta \sigma_j|_{\sigma=\sigma_0} \qquad (4.14)$$

or finally, in compact vector and matrix notation, the explicit linearized forward problem becomes:

$$\Delta \boldsymbol{v} = \boldsymbol{S} \, \Delta \boldsymbol{\sigma} \qquad (4.15)$$

where $\Delta \boldsymbol{v}$ represents the *change in the measured voltage* at the receivers in consequence of a *small change in the conductivity* of the target medium $\Delta \boldsymbol{\sigma}$, and $\boldsymbol{S}$ is the *sensitivity matrix*.

Thus, equation (4.15) describes a linear system wherein $\Delta \boldsymbol{v}$ is a linear function of $\Delta \boldsymbol{\sigma}$, yet not without any restrictions. It must be emphasized that the above-mentioned initial conductivity distribution $\boldsymbol{\sigma_0}$ is not to be arbitrarily chosen, but only in close vicinity to the true conductivity distribution $\boldsymbol{\sigma}$ so that the conductivity change $\{\Delta \boldsymbol{\sigma} = \boldsymbol{\sigma} - \boldsymbol{\sigma_0}\}$ is small enough to be within the region of linearity of the system (4.15). In other words, the smoothness of $s_i(\boldsymbol{\sigma})$ defines the range or limits within which the linearization is valid.
Equation (4.15) will have the direct inverse solution (4.16) if and only if the system matrix $\boldsymbol{S}$ is strictly invertible:

$$\Delta \boldsymbol{\sigma} = \boldsymbol{S}^{-1} \Delta \boldsymbol{v} \qquad (4.16)$$

However, S is a *256*-by-*30000* matrix, i.e., non-square and hence strictly non-invertible. For this reason, optimization methods come into use.

4.5.3   Problem Optimization

In order to solve the equation system (4.16) in terms of mathematical optimization, the so-called *objective (goal) function* has to be defined. In this regard, one of the most common optimization methods is the *least squares method (LS)* where the standard objective function is the squared L_2 *(Euclidean) norm* of the *residuals*. The residuals are the difference between the observed (measured) data Δv and the predicted (estimated) data *(S $\Delta\sigma$)*:

$$r = \Delta v - S \, \Delta\sigma \qquad (4.17)$$

Thus, the LS objective function reads as follows:

$$\Psi_{LS} = \|r\|_2^2 = r^T r = \|\Delta v - S \, \Delta\sigma\|_2^2 = [\Delta v - S \, \Delta\sigma]^T [\Delta v - S \, \Delta\sigma] \qquad (4.18)$$

where the superscript T stands for the *transpose*.

The corresponding optimal LS-based inverse solution of equation (4.15) is that $\Delta\sigma$ which minimizes Ψ_{LS}:

$$\Delta\sigma_{opt} = argmin_{\Delta\sigma} (\Psi_{LS}) = argmin_{\Delta\sigma} ([\Delta v - S \, \Delta\sigma]^T [\Delta v - S \, \Delta\sigma]) \qquad (4.19)$$

In order to solve this minimization problem, the *first-order optimality condition* has to be applied, i.e., the gradient of Ψ_{LS} with respect to $\Delta\sigma$ has to be set to zero:

$$\nabla_{\Delta\sigma}\Psi_{LS} = \partial\Psi_{LS} / \partial\Delta\sigma = 2S^T (S \, \Delta\sigma - \Delta v) = 0 \qquad (4.20)$$

The sought optimal $\Delta\sigma$ (the subscript *opt* will henceforth be dropped) can thus be simply obtained by solving this equation for $\Delta\sigma$. Thus, assuming that $[S^T S]^{-1}$ exists, the inverse solution of the linearized problem can be explicitly stated as:

$$\Delta\sigma = [S^T S]^{-1} S^T \Delta v \qquad (4.21)$$

where $[S^T S]$ is an approximation of the *Hessian* and therefore frequently termed

Hessian matrix; $([S^T\ S]^{-1}\ S^T)$ is the *Moore-Penrose inverse* or *pseudoinverse* of S, to be symbolized as S^+.

According to the Moore-Penrose inverse definition, the pseudoinverse S^+ in equation (4.21), stated separately as S_l^+ in the following equation, represents a *left inverse* valid when the *m*-by-*n* matrix S has a full rank, its *n* columns are linearly independent and hence the *n*-by-*n* matrix $[S^T\ S]$ is invertible (mathematically, yet not numerically, all *m*-by-*n* sensitivity matrices S used throughout this work have a full rank *m*, i.e., *256*):

$$S_l^+ = [S^T\ S]^{-1}\ S^T \qquad\qquad (4.22)$$

The *n*-by-*n* Hessian matrix $[S^T\ S]$ in S_l^+ has the dimensions *(30000 x 30000)*. The inversion of such a large-size matrix was extremely memory-consuming for the central PC of the MITS tomograph as additional considerable memory was required for the PC operation, involved application programs, calculation process, etc. As, in the mathematical sense, the *m*-by-*n* matrix S has a full rank *m*, its *m* rows are linearly independent and hence the *m*-by-*m* matrix $[S\ S^T]$ is invertible, then according to the Moore-Penrose inverse definition, the left inverse S_l^+ can be restated and computed as a *right inverse* S_r^+ in the following way:

$$S_r^+ = S^T\ [S\ S^T]^{-1} \qquad\qquad (4.23)$$

The *m*-by-*m* Hessian matrix $[S\ S^T]$ in S_r^+ has the dimensions *(256 x 256)*, and the inversion thereof requires much less memory than the inversion of the large-dimensioned *30000*-by-*30000* one $[S^T\ S]$ in S_l^+. Accordingly, switching between S_l^+ and S_r^+, the inverse solution (4.21) can be restated in the following memory-efficient version:

$$\Delta\sigma = S^T\ [S\ S^T]^{-1}\ \Delta v \qquad\qquad (4.24)$$

At this stage of the solution process, equations (4.21) and (4.24) answer the questions regarding the physical, mathematical and computational stability of the underlying biomedical MITS problem, but not those regarding its numerical instability. This inherent instability has to be analyzed in terms of solution existence, uniqueness and stability, i.e., in terms of ill-posedness of the linearized systems (4.21) and (4.24). Being considerably underdetermined due to *{m « n}*, they may have no solution at all, i.e., be inconsistent; even if a solution existed, there are not enough

independent data Δv to uniquely solve these systems for the parameters $\Delta\sigma$. This non-existence or non-uniqueness of the solution arises from the numerically rank-deficiency and hence singularity of the Hessian matrix, i.e., from its numerical non-invertibility. This non-invertibility is in turn caused by many considerably small singular values in the m-by-m $[S\ S^T]$ and even much more and much smaller, quasi-zero ones in the n-by-n $[S^T\ S]$, leading to a considerably large condition number of the former and a much larger, quasi-infinite one of the latter. Consequently, this severe ill-conditioning gives the inverse mapping S^+ the tendency to amplify low-level noise affecting the measured Δv to extremely high-level noise onto the reconstructed $\Delta\sigma$, preventing thereby a stable solution. Therefore, the ill-posedness of the afore-stated inverse formulations has to be overcome in order to enable a regular numerical inversion and hence a stable solution. For this purpose, regularization methods come into use.

4.5.4   Problem Regularization

4.5.4.1   Tikhonov Regularization

In order to solve the equation systems (4.21) and (4.24) in terms of numerical regularization, the corresponding LS objective function (4.18) has to be extended by some a priori information about the parameters. In this regard, *Tikhonov regularization* is one of the most commonly used methods for the regularization of linear ill-posed problems. It can be implemented by including the a priori information as an additional regularization (penalty) function in the objective function of the ill-posed problem to be optimized. Accordingly, the Tikhonov-regularized LS objective function of the biomedical MITS problem reads as follows:

$$\Psi_{LS\text{-}reg} = \Psi_{LS} + \Psi_{reg} = \left\| \Delta v - S\ \Delta\sigma \right\|_2^2 + \lambda \left\| R\ \Delta\sigma \right\|_2^2$$

$$= [\Delta v - S\ \Delta\sigma]^T [\Delta v - S\ \Delta\sigma] + \lambda [R\ \Delta\sigma]^T [R\ \Delta\sigma] \qquad (4.25)$$

where Ψ_{reg} is the *regularization function*; λ and R are usually termed *regularization parameter* and *regularization matrix*, respectively.

In an analogous manner to the mathematical formulations of the unregularized LS-optimized problem in the previous paragraph, the solution steps can be stated as follows:

Firstly, the Tikhonov-regularized LS optimization (minimization) problem becomes:

$$\Delta\boldsymbol{\sigma}_{opt\text{-}reg} = argmin_{\Delta\sigma} (\Psi_{LS} + \Psi_{reg})$$

$$= argmin_{\Delta\sigma} ([\Delta\boldsymbol{v} - \boldsymbol{S} \, \Delta\boldsymbol{\sigma}]^T [\Delta\boldsymbol{v} - \boldsymbol{S} \, \Delta\boldsymbol{\sigma}] + \lambda \, [\boldsymbol{R} \, \Delta\boldsymbol{\sigma}]^T [\boldsymbol{R} \, \Delta\boldsymbol{\sigma}]) \qquad (4.26)$$

Secondly, the first-order optimality condition becomes:

$$\nabla_{\Delta\sigma}\Psi_{LS\text{-}reg} = \partial(\Psi_{LS} + \Psi_{reg}) \, / \, \partial\Delta\boldsymbol{\sigma} = 2 \, \boldsymbol{S}^T \, (\boldsymbol{S} \, \Delta\boldsymbol{\sigma} - \Delta\boldsymbol{v}) + 2 \, \lambda \, \boldsymbol{R}^T \, \boldsymbol{R} \, \Delta\boldsymbol{\sigma} = 0 \qquad (4.27)$$

Thirdly, the explicit LS-optimized Tikhonov-regularized inverse solution of the linearized biomedical MITS problem becomes (the subscript *opt-reg* will henceforth be dropped):

$$\Delta\boldsymbol{\sigma} = [\boldsymbol{S}^T \, \boldsymbol{S} + \lambda \, \boldsymbol{R}^T \, \boldsymbol{R}]^{-1} \, \boldsymbol{S}^T \, \Delta\boldsymbol{v} \qquad (4.28)$$

Finally, the memory-efficient version of the inverse solution becomes:

$$\Delta\boldsymbol{\sigma} = \boldsymbol{S}^T \, [\boldsymbol{S} \, \boldsymbol{S}^T + \lambda \, \boldsymbol{R}^T \, \boldsymbol{R}]^{-1} \, \Delta\boldsymbol{v} \qquad (4.29)$$

However, despite similarity, the latter solution formula cannot be derived in the same manner presented in the previous paragraph based on the Moore-Penrose inverse definition due to the (existence of the) regularization term $(\lambda \, [\boldsymbol{R}^T \, \boldsymbol{R}])$ disallowing such direct derivation. $[\boldsymbol{R}^T \, \boldsymbol{R}]$ in the original solution equation (4.28) is an *n*-by-*n* matrix, but an *m*-by-*m* one in the computationally efficient version (4.29). Equation (4.28), however, is the outcome of the regularized LS minimization problem (4.26). Thus, an *m*-by-*m* $[\boldsymbol{R}^T \, \boldsymbol{R}]$ as a part of the regularization term and thus an inverse solution in the form of equation (4.29) can only be validated if it represents the outcome of a logically consistent derivation, not necessarily a Tikhonov-based derivation, and hereunder are two examples thereof:

❖   Based on the Bayesian *maximum a posteriori estimator (MAP)*, the solution of the underlying problem may be stated in the following form:

$$\Delta\boldsymbol{\sigma} = <\Delta\boldsymbol{\sigma}> + \boldsymbol{C}_{\Delta\sigma} \, \boldsymbol{S}^T \, [\boldsymbol{S} \, \boldsymbol{C}_{\Delta\sigma} \, \boldsymbol{S}^T + \boldsymbol{C}_{\Delta v}]^{-1} \, [\Delta\boldsymbol{v} - \boldsymbol{S} \, <\Delta\boldsymbol{\sigma}>] \qquad (4.30)$$

where $<\Delta\boldsymbol{\sigma}>$ represents the *a priori estimation of* $\Delta\boldsymbol{\sigma}$; $\boldsymbol{C}_{\Delta\sigma}$ and $\boldsymbol{C}_{\Delta v}$ represent the *covariance matrices* of $\Delta\boldsymbol{\sigma}$ and $\Delta\boldsymbol{v}$, respectively.

Assuming that $<\Delta\boldsymbol{\sigma}>$ is zero, and that the *n* elements of $\Delta\boldsymbol{\sigma}$ are uncorrelated and distributed according to a standard normal (Gaussian) distribution with zero mean and unit variance; thus, $<\Delta\boldsymbol{\sigma}>$ can be dropped and the covariance matrix $\boldsymbol{C}_{\Delta\sigma}$ can be replaced by the identity matrix, reducing thereby the original MAP solution (4.30) to the following simplified one:

$$\Delta\boldsymbol{\sigma} = \boldsymbol{S}^T [\boldsymbol{S}\ \boldsymbol{S}^T + \boldsymbol{C}_{\Delta v}]^{-1}\ \Delta\boldsymbol{v} \qquad (4.31)$$

which represents the first of three memory-efficient formulations of the solution equation system used in image reconstruction in this chapter.

The solution (4.31) is only penalized according to the variances of the acquired signals $\Delta\boldsymbol{v}$, i.e., according to their quality or reliability without any additional weighting of $\boldsymbol{C}_{\Delta v}$ through a regularization parameter, which represents the principal argument behind the use of such reduced or simplified MAP solution in this study.

❖   [Merwa 2004] showed the equivalence of the following two equations:

$$\Delta\boldsymbol{\sigma} = [\boldsymbol{S}^T\ \boldsymbol{S} + \lambda\ \boldsymbol{I}_n]^{-1}\ \boldsymbol{S}^T\ \Delta\boldsymbol{v} \qquad (4.32)$$

$$\Delta\boldsymbol{\sigma} = \boldsymbol{S}^T [\boldsymbol{S}\ \boldsymbol{S}^T + \lambda\ \boldsymbol{I}_m]^{-1}\ \Delta\boldsymbol{v} \qquad (4.33)$$

where $\boldsymbol{I}_n$ and $\boldsymbol{I}_m$ represent the *n-by-n* and *m-by-m Identity matrices*, respectively, and the latter formula (4.33) represents the second memory-efficient formulation of the solution equation system used in image reconstruction in this chapter (and in the next chapter as well).

Remarks

It often happens to find equation (4.31) in the literature in the following form:

$$\Delta\boldsymbol{\sigma} = \boldsymbol{S}^T [\boldsymbol{S}\ \boldsymbol{S}^T + \lambda\ \boldsymbol{C}_{\Delta v}]^{-1}\ \Delta\boldsymbol{v} \qquad (4.35)$$

This form additionally involves some kind of ad-hoc regularization parameter λ for adjusting $\boldsymbol{C}_{\Delta v}$ when it is -by itself- not able to satisfactorily overcome the ill-conditioning of $[\boldsymbol{S}\ \boldsymbol{S}^T]$. Actually, equation (4.35) can already be ad hoc derived from equation (4.33) through simply substituting $\boldsymbol{I}_m$ in the latter one with $\boldsymbol{C}_{\Delta v}$. Thus, the reduced MAP solution (4.31) can also be observed as an LS-optimized Tikhonov-

regularized solution with an implied λ of unity.

In summary, in contrast to the unregularized solutions (4.21) and (4.24), their respective regularized versions (4.28) and (4.29) have the penalty term $(\lambda \ [R^T \ R])$ which improves the conditioning of the Hessian matrix and thus enables a regular numerical inversion, i.e., a stable solution.

4.5.4.2   Truncated Singular Value Decomposition Regularization

Another very common and even much simpler method of regularization than the Tikhonov one is *truncated singular value decomposition (TSVD)*, the name whereof reveals its methodology based on the most common matrix factorization form, *singular value decomposition (SVD)*. When applied to S, SVD yields the following factorization *(m = 256, n = 30000)*:

$$S_{mxn} = U_{mxm} \ K_{mxn} \ (V_{nxn})^T \tag{4.36}$$

where all vectors and matrices in this subparagraph's equations will be indexed with their *dimensions (#x#)* for better understanding of the TSVD functioning; U and V are orthogonal matrices, the columns whereof are the *left* and *right singular vectors* of S, spanning the *data* and *model spaces* corresponding to Δv and $\Delta \sigma$, respectively; K is a real diagonal matrix, the diagonal entries whereof are the non-zero positive *singular values* of S, intrinsically gradually descending with ascending order:

$$k = (k_1, \ ..., \ k_m) = diag(K_{mxn}) = (K_{11}, \ ..., \ K_{mm}) \tag{4.37}$$

where *diag(#)* symbolizes the extraction of the *diagonal entries* from the bracketed matrix; $\{k_1 \geq ... \geq k_m > 0\}$, i.e., $\{K_{11} \geq ... \geq K_{mm} > 0\}$.

Inserting equation (4.36) in the direct inverse solution (4.16) of the linearized problem, i.e., in $\{\Delta \sigma = S^{-1} \ \Delta v\}$, is mathematically impossible due to the non-invertibility of the non-square matrix K. In such cases, it is usual to use a reduced or compact version of SVD that enables such inversion through involving only the m columns of K and V in the decomposition. Accordingly, still abbreviated as S, the corresponding reduced or compact version of the sensitivity matrix reads as follows:

$$S_{mxn} = U_{mxm} \ K_{mxm} \ (V_{nxm})^T \tag{4.38}$$

The pseudoinverse of the reduced **S** is given then by the following factorization assuming herein that K^{-1} mathematically, not necessarily numerically, exists:

$$S^+_{nxm} = (S_{mxn})^{-1} = V_{nxm} \ (K_{mxm})^{-1} \ (U_{mxm})^T \tag{4.39}$$

Inserting now equation (4.39) in equation (4.16) yields the following inverse solution:

$$\Delta\sigma_{nx1} = S^+_{nxm} \ \Delta v_{mx1} = V_{nxm} \ (K_{mxm})^{-1} \ (U_{mxm})^T \ \Delta v_{mx1} \tag{4.40}$$

This equation, however, is only mathematically solvable, yet not numerically due to the strong ill-conditioning of **S** signified, as will be seen later, by a considerably large *condition number (CN)*:

$$CN = max(k) \ / \ min(k) = k_1 \ / \ k_m \geq 1 \tag{4.41}$$

And right here comes the role of TSVD which truncates (whence the name) those singular values of too small magnitudes causing the numerical instability as shown in equation (4.42) which represents the third memory-efficient formulation of the solution equation system used in image reconstruction in this chapter:

$$\Delta\sigma_{nx1} = V_{nxtl} \ (K_{tlxtl})^{-1} \ (U_{mxtl})^T \ \Delta v_{mx1} \tag{4.42}$$

where the subscript *tl* denotes the *truncation level*.

Thus, TSVD regularizes the inverse solution by involving only the *tl* columns of the three matrices **V**, **K** and **U** and the *tl* rows of **K** in the decomposition, in other words, by considering only those *tl* left and right singular vectors of **S** in **U** and **V**, respectively, corresponding to the *tl* largest singular values of **S** in **K**.

In summary, it is now more obvious why only a few considerably small singular values in **S** can lead to a considerable numerical instability, and why in contrast to the classic SVD-based solution (4.40) its TSVD-regularized version (4.42) avoids such consequences through the truncation procedure which improves the conditioning of **S** and thus enables a regular numerical inversion, i.e., a stable solution.

4.5.5   Implementation

Usually, the inverse problem of many imaging modalities including MITS is solved by employing iterative schemes, such as the well-known *Newton* or *Gauss-Newton* algorithms. Due to their iterative nature, such schemes demand the most computational power of the host PC and are therefore intensively time-consuming. Fortunately, it has already been shown in the literature that the first iteration of such algorithms preserves the most relevant features of the desired image. In this respect, however, it is not expected that this one single iteration will allow for *absolute (static) imaging (ABS)*. Even the iterative solution of the linearized or original nonlinear MITS problem has actually not shown correct absolute imaging so far. The single-iteration (one-step) approach is particularly appropriate for *differential imaging*, e.g.:

- *Dynamic imaging*, e.g., between different states of interest regarding the ROI, i.e., *state-differential imaging (SD)*.
- *Parametric imaging*, e.g., between different frequencies of interest, i.e., *frequency-differential imaging (FD)*.
- *Dynamic-parametric imaging*, e.g., between different states and frequencies of interest, i.e., *state-frequency-differential imaging (SFD)*. This hybrid imaging type represents a combination of the two latter ones, to be thematized and experimentally performed for the very first time so far in MITS.

As will be experimentally seen in this and the next chapter, the implemented one-step image reconstruction algorithms were able to satisfactorily accomplish all of the above-stated types of differential imaging considering phantoms of physiological conductivity.

Figure (4.4) schematically summarizes the main steps throughout the data post-processing and inverse solution stage of the MITS imaging process, performed by the programmed image reconstruction GUI.

The three main steps of this stage will be explained in the following three subparagraphs, respectively, in their prescribed order shown in figure (4.4). (v_{ABS}, Δv_{SD}, Δv_{FD}, Δv_{SFD}) and ($C_{v_{ABS}}$, $C_{\Delta v_{SD}}$, $C_{\Delta v_{FD}}$, $C_{\Delta v_{SFD}}$) stand for the *data vectors* and their respective *covariance matrices* outputted by the ABS, SD, FD and SFD data post-processing routines, respectively. Although no iterative inverse solution is implemented in this stage, the static (ABS) imaging type undergoes its first (data post-processing) step for possible future implementation.
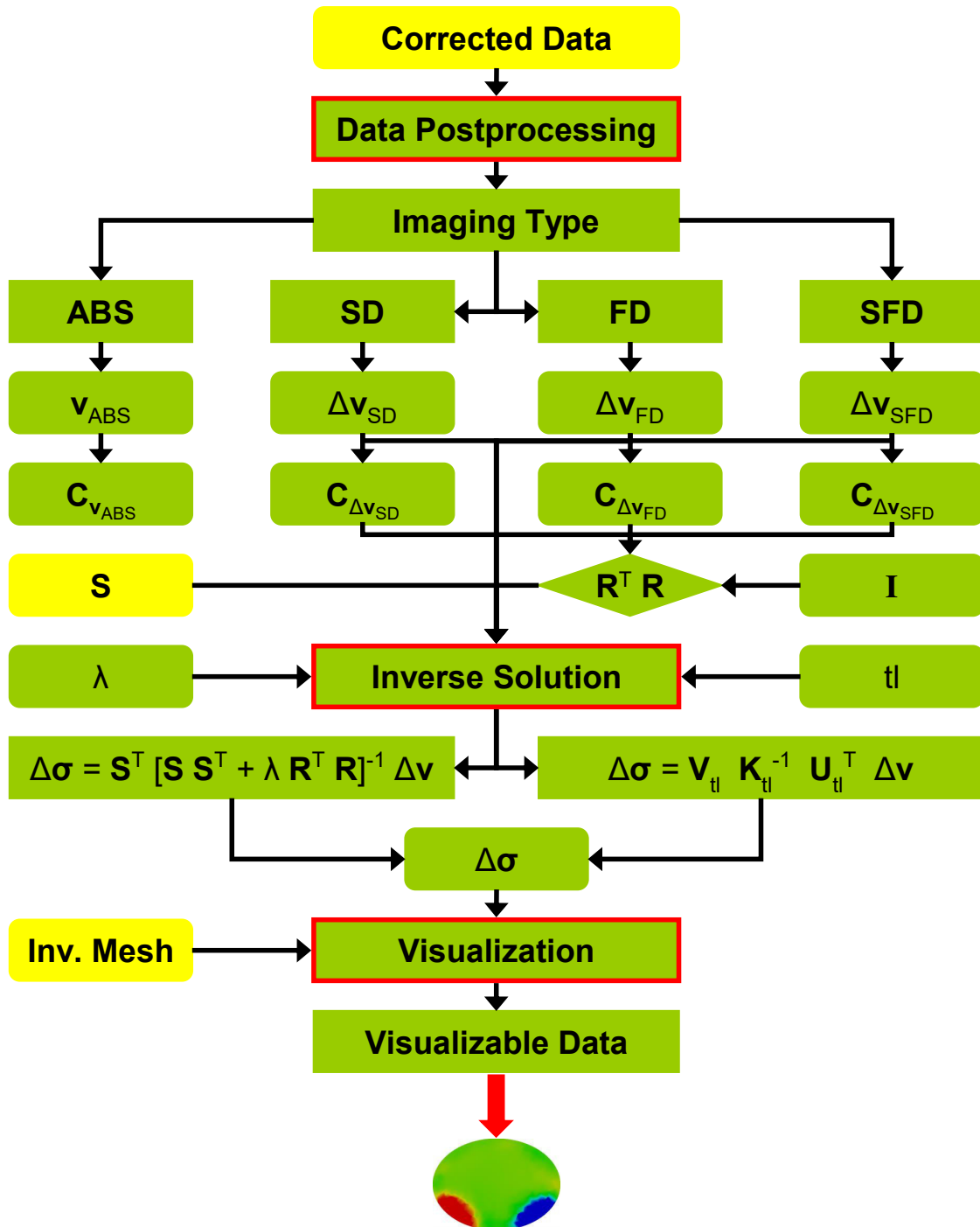
Figure (4.4): Data postprocessing and inverse solution sequence. This sequence represents the third and final stage of the MITS imaging process, i.e., image reconstruction. The yellow inputs, i.e., the corrected data, the sensitivity matrix **S** and the inverse mesh, are the outputs of the first and second stages of the imaging process (see figures (4.1-4.3)). As can be inferred from this schematic diagram, the frequency is the reference parameter of interest that influences the conductivity in parametric (FD) and hybrid dynamic-parametric (SFD) imaging.

4.5.5.1 Data Postprocessing

The corrected signals inputted to this step will be prepared according to the intended imaging type before inputting them to the subsequent inverse solution step. Hereof, as shown in figure (4.4), it can be distinguished between the following four different imaging types:

❖   **Absolute Imaging (ABS)**

This is the static case wherein the absolute conductivity distribution in the target medium is in focus. This imaging type may allow for reconstructing the true conductivity distribution in most body regions if a competent iterative algorithm with a stable convergence behaviour is properly implemented. However, due to their computational appropriateness, single-step solution algorithms were preferred to be implemented in the image reconstruction GUI, and static imaging was therefore beyond the scope of this study. The received *absolute signal* v_{ABS} may be presented as follows:

$$v_{ABS} = v \qquad\qquad (4.43)$$

where v represents the *measured signal* in one and the same state at one and the same frequency.

Of course, in the programming as well as mathematical sense, v_{ABS} can further uninterruptedly flow through the inverse solution and visualization steps of the image reconstruction GUI in figure (4.4); however, needless to say, no absolute images can be hoped for due to the non-iterative and hence non-converging nature of the used reconstructors. Even an iterative reconstructor may not ensure correct absolute imaging if no appropriate line-search routine is additionally implemented in order to readjust the step size after each iteration and hence to possibly converge towards the correct absolute conductivity distribution.

❖   **State-Differential Imaging (SD)**

This is the dynamic case wherein the local conductivity changes in the target medium are in focus. This imaging type is particularly appropriate for reconstructing the conductivity changes in non-stationary (non-motionless) body regions between

different states, e.g., in the thoracic or cardiac region between inspiration and expiration or systole and diastole. The resulting *state-differential signal* $\Delta\boldsymbol{v}_{SD}$ may be presented as follows:

$$\Delta\boldsymbol{v}_{SD} = \boldsymbol{v}_{s2} - \boldsymbol{v}_{s1} \qquad (4.44)$$

where $\boldsymbol{v}_{s1}$ and $\boldsymbol{v}_{s2}$ represent the *measured signal* in the *first* and *second state*, respectively, at one and the same frequency.

❖   **Frequency-Differential Imaging (FD)**

This is the parametric case wherein the spectroscopic conductivity changes in the target medium are in focus. This imaging type is very useful for reconstructing the conductivity changes of most biological tissues between different frequencies, particularly those exhibiting a distinct dispersive behaviour. Furthermore, in motionless organs, such as the brain, if ABS imaging is practically not implementable and SD imaging is not the type of choice, then FD imaging may be the only available choice. The resulting *frequency-differential signal* $\Delta\boldsymbol{v}_{FD}$ may be presented as follows:

$$\Delta\boldsymbol{v}_{FD} = \boldsymbol{v}_{f2} - \boldsymbol{v}_{f1} \qquad (4.45)$$

where $\boldsymbol{v}_{f1}$ and $\boldsymbol{v}_{f2}$ represent the *measured signal* in one and the same state at the *first* and *second frequency* f_1 and f_2, respectively.

❖   **State-Frequency-Differential Imaging (SFD)**

This is the hybrid dynamic-parametric case wherein both the local and spectroscopic conductivity changes in the target medium are in focus. This imaging type combines the functions or properties of the latter two SD and FD imaging types and can therefore be of particular usefulness for reconstructing the conductivity changes in non-motionless body regions between different states and frequencies, e.g., the conductivity changes in the pulmonary or cardiac region between inspiration and expiration or systole and diastole between different frequencies. The resulting *state-frequency-differential signal* $\Delta\boldsymbol{v}_{SFD}$ may be presented as follows:

$$\Delta\boldsymbol{v}_{SFD} = (\boldsymbol{v}_{s2} - \boldsymbol{v}_{s1})|_{f2} - (\boldsymbol{v}_{s2} - \boldsymbol{v}_{s1})|_{f1} = (\Delta\boldsymbol{v}_{SD})|_{f2} - (\Delta\boldsymbol{v}_{SD})|_{f1} \qquad (4.46)$$

stating that the SFD signal is the difference between two SD signals measured at two different frequencies f_1 and f_2, respectively.

In respect of these different imaging types, it is important to make aware of two relevant facts. On the one hand, the excitation current delivered by the PA of the implemented transmitting circuitry decreases with increasing frequency; this fact was of course taken into consideration in the data analysis and preprocessing stage of the imaging process, i.e., the actual (true) frequency-dependent excitation current was recovered and hence the received signal at whatever frequency was accordingly corrected prior to image reconstruction. On the other hand, the received signal and hence the sensitivity in MITS is proportional to the square of the applied excitation frequency. On this account, $\Delta\mathbf{v}_{FD}$ and $\Delta\mathbf{v}_{SFD}$ in the data post-processing step of figure (4.4) have to be scaled, corrected or weighted according to the excitation frequencies f_1 and f_2 and the corresponding PA output currents before inputting them to the succeeding inverse solution step, whereas this scaling is not required for $\mathbf{v}_{ABS}$ and $\Delta\mathbf{v}_{SD}$ because each of them is gained at one and the same frequency, hence, at one and the same excitation current.

Actually, the scaling of $\Delta\mathbf{v}_{FD}$ and $\Delta\mathbf{v}_{SFD}$ is already implied in figure (4.4) and their respective equations (4.45) and (4.46), and the implied *scaling factor γ* was simply calculated through relating the excitation frequencies to the corresponding currents in the correct way taking into consideration the quadratic dependence of the MITS signal on the applied field frequency:

$$\gamma = (I_2 / I_1) \, (f_2 / f_1)^2 \tag{4.47}$$

where I_1 and I_2 represent the *measured excitation current* at the *first* and *second* frequency f_1 and f_2, respectively.

Accordingly, the explicitly scaled versions -still abbreviated as $\Delta\mathbf{v}_{FD}$ and $\Delta\mathbf{v}_{SFD}$- used in the image reconstruction algorithm were, respectively:

$$\Delta\mathbf{v}_{FD} = \mathbf{v}_{f2} - \gamma \, \mathbf{v}_{f1} \tag{4.48}$$

$$\Delta\mathbf{v}_{SFD} = (\Delta\mathbf{v}_{SD})|_{f2} - \gamma \, (\Delta\mathbf{v}_{SD})|_{f1} \tag{4.49}$$

whereas $\mathbf{v}_{ABS}$ and $\Delta\mathbf{v}_{SD}$, per se, were ready to use in the algorithm.

In line therewith, the corresponding $C_{\Delta v_{FD}}$ and $C_{\Delta v_{SFD}}$ were in turn calculated in the data postprocessing step from these scaled signals Δv_{FD} and Δv_{SFD}, respectively, before inputting them to the subsequent inverse solution step, whereas $C_{v_{ABS}}$ and $C_{\Delta v_{SD}}$ were calculated from the corresponding ready-to-use signals v_{ABS} and Δv_{SD}, respectively.

Mathematically, the variances of v_{ABS}, Δv_{SD}, Δv_{FD} and Δv_{SFD} were calculated according to the following four equations, respectively, assuming uncorrelated received signals in the different states at the different frequencies due to the independent TX-RX measurement combinations:

$$var(v_{ABS}) = var(v) = std^2(v) \tag{4.50}$$

$$var(\Delta v_{SD}) = var(v_{s2}) + var(v_{s1}) = std^2(v_{s2}) + std^2(v_{s1}) \tag{4.51}$$

$$var(\Delta v_{FD}) = var(v_{f2}) + \gamma^2\, var(v_{f1}) = std^2(v_{f2}) + \gamma^2\, std^2(v_{f1}) \tag{4.52}$$

$$var(\Delta v_{SFD}) = var(\Delta v_{SD})|_{f2} + \gamma^2\, var(\Delta v_{SD})|_{f1}$$
$$= (std^2(v_{s2}) + std^2(v_{s1}))|_{f2} + \gamma^2\, (std^2(v_{s2}) + std^2(v_{s1}))|_{f1} \tag{4.53}$$

where $std(\#)$ and $var(\#)$ denote the *standard deviation* and *variance* of the bracketed signal, respectively.

Consequently, the resulting covariance matrices $C_{v_{ABS}}$, $C_{\Delta v_{SD}}$, $C_{\Delta v_{FD}}$ and $C_{\Delta v_{SFD}}$ of the data vectors v_{ABS}, Δv_{SD}, Δv_{FD} and Δv_{SFD}, respectively, were diagonal matrices with the respective variances on the diagonal:

$$C_{v_{ABS}} = diag(var(v_{ABS})) \tag{4.54}$$

$$C_{\Delta v_{\#}} = diag(var(\Delta v_{\#})) \tag{4.55}$$

where $diag(\#)$ symbolizes herein the formation of a *diagonal matrix* from the bracketed vector; the subscript $\#$ in equation (4.55) and the rest of this chapter stands for the three abbreviations *SD*, *FD* and *SFD* (recall that v_{ABS} and $\Delta v_{\#}$ implicitly represent $Im(v_{ABS})$ and $Im(\Delta v_{\#})$, respectively; hence, $C_{v_{ABS}}$ and $C_{\Delta v_{\#}}$ implicitly represent $C_{Im(v_{ABS})}$ and $C_{Im(\Delta v_{\#})}$, respectively).

4.5.5.2 Inverse Solution

As demonstrated in figure (4.4), this step allows for three different solutions of the linearized problem. These memory-efficient solutions were previously derived and stated in equations (4.31), (4.33) and (4.42); hereunder, they are restated in a more contextual form, i.e., as used in the image reconstruction algorithm:

❖   **MAP Solution**

$$\Delta\boldsymbol{\sigma}_\# = \boldsymbol{S}^T \left[\boldsymbol{S}\ \boldsymbol{S}^T + \boldsymbol{C}_{Im(\Delta\boldsymbol{v}_\#)}\right]^{-1} Im(\Delta\boldsymbol{v}_\#) \qquad (4.56)$$

❖   **Tikhonov Solution**

$$\Delta\boldsymbol{\sigma}_\# = \boldsymbol{S}^T \left[\boldsymbol{S}\ \boldsymbol{S}^T + \lambda\ \boldsymbol{I}_m\right]^{-1} Im(\Delta\boldsymbol{v}_\#) \qquad (4.57)$$

❖   **TSVD Solution**

$$\Delta\boldsymbol{\sigma}_\# = \boldsymbol{V}_{tl}\ \boldsymbol{K}_{tl}^{-1}\ \boldsymbol{U}_{tl}^T\ Im(\Delta\boldsymbol{v}_\#) \qquad (4.58)$$

Due to the previously explained data scaling by the factor γ, $\boldsymbol{S}$ is the same in all three solutions. Besides the signals $Im(\Delta\boldsymbol{v}_\#)$, the preceding data postprocessing step provides the inverse solution step with the following inputs:

- The various data covariance matrices $\boldsymbol{C}_{Im(\Delta\boldsymbol{v}_\#)}$ required for the MAP solution.
- The identity matrix $\boldsymbol{I}_m$ *(m = 256)* and the regularization parameter λ required for the Tikhonov solution.
- The truncation level *tl* required for the TSVD solution.

λ and *tl* adjust the amount of regularization, and their correct choice is of paramount importance for attaining meaningful images. In this context, it is usual to benefit from the regularization toolbox [Hansen 1994] and some ready-to-use iterative routines implemented therein, such as the *L-curve* [Hansen 1992], the *generalized cross-validation (GCV)* [Golub et al. 1979] and especially the best-known *discrepancy principle* [Morozov 1984]. However, in many cases, the optimal λ and *tl* cannot be predicted accurately, and empirical manual tuning becomes absolutely necessary, which can be extremely time-consuming. Thus, it became necessary to

develop alternative approaches that straightforwardly provide appropriate λ and tl without inconvenient trial-and-error tasks. To this end, two simple statements, respectively, were thought out in agreement with the physical, mathematical and numerical backgrounds in this context. Both statements have proved their applicability and offered the following several advantages:

- They always directly deliver appropriate λ and tl.
- They do not require iterative implementation, avoiding thereby all related problems.
- They do not require computing the norm of any term whatever, avoiding thereby the initial guess or a priori estimate of any parameter whatever (recall for instance that the residual norm, herein $\left\| \Delta \boldsymbol{v}_\# - \boldsymbol{S}\, \Delta \boldsymbol{\sigma}_\# \right\|_2$, is shared between all of the three methods cited above).

4.5.5.2.1 Appropriate Choice of the Regularization Parameter

Statement: *The mean value of the data variances is an appropriate regularization parameter (λ_{app}) if the ratio of the standard deviation of these variances to their mean is lower than one order of magnitude.* , i.e.:

$$\lambda_{app} = mean\{var(Im(\Delta \boldsymbol{v}_\#))\} \tag{4.59}$$

subject to the constraint:

$$std\{var(Im(\Delta \boldsymbol{v}_\#))\} \,/\, mean\{var(Im(\Delta \boldsymbol{v}_\#))\} < 10 \tag{4.60}$$

The Tikhonov-like reduced MAP solution (4.56) does not require such λ_{app} because it already implies a λ_{app} of unity; thus, the penalization occurs unequally according to the different data variances in the diagonal $\boldsymbol{C}_{Im(\Delta \boldsymbol{v}_\#)}$. In contrast, λ_{app} will enforce equal penalization according to unified (averaged) data variances in the Tikhonov solution (4.57). Thus, the (new) regularization term ($\lambda_{app}\,\boldsymbol{I}_m$) represents a Gaussian-distributed version of $\boldsymbol{C}_{Im(\Delta \boldsymbol{v}_\#)}$ with equal variances on its diagonal, and can be considered as an approximation of $\boldsymbol{C}_{Im(\Delta \boldsymbol{v}_\#)}$. In this regard, it might be relevant to recall the Morozov criterion, stated hereunder within the underlying context:

$$\lambda_{opt} = argmin_\lambda\, \{var[\boldsymbol{r}] - var[Im(\boldsymbol{N})]\}$$
$$= argmin_\lambda\, \{var[Im(\Delta \boldsymbol{v}_\#) - \boldsymbol{S}\, \Delta \boldsymbol{\sigma}_\#(\lambda)] - var[std(Im(\Delta \boldsymbol{v}_\#))]\} \tag{4.61}$$

where λ_{opt} represents the *optimal regularization parameter*; **r** and **N** are again the *residuals* and *measurement noise* explained previously, respectively.

It is obvious that statement (4.59) and the associated constraint (4.60) imply together the discrepancy principle to a certain degree, even though they do not consider the residuals explicitly; the better condition (4.60) is met, the more obvious this implication is and the more avoidable under- and over-regularization are.

4.5.5.2.2   Appropriate Choice of the Truncation Level

Statement: *The numerically usable rank ($rank_{num}$) of the sensitivity matrix is an appropriate truncation level (tl_{app}):*

$$tl_{app} = rank_{num} \ (\boldsymbol{S}) \qquad\qquad (4.62)$$

Although it is mathematically a full-rank matrix, **S** is numerically rank-deficient, as shown in its singular values' decay in figure (4.5) where a discontinuity occurs at a certain index. This index represents the actual rank of **S** usable in the numerical solution. If **S** were numerically a full-rank matrix, its singular values would decay continuously without any remarkable interruptions (gaps) therebetween, as is the case in the example decay of **k** in figure (4.6).

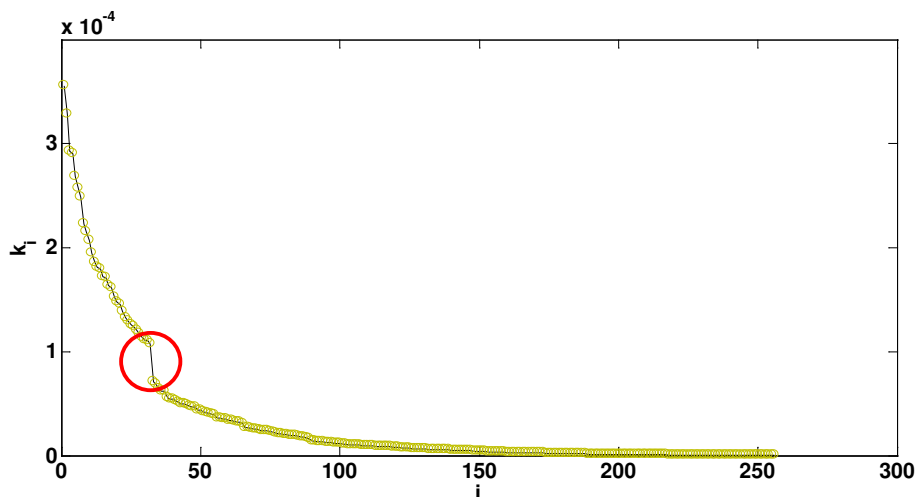*Figure (4.5): Singular values **k** of the SVD-factorized sensitivity matrix **S**. The red circle marks a rapid jump between two consecutive singular values.*
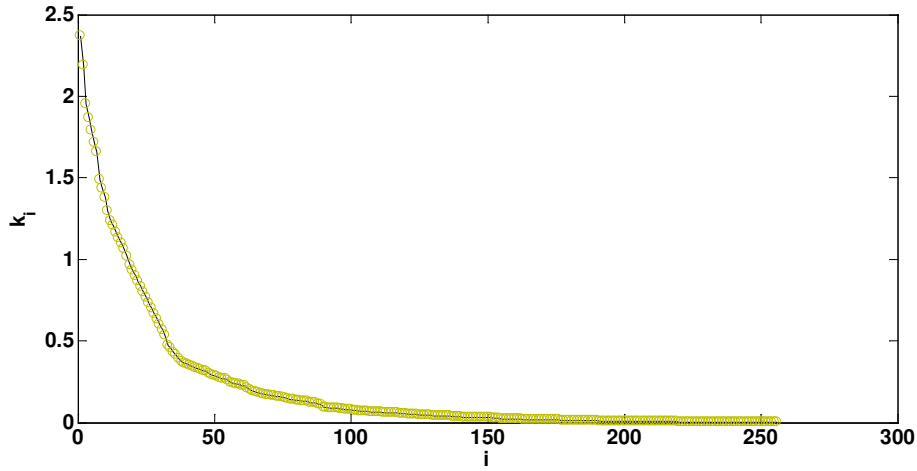
Figure (4.6): Example representation of the singular values decay of a full-rank sensitivity matrix. In contrast to the previous decay in figure (4.5), this one undergoes no discontinuity.

As is the case with the previous statement for λ_{app}, a clear and simple interpretation underlies this statement, namely, it is meaningless to involve those singular values mostly responsible for the numerical instability in the solution, and it is most probably useless to choose a truncation level -relatively- far lower or far higher than the numerically usable rank as this will certainly result in considerable over- or under-regularization, respectively.

4.5.5.3 Visualization

As shown in figure (4.4), this is the third and final step whereto the reconstructed imaging data $\Delta\boldsymbol{\sigma}_{\#}$ in the preceding inverse solution step is to be inputted for tomographic visualization. There are *15* vectors $\Delta\boldsymbol{\sigma}_{\#}$ to be visualized in this step, which will be grouped for the sake of consistency according to the used reconstruction method as follows:

- *5* MAP-reconstructed images: 2 $\Delta\boldsymbol{\sigma}_{SD}$, 2 $\Delta\boldsymbol{\sigma}_{FD}$ and *1* $\Delta\boldsymbol{\sigma}_{SFD}$.
- *5* Tikhonov-reconstructed images: 2 $\Delta\boldsymbol{\sigma}_{SD}$, 2 $\Delta\boldsymbol{\sigma}_{FD}$ and *1* $\Delta\boldsymbol{\sigma}_{SFD}$.
- *5* TSVD-reconstructed images: 2 $\Delta\boldsymbol{\sigma}_{SD}$, 2 $\Delta\boldsymbol{\sigma}_{FD}$ and *1* $\Delta\boldsymbol{\sigma}_{SFD}$.

Due to the single-step nature of the used image reconstruction algorithms, the pixel values on the colour bars of these images cannot be interpreted quantitatively

so as to estimate absolute conductivity changes; they rather help to estimate the contrast between the ROI and the background or between the different frequencies. However, using one and the same (global) λ or tl for all *5* reconstructions in the respective solution will allow using the pixel values in the quantitative comparison between the different images $\Delta\boldsymbol{\sigma}_{\#}$ with respect to the different signals $\Delta\boldsymbol{v}_{\#}$ as well as in the validation of the new hybrid dynamic-parametric imaging approach.

❖   **MAP-reconstructed images**

Due to its form, the MAP solution already implies a global λ of unity.

❖   **Tikhonov-reconstructed images**

Thanks to the attained high *SNR* at the lowest applied frequency in this chapter's measurements *(46.39-47.79 dB at 200 kHz)*, it was easily possible to use a global λ in the Tikhonov solution. This global λ was obtained through a simple two-step procedure. First, the previous statement (4.59) was applied to each of the *5* involved $\Delta\boldsymbol{v}_{\#}$ in order to obtain *5* λ_{app}, respectively; second, the *5* resulting λ_{app} were averaged in order to obtain a global λ_{app}. This procedure yielded a global λ_{app} of *(4.85 x 10^{-17})*.

❖   **TSVD-reconstructed images**

As one and the same $\boldsymbol{S}$ is used, the outcome of the previous statement (4.62) already represents a global tl_{app} for the TSVD solution. This statement delivered a global tl_{app} of *35*.

4.6   Measurements

4.6.1   Measurement Model

Figure (4.7) demonstrates a simplified equivalent measurement diagram illustrating a biological target located in the space between the transmitter and the receiver (redrawn from [Scharfetter et al. 2001]). As already proved in the previous chapter, the implemented electrostatic shielding of the coil system is so effective that no parasitic capacitive coupling above the low noise level can be detected. Therefore, this electromagnetic measurement model and the associated analysis only consider the inductive coupling between the different components.
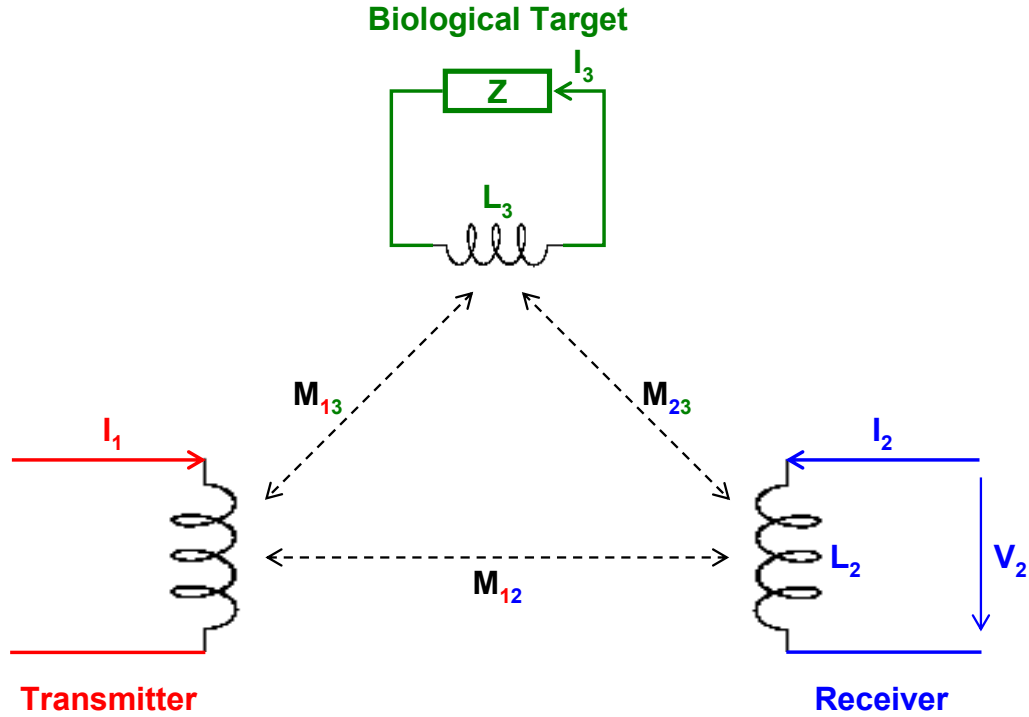
Figure (4.7): Equivalent measurement model for a biological target in MITS. Z: impedance of the biological target consisting of a resistance and a capacitive reactance, i.e., {Z = R + (1 / jωC)}; $L_{\#}$, $I_{\#}$, $V_{\#}$: inductance, current and voltage, respectively, with respect to the indexed component; $M_{\#\#}$: mutual inductance between the two indexed components.

Based on the inductive coupling model in figure (4.7), the acquired signal at L_2 can be stated as follows:

$$V_2 = j\omega M_{12}\, I_1 + j\omega L_2\, I_2 + j\omega M_{23}\, I_3 \qquad (4.63)$$

Taking into consideration the high-impedance termination of the sensing coil L_2 in the implemented receiving circuitry, i.e., $(I_2 = 0)$, the above-stated V_2 reduces to the received signal at L_2 from the transmitter and the target:

$$V_2 = j\omega M_{12}\, I_1 + j\omega M_{23}\, I_3 \qquad (4.64)$$

The induced current I_3 can be explicitly stated with respect to the excitation current I_1 by reformulating the following transmitter-target relationship:

$$j\omega M_{13} I_1 + (Z + j\omega L_3) I_3 = 0 \qquad (4.65)$$

which results in the following relation:

$$I_3 = -(j\omega M_{13} / (Z + j\omega L_3)) I_1 \qquad (4.66)$$

Thus, inserting equation (4.66) in equation (4.64), V_2 can then be restated in the following form:

$$V_2 = j\omega M_{12} I_1 + (\omega^2 M_{13} M_{23} / (Z + j\omega L_3)) I_1 \qquad (4.67)$$

This equation can be rewritten in a simplified or approximated version when assuming that, on the one hand, Z dominates over the inductive term $(j\omega L_3)$, i.e., {$|Z|$ » ωL_3}, on the other hand, the resistive term of Z dominates over its capacitive one, i.e., {R » $1 / \omega C$} and hence {$Z \approx R$}. Accordingly, the received signal at L_2 reads finally as follows:

$$V_2 \approx j\omega M_{12} I_1 + (\omega^2 M_{13} M_{23} / R) I_1 = V_{car} + V_{tar} \qquad (4.68)$$

where the first right-hand-side term corresponds to the primary field and represents the *carrier signal V_{car}*, whilst the second one corresponds to the secondary field and represents the *target signal V_{tar}*.

V_{tar} in equation (4.68) is a real signal with respect to the imaginary signal *V_{car}*, but when defining *V_{car}* as the reference real signal of the underlying phasor diagram with phase angle *($\Phi = 0°$)*, *V_{tar}* becomes an *imaginary signal* with respect to the reference real signal *V_{car}*, namely, the previously explained signal of utmost interest in biomedical MITS to be used in image reconstruction. In contrast, *V_{car}* represents in terms of equation (4.68), i.e., in the receiving coil, a signal of no interest at all to be suppressed as much as possible. Fortunately, due to the differential nature of *$\Delta v_{\#}$*, *V_{car}* can indeed be eliminated in the SD and consequently SFD measurements without further ado. As for the SD case (4.44), the subtraction of two signals, each of the form of *V_2* in equation (4.68), measured at one and the same frequency automatically cancels *V_{car}*. Thus, the resulting signal *Δv_{SD}* does not require any correction in this respect. The same applies to the SFD case (4.49) because the resulting signal *Δv_{SFD}* is the difference between two *Δv_{SD}*, and *V_{car}* is already cancelled in each of them regardless of the applied frequency. In contrast, in the FD case (4.48), the subtraction of two *V_2* measured at two different frequencies,

respectively, does not cancel V_{car} totally due to its different magnitudes at the different frequencies. Therefore, the resulting signal Δv_{FD} needs to be further corrected. This correction can logically be made through subtracting V_{car} from V_2 (or vice versa) at each of the two frequencies, respectively, prior to the systematic subtraction for obtaining Δv_{FD}. Accordingly, the final corrected version of equation (4.48) to be used in the image reconstruction algorithm has the following form:

$$\Delta v_{FD} = (v_{tot} - v_{bg})|_{f2} - \gamma \, (v_{tot} - v_{bg})|_{f1} \qquad (4.69)$$

where v_{tot} and v_{bg} are new, contextually more appropriate abbreviations than V_2 and V_{car}, respectively, to be also used in the next chapter in order to denote the *total signal* and the *background signal* measured with and without the biological target, respectively.

4.6.2   Measurement Setup

The measurement setup is depicted in figure (4.8). A whole organic potato served as a biological phantom representing the ROI; it was prepared (peeled) -as accurately as possible- in the shape of an ellipsoid with a major axis of *100 mm* and equal minor axes of *40 mm.*
The previously described plastic tank was filled with *15.55 ℓ* saline solution *(sodium chloride NaCl)* of *0.15 S/m* conductivity and served as a background medium of physiological conductivity containing the ROI; it was the same custom-made container with the shape of an elliptical cylinder described and used in the previous chapter.

For the sake of consistency and comparability, no other potato than the mentioned one was used in whatever type of measurements; the same applies to the mentioned background medium.

4.6.3   Measurement Process

All measurements in this chapter were performed in a multifrequency, multiframe and differential manner. They were conducted at *(f_1 = 200 kHz)* and *(f_2 = 500 kHz)*; at these two frequencies, the TXs were driven by excitation currents of *(I_1 = 0.46 A_{rms})* and *(I_2 = 0.34 A_{rms})*, respectively.
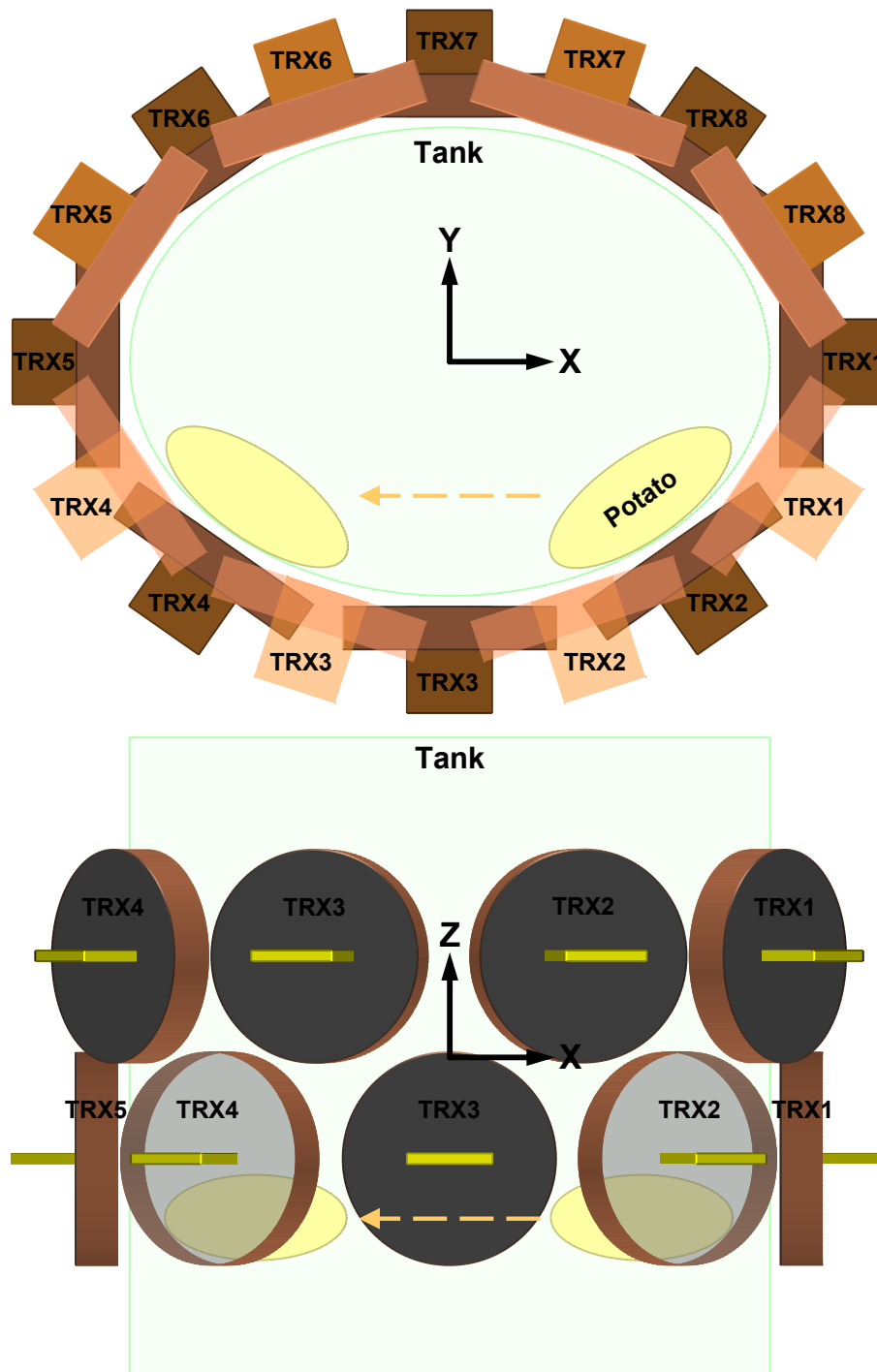
Figure (4.8): Experimental setup. Top: top view, bottom: long-side view. For the sake clarity, some TXs and RXs are made transparent. The dashed light-brown arrow denotes the displacement of the potato from one position to another in the SD and SFD measurements; at these very same two positions, the potato was fixed in two separate FD measurements, respectively. Dimensions of the TRX, the whole array and the tank can be taken from figures (3.3), (3.5) and (3.10), respectively.

❖ State-Differential Measurements (SD)

The SD measurement was carried out in two successive phases representing two different states of the ROI and thus of the target medium during one and the same measurement; in each state, *15 frames* were acquired and averaged. In the first state, the target medium, i.e., the saline tank including the potato, was measured with the potato at an initial position *(90, -65, -75)* in front of the lower TRX2. In the second state, the potato was displaced within the tank to a new position at *(-90, -65, -75)* in front of the lower TRX4, and the measurement cycle was then resumed. The resulting signal Δv_{SD} between the two states was finally calculated according to equation (4.44), once at each of the two applied frequencies f_1 and f_2.

❖ Frequency-Differential Measurements (FD)

Two FD measurements were performed independently; in each one, *15 frames* were acquired and averaged. In the first measurement, the target medium was measured with the potato at the position *(90, -65, -75)* in front of the lower TRX2. In the second measurement, the target medium was measured with the potato at the position *(-90, -65, -75)* in front of the lower TRX4. The resulting signal Δv_{FD} between the two frequencies f_1 and f_2 was finally calculated according to equation (4.69), once for each of the two conducted measurements.

❖ State-Frequency-Differential Measurements (SFD)

There was no need to conduct separate SFD measurements because the two gained datasets at the two applied frequencies f_1 and f_2, respectively, in the SD measurements could be directly reused to obtain the SFD signal. The resulting signal Δv_{SFD} between the two signals Δv_{SD} at the two frequencies f_1 and f_2, respectively, was finally calculated according to equation (4.49).

4.7   Performance Measures

For a quantitative comparison and subsequent assessment of the acquired signals $\Delta v_{\#}$ and the corresponding reconstructed images $\Delta \sigma_{\#}$ on the one hand, and for the validation of the hybrid dynamic-parametric imaging concept on the other hand, the following performance criteria were used:

4.7.1   Signal Quantification Measures

The signal is conveniently characterized by its magnitude, the noise and the resulting *SNR*. The latter was calculated as follows:

$$SNR = 20 \, log(|Im(\Delta v_\#)| \, / \, Im(N)) \qquad (4.70)$$

where the *signal $\Delta v_\#$* represents one entry in the data vector $\boldsymbol{\Delta v_\#}$ corresponding to one TX-RX measurement combination (see the remark hereunder), and the *noise N* represents the standard deviation of this entry over the series of the acquired signal frames.

Remark

As the phantom was located in front of the lower TRX2 or TRX4 during all measurements (see figure (4.8)), the two measurement combinations (channels) TX2-RX2 and TX4-RX4 of the lower plane and hence the corresponding two entries in $\boldsymbol{\Delta v_\#}$ had the greatest impact on the reconstructed images $\boldsymbol{\Delta \sigma_\#}$; therefore, only the data of these two entries are provided in the results.

4.7.2   Image Quantification Measures

A frequently used measure of merit in imaging is the *contrast-to-noise ratio (CNR)*, calculated in this chapter from the highest contrast of the reconstructed ellipsoidal perturbation (ROI) and the noise of the image background surrounding the ROI:

$$CNR = |\Delta \sigma_\#| \, / \, N_{bg} \qquad (4.71)$$

where the *contrast $\Delta \sigma_\#$* represents one entry in the solution vector $\boldsymbol{\Delta \sigma_\#}$ corresponding to the central element (centre of gravity) of the ROI, which turned out to be very close to the mean value of the ROI elements, and the *noise N_{bg}* represents the standard deviation of the image background elements.

Further, the accuracy of the reconstructed hybrid SFD images was assessed with reference to the SD ones at f_1 and f_2 subtracted from each other based on the following *relative percent error ($\delta_\%$)*:

$$\delta_\% = 100\% \, \{1 - (|\Delta \sigma_{SFD}| \, / \, |\Delta \sigma_{SD@f2} - \Delta \sigma_{SD@f1}|)\} \qquad (4.72)$$

where, again, $\Delta\sigma_\#$ corresponds to the central pixel (highest contrast) of the reconstructed perturbation.

4.8   Results

The reconstructed (imaginary) images are presented in figures (4.9-4.14). Each of the *5* figures (4.9-4.13) contains *3* images corresponding to the *3* different reconstruction or regularization strategies. Figure (4.14) contains a thumbnail view with a complete representation of all *15* images together for an easier general comparison. All images are transversal cross-sectional slices taken through the centre of the ellipsoidal ROI (potato) at *(z = -75 mm)*. The dashed white ellipses mark the true position of the potato in the respective measurement (see figure (4.8)). The quantification parameters of the different signals $\Delta v_\#$ are summarized in table (4.1); each of the *3*-image figures (4.9-4.13) or each *3*-image row in figure (4.14) occupies an own single- or double-line row in this table; in case of two ROIs, corresponding colours are used, otherwise black. The quantification parameters of the different images $\Delta\sigma_\#$ in the *5* figures (4.9-4.13) are summarized in the *5* tables (4.2-4.6), respectively; each image in each figure occupies an own single- or double-line row in the respective table; in case of two ROIs, corresponding colours are used, otherwise black. The quantification of the accuracy of the hybrid images is summarized in table (4.7).

Measurement	f [kHz]	Im(Δv) [V]	Im(N) [V]	SNR [dB]
SD	500	-6.89×10^{-6}	5.41×10^{-9}	62.10
		6.82×10^{-6}	4.97×10^{-9}	62.75
SD	200	-1.02×10^{-6}	4.89×10^{-9}	46.39
		1.01×10^{-6}	4.12×10^{-9}	47.79
FD	500 - 200	5.51×10^{-6}	5.46×10^{-9}	60.08
FD	500 - 200	5.49×10^{-6}	4.95×10^{-9}	60.90
SFD	500 - 200	-5.87×10^{-6}	5.51×10^{-9}	60.55
		5.81×10^{-6}	5.05×10^{-9}	61.22

Table (4.1): Quantitative data on the measured differential signals Im($\Delta v_\#$) relevant to the reconstructed differential images $\Delta\sigma_\#$ in figures (4.9-4.14).

Figure (4.9): SD images at 500 kHz for the phantom translated from the TRX2 site to the TRX4 site in the lower plane. 1: MAP reconstruction, 2: Tikhonov reconstruction, 3: TSVD reconstruction.

Image	$\Delta\sigma_{SD}$ [S/m]	N_{bg} [S/m]	CNR [1]
1	-1.769	3.329 x 10^{-2}	53.14
	1.743		52.36
2	-1.784	3.387 x 10^{-2}	52.67
	1.762		52.02
3	-1.895	3.678 x 10^{-2}	51.52
	1.888		51.33

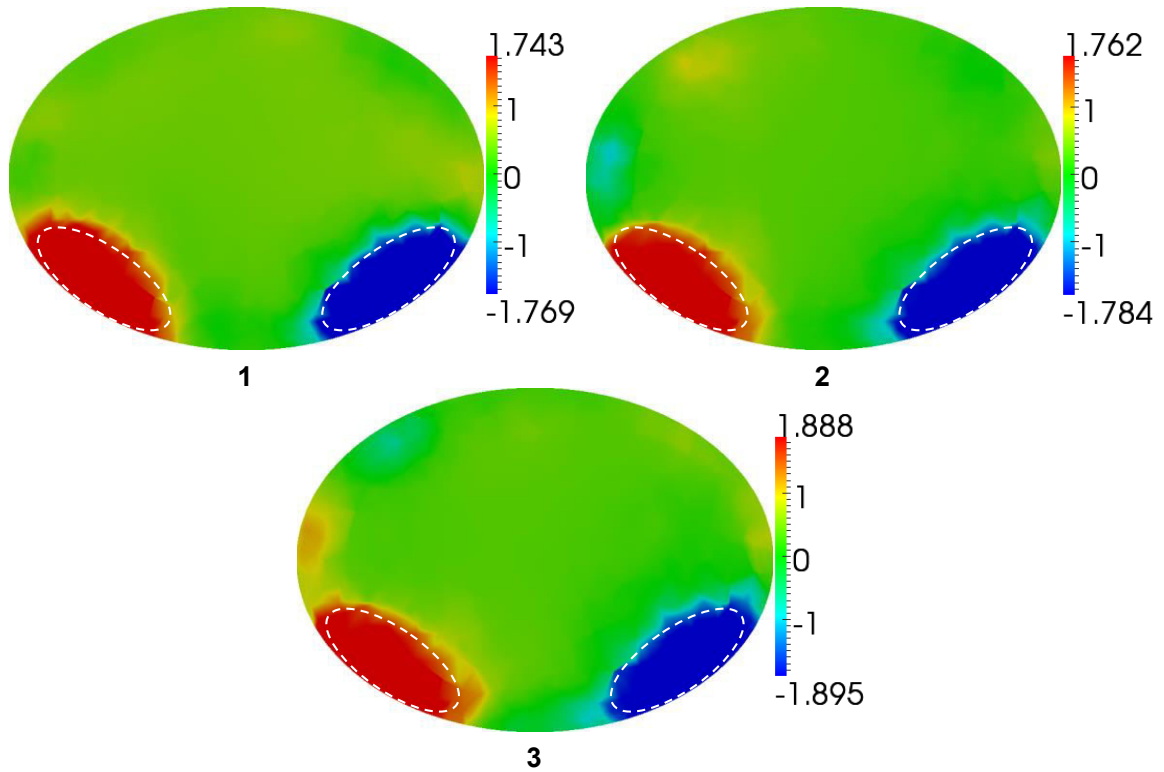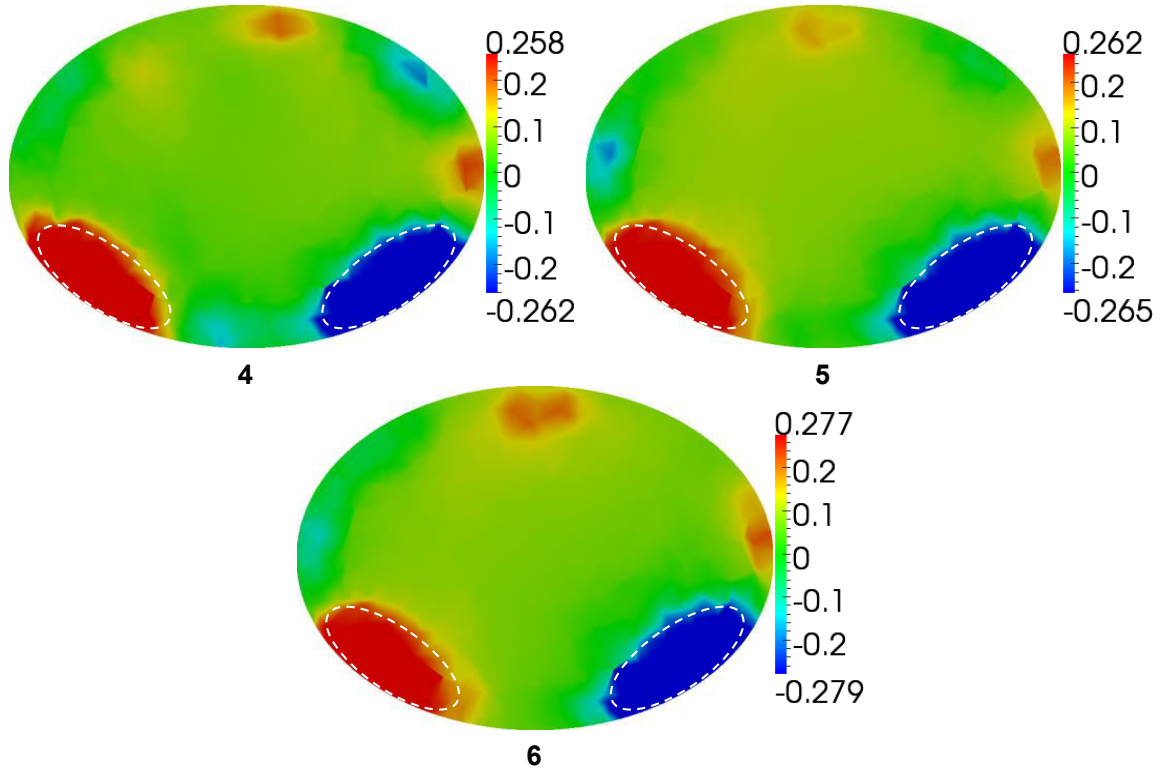Table (4.2): Quantitative data on the SD images in figure (4.9).

Figure (4.10): SD images at 200 kHz for the phantom translated from the *TRX2* site to the *TRX4* site in the lower plane. 4: MAP reconstruction, 5: Tikhonov reconstruction, 6: TSVD reconstruction.

Image	$\Delta\sigma_{SD}$ [S/m]	N_{bg} [S/m]	CNR [1]
4	-0.262	0.673×10^{-2}	38.93
	0.258		38.34
5	-0.265	0.656×10^{-2}	40.40
	0.262		39.94
6	-0.279	0.707×10^{-2}	39.46
	0.277		39.18

Table (4.3): Quantitative data on the SD images in figure (4.10).

Figure (4.11): FD images between 500 and 200 kHz for the stationary phantom in front of the lower TRX2. 7: MAP reconstruction, 8: Tikhonov reconstruction, 9: TSVD reconstruction.

Image	Δσ$_{FD}$ [S/m]	N$_{bg}$ [S/m]	CNR [1]
7	1.431	2.929 x 10^{-2}	48.86
8	1.426	2.904 x 10^{-2}	49.10
9	1.527	3.112 x 10^{-2}	49.07

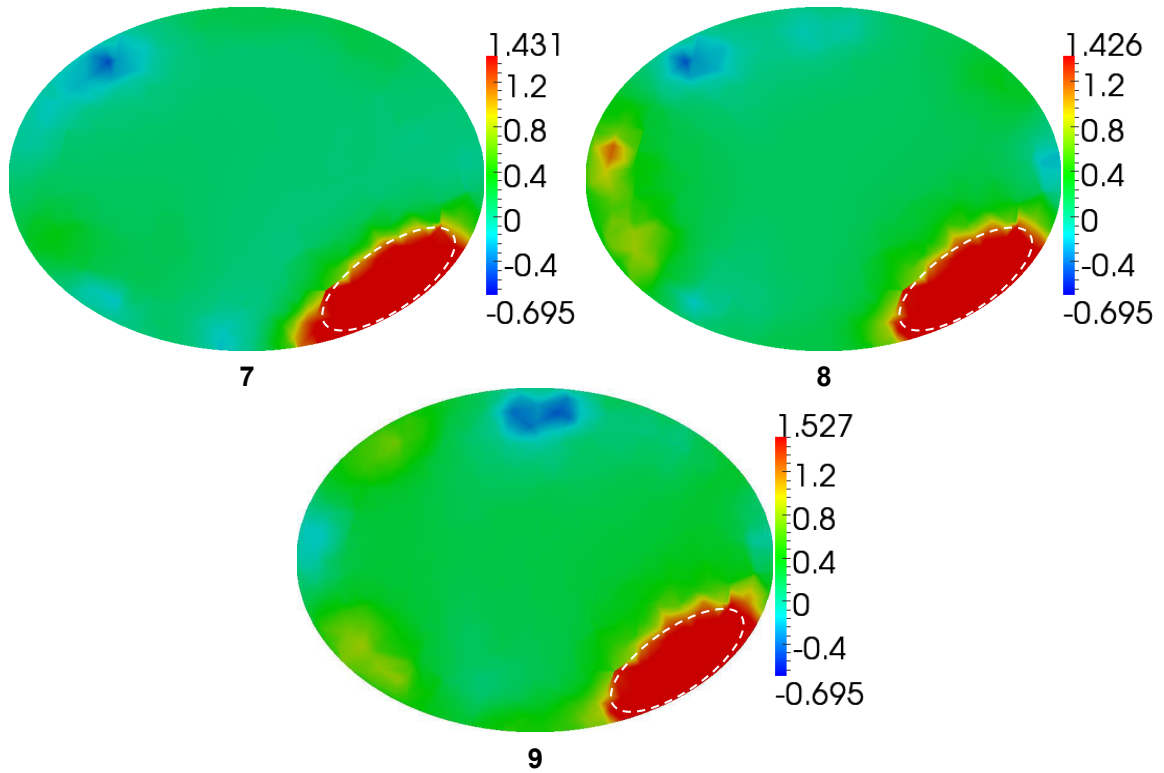*Table (4.4): Quantitative data on the FD images in figure (4.11).*
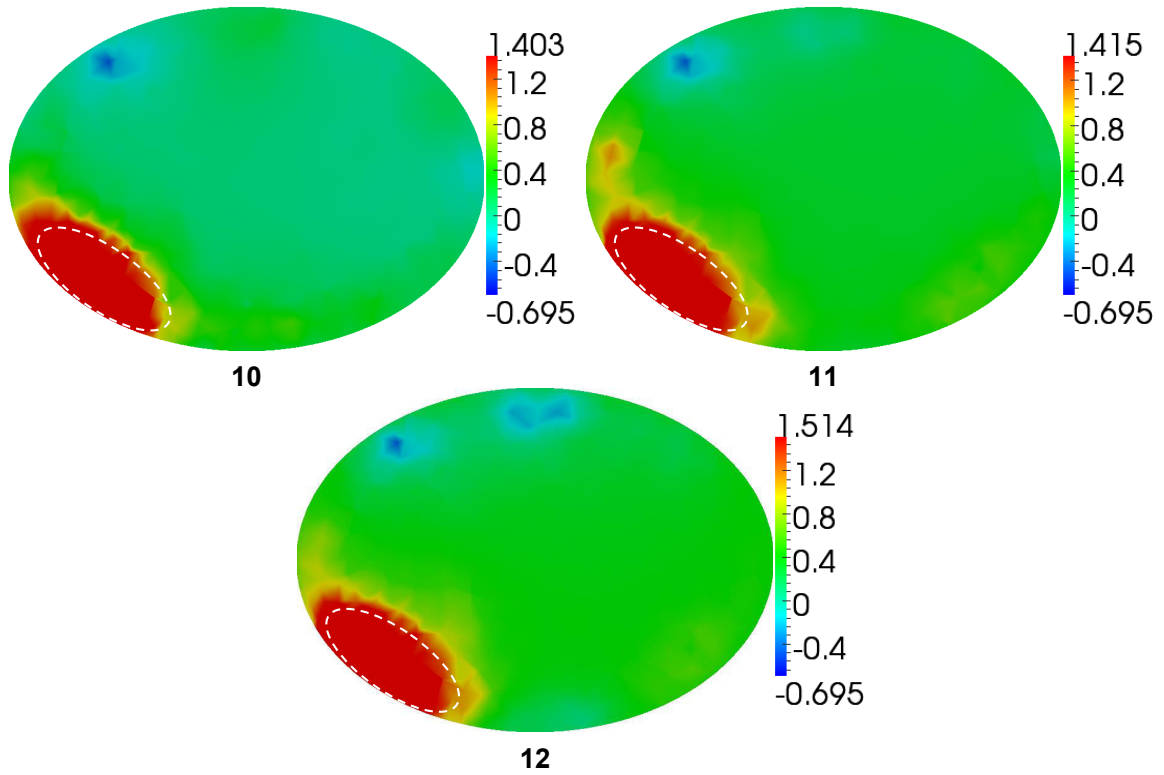
Figure (4.12): FD images between 500 and 200 kHz for the stationary phantom in front of the lower TRX4. 10: MAP reconstruction, 11: Tikhonov reconstruction, 12: TSVD reconstruction.

Image	$\Delta\sigma_{FD}$ [S/m]	N_{bg} [S/m]	CNR [1]
10	1.403	2.890×10^{-2}	48.55
11	1.415	2.911×10^{-2}	48.61
12	1.514	3.024×10^{-2}	50.07

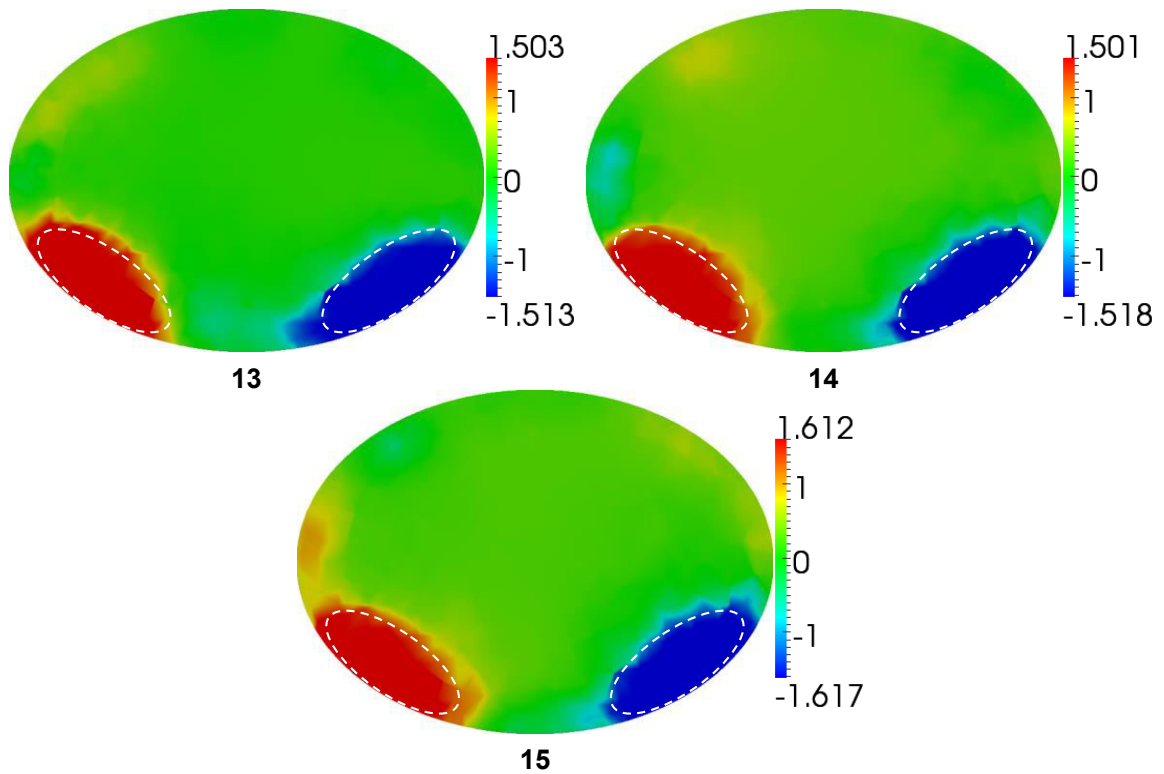*Table (4.5): Quantitative data on the FD images in figure (4.12).*

Figure (4.13): SFD images between 500 and 200 kHz for the phantom translated from the TRX2 site to the TRX4 site in the lower plane. 13: MAP reconstruction, 14: Tikhonov reconstruction, 15: TSVD reconstruction.

Image	$\Delta\sigma_{SFD}$ [S/m]	N_{bg} [S/m]	CNR [1]
13	-1.513	2.968×10^{-2}	50.98
	1.503		50.64
14	-1.518	2.893×10^{-2}	52.47
	1.501		51.88
15	-1.617	3.145×10^{-2}	51.41
	1.612		51.26

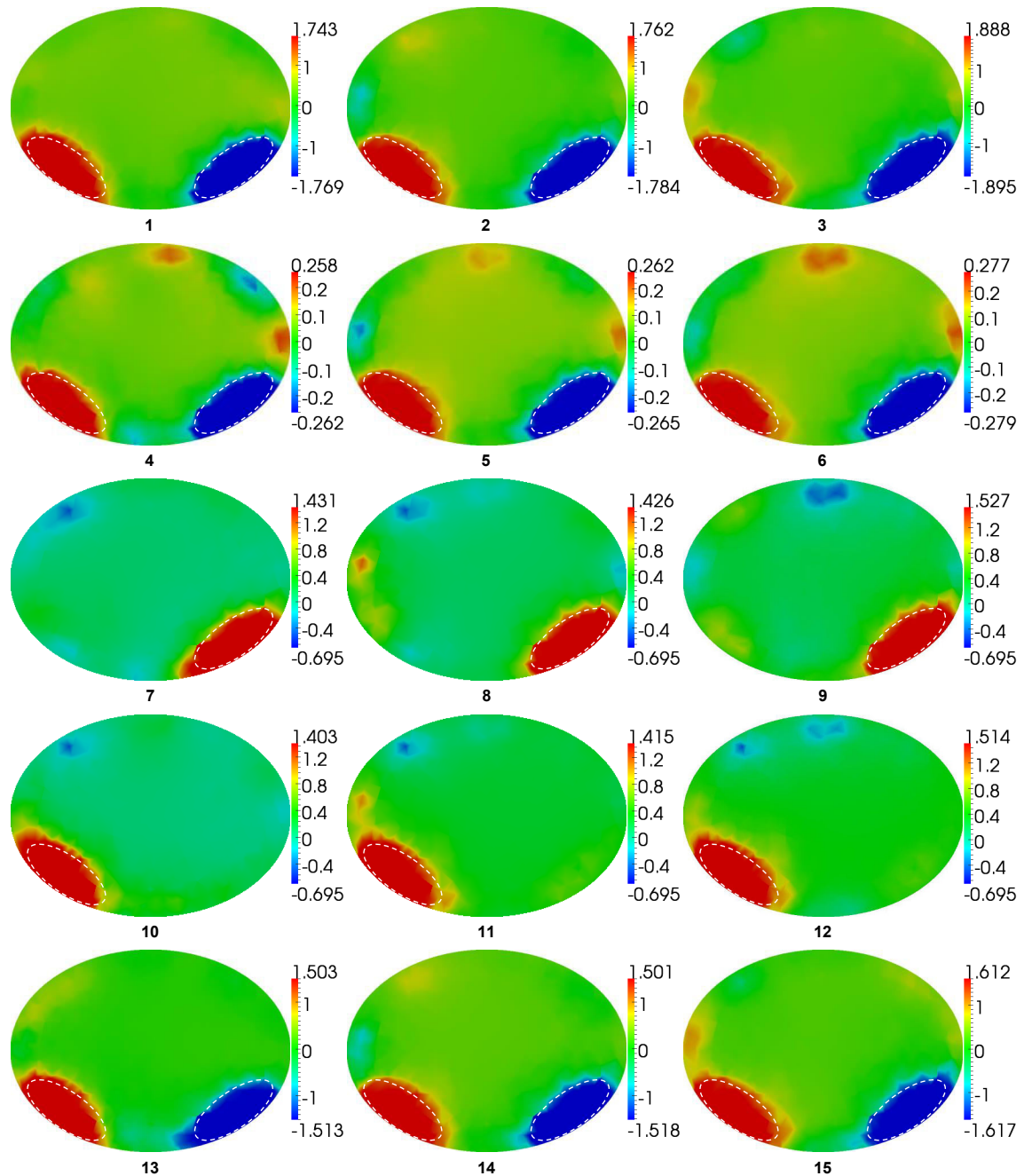*Table (4.6): Quantitative data on the SFD images in figure (4.13).*

Figure (4.14): Compact overview of all images in figures (4.9-4.13). Left column: MAP reconstructions, middle column: Tikhonov reconstructions, right column: TSVD reconstructions.

Regularization	$\Delta\sigma_{SD@500kHz}$ [S/m]	$\Delta\sigma_{SD@200kHz}$ [S/m]	$\Delta\sigma_{SFD}$ [S/m]	$\delta_\%$
MAP	-1.769	-0.262	-1.513	0.40
	1.743	0.258	1.503	1.21
Tikhonov	-1.784	-0.265	-1.518	0.07
	1.762	0.262	1.501	0.07
TSVD	-1.895	-0.279	-1.617	0.06
	1.888	0.277	1.612	0.06

Table (4.7): Accuracy of the reconstructed hybrid SFD images. $\Delta\sigma_{SD@500kHz}$, $\Delta\sigma_{SD@500kHz}$ and $\Delta\sigma_{SFD}$ are taken from tables (4.2), (4.3) and (4.6), respectively.

4.9   Discussion

4.9.1   General Inspection

As can be clearly seen in all images, the different positions of the perturbing potato, whether of the translated or static one, could be well reconstructed; it would be possible through only a visual inspection and without any a priori knowledge of its position to localize it satisfactorily within the conducting background medium. Generally, the *3* images in each of the figures (4.9-4.13) (or of the rows in figure (4.14)) corresponding to the *3* different solutions are similar. This can be seen qualitatively through a visual inspection as well as quantitatively when comparing the respective image performance parameters in the corresponding tables (4.2-4.6). This general similarity is logically expected as each of these *3*-image groups resulted from one and the same imaginary signal *Im(Δv#)* used in the *3* different solutions. Although there exist some background artefacts independent of the used reconstruction or regularization method, they do not affect the detectability of the ellipsoidal perturbation, not even at *200 kHz* despite the lower sensitivity and hence lower *SNR* as can be seen in the SD images (4-6) where the lower *SNR* merely led to comparatively insignificant additional background oscillations and consequently to lower *CNR* (see the corresponding table (4.3) and second double-line row in table (4.1)). Of more relevance to the discussion than the background artefacts is the ROI blurring, being one of the most characteristic artefacts in MITS due

to the broad main lobe of the (sinc-like) *point spread function (PSF)* of this imaging modality. As can be seen in the figures, all images are affected by more or less blurring around the reconstructed potato independent of the *SNR*, the reason why its almost elliptical periphery could not be sharply reconstructed. In contrast to the background artefacts, the extent of this blurring does depend to some degree on the used regularization method. This inference can be supported by the following observations:

- The averaged (approximated) data covariance matrix $(\lambda_{app}\ \boldsymbol{I}_m)$ in the Tikhonov solution was able to suppress the blurring on the left side of the left (red) perturbation in images (2), (5) and (14) so that the elliptical shape of the potato could be maintained on this side, though Tikhonov regularization is known to be a none-edge-preserving method. The same observation applies to the TSVD-reconstructed image (6).
- The normal data covariance matrix $\boldsymbol{C}_{lm(\Delta v_{\#})}$ in the (Tikhonov-like) MAP solution enforced more blurring on the left side of the perturbation in images (7) and (10) as well as the right (blue) perturbation in image (13), though it is expected that $\boldsymbol{C}_{lm(\Delta v_{\#})}$ should avoid overregularization due to the low data variances.

Thus, considering these observations together with a reconsideration of all *15* images in the overall view in figure (4.14) allows concluding that the regularized solution with the averaged (Gaussian-distributed) data covariance matrix delivered qualitatively, i.e., visually, better images (Tikhonov: middle group). This infers in turn that it is sometimes more appropriate to penalize all image elements equally with the average of the data variances rather than unequally with the true variances (MAP: left group), even though a stronger physical interpretation would suggest the latter approach. The regularized solution through truncating after the numerically usable rank of the system matrix (TSVD: right group) may not have delivered qualitatively (visually) better images than the former group, but than the latter one anyway, thus, ascertaining the appropriateness of this regularization choice as well.

4.9.2 Close Inspection

In order to get off to a good start with the numerical inspection of the used $\{\boldsymbol{S}_{mxn} = \boldsymbol{U}_{mxm}\ \boldsymbol{K}_{mxm}\ (\boldsymbol{V}_{nxm})^T;\ m = 256 \ll n = 30000\}$ in image reconstruction and thus with the analysis of the problem ill-posedness, it would be very helpful to recall the decay

of the singular values k of S from the previous figure (4.5). According to this decay, equation (4.41) yields a CN as large as $\{k_1 / k_{256} = 8916\}$, indicating a seriously ill-conditioned S. The adequate truncation index that discards the problematic singular values in the TSVD solution, i.e., tl_{app}, was found at the discontinuity between k_{35} and k_{36}, thus, reducing CN to $\{k_1 / k_{35} = 3\}$ and allowing thereby for a numerically stable solution. Equivalently, the problematic singular values were neutralized in the MAP and Tikhonov solutions by $C_{Im(\Delta v_{\#})}$ and $(\lambda_{app}\, I_m)$, respectively. In order to see how such problematic singular values would have amplified and mapped the small noise on Δv in the data space into large noise onto $\Delta \sigma$ in the model space, it would be further helpful to involve the left and right singular vectors U and V of S spanning the data and model spaces, respectively, in the analysis. This can be best done by plotting some of the left vectors and imaging some of the right ones throughout the two spaces, respectively, and inspecting the extent of the desired information available therein, put another way, the extent of the undesired noise included therein. With this in view, two arbitrary 8-vector series from U and V roughly covering the data and model spaces with the orders 11, 22, 33, 44, 55, 88, 111 and 222 are plotted or imaged in figures (4.15) and (4.16), respectively. It can be clearly seen in both figures how the oscillations in the singular vectors and images increase with their order. The first three singular images V_{11}, V_{22} and V_{33} obviously contain some portions or patterns of information; the same applies to the corresponding singular vectors U_{11}, U_{22} and U_{33}. In contrast, the last three ones V_{88}, V_{111} and V_{222} do not make the same impression; the same applies again to the corresponding U_{88}, U_{111} and U_{222}. V_{44} and V_{55} probably contain both, a piece of information together with noise to some extent; thus, no direct decision about their usefulness might be made visually. However, the corresponding U_{44} and U_{55} do allow making such decision; they clearly suffer from oscillations to a not inconsiderable extent so that considerable noise may be inversely mapped onto V_{44} and V_{55}. This observation proved to be true; the TSVD reconstructions performed at $[55 \geq tl \geq 39]$ resulted in useless or unsatisfactory images, particularly the SD ones at $200\ kHz$. Accordingly, there is a large number of oscillatory singular vectors in U and V, as large as the number of the problematic singular values in K that mostly affect the numerical stability of the solution and need to be truncated (TSVD) or rendered harmless (MAP and Tikhonov). Thus, all highly oscillatory singular vectors associated with these problematic singular values practically belong to the null space of U and V and cannot map any information but noise onto the sought $\Delta \sigma$; in other words, all those entries in $\Delta \sigma$ associated with the noisy left singular vectors in U are actually represented by the null space of V and cannot be reconstructed, whence the non-uniqueness of the solution.
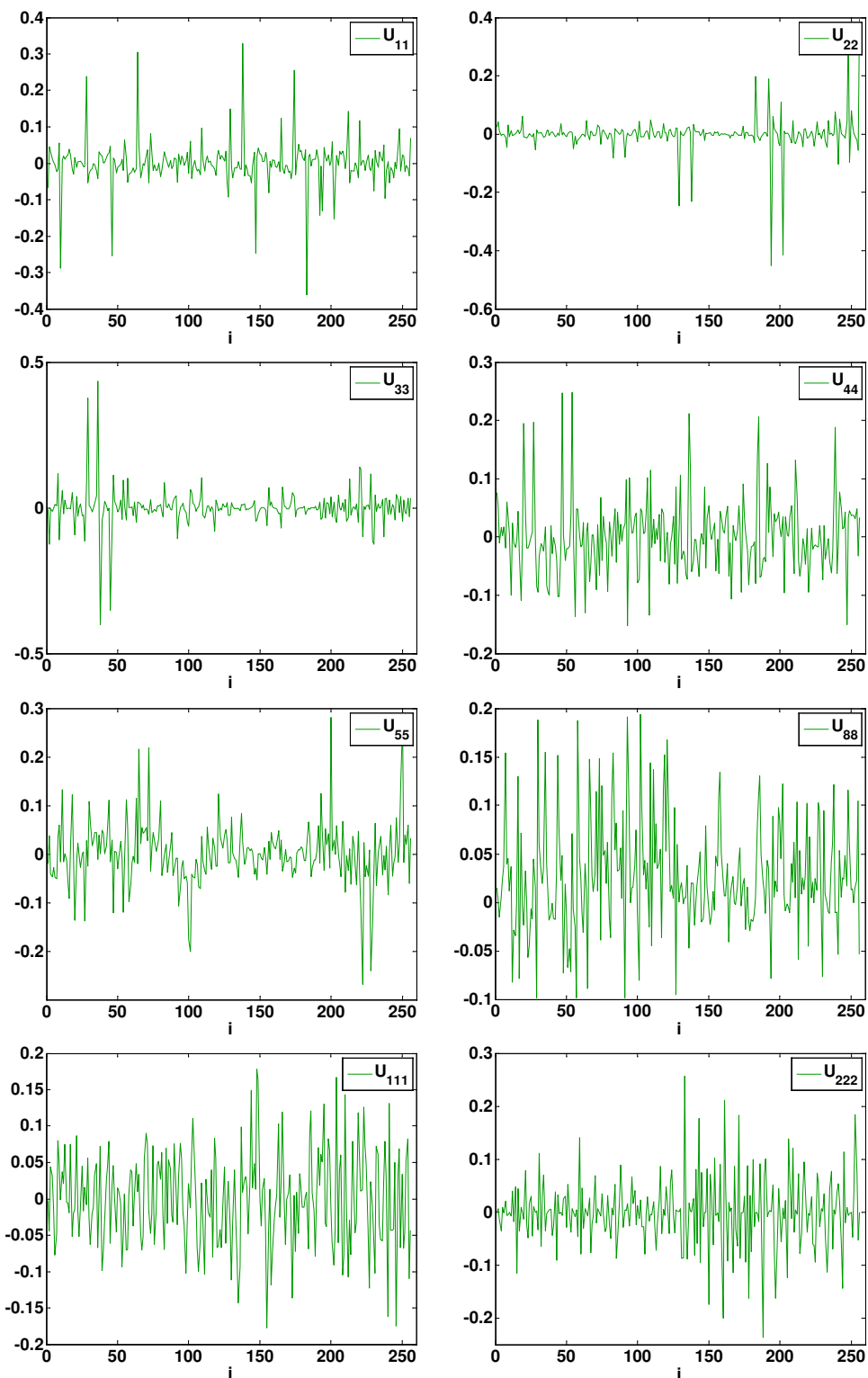
*Figure (4.15): Some singular vectors of the data space **U**. Increasing oscillations with increasing vector order is an inherent feature of ill-posed problems. Of course, the same characteristic applies to the singular vectors of the model space **V**.*
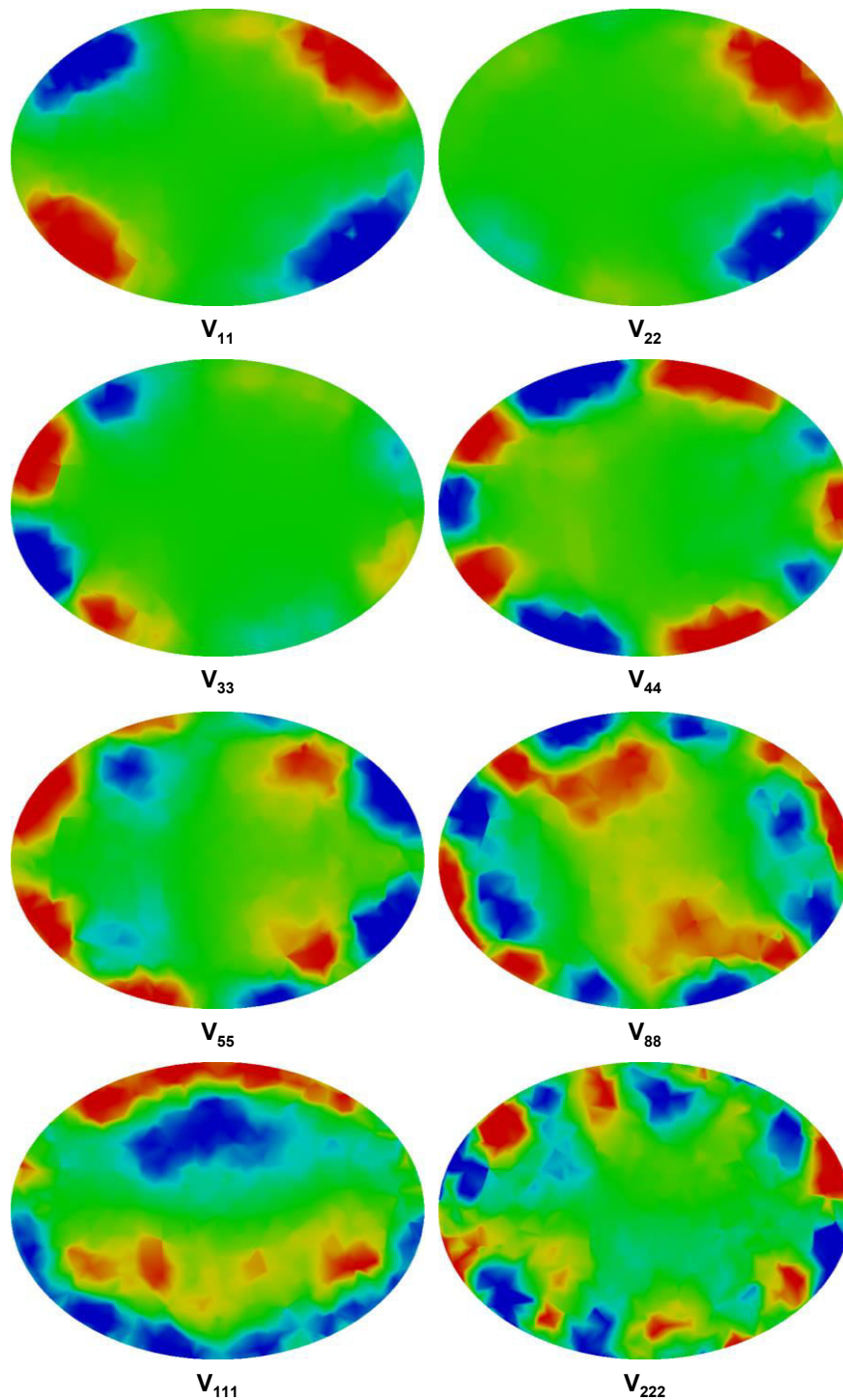
Figure (4.16): Some singular images of the model space **V**. These images are transversal cross-sectional slices taken at (z = -75 mm) whereat all previous slices of the phantom in figures (4.9-4.14) were taken. Due to the severe ill-conditioning of the underlying system, the information in high-order vectors and hence images is totally hidden in the noise.

In summary, the gained deep insight into the ill-posedness of the underlying problem allows concluding that the attained useful images necessarily reflect well-thought-out regularization, especially the Tikhonov and TSVD schemes:

- As regards Tikhonov regularization, statement (4.59) provided an already appropriately tuned regularization parameter. Thanks to the low ratio of *2.97* (average ratio over the *5* involved $\Delta v_{\#}$) obtained from the associated constraint (4.60), neither under- nor over-regularization could be ascertained. Due to less ROI blurring in some of the reconstructed images using the provided λ_{app}, they were judged to be the best images amongst all ones.

- As regards TSVD regularization, statement (4.62) also provided an already appropriately tuned truncation level. The reconstructed images using this tl_{app} proved to be the best compromise between letting through too much noise, i.e., underregularization, and filtering out too much information, i.e., overregularization.

- As regards MAP regularization, the use of the data covariance matrix alone in line with the underlying rationale could not provide as appropriately tuned regularization as in the latter two cases. Due to a few relatively large data variances, some of the reconstructed images using $\boldsymbol{C}_{Im(\Delta v_{\#})}$ suffered from a slight overregularization and consequently additional ROI blurring; however, this slight blurring did not preclude the detection of the perturbing object.

4.9.3   Further Inspection and Hybrid Imaging Validation

In order to further assess the relevance of the obtained image reconstruction results to biomedical MITS, it would be very helpful to gain an insight into the dispersive behaviour of the imaged organic potato regarding its admittivity sufficiently around the applied excitation frequencies in the measurements (*200* and *500 kHz*), for instance, within the frequency range *0.1-1 MHz* which covers an important part of the β-dispersion of biological tissues [Gabriel et al. 2009]. For this purpose, an auxiliary reference measurement of the admittivity spectrum of the potato was conducted by means of an impedance spectrometer; for a detailed description of this electrode-based measurement, the reader is referred to appendix (B). The obtained admittivity spectrum is shown in figure (4.17).

According to the PEP database in [Gabriel et al. 1996 (a), 1996 (b), 1996 (c)], many biological tissues undergo within *0.1-1 MHz* more or less similar dispersive behaviour to that of the potato in figure (4.17), and hence exhibit conductivity

changes close to those noted, e.g., myocardium, muscle (transversal direction), kidney (cortex), colon, cornea, etc. Thus, this spectrum of the potato may be observed as a subspectrum of the β dispersion of these tissues. This indicates how relevant the performed imaging tasks and the proposed hybrid imaging approach to biomedical MITS could be.

Reconsidering the noted conductivity differences in figure (4.17) together with the listed differential signals in table (4.1) and the reconstructed images in figure (4.14), it can be seen how small conductivity changes of the order of 10^{-1} S/m could be successfully mapped onto small signal changes of the order of 10^{-6} V, resulting in reasonable localization of the perturbing potato within the conducting background medium and useful application of the hybrid imaging approach.
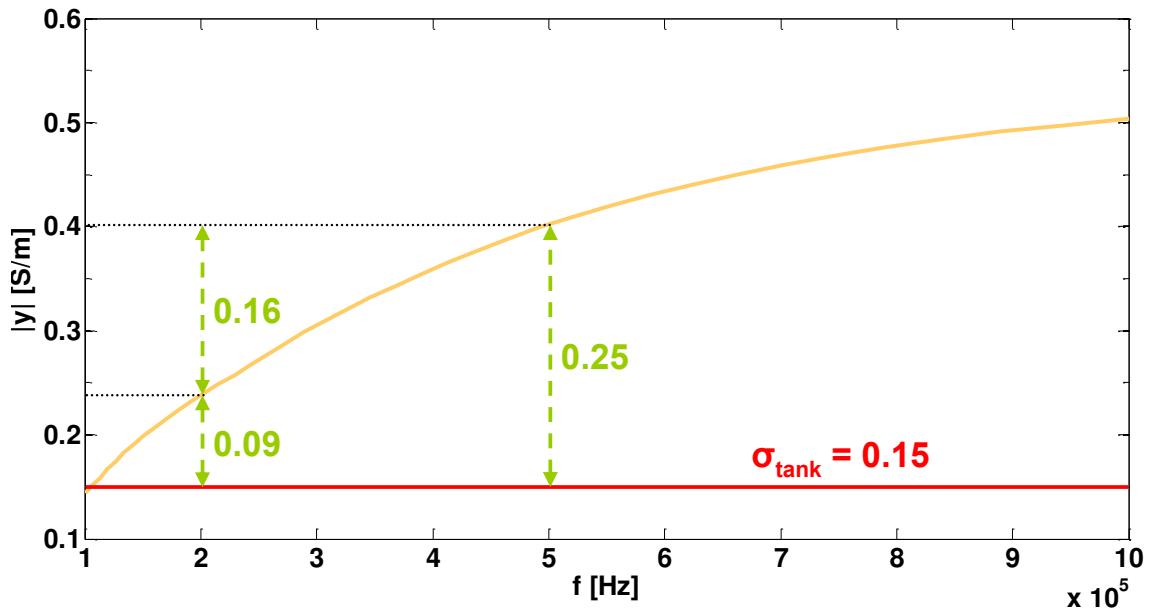

Figure (4.17): Dispersion of the imaged organic potato regarding its admittivity modulus. As is theoretically the case with ionic solutions like aqueous NaCl below 1 MHz, the background tank exhibited almost no dispersive behaviour within 0.1-1 MHz, the reason why its conductivity spectrum is plotted as a constant function {$\sigma_{tank}(f)$ = 0.15 S/m}. The conductivity differences annotating the dashed green double arrows represent the perturbation dealt with in the imaging experiments.

SD or FD imaging deals with a target undergoing local or spectroscopic conductivity changes, respectively, and accordingly provide the desired information thereon. As for hybrid SFD imaging, it deals with a target undergoing the cooccurrence of both kinds of changes. According to the suggested approach, it should necessarily provide the desired information on both local and spectroscopic conductivity

changes in one and the same image from one and the same measurement. Indeed, as obvious in figure (4.14), the changed location of the ROI (perturbation) is as clear in the hybrid SFD images (13-15) as in the SD ones (1-6). This local change of the ROI led to a certain conductivity change $\Delta\boldsymbol{\sigma}_{SD}$ at a certain frequency. As can be clearly seen in tables (4.2) and (4.3) or on the corresponding colour bars in the SD images (1-6), the change in the applied field frequency by *300 kHz*, i.e., between *200* and *500 kHz*, resulted in an expected considerable increase in $|\Delta\boldsymbol{\sigma}_{SD}|$; more precisely, $|\Delta\boldsymbol{\sigma}_{SD}|$ at *500 kHz* is expectedly *6.73-6.82* times greater than $|\Delta\boldsymbol{\sigma}_{SD}|$ at *200 kHz*, i.e., $\{\Delta\boldsymbol{\sigma}_{SD@500kHz} / \Delta\boldsymbol{\sigma}_{SD@200kHz} = 6.73\text{-}6.82\}$, being in line with the respective ratios between the corresponding signal changes $|\Delta\boldsymbol{v}_{SD}|$ at *200* and *500 kHz* in table (4.1), namely, $\{\Delta\boldsymbol{v}_{SD@500kHz} / \Delta\boldsymbol{v}_{SD@200kHz} = 6.75\}$. And right here comes the role of the reconstructed hybrid conductivity change $\Delta\boldsymbol{\sigma}_{SFD}$ which combines or reflects these local as well as spectroscopic changes together; it is actually no more than the difference between both reconstructed $\Delta\boldsymbol{\sigma}_{SD}$ at *200* and *500 kHz*, i.e., $\{\Delta\boldsymbol{\sigma}_{SFD} = \Delta\boldsymbol{\sigma}_{SD@500kHz} - \Delta\boldsymbol{\sigma}_{SD@200kHz}\}$, which is in agreement with the definition of the SFD signal, herein $\{\Delta\boldsymbol{v}_{SFD} = \Delta\boldsymbol{v}_{SD@500kHz} - \Delta\boldsymbol{v}_{SD@200kHz}\}$. This fact can be evidently seen when subtracting the highest perturbation values in the reconstructed SD images (4-6) at *200 kHz* ($\Delta\boldsymbol{\sigma}_{SD}$ in table (4.3)) from the highest perturbation values in the reconstructed SD images (1-3) at *500 kHz* ($\Delta\boldsymbol{\sigma}_{SD}$ in table (4.2)), respectively, and comparing the subtraction results with the highest perturbation values in the reconstructed hybrid SFD images (13-15) between *500* and *200 kHz* ($\Delta\boldsymbol{\sigma}_{SFD}$ in table (4.6)), respectively. According to table (4.7), this subtraction and comparison procedure yields amazingly accurate results, as precise as *98.79-99.94%* thanks to the negligible error $\delta_\%$ of *0.06-1.21%*.

In addition, if $\Delta\boldsymbol{\sigma}_{SD}$ at *200* and *500 kHz* were absolute conductivity changes, $\Delta\boldsymbol{\sigma}_{SFD}$ would necessarily be absolute as well. In other words, the non-iterative and linearized nature of the different implemented image reconstruction algorithms could not preclude the accurate reconstruction of the hybrid SFD images and hence the verification of the underlying approach.

In conclusion, it can be stated that the imaging results, i.e., the ability to image biological targets at medium frequencies, emphasize the proper performance of the optimized MITS tomograph regarding applications in the physiological conductivity range and in the β-dispersion frequency range, thus, supporting its preliminary biomedical applicability. Under these challenging conditions in biomedical MITS, the new hybrid dynamic-parametric (state-frequency-differential) imaging concept proved its applicability as well.

Chapter 5

Measurement Optimization

This chapter introduces the new detection and elimination technique in biomedical MITS to be integrated into the measurement process in this thesis for the detection and elimination of motion-induced signal errors prior to image reconstruction. It discusses the performed measurement optimization stage in conjunction with control and imaging experiments qualifying the overall performance of the MITS tomograph with regard to the optimized measurement.

5.1 Target Motion and Image Artefacts

In biomedical MITS, signal errors caused by unintentional movements of the target during measurement lead to voltage changes which may severely corrupt the useful signal. Consequently, they cause image artefacts unless they can be filtered out prior to image reconstruction.

In the previous chapter, the movement of the potato from one position to another within the saline tank during the SD and SFD measurements was intended in the measurement protocol in order to obtain the aimed SD and SFD signals and hence images. If, however, the potato had moved *1* or *2 cm* during the FD measurements, e.g., due to lack of fixation in the tank, this unintended movement would have distorted the expected FD signal and hence caused considerable ROI blurring in the resulting FD images. As a consequence, the potato may not have been correctly localized.

As the motional behaviour of the patient can sometimes be unpredictable or non-controllable during measurement, it is of fundamental importance to develop a methodology for detecting undesired movements and removing the induced errors. An ideal approach would be tracking of body motion during the measurement process and subsequent motion correction or artefact elimination during the image reconstruction process. If, however, such motion tracking and correction approaches are not implementable or infeasible, then a good alternative approach is to discard those signal frames acquired after the first unintentional patient movement in each image frame (an image frame is usually being reconstructed from multiple signal frames).

In this regard, it would be further of particular usefulness to retrieve the tracking information from the MITS signal itself in order to avoid using any motion sensors or surveillance devices whatsoever.

Within the context of *target motion and image artefacts* discussed above, terms such as *target motion*, *target movements*, etc. are to be understood as *any change of the target's position relative to the transmitters and/or receivers*, which can hence be also caused by movements of the transmitters and/or receivers, e.g., due to lack of mechanical stability of their supporting structure (for specific information on such kind of systematic errors and possible correction approaches, the reader is referred to [Scharfetter et al. 2001 (b), 2003; Scharfetter 2005, 2007; Scharfetter and Issa 2008]).

5.2   Detection and Elimination Technique (D&E)

The D&E technique aims at the detection and elimination of those datasets corrupted by motion artefacts prior to image reconstruction. D&E certainly represents the most simple and appropriate approach as long as sophisticated motion detection and artefact elimination methods are impossible or ineffective.

5.2.1   D&E Process and Methodology

The *D&E process* comprises two main procedures, an on-line *error detection procedure* to be performed during the measurement process and a subsequent off-line *error elimination procedure* to be performed after the measurement process during data postprocessing. The D&E methodology relies on the previously explained fact that biological materials induce weak primary field perturbations and thereby quasi-pure imaginary signals representing conductivity signals. In contrast, electrically high-conductive or magnetically high-permeable materials induce strong primary field perturbations and thereby strong quasi-pure real signals representing conductivity or permeability signals, respectively. Based thereon, if specifically chosen materials that strongly perturb the primary field and only affect the real part of the MITS signal are employed as *markers* on the surface of a *biological target*, then the *target* and the *marker* will induce an *imaginary signal* and a *real signal*, respectively. Thus, if the *marked target* (a target with one or more markers mounted on its surface) unintentionally undergoes any kind of motion during measurement, then the *target signal* and *marker signal* will change accordingly. The change in the latter (real) one represents the *detection signal* to be used to identify the motion, whilst the change in the former (imaginary) one represents the motion-induced *signal error* to be eliminated.

Figure (5.1) graphically summarizes the above D&E process and methodology. The abscissa's label implies that the MITS measurement is to be conducted in a multiframe manner. If unintentional target movements occur during measurement, they will, in the simplest case, cause sudden well identifiable changes in the marker signal. The first occurrence of such a change, corresponding to the first target movement, pinpoints the -henceforth called- *index of truncation (IoT)* required for the D&E process. Thus, all target frames with index *{i ≥ IoT}*, i.e., those affected by movement errors, are to be truncated from the dataset, whereas all remaining ones with index *{i < IoT}*, i.e., those assumed to be free of movement errors, are to be retained for image reconstruction.
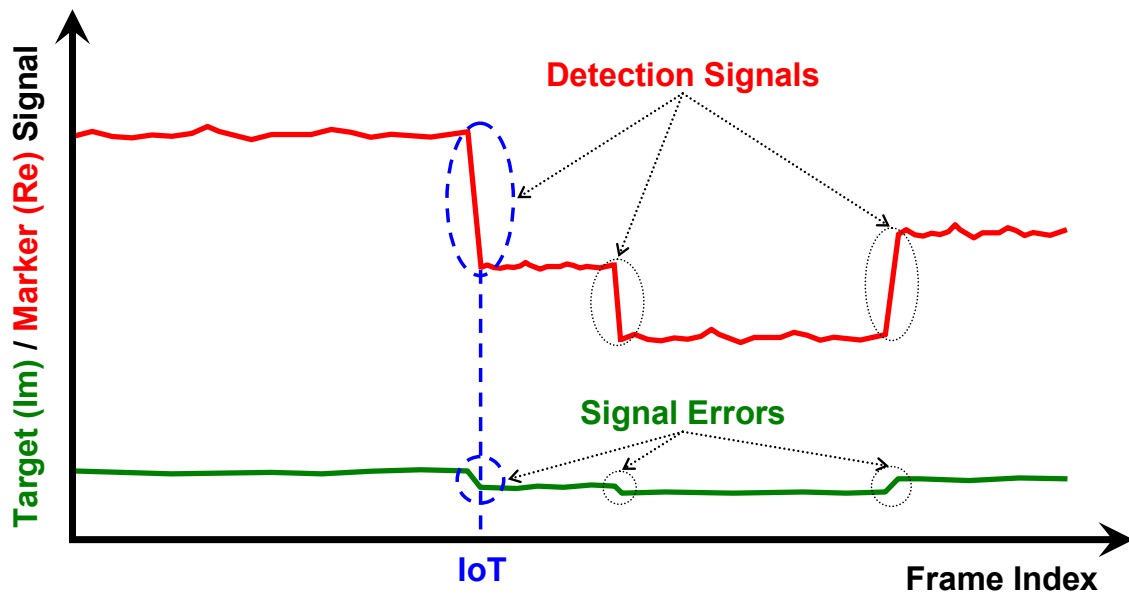
Figure (5.1): Functional concept of the D&E technique. Green curve: imaginary target signal; red curve: real marker signal; IoT: index of truncation. The red sharp jumps indicate the occurrence of sudden unwanted target movements during measurement. These jumps in the signal's real part, i.e., the detection signals, are used to identify the corresponding changes in the signal's imaginary part, i.e., the signal errors, for removing the corrupted data.

The marker signal represents a sensor through which any motion possibly occurring during measurement can be tracked. The D&E mechanism described in figure (5.1) is always applicable no matter how many movements occur and at whatever frames they occur because the erroneous frames to be eliminated are always determined by the *IoT*, and the *IoT* is in turn always determined by that frame whereat the first movement occurs, i.e., by the first detection signal. Hereof, the quality of the corrected images by means of the D&E technique depends only on the quality of the remaining error-free frames *{i < IoT}* after the error elimination procedure including their number, i.e., on their reliability regarding noise, *SNR*, drifts, outliers, etc. Thus, even if an unintended movement occurs immediately after the first received frame, i.e., if *(IoT = 2)*, then this one single remaining frame will deliver useful images if it is reliable. If it comes to the worst and the motion occurs at the very first acquired frame, i.e., if *(IoT = 1)*, then the D&E process reduces to its error detection procedure informing that *(IoT = 1)* and signifying therewith that the performed measurement failed and needs to be repeated.

The introduction of the *IoT* represents a quick and simple form of error detection, but it might sometimes give raise to misclassifications. As for instance, it might sometimes be of interest not to reject physiological signals that also cause fluctuations in the real part of the MITS signal, such as the periodic signals caused by breathing or cardiac activity. In such cases, more sophisticated methods might be required, such as the assessment of the signal dynamics in comparison to a priori known patterns gained from such physiological signals, e.g., by matched filters. Another simple approach would be the determination of a certain threshold for the magnitude of the first jump in the real part corresponding to the *IoT*. The a priori information regarding such threshold can be gained from reference measurements wherein a sufficient set of the intended markers are distributed on the patient's torso. In any case, this threshold should be high enough so as to avoid misclassifications due to noise. An appropriate criterion in this respect would be to define *a first marker signal change* as *the wanted detection signal having the IoT* if this change is at least two orders of magnitude larger than the noise (standard deviation) of those marker signal frames directly acquired before it.

In addition to the simplicity of the demonstrated D&E process, it is also important to realize its error detection procedure technically in a simple way without any negative effects on the measurement setup or the measurement process. In the following three paragraphs, two error detection methods, *active detection* and *passive detection*, employing two different kinds of markers, an *active marker* and a *passive marker*, respectively, will be presented. In other words, it will be distinguished between two types of the D&E process, *active D&E* and *passive D&E*, applying two technically different error detection procedures, yet sharing the same error elimination procedure.

5.2.2   Active Marker and Active Detection

In active detection, the marker mounted on the target surface can be periodically frame-wise activated and deactivated during measurement; in this study, the suggested active marker is a small coil with a load, which can be switched between *open (off state)* and *terminated (on state).* If any unintentional movements occur, then during the *on* phase, these movements lead to the distortion of the target (imaginary) signal (signal errors) on the one hand, and to sharp changes in the marker (real) signal (detection signals) on the other hand, whereas during the *off*

phase, the marker induces no signal. Thus, the first detection signal in the *on* phase identifies the sought *IoT*.

5.2.3   Passive Marker and Passive Detection

In passive detection, the marker mounted on the target surface is always active during measurement and hence induces a permanent signal; in this study, the suggested passive marker is a small ferromagnetic plate. Again, unwanted movements induce imaginary signal errors and real detection signals where the first detection signal defines the required *IoT*.

5.2.4   Active D&E versus Passive D&E

The main differences between active and passive D&E are summarized in the following lines:

❖   In active D&E, the signal of the inductive marker is based on the eddy currents induced in the coil and only exists beside the target signal during the *on* phase, i.e., it is a *non-permanent signal*. In passive D&E, the signal of the ferromagnetic marker is based on the magnetic permeability of its material and always exists beside the target signal, i.e., it is a *permanent signal*.

❖   In active D&E, the marker requires an electronic circuitry in order to control its on-off operation during measurement as well as a software routine in order to synchronize this circuitry with the MITS tomograph. This implies in turn a galvanic connection between the tomograph and the patient on the one hand (otherwise the on-off switching is being remotely controlled), and two signal acquisitions during the *on* and *off* periods, respectively, on the other hand. In passive D&E, in contrast, the marker does not require any additional hardware or software at all to accomplish its function as there is no on-off switching during measurement. Accordingly, besides being amazingly cheap, passive D&E retains the contactless MITS measurement manner on the one hand, and the corresponding measurements take half of the time in comparison to active D&E on the other hand.

❖   In active D&E, the on-off operation offers a choice between two received versions of the target signal; only one of them needs to be cleared of movement er-

rors and used in image reconstruction. This choice can be made based on some criterion, e.g., noise, outliers, etc; better would be however to correct both of them and then to choose. For the same reason, active D&E offers two signal acquisition windows with (*on* phase) and without (*off* phase) the real marker signal, respectively, which can be very useful for comprehensive signal analysis. In passive D&E, there are no such issues as the marker is permanent and hence there is only one target signal to be received.

❖   In active D&E, care has to be taken when designing the associated control circuitry as parasitic eddy currents may be induced in the metallic parts contained therein which might contaminate the target signal. In passive D&E, care has to be taken when choosing the ferromagnetic material forming the marker. It must have a very low loss factor, i.e., a very high quality factor, within the measurement frequency range of interest as otherwise it will not produce a quasi-pure real signal. In other words, the imaginary (loss) part μ_r'' of its relative magnetic permeability $\{\mu_r = \mu_r' - j * \mu_r''\}$ must be negligible in comparison to the real part μ_r' as otherwise μ_r'' may cause a spurious imaginary signal which might falsify the imaginary target signal. In this respect, the ability to choose a high quality factor for the ferromagnetic marker represents an advantage over the inductive one.

5.3 Measurements

5.3.1 Measurement Model

The previous equivalent electromagnetic measurement diagram in figure (4.7) needs now to be extended to the one depicted in figure (5.2) due to the presence of the marker on the surface of the biological target. The mutual coupling between the target medium and the marker is disregarded in this model as it represents only a very weak effect of higher order.

In an analogous manner to the previous derivation of V_2 according to figure (4.7), the derivation steps according to figure (5.2) can be summarized as follows:

V_2 reads first as:

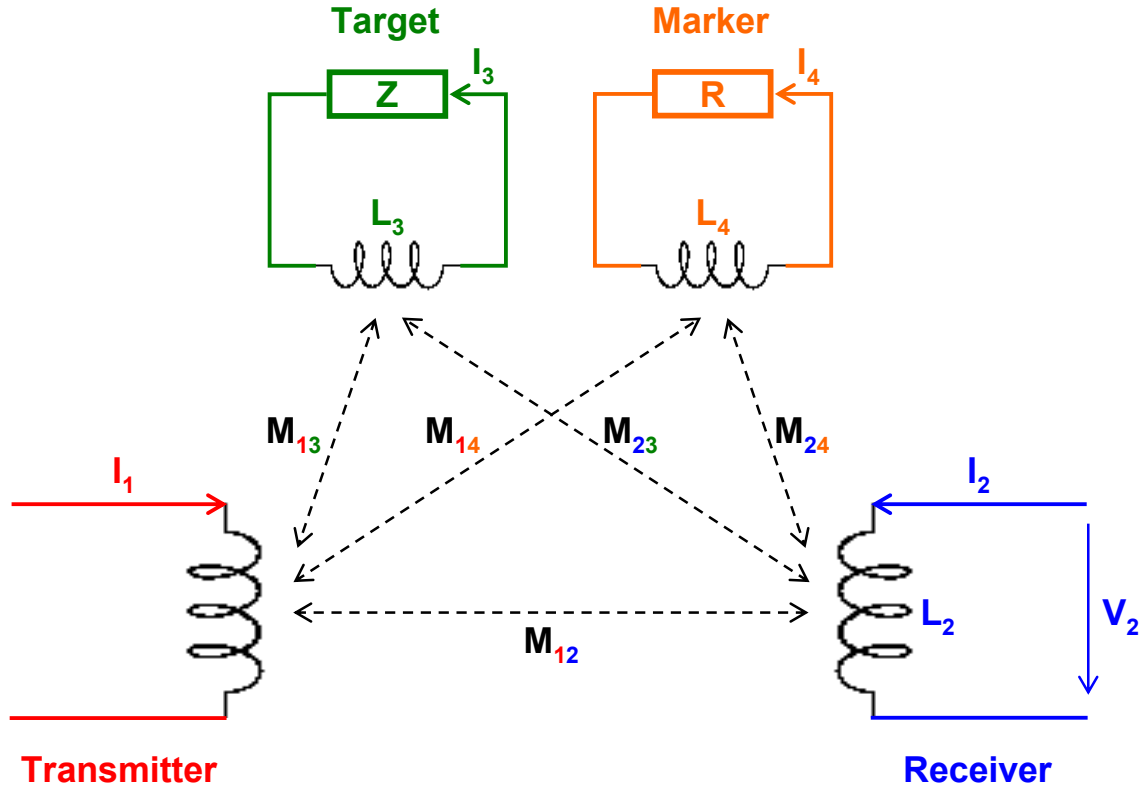$$V_2 = j\omega M_{12} I_1 + j\omega L_2 I_2 + j\omega M_{23} I_3 + j\omega M_{24} I_4 \qquad (5.1)$$

Figure (5.2): Equivalent measurement model for a marked biological target in MITS. R: resistance of the marker; Z: impedance of the biological target consisting of a resistance and a capacitive reactance, i.e., {Z = R_T + (1 / $j\omega C_T$)}; $L_\#$, $I_\#$, $V_\#$: inductance, current and voltage, respectively, with respect to the indexed component; $M_{\#\#}$: mutual inductance between the two indexed components.

Due to the high-impedance termination of L_2, i.e., due to *(I_2 = 0)*, V_2 reduces to:

$$V_2 = j\omega M_{12} I_1 + j\omega M_{23} I_3 + j\omega M_{24} I_4 \qquad (5.2)$$

Based on the following transmitter-target and transmitter-marker relationships, respectively:

$$j\omega M_{13} I_1 + (Z + j\omega L_3) I_3 = 0 \qquad (5.3)$$

$$j\omega M_{14} I_1 + (R + j\omega L_4) I_4 = 0 \qquad (5.4)$$

I_3 and I_4 can be explicitly stated as:

$$I_3 = - (j\omega M_{13} / (Z + j\omega L_3)) \, I_1 \qquad\qquad (5.5)$$

$$I_4 = - (j\omega M_{14} / (R + j\omega L_4)) \, I_1 \qquad\qquad (5.6)$$

Inserting equations (5.5) and (5.6) in equation (5.2), V_2 reads then as:

$$V_2 = j\omega M_{12} \, I_1 + (\omega^2 I_1 / (Z + j\omega L_3)) \, M_{13}M_{23} + (\omega^2 I_1 / (R + j\omega L_4)) \, M_{14}M_{24} \quad (5.7)$$

Assuming again that $\{|Z| \gg \omega L_3\}$ and $\{R_T \gg 1 / \omega C_T\}$, and choosing a marker with a high quality factor, i.e., $\{\omega L_4 \gg R\}$, V_2 reads then finally as:

$$V_2 \approx j\omega M_{12} \, I_1 + (\omega^2 I_1 / R_T) \, M_{13}M_{23} + (\omega^2 I_1 / j\omega L_4) \, M_{14}M_{24} = V_{car} + V_{tar} + V_{mar} \;\; (5.8)$$

where the first right-hand-side term corresponds to the primary field and represents the *carrier signal* V_{car} to be suppressed as much as possible, whilst the second and third ones correspond to the secondary field and represent the useful *target signal* V_{tar} and *marker signal* V_{mar}, respectively.

V_{tar} and V_{mar} in equation (5.8) are real and imaginary signals, respectively, with respect to the imaginary signal V_{car}, but when defining again V_{car} as the reference real signal of the underlying phasor diagram with phase angle $(\Phi = 0°)$, V_{tar} and V_{mar} become an *imaginary signal* and a *real signal*, respectively, with respect to the reference real signal V_{car}. The two factors $(M_{13}M_{23})$ and $(M_{14}M_{24})$ depend on the position of the target and the marker, respectively, with respect to the transmitter and the receiver, i.e., on the position or distance of the *marked target* relative to the transmitter and the receiver. As can be seen in equation (5.9), these two factors represent the key quantities when observing a change in the received signal due to a change in the position of the marked target:

$$\partial V_2 / \partial(x,y,z) = \omega^2 I_1 \, \partial(M_{13}M_{23} / R_T) / \partial(x,y,z) + \omega^2 I_1 \, \partial(M_{14}M_{24} / j\omega L_4) / \partial(x,y,z) \quad (5.9)$$

where (x, y, z) represents any *point* shared by the target and the marker mounted on its surface.

Accordingly, equation (5.9) represents the response of the receiver to whatever relative movement of the marked target with respect to the transmitter and/or receiver. Thus, if any such movement occurs, then (recall that V_{car} is already defined as the reference real signal) the *imaginary response* and *real response* corre-

sponding to the first and second right-hand-side term, respectively, shall represent the *signal error (V_{err})* and *detection signal (V_{det})* in question, respectively (see figure (5.1)), as shown in the following simplified form of this response summarizing the basic rationale behind the D&E technique:

$$\partial V_2 / \partial(x,y,z) = \partial(V_{tar}) / \partial(x,y,z) + \partial(V_{mar}) / \partial(x,y,z) = V_{err} + V_{det} \qquad (5.10)$$

5.3.2 Measurement Setup

The measurement setup is depicted in figure (5.3). A saline sphere of *15 mm* radius and *2 S/m* conductivity (homogeneous conductivity distribution) served as a phantom of physiological conductivity representing the ROI.
The previously described plastic tank was filled with *15.55 ℓ NaCl* solution of *0.2 S/m* conductivity and served as a background medium of physiological conductivity containing the ROI.
The used active and passive markers, described in the following two subparagraphs, were fixed on the lateral surface of the tank. The red marker in figure (5.3) represents both of them; however, the corresponding active and passive D&E measurements were performed separately, i.e., the tank was marked with only one of the two ones in two independent measurements, respectively.

For the sake of consistency and comparability, no other saline sphere and background medium than the mentioned ones were used in whatever type of measurements; the same applies to the used active and passive markers.

5.3.2.1 Active Marker

The used active marker was a single-turn circular coil of *10 mm* diameter. The software-controlled switching was implemented with the N-channel enhancement mode MOSFET *BSN20* from *Philips Semiconductors*. Measures had to be taken in order to avoid the induction of parasitic eddy currents by the marker or its circuit and thereby the contamination of the phantom signal, particularly at high frequencies. To this end, the MOSFET was chosen as the smallest available SMD package *(SOT23, max(LxWxH) = 3x2.5x1.1 mm)* and mounted outside the sensitive region of the transceiver system. Moreover, the copper wire forming the marker loop was made as thin as *0.1 mm*. The marker circuit is shown in figure (5.4); it was implemented as previously tested in [Scharfetter et al. 2010].
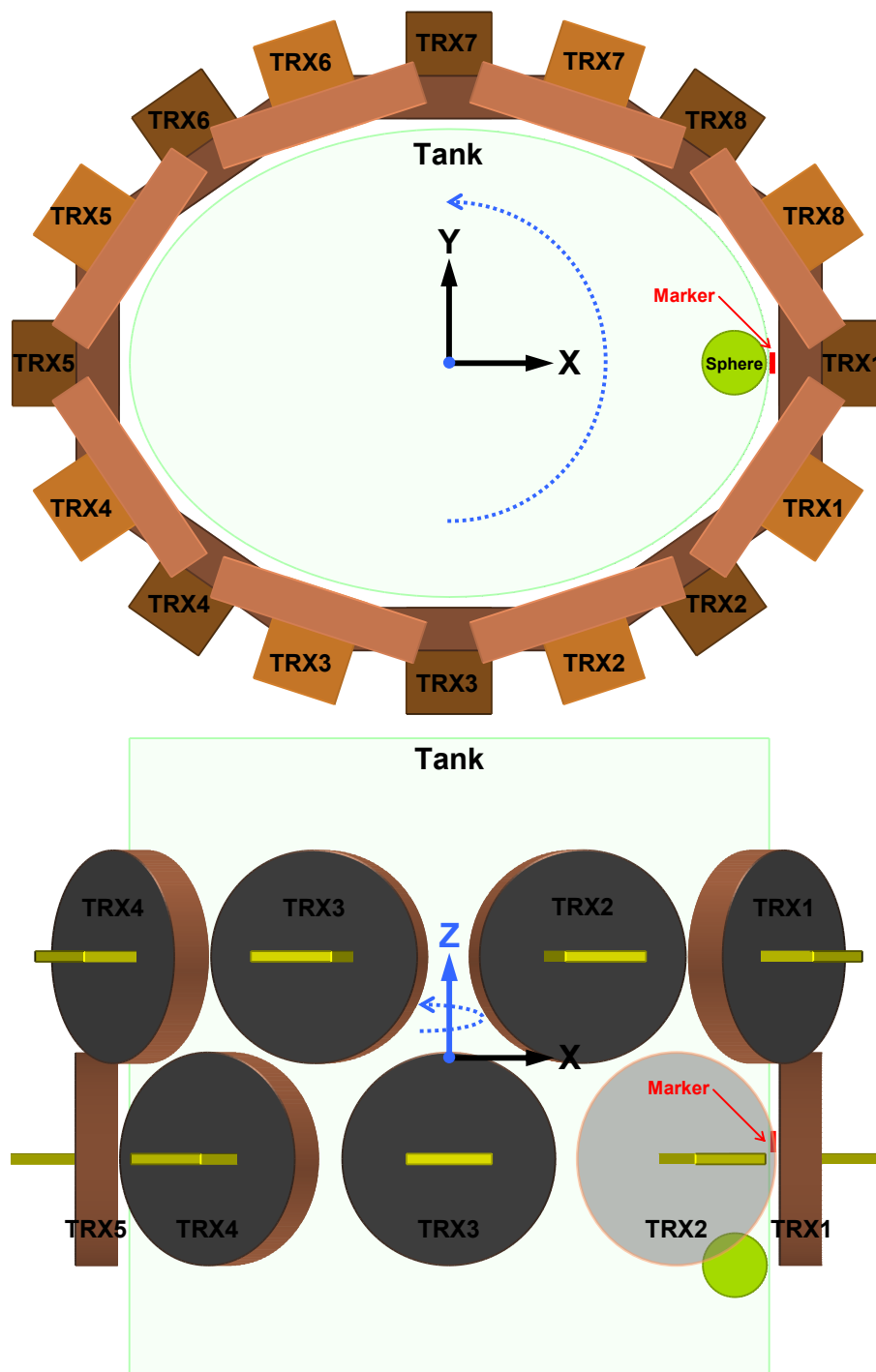
Figure (5.3): Experimental setup. Top: top view, bottom: long-side view. For the sake clarity, the lower TX2 is made transparent and its 3D view is deactivated. The red marker is either an active or a passive one, depending on the intended D&E measurement. The dotted, curved blue arrow denotes an unwanted (rotational) movement of the whole measured medium. Dimensions of the TRX, the whole array and the tank can be taken from figures (3.3), (3.5) and (3.10), respectively.
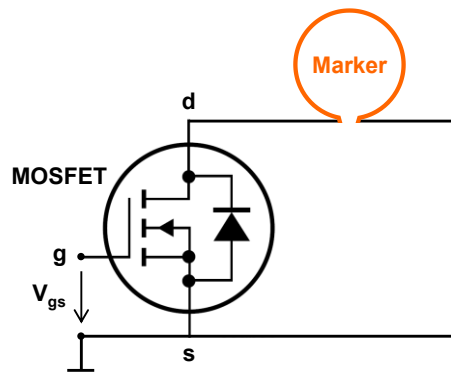
Figure (5.4): Control circuit of the inductive marker. The gate-source voltage V_{gs} is controlled by a digital port (TTL levels) via the imaging console.

5.3.2.2 Passive Marker

The used passive marker was made by pressing *nickel-zinc (Ni-Zn)* ferrite powder *K 250* from *Kaschke Components* in the shape of a thin square plate with the dimensions *LxWxH* of *10x10x0.1 mm*. According to figure (5.5) [Kaschke Components 2015], the complex relative permeability of this ferromagnetic material is $\{\mu_r = \mu_r{}' - j * \mu_r{}'' \approx 200 - j * 1.6\}$ at *1 MHz*. This yields a *loss factor* of $\{\mu_r{}'' / \mu_r{}' = 0.008\}$, or inversely, a *quality factor* of $\{\mu_r{}' / \mu_r{}'' = 125\}$, and hence an almost negligible *loss $\mu_r{}''$* within the low part of the β-dispersion frequency range. The DC resistivity of the used *Ni-Zn* ferrite is specified to be $\geq 10^5$ *Ω.m* at *25 °C*.
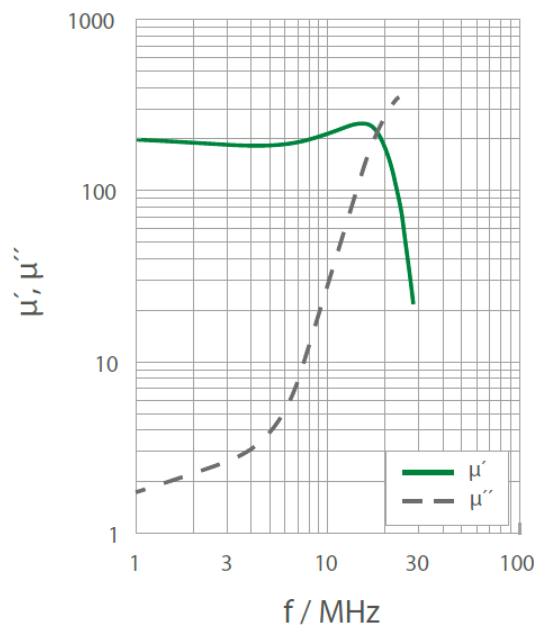

Figure (5.5): Frequency response of the ferromagnetic marker regarding its complex relative permeability. The loss tangent $\mu_r{}''/\mu_r{}'$ is less than 1% up to ca. 2 MHz.

5.3.3   Measurement Process and Measurement Data

All measurements in this chapter were performed in a multifrequency, multiframe and state-differential manner. Besides the principal measurements on active and passive D&E, separate reference measurements were performed for verification purposes. All these measurements were conducted at *200* and *500 kHz*; at these two frequencies, the TXs were driven by excitation currents of *0.46* and *0.34 A$_{rms}$*, respectively. Each reference or D&E measurement was carried out in two or three successive phases representing two or three different states of the target medium, respectively, during one and the same measurement; in each state, *15 frames* were acquired and averaged where in the active D&E measurements these signal frames were to be acquired two times during the *on* and *off* periods, respectively.

5.3.3.1   D&E Measurements

The D&E experiments comprised three consecutive measurement phases according to the following three different states of the target medium, respectively:

❖   Background saline tank marked with either an active or a passive marker and oriented as exactly shown in figure (5.3) with the saline sphere lying therein at an initial position *(135, 0, -97.5) mm*. The measured signal frames in this state will be called *error-free frames $v_{err\text{-}free}$*.

❖   The same marked tank containing the sphere, but rotated as a whole by ca. *4°* about the z-axis (corresponding to *1 cm* arc length) in order to simulate an unintentional movement, leading to a new sphere position at *(134, 9, -97.5) mm*. The measured signal frames in this state will be called *erroneous frames v_{err}*.

❖   Background saline tank without the sphere or any marker (pure background medium) oriented as exactly shown in figure (5.3), i.e., non-rotated. The measured signal in this state will be called *background signal v_{bg}*.

Naturally, as has always been the case, the imaginary part of the above-stated signals was used in image reconstruction as it carries the conductivity information in biomedical MITS.
A key quantity is the difference between v_{err} and $v_{err\text{-}free}$ representing the *movement-induced signal change (Δv_{error})* which needs to be decomposed into its imagi-

nary and real parts, respectively:

$$Im(\Delta \boldsymbol{v}_{error}) = Im(\boldsymbol{v}_{err}) - Im(\boldsymbol{v}_{err\text{-}free}) \qquad (5.11)$$

$$Re(\Delta \boldsymbol{v}_{error}) = Re(\boldsymbol{v}_{err}) - Re(\boldsymbol{v}_{err\text{-}free}) \qquad (5.12)$$

where $Im(\Delta \boldsymbol{v}_{error})$ and $Re(\Delta \boldsymbol{v}_{error})$ are no more than the *signal error* and *detection signal* in question, abbreviated previously in equation (5.10) as V_{err} and V_{det}, respectively; in other words, $Im(\Delta \boldsymbol{v}_{error})$ will corrupt the images to be reconstructed and must be cancelled out, whereas $Re(\Delta \boldsymbol{v}_{error})$ will be used to detect $Im(\Delta \boldsymbol{v}_{error})$, i.e., to identify the onset of $Im(\boldsymbol{v}_{err})$ corresponding to the sought *IoT*.

The whole received signal is a *30-frame* signal comprising the two consecutively acquired *15-frame* signals in the first and second state before and after the simulated unintentional movement, $\boldsymbol{v}_{err\text{-}free}$ and $\boldsymbol{v}_{err}$, respectively. This *30-frame* overall signal is affected by the motion-induced $\Delta \boldsymbol{v}_{error}$ and will hence produce erroneous images affected by motion artefacts independent of the applied imaging type, whether static, dynamic, parametric, etc. If, for instance, these *erroneous images* $(\Delta \boldsymbol{\sigma}_{err})$ are intended to be reconstructed state-differentially (dynamically), then the corresponding *erroneous signals* $(\Delta \boldsymbol{v}_{err})$ can simply be obtained as shown in equation (5.13) through averaging the total received signal $(\boldsymbol{v}_{err\text{-}free} + \boldsymbol{v}_{err})$ and subtracting it from the other signal gained from the other intended state, herein, the background signal $\boldsymbol{v}_{bg}$ gained from the third state:

$$Im(\Delta \boldsymbol{v}_{err}) = Im(\boldsymbol{v}_{bg}) - mean(Im(\boldsymbol{v}_{err\text{-}free}) + Im(\boldsymbol{v}_{err})) \qquad (5.13)$$

In order to avoid motion artefacts in the images to be reconstructed, the *IoT* was identified and all data frames with index $\{i \geq IoT\}$ were discarded. The *D&E-corrected images* $(\Delta \boldsymbol{\sigma}_{corr})$ were then reconstructed as originally intended state-differentially from the corresponding *D&E-corrected signals* $(\Delta \boldsymbol{v}_{corr})$:

$$Im(\Delta \boldsymbol{v}_{corr}) = Im(\boldsymbol{v}_{bg}) - Im(\boldsymbol{v}_{err\text{-}free}) \qquad (5.14)$$

5.3.3.2 Reference Measurements

The validation of the D&E technique required the D&E-corrected signals and images to be qualitatively and quantitatively compared to reference (true) ones

gained from independent measurements. The reference experiments comprised two consecutive measurement phases according to the following two different states of the target medium, respectively:

❖   The same non-rotated target medium measured in the first state of the D&E experiments and shown in figure (5.3), but without any marker at all. In consistence with the *30-frame* overall signal *($v_{err\text{-}free}$ + v_{err})* in the D&E measurements, *30 frames* were exceptionally acquired and averaged in this state rather than the usual *15 frames*. The measured signal in this state will be called *total signal v_{tot}*.

❖   The exact non-rotated pure background medium measured in the third state of the D&E experiments. The measured signal in this state will still be called *background signal v_{bg}*.

Thus, as originally intended, the reference *true images ($\Delta\sigma_{true}$)* were reconstructed state-differentially from the corresponding reference *true signals (Δv_{true})*:

$$Im(\Delta v_{true}) = Im(v_{bg}) - Im(v_{tot}) \tag{5.15}$$

Remarks

The used global subscripting with the symbol # in the previous chapter will still be used in order to avoid inconvenient repeating of the different signals $\Delta v_{\#}$ and images $\Delta\sigma_{\#}$. In addition, the inconvenient imaginary notation of $\Delta v_{\#}$, i.e., *$Im(\Delta v_{\#})$*, will henceforth not be used unless needed.

5.4   Image Reconstruction

The previous measurements provided *10* different data vectors $\Delta v_{\#}$. Correspondingly, *10* different images $\Delta\sigma_{\#}$ needed to be reconstructed. The memory-efficient, LS-optimized Tikhonov-regularized inverse solution (4.57) employing a single-step Gauss-Newton formulation was used in this chapter for all *10* reconstructions. When replacing the symbol λ by λ_{app}, this solution reads as follows:

$$\Delta\sigma_{\#} = S^T [S\ S^T + \lambda_{app}\ I_m]^{-1}\ Im(\Delta v_{\#}) \tag{5.16}$$

As for λ_{app}, thanks to the low ratio of *3.02-3.69* obtained from the constraint (4.60)

regarding the *10* different $\Delta v_{\#}$, the use of the associated statement (4.59) to determine *10* appropriate regularization parameters λ_{app}, respectively, was perfectly possible. Furthermore, thanks to the attained high *SNR* at the lowest applied frequency in this chapter's measurements *(51.29-56.91 dB at 200 kHz)*, it was easily possible to find an appropriate global λ_{app} for all performed reconstructions through simply averaging the *10* resulting λ_{app}, yielding a global λ_{app} of *(4.23 x 10^{-17})*. This global λ_{app} allowed in turn for a better use of the arbitrarily scaled (non-absolute) colour bars (pixel values) in the quantitative comparison between the different images $\Delta\boldsymbol{\sigma}_{\#}$ with respect to the different signals $\Delta\boldsymbol{v}_{\#}$ as well as in the validation of the new D&E technique. In this respect, it might be recalled that the regularization term $(\lambda_{app} \boldsymbol{I}_m)$ represents an averaged, approximated or Gaussian-distributed version of the data covariance matrix. As regards the sensitivity matrix $\boldsymbol{S}$, it should be mentioned that it remained almost unchanged after the slight tank rotation by less than *4°*; therefore, no own $\boldsymbol{S}$ needed to be calculated for the rotated tank.

5.5   Performance Measures

For the validation of the D&E technique, the acquired signals $\Delta\boldsymbol{v}_{\#}$ and the corresponding reconstructed images $\Delta\boldsymbol{\sigma}_{\#}$ were quantitatively compared and subsequently assessed based on the following performance criteria, where many of them were already presented in the previous chapter:

5.5.1   Signal Quantification Measures

The involved quantities in previous chapter's equation (4.70) *{SNR = 20 log(|Im(Δv$_{\#}$)| / Im(N))}* were used again, but also with respect to the real parts as this chapter additionally deals with the real marker signal.

Further, the accuracy of the D&E-corrected signals was assessed with reference to the true ones based on the following *relative percent error ($\delta_{\%}(\Delta v_{corr})$)*:

$$\delta_{\%}(\Delta v_{corr}) = 100\% \ |Im(\Delta v_{true}) - Im(\Delta v_{corr})| \ / \ |Im(\Delta v_{true})| \qquad (5.17)$$

where $\Delta v_{\#}$ represents one entry in the data vector $\Delta\boldsymbol{v}_{\#}$ corresponding to the measurement combination (channel) TX1-RX1 of the lower plane which had the greatest impact on the reconstructed images $\Delta\boldsymbol{\sigma}_{\#}$ as the phantom was located in front

of the lower TRX1 during all measurements (see figure (5.3)).

5.5.2   Image Quantification Measures

The involved quantities in previous chapter's equation (4.71) $\{CNR = |\Delta\sigma_\#| \,/\, N_{bg}\}$ were used again.

Further, the accuracy of the D&E-corrected images was assessed with reference to the true ones based on the following *relative percent error* ($\delta_\%(\Delta\sigma_{corr})$):

$$\delta_\%(\Delta\sigma_{corr}) = 100\% \; |\Delta\sigma_{true} - \Delta\sigma_{corr}| \,/\, |\Delta\sigma_{true}| \qquad (5.18)$$

where $\Delta\sigma_\#$ represents one entry in the solution vector $\Delta\sigma_\#$ corresponding to the central element (centre of gravity, highest contrast) of the reconstructed spherical perturbation (ROI).

5.6   Results

The reconstructed erroneous, D&E-corrected and true images are presented in figures (5.6), (5.8) and (5.9), respectively. All images are transversal cross-sectional slices taken through the centre of the spherical ROI (saline sphere) at *(z = -97.5 mm)*. For the sake of clarity and comparability, a zoom-in screenshot of the ROI and the close surrounding background is additionally provided. The dotted white and cyan circles in figure (5.6) mark the initial and final positions of the sphere before and after medium rotation, respectively, in the active and passive D&E measurements; the white circle in figure (5.8) marks the same initial position of the sphere in figure (5.6); the white circle in figure (5.9) marks the sphere position before taking it out of the tank in the reference measurements which is also identical to its initial position in the D&E measurements. The acquired real and imaginary signal frames in the active and passive D&E measurements are presented in figure (5.7). The quantification parameters of the different signals $\Delta v_\#$ and images $\Delta\sigma_\#$ are summarized in the *8* tables (5.1-5.8) with each two thereof corresponding to one of the *4* figures (5.6-5.9), respectively; each image in figures (5.6), (5.8) and (5.9) or graph in figure (5.7) occupies an own row in each of the two respective tables. The quantification of the accuracy of the D&E-corrected signals and images is summarized in tables (5.9) and (5.10), respectively.
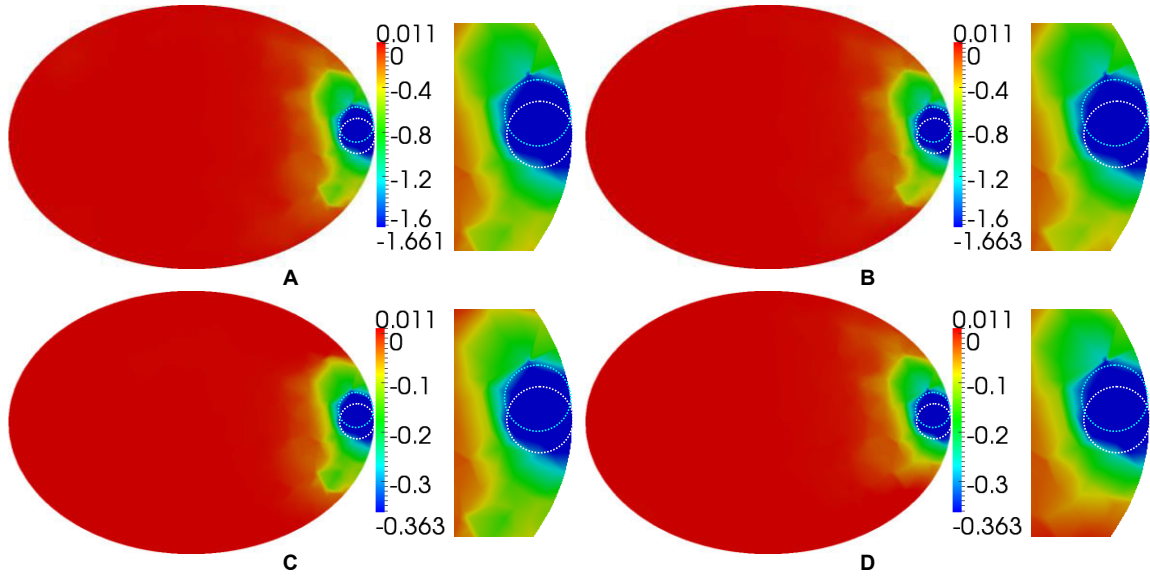
Figure (5.6): Erroneous images of the rotated target medium. A: active D&E at 500 kHz, B: passive D&E at 500 kHz, C: active D&E at 200 kHz, D: passive D&E at 200 kHz.

Marker	Image	f [kHz]	Im(Δv_{err}) [V]	Im(N) [V]	SNR [dB]
Active	A	500	-10.09×10^{-6}	4.94×10^{-9}	66.20
	C	200	-2.27×10^{-6}	5.28×10^{-9}	52.67
Passive	B	500	-10.11×10^{-6}	4.91×10^{-9}	66.27
	D	200	-2.27×10^{-6}	6.19×10^{-9}	51.29

Table (5.1): Quantitative data on the erroneous signals relevant to the erroneous images in figure (5.6).

Marker	Image	f [kHz]	$\Delta\sigma_{err}$ [S/m]	N_{bg} [S/m]	CNR [1]
Active	A	500	-1.661	2.856×10^{-2}	58.16
	C	200	-0.363	0.815×10^{-2}	44.54
Passive	B	500	-1.663	2.824×10^{-2}	58.89
	D	200	-0.363	0.802×10^{-2}	45.26

Table (5.2): Quantitative data on the erroneous images in figure (5.6).
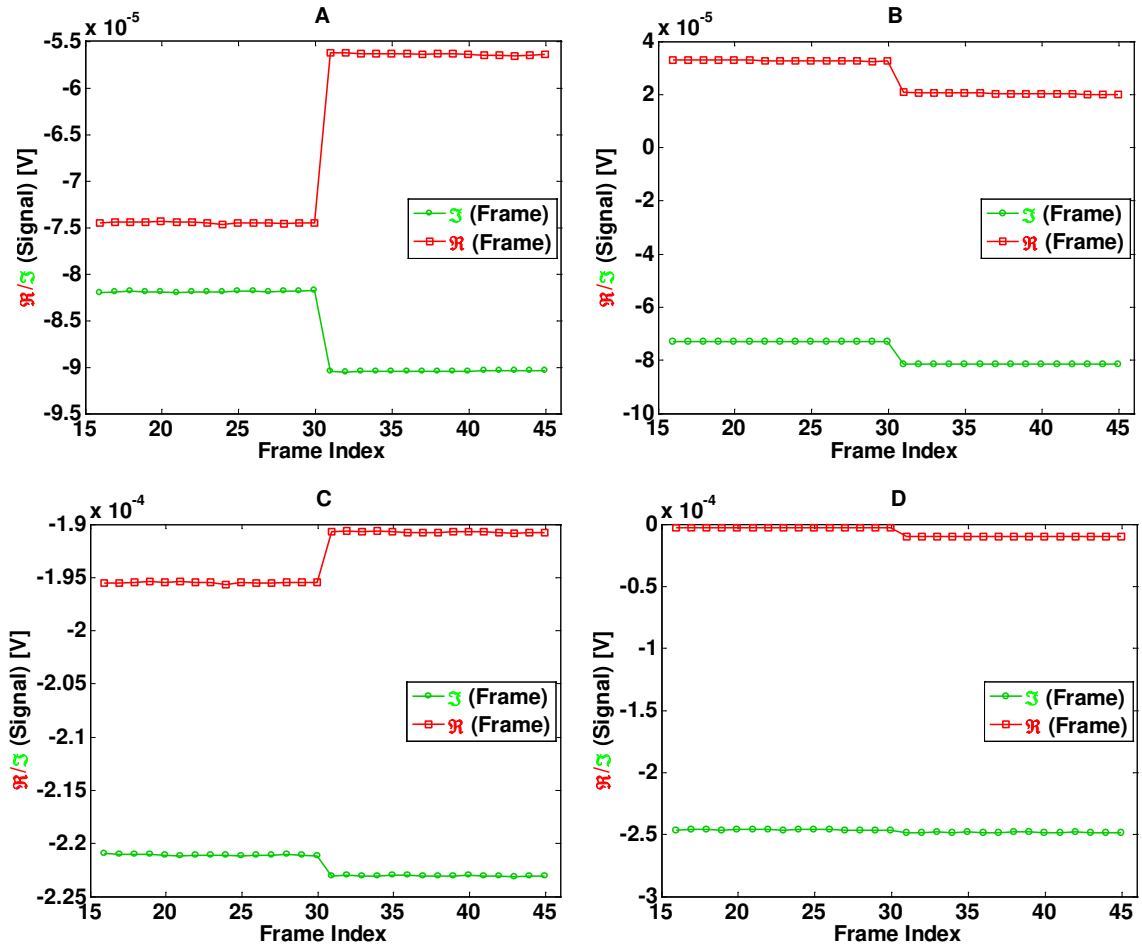
Figure (5.7): Real and imaginary signal frames of the rotated target medium. A: active D&E at 500 kHz, B: passive D&E at 500 kHz, C: active D&E at 200 kHz, D: passive D&E at 200 kHz. Red curve: real (marker) signal containing the motion-induced detection signal Re(Δv_{error}); green curve: imaginary (target) signal containing the motion-induced signal error Im(Δv_{error}). Note the differently scaled y-axes of the graphs. The first invisible 15 frames belong to the required calibration cycle for phase correction and are therefore not shown.

Marker	Graph	f [kHz]	Re(Δv_{error}) [V]	Re(N) [V]	SNR [dB]
Active	A	500	18.18×10^{-6}	4.42×10^{-9}	72.28
	C	200	4.75×10^{-6}	5.90×10^{-9}	58.12
Passive	B	500	-12.38×10^{-6}	6.20×10^{-9}	66.01
	D	200	-7.15×10^{-6}	4.71×10^{-9}	63.63

Table (5.3): Quantitative data on the detection signals in figure (5.7).

Marker	Graph	f [kHz]	Im(Δv_{error}) [V]	Im(N) [V]	SNR [dB]
Active	A	500	-8.56 x 10^{-6}	3.75 x 10^{-9}	67.17
	C	200	-1.96 x 10^{-6}	5.01 x 10^{-9}	51.85
Passive	B	500	-8.55 x 10^{-6}	3.58 x 10^{-9}	67.56
	D	200	-1.96 x 10^{-6}	5.33 x 10^{-9}	51.31

Table (5.4): Quantitative data on the signal errors in figure (5.7).
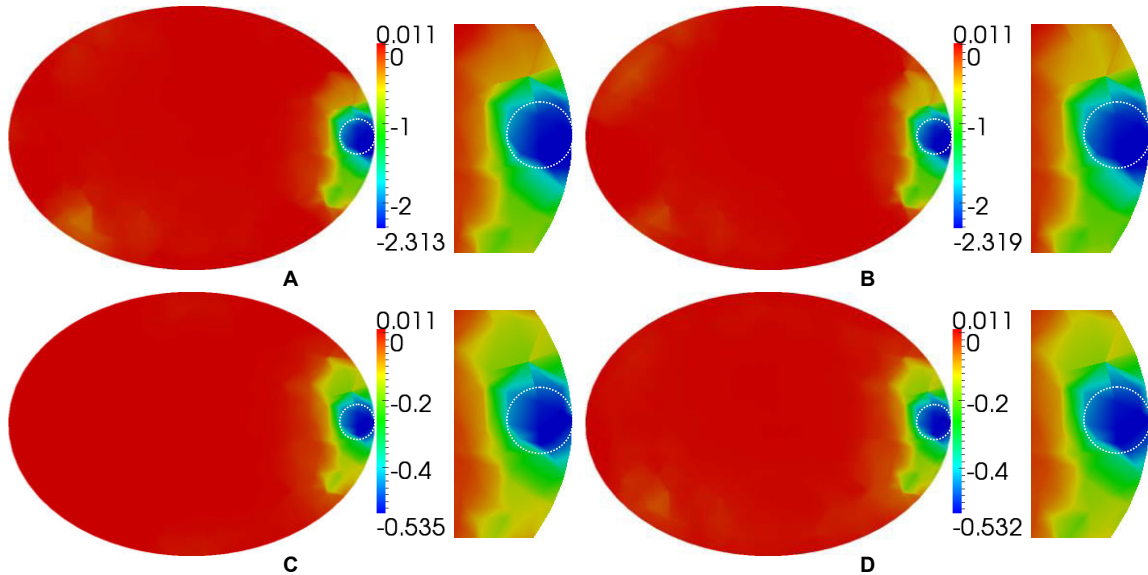
Figure (5.8): D&E-corrected images of the rotated target medium. These images A, B, C and D are the corrected versions of the erroneous images A, B, C and D in figure (5.6), respectively.

Image	f [kHz]	Im(Δv_{corr}) [V]	Im(N) [V]	SNR [dB]
A	500	-14.11 x 10^{-6}	6.15 x 10^{-9}	67.21
C	200	-3.34 x 10^{-6}	5.55 x 10^{-9}	55.59
B	500	-14.15 x 10^{-6}	6.21 x 10^{-9}	67.15
D	200	-3.32 x 10^{-6}	7.06 x 10^{-9}	53.45

Table (5.5): Quantitative data on the D&E-corrected signals relevant to the D&E-corrected images in figure (5.8).

Image	f [kHz]	$\Delta\sigma_{corr}$ [S/m]	N_{bg} [S/m]	CNR [1]
A	500	-2.313	4.351×10^{-2}	53.16
C	200	-0.535	1.183×10^{-2}	45.22
B	500	-2.319	4.289×10^{-2}	54.07
D	200	-0.532	1.233×10^{-2}	43.15

Table (5.6): Quantitative data on the D&E-corrected images in figure (5.8).
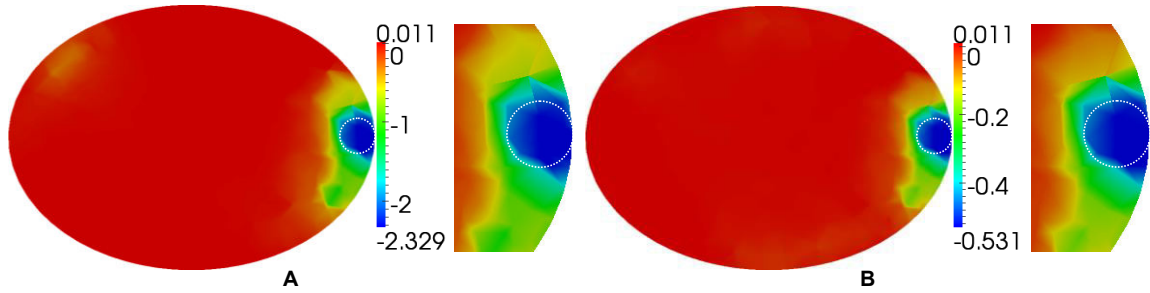
Figure (5.9): True images of the non-rotated target medium. A: at 500 kHz, B: at 200 kHz.

Image	f [kHz]	$Im(\Delta v_{true})$ [V]	$Im(N)$ [V]	SNR [dB]
A	500	-14.21×10^{-6}	6.65×10^{-9}	66.60
B	200	-3.30×10^{-6}	4.71×10^{-9}	56.91

Table (5.7): Quantitative data on the true signals relevant to the true images in figure (5.9).

Image	f [kHz]	$\Delta\sigma_{true}$ [S/m]	N_{bg} [S/m]	CNR [1]
A	500	-2.329	4.327×10^{-2}	53.82
B	200	-0.531	1.205×10^{-2}	44.07

Table (5.8): Quantitative data on the true images in figure (5.9).

f [kHz]	Im(Δv_{true}) [V]	Im(Δv_{corr}) [V]	$\delta_\%(\Delta v_{corr})$
500	-14.21×10^{-6}	-14.11×10^{-6}	0.70
		-14.15×10^{-6}	0.42
200	-3.30×10^{-6}	-3.34×10^{-6}	1.21
		-3.32×10^{-6}	0.61

Table (5.9): Accuracy of the D&E-corrected signals. Im(Δv_{corr}) and Im(Δv_{true}) are taken from tables (5.5) and (5.7), respectively.

f [kHz]	$\Delta\sigma_{true}$ [S/m]	$\Delta\sigma_{corr}$ [S/m]	$\delta_\%(\Delta\sigma_{corr})$
500	-2.329	-2.313	0.69
		-2.319	0.43
200	-0.531	-0.535	0.75
		-0.532	0.19

Table (5.10): Accuracy of the D&E-corrected images. $\Delta\sigma_{corr}$ and $\Delta\sigma_{true}$ are taken from tables (5.6) and (5.8), respectively.

5.7   Discussion

5.7.1   Motion Artefacts and Erroneous Images

As can be seen in all images of figure (5.6), the slight rotational movement of the target medium resulted in considerable motion blurring of the reconstructed spherical perturbation in its movement direction, i.e., anticlockwise (see figure (5.3)), extending thereby its original circular area about *40%* and preventing a correct localization within the surrounding background.

The images gained from the active D&E measurements at *200* and *500 kHz* closely resemble those gained from the passive ones, respectively. This close resemblance can be qualitatively ascertained through a visual inspection as well as quantitatively through comparing the respective image quantification measures in

table (5.2). As can be seen in table (5.1), this close similarity is logically expected as these images resulted from quasi-equal imaginary signals, respectively, and the only difference between the active and passive D&E measurements was the used marker affecting the real part of the received signal. Moreover, aside from the image performance parameters in table (5.2), the reconstructed images at *200 kHz* are visually very similar to those reconstructed at *500 kHz*.

The expectable close resemblance or similarity among the erroneous images is actually not the point of major concern, rather the motion artefacts affecting all of them and preventing thereby any correct localization of the phantom in the imaged medium. And right here comes the role of the D&E technique.

5.7.2   D&E Application and Corrected Images

In order to get rid of the movement artefacts by means of the D&E method, the frame-wise behaviour of the real part of the total received signal containing the *detection signal Re(Δv_{error})* has at first to be inspected together with that of its imaginary part containing the *signal error Im(Δv_{error})* throughout the *30-frame* measurement cycle. As can be seen in figure (5.7), independent of the used type of marker or the applied frequency in the D&E measurements, the real signal undergoes a jump at the *31st* frame. This jump indicates the occurrence of a movement during measurement, the reason why another jump happens at the very same frame in the imaginary signal.

Actually, it is not necessarily important to recognize the imaginary jump representing the signal error, rather the real one representing the detection signal because the latter is being methodologically used to pinpoint the former due to its relatively high magnitude. The conductivity of the saline sphere was intentionally chosen to be *2 S/m* for reasons of clarity and comprehensibility; if a human brain had been measured instead, it would not have been possible to distinguish the signal error in the green curves of figure (5.7). The small dimensions of the used markers were intentionally chosen so that they produce detection signals about of the order of the signal errors at the applied frequencies (see tables (5.3) and (5.4)). Thus, even though small, they indeed induced adequate detection signals and are due to their small dimensions very convenient for real applications.

The above-mentioned *31ˢᵗ* frame marks the searched-for *IoT*, i.e., *(IoT = 31)*. Hence, all imaginary frames with index *(i ≥ 31)* were discarded, whereas the remaining ones were used to reconstruct the motion-artefact-free images in figure (5.8). As for these D&E-corrected images, as was the case with their original erroneous versions in figure (5.6), there is a close similarity between the D&E-corrected images at *200* and *500 kHz*, respectively. Again, on the one hand, this close similarity is already predictable when comparing the respective imaginary signals in table (5.5); on the other hand, it is qualitatively evident through a visual inspection as well as quantitatively through comparing the respective image performance indicators in table (5.6). Moreover, the images are visually very similar independent of the applied frequency.

The expected close resemblance among the D&E-corrected images, however, is not of that relevance to the discussion; of most relevance are actually the consequences of the applied D&E technique on the movement artefacts in the original erroneous images in figure (5.6). Comparing now the latter ones with their D&E-corrected versions in figure (5.8), it can be clearly seen that the considerable motion-induced ROI blurring has reduced to a great extent (compare the zoom-in screenshots of both groups of images). Moreover, the green ringing artefact around the perturbation, being typical of MITS, has considerably reduced on the upper side; this means that the rotational movement led also to an increase in the extent of the ringing artefact in the movement direction. The remaining slight blurring and ringing are in no way a consequence of motion; they already exist without any target motion, as will be proved in the next paragraph when involving the reconstructed true (reference) images of the static target medium in the discussion. Both kinds of artefacts are characteristically inherent and hence expected in MITS; while blurring arises from the broad main lobe of the PSF of this imaging modality, ringing is to be attributed to the oscillating and attenuating side lobes of the PSF. In addition, due to its non-edge-preserving (smoothing) properties, the used Tikhonov regularization method cannot usually suppress such artefacts completely.

Thus, based on the foregoing results and conclusions, it can be stated at this point in the discussion that the motion artefacts could be successfully eliminated by means of the D&E technique. In order to doubtlessly prove this statement, a final comparison was drawn in the following paragraph between the D&E-corrected images and the true ones of the non-rotated target medium in the reference measurements.

5.7.3   True Images and D&E Validation

It can be clearly seen through only a visual comparison how remarkably similar the D&E-corrected images in figure (5.8) are to the true ones in figure (5.9). This remarkable similarity shall be more evident when comparing the respective image performance indices in tables (5.6) and (5.8); however, it is already to be expected when comparing the respective signal performance indices in tables (5.5) and (5.7). These comparisons are even demonstrated more concretely in tables (5.9) and (5.10). While the latter shows a perfect agreement between the D&E-corrected and true conductivity changes with an average error $\delta_{\%}(\Delta\sigma_{corr})$ as small as *0.51%*, the former shows a perfect agreement between the underlying D&E-corrected and true signal changes with an average error $\delta_{\%}(\Delta v_{corr})$ as small as *0.73%*. Even this negligible $\delta_{\%}(\Delta v_{corr})$, and hence $\delta_{\%}(\Delta\sigma_{corr})$, was most probably caused by some experimental noise.

5.7.4   D&E Methodology and Application Aspects

Some relevant application aspects of the D&E technique with regard to its methodology ought to be addressed or reemphasized:

❖   Each of active and passive D&E has its own advantages; depending on the underlying application and the available measurement setup including the surrounding measurement environment, one of the two methods may be preferred to the other.

The contactless measurement manner of MITS remains unaffected in passive D&E as there is no need for any additional electrics, electronics and related accessories whatsoever to be mounted on or connected to the patient. Of course, the active coil marker can be permanently short-circuited during measurement and used as a passive coil marker. Although it wins thereby the advantages of passive D&E, it loses those of active D&E, particularly the additional signal acquisition window during the *off* phase which can be of great usefulness for further signal analysis, especially in case of any systematic or unsystematic error that predominantly affects the real part of the MITS signal. An advantage of the ferromagnetic passive marker over the inductive passive marker (and the inductive active one as well) is that the former can be conveniently chosen to have a higher quality factor than the latter. Anyway, it is a matter of course that any intended marker, whether an active

or a passive one, must induce sufficiently strong detection signals, even in case of pretty slight movements of the order of *[mm]*. As shown in graph (C) of figure (5.7) and in the corresponding row of table (5.3), a detection signal as low as *4.75 µV* was sufficient to exactly identify the aimed *IoT*.

❖   Recall that the whole discussion in this chapter shall not only apply to unintentional movements of the target, but also to those unwanted ones of the transceiver system; however, in order to avoid repetition of different measurements yielding the same results and conclusions, the performed measurements were concentrated on target movements, and the whole discussion was thus related thereto.

Indeed, intuitively, it can be inferred that the same D&E results presented in this chapter would have been obtained if the transceiver array itself rather than the target medium had been rotated in the reverse direction by the very same angle of *4°* about the z-axis, i.e., clockwise (see figure (5.3)). Accordingly, the proposed D&E technique is as much applicable to the patient as to the transceiver system; in other words, it can be used for the detection and elimination of signal errors caused by undesired movements of the patient as well as of the transmitters and/or receivers. However, it should be mentioned that any movement of the transmitters and/or receivers during measurement is necessarily supposed not to occur unless it is already planned, e.g., in case of mechanical scanning. This is because MITS transceiver arrays and their supporting mechanics must be well fixed in place in order to avoid any unwanted movements on the one hand, and to provide the image reconstruction algorithm with the exact positions of the transmitters and receivers -being one of its most important inputs- on the other hand. For these reasons, as shown in chapter (3), the new transceiver array and its mechanical body were firmly and robustly constructed.

In conclusion, it can be stated that the new D&E technique allows converting MITS measurements and hence images affected by motion artefacts into motion-artefact-free ones without any need to repeat the measurements, optimizing thereby the measurement process in this imaging modality. Having dealt with physiological conductivities in the β-dispersion frequency range, this measurement optimization technique enhances the biomedical applicability of the optimized MITS tomograph.

Chapter 6

Conclusion

This chapter provides a brief summary of this thesis and highlights the novelties therein. In its second subchapter, it calls attention to some needful future directions in biomedical MITS research.

6.1   Summary

6.1.1   Hardware Optimization

The transceiver system represents one of the most important subsystems of any MITS imaging system and must therefore meet various requirements, particularly in biomedical MITS due to the challenging measurement conditions. On this account, many relevant aspects were taken into consideration during the design and construction of the novel MITS transceiver system.

Not to mention the stable and robust mechanical structure or the fair number of independent TX-RX channels and the related advantages, the dual-plane elliptical layout of the MITS transceiver system is geometrically very appropriate for measurements on subjects or realistic models, particularly in truncal (thoracic, abdominal and pelvic) applications. Therefore, it was configured according to the true truncal measures of a slim subject (default dimensions). Moreover, its detachable *2* halves or *4* quarters can be separated and freely repositioned in order to enclose subjects or phantoms with measures exceeding the default ones. In this case, the imaging process requires nothing additional except updating the reconstruction algorithm with the new coordinates of the TRXs after repositioning.

The configuration of the transceiver array allows suppressing the carrier signal within each transceiver plane to such an extent that an effective SCR_{BM} of up to a few % can be reached in the low part of the β-dispersion frequency range.

Furthermore, depending on the applied frequency, volume of the target, its conductivity and location inside the coil array, an SNR of up to several tens of *[dB]* can be reached in the lower β-dispersion frequency range due to the very low measurement noise of few *[µV]*.
Such low-level noise and high-level SNR doubtlessly prove the electromagnetic and electrostatic immunity of the optimized hardware and therewith the adequacy of the implemented individual shielding of the different electric and electronic components, which furthermore allowed sparing the necessity for any complex shielding screen covering or enclosing the whole transceiver array, such as Faraday cage, which would have been inappropriate for the intended mechanical flexibility of the transceiver system and thus inconvenient for the experimental arrangement of certain measurement schemes.

6.1.2   Software Optimization

The software environment of the optimized MITS tomograph comprises two main packages responsible for the measuring and imaging processes, respectively. As shown throughout the thesis, while some of the contained suites and subordinated routines were partially modified or reprogrammed, some other ones were completely newly programmed, especially the main data postprocessing and image reconstruction suite dedicated to the ultimate aim of MITS, i.e., imaging. Imaging in MITS research is an indispensable tool or a must-do task whenever a novelty is to be presented and there is no other tool or task available to reliably assess its feasibility or applicability. Even if the measurement results are conclusively convincing, imaging may substantially support these results, and this study is a case example in this respect. In other words, besides the highly persuasive measurements' outcomes attained in this study, the imaging results played a key role in proving the biomedical applicability of the optimized MITS tomograph and therewith of the related novelties: the transceiver system, the hybrid dynamic-parametric imaging concept, the appropriate choice of the Tikhonov regularization parameter and TSVD truncation level, and the D&E measurement optimization technique.

As for the novel hybrid dynamic-parametric imaging concept, with regard to state-frequency-differential imaging, this concept has the advantage of combining the objectives of both state- and frequency-differential imaging. Naturally, the frequency was chosen as the influencing parameter regarding parametric imaging because it is of most relevance to the in-depth investigation of the PEP of biological tissue and hence to biomedical MITS. However, the focus might also be laid on other parameters of interest that influence the bioconductivity than frequency, as will be exemplified hereinafter.

Finally, it is worth mentioning that the presented hybrid imaging approach completely differs from the -differently called in the literature- multimodal, combined-, hybrid- or dual-modality tomography discussed previously in chapter (2). The underlying methodology neither requires the problematic and expensive combination of MITS with another tomographic modality or receiving system nor the complex reprogramming of the forward and inverse solvers into consistent hybrid algorithms. Furthermore, it does not require any fusion or merging of images at all; in other words, the desired hybrid dynamic-parametric tomographic data (herein hybrid state-frequency-differential data) are reconstructed together into one and the same image, gained from one and the same measurement (contingent upon multi-frequency hardware).

6.1.3   Measurement Optimization

Elimination of misleading motion-induced image artefacts in biomedical MITS represents an important advancement of such an imaging modality being already known for its low spatial resolution. This advancement is achieved by means of the novel measurement optimization technique in biomedical MITS, the D&E technique.

Not to mention the simple implementation or the unelaborate integration into the MITS measurement process, the novel D&E technique allows detecting and eliminating any motion-induced signal errors whatsoever prior to image reconstruction, whether those caused by the patient, the transceiver system or both together. Thus, it spares the examiner as well as the patient the necessity and therewith the effort of repeating the time-consuming measuring and imaging processes on the one hand, and any inconvenient or unpractical fixation of the patient during measurement on the other hand.

Besides biomedical applicability, the D&E methodology has proved application flexibility; it offers a practical choice between two different types of markers, active and passive markers, thus, active and passive D&E. Advantage can be taken of each type; while passive D&E is almost costless, very simple to implement, does not prolong the acquisition time and retains the MITS measurement contactless, active D&E, besides being not that expensive, offers a parallel measurement of an unmarked target and thereby a parallel very helpful signal analysis window on the one hand, and an attractive choice between two versions of the biological signal on the other hand. In addition, it has been shown that markers, whether active or passive ones, of large dimensions ought not necessarily to be used as long as small ones provide adequate detection signals.

Furthermore, aside from the matter-of-course error detection and elimination functions themselves, it should be mentioned that the key advantage of the D&E technique is that the required information on motion detection during data acquisition is gained from the MITS measurement itself; in other words, the detection signal is a part of the total received MITS signal and there is no need for own receiving circuitry and data processing routine. Thus, the novel D&E technique obviates the need for any costly or complex tracking and surveillance devices for motion detection on the one hand, and any time-consuming or sophisticated correction algorithms for artefact elimination on the other hand. As for instance, installing an ap-

propriately distributed high-resolution multiple-camera system and/or an array of movement and distance sensors would be too expensive and less favourable for the measurement setup on the one hand; on the other hand, such equipments may only provide information about whether undesired movements occurred or not, but not about the exact frames whereat these movements possibly occurred unless they are precisely synchronized in some proper way with the multiframe measurement cycle to accomplish this task.

Naturally, due to the methodological and technical common ground of biomedical and industrial MITS, the summarized novelties in this subchapter can be as much useful in the industrial research as in the biomedical one, of course, depending on the intended application.

6.2   Future Research

Despite a lot of effort that has hitherto been put into biomedical -or industrial- MITS research, unfortunately, the MITS modality is still in the experimental phase beyond clinical -or industrial- application. It is therefore of fundamental importance to raise and generalize the knowledge in this field of research through building thereon and proceeding therewith on the most relevant aspects of its hardware, software and measurement subfields, and hereunder are some thereof.

6.2.1   Hardware

Hardware has formed lesser obstacles to MITS progress than software, yet it can certainly still be improved in many respects. Principally, the hardware structure of an MITS tomograph can be categorized or subdivided into three main substructures: the host system (central computer, peripherals, interfaces, etc.), the DAQ system (DACs, ADCs, demodulators, etc.) and the transceiver system comprising mechanics, electrics and electronics (body, coils, amplifiers, etc.). Optimizing an MITS tomograph by means of high-performance host hardware as well as high-precision, high-resolution and high-speed DAQ hardware is beyond all doubt one of the most effective tools for optimizing the software and measurement performance of the tomograph due to the capability to perform a fast (iterative) imaging process on the one hand and a fast (multiframe) measuring process on the other

hand. However, neither of the two mentioned hardware categories is MITS-specific, and a competent generation thereof is already commercially available; thus, the hardware optimization in this respect is actually more of a question of cost than research. Therefore, it is recommended to concentrate the research on the third MITS-specific category, as is the case in chapter (3) of this thesis, in order to address other relevant issues that have not been treated or thoroughly investigated before, as exemplified in the following lines dealing with the measurement frequency range in MITS.

To date, most of the gained MITS images from real measurement data have been reconstructed in the lower β-dispersion frequency range below 1 MHz; examples thereof are most of the presented images in the experimental MITS studies cited in this thesis. Other than that, in order to reduce phase instabilities and external interferences at high frequencies, some research groups have employed heterodyne signal down-conversion in the receiving circuitry of their measurement systems (a detailed example of a heterodyne frequency down-conversion circuitry can be found in [Watson et al. 2002 (a)]). In this case, however, their MIT systems have been necessarily designed, i.e., enforced, to measure at a fixed frequency of, e.g., *10 MHz* in [Watson et al. 2008; Vauhkonen et al. 2008] and *20 MHz* in [Korjenevsky et al. 2000], the highest applied frequency thus far (of course, still speaking of the applied measurement frequency in real imaging experiments). In contrast, [Wei and Soleimani 2012 (a)] have found the required electronics and extra signal sources for the down-conversion circuitry of the received signal to be additional complicating factors for the system design, hardware synchronization and possible future modifications, and have therefore preferred to dispense therewith when receiving their single *10 MHz* signal, or the *13 MHz* one using the same measurement system in [Wei and Soleimani 2012 (b); Ma et al. 2016]. In [Xiang et al. 2019] as well, their single *10 MHz* signal was received without any down-conversion. In contrast to the foregoing examples, thanks to the available multifrequency hardware, the used MITS tomograph in this work allows for spectroscopic measurements within *0.01-1 MHz* with a high frequency resolution of *1 Hz*. However, neither such low, narrow frequency ranges in the lower part of the β-dispersion nor the individual higher frequencies in the middle part of the β-dispersion necessarily allow inferring or estimating the whole dispersive behaviour of the heterogeneous biological tissues. Therefore, it is strongly recommended to extend the operating frequency range of biomedical MITS tomographs to the upper part of the β-dispersion. Besides the higher sensitivity and hence larger signals, this will doubtlessly allow getting a more comprehensive overview of the spectroscopic behaviour of

the different living tissues and accordingly drawing many relevant inferences.

As a matter of course, utmost care must be taken when designing and implementing the tomograph's transceiver system and its transmitting and receiving circuitries due to the many specific technical difficulties and measurement problems to be confronted with at high frequencies, particularly, on the one hand, the various parasitic effects, especially the serious electromagnetic interferences and capacitive coupling, on the other hand, the various resonance effects, especially the coils' self-resonance. In other words, the hardware design and implementation have to consider the different relevant aspects in this regard, particularly high-stability electronics, electromagnetic and electrostatic immunity, and coils' design and specifications.

6.2.2   Software

Needless to say, image reconstruction algorithms represent the problematic substructure of the software structure of an MITS tomograph because they deal with the MITS problem itself which, based on the research outcomes published thus far, represents in turn the main stumbling block to MITS progress due to its severe ill-posedness, not to mention its nonlinear nature. Therefore, future research needs to concentrate on improving the available image reconstruction algorithms or developing new ones on the one hand, and to test the recent developed ones, especially in similar research fields, in the MITS field on the other hand. This might end up finding out an appropriate approach able to tackle the intractable ill-posedness of the MITS problem more competently than those already tried.

As for this study, the single-step Tikhonov, TSVD and MAP algorithms were chosen for no other reason than that the proof of the general imaging performance of the optimized MITS tomograph would be much more positive, demonstrative and thus persuasive when successfully employing the most common and simplest solution schemes ever employed in image reconstruction, even though these three solutions are already known for their inherent smoothing characteristic. The latter disadvantage was however compensated for to a not inconsiderable extent through well-thought-out regularization. Nevertheless, following the future research direction recommended above might allow reaching an optimal iterative algorithm, hopefully, ensuring a denoised, stable and edge-preserving inverse solution, whether to the linearized or original nonlinear MITS problem. The latter could even make absolute (static) imaging more feasible than ever before.

Besides static imaging, differential imaging is still an open and promising research direction, particularly its parametric and hence hybrid dynamic-parametric type when other reference parameters of interest than or besides frequency that influence the bioconductivity are also in focus. A good example parameter in this respect would be the temperature, i.e., when changes of the conductivity in consequence of thermal changes of the biological target are of interest, whether thermal changes alone or together with local and/or spectroscopic changes. If alone, then speaking of temperature-differential imaging, a typical (single)-parametric imaging type; if together with spectroscopic changes, then speaking of frequency-temperature-differential imaging, a (dual)-parametric imaging type; both types can be used for reconstructing the conductivity changes of most biological tissues in most body regions. If together with local changes, then speaking of another application example of the presented hybrid dynamic-parametric imaging approach, namely, hybrid state-temperature-differential imaging providing information on a biological target undergoing the cooccurrence of both local and thermal conductivity changes, for instance, when applying this hybrid imaging type to a fever patient (or in pyrotherapy: therapeutic or artificial fever) to monitor the conductivity changes in the pulmonary region between inspiration and expiration as well as between fever and normal temperatures during the progress of the disease. Finally, it would be of great interest to gather information on local, spectroscopic and thermal bioconductivity changes from one single hybrid dynamic-parametric image reconstructed from hybrid state-frequency-temperature-differential measurement data.

6.2.3 Measurement

Measurement in biomedical MITS deserves also to be a regular topic in future research as the quality of the reconstructed images is strongly dependent on the quality of the measured signals.

Employing efficient host and DAQ hardware allows performing fast measurements with a true acquisition speed of several *[frame/s]*; however, as mentioned hereinbefore, this is merely a matter of expense and is thus not the point of concern in this discussion, rather experimental errors affecting the MITS signal and hence the image quality. In chapter (2), experimental errors have been divided into human and measurement errors, and the latter in turn into systematic and unsystematic (random) ones. As regards human errors, they are usually easy to avoid when preparing and conducting the measurement carefully. Naturally, it has already been

shown in the last chapter that, despite carefulness, they might sometimes be un-avoidable as in case of reflex patient movements or unforeseeable transmitter and/or receiver movements, for which reason the D&E technique has been invent-ed. As regards unsystematic errors, although unpredictable, they can usually be effectively corrected when increasing the signal frames to be acquired and using their average in image reconstruction. Systematic errors, however, represent a ra-ther more complex issue and thus deserve more attention because they are usual-ly difficult to detect and hence to prevent. Unfortunately, except in [Scharfetter et al. 2001 (b); Scharfetter 2005, 2007; Scharfetter and Issa 2008] (and the dominant part in [Scharfetter et al. 2003]), specific studies thereon have rarely been con-ducted. Therefore, there is a particular need for much further research on system-atic errors in biomedical MITS in order to ascertain their main sources or causes. If they can be exactly identified, this will allow considerably reducing or even elimi-nating most kinds of systematic errors, whether before, during or after measure-ment.

As mentioned previously, as far as possible and practicable, it would be much more advisable in MITS research to concentrate on experimental work rather than only on simulation work as many of the obstacles to be encountered during the re-al implementation of the technique are unpredictable, extremely difficult to simu-late or cannot be simulated. This recommendation applies to all three subfields of MITS research discussed in this subchapter, hardware, software and measure-ment, and is the reason behind the presented thesis to be completely based on experimental research; the whole parallelly performed simulation research served merely as an auxiliary tool, but played no decisive role at all during the tomograph optimization process.

Of course, experimental MITS research means a multichannel hardware configu-ration of DACs, TRXs, amplifiers, filters, ADCs, etc., and such an implementation involves indeed a great deal of work and expense; however, the research will ex-pectably start with a single-channel configuration, and this thesis is no exception. The single-TRX measurements in the early phase of this work showed that slight constructional inaccuracies of the TRX are able to prevent the PZFC from satisfac-torily suppressing the carrier signal. This aspect was considered in the *16*-channel construction through equipping each TRX with an own adjustment mechanism, re-sulting in effective carrier signal reduction. Another example in this respect is the *8*-channel high-level excitation signal preamplification card implemented between

the *8* DACs and the *8* PAs. The single-channel circuit exhibited strong electromagnetic coupling between its input and output after integrating it into the housing chassis of the tomograph's electronics. This aspect was considered in the *8*-channel implementation through increasing the distance between the card's inputs and outputs on the PCB as well as on the chassis on the one hand, and replacing all internal and external shielded cables connected to the card with double-shielded ones on the other hand, resulting in total elimination of the already mentioned parasitic interference. Hereof, neither of the two foregoing example problems were encountered during the simulation work; thus, if the final multichannel design had been directly implemented based on the problem-free simulation results, laborious modifications or even redesign and reimplementation of the whole transceiver system and preamplification unit would have been unavoidable.

Likewise, judging a certain solution algorithm by -as is usually the case- simulating a measurement with some pseudorandom standard white Gaussian noise and applying the algorithm to the resulting simulated MITS signals neither reflects the whole truth about the stability of the solution and hence appropriateness of the algorithm nor about the reliability of the simulated measurement itself. The whole truth is that real MITS signals may be prone to much more noise than some uncorrelated standard normal noise, particularly systematic errors; the sources of such noise are unseen in the simulation setup, and a real measurement setup may therefore be indispensable for any reliable conclusions.

Naturally, most of the discussed suggestions on future MITS research in this subchapter can be as much relevant to the industrial field as to the biomedical one.

This thesis treated some core issues and aspects of biomedical MITS, addressed some key problems and limitations thereof, and introduced some possible solutions thereto. It might hopefully represent one of those many positive research contributions to biomedical MITS progress in hopes of seeing the modality in the foreseeable future in the diagnostic field of academic medicine.

Appendix

A.   High-Level Excitation Signal Preamplification Unit
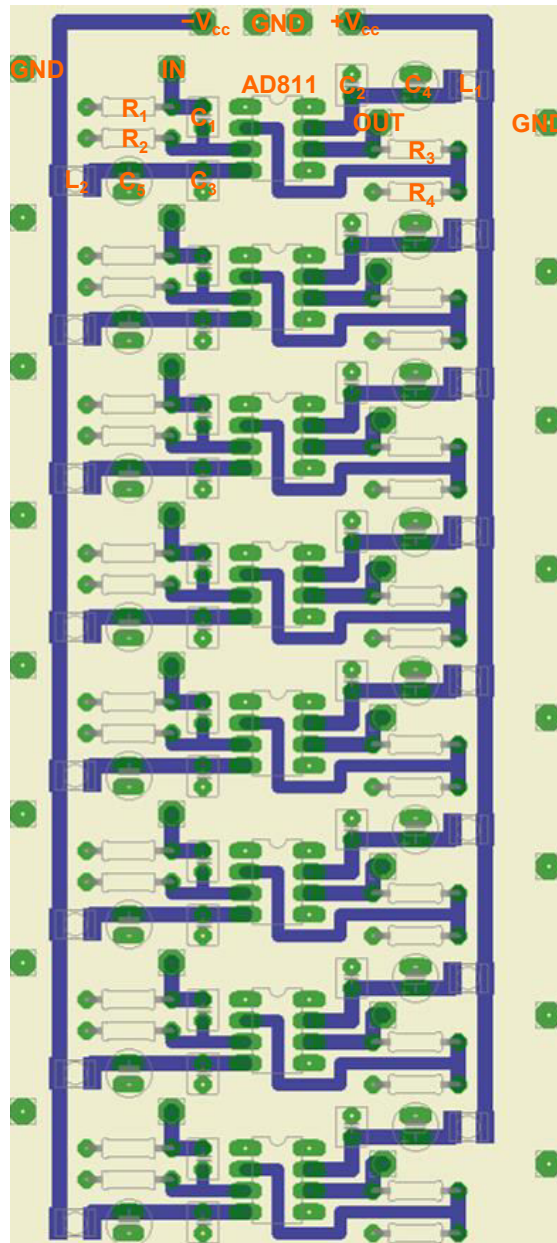
Figure (A.1): Multichannel PCB card for the high-level preamplification of the MITS excitation signal. For the sake of simplicity, only one of the 8 identical channels of the card is annotated. IN: channel input, OUT: channel output, GND: channel ground. The functions and values of the different electronic components and voltages are provided in the corresponding schematic circuit diagram in figure (3.8) and the accompanying description.

B. Measurement of the Admittivity Spectrum of the Biological Target

This measurement was performed by means of the impedance and gain-phase analyzer *SI 1260* from *Solartron Analytical* in order to attain the auxiliary reference dispersion curve of the imaged organic potato regarding its admittivity modulus shown in figure (4.17). To this end, a *4*-needle electrode was used to gain *4* individual impedance spectra from *4* different points within the peeled potato, respectively, where each of these spectra comprised *100* samples acquired at *100* logarithmically-spaced frequencies, respectively, between *0.1* and *1 MHz*. The *4* measured impedance spectra of the potato were then averaged into one single impedance spectrum. In order to accomplish this measurement task, two necessary procedures had to be performed, namely, a correction procedure followed by a conversion procedure. In the first procedure, the systematic phase and hence amplitude errors pertaining to the measurement by the used frequency response analyzer were corrected based on a certain calibration scheme including a dedicated software routine [Bruckner and Schlaminger 2003]; in the second procedure, the corrected mean *impedance spectrum Z(ω)* was converted into an *admittivity spectrum y(ω)* based on the following reformulation:

$$y(\omega) = c_c \, / \, Z(\omega) \tag{C.1}$$

where c_c is the *cell constant* of the used measuring electrode which was simply determined by using the electrode itself to measure the *impedance Z_{NaCl}* (or *resistance R_{NaCl}*) *of an NaCl solution* of known *conductivity σ_{NaCl}* and inserting both measured parameters in the following equation:

$$c_c = \sigma_{NaCl} \; Z_{NaCl} \tag{C.2}$$

where Z_{NaCl} resulted from averaging *10* samples acquired at *10* logarithmically-spaced frequencies, respectively, between *10* and *100 kHz* within which the saline solution was non-dispersive, i.e., *{$Z_{NaCl} = R_{NaCl}$ = constant}*.

C. Abbreviations

Most of the listed abbreviations are used in text as stand-alone ones as usual or followed by a noun; some ones are only used as indices (subscripts); some other ones are used as both, stand-alone abbreviations and indices. Abbreviations of some mathematical operators including statistical ones are also included.

ABS / abs	ABSolute
ADC	Analog to Digital Converter
app	APPropriate
bg	BackGround
BM	BioMedical / Biological Material
c	Coaxial
car	CARrier
CG	Conjugate Gradient
CL	Closed Loop
CM	Cell Membrane
CN	Condition Number
CNR	Contrast to Noise Ratio
corr	CORRected
CSRR	Carrier Signal Reduction Ratio
DAC	Digital to Analog Converter
D&E	Detection and Elimination
DAQ	Data AcQuisition
det	DETection
diag	DIAGonal
dw	Distilled Water
ECF	ExtraCellular Fluid
ECS	ExtraCellular Space
ECT	Electrical Capacitance Tomography
EHF	Extremely High Frequency
EIT	Electrical Impedance Tomography
ELF	Extremely Low Frequency
err	ERRor / ERRoneous
es	Empty Space

EVT	Electromagnetic Velocity Tomography
exc	EXCitation
FD	Frequency-Differential
FE	Finite Element
FEM	Finite Element Method
FPBW	Full Power BandWidth
GCV	Generalized Cross-Validation
GND	GrouND
GRAD	GRADiometer
GUI	Graphical User Interface
HF	High Frequency
ICEIT	Induced-Current EIT
ICF	IntraCellular Fluid
ICS	IntraCellular Space
ILU	Incomplete Lower-Upper
Im	IMaginary
IN / In / in	INput
IoT	Index Of Truncation
LF	Low Frequency
LS	Least Squares
LxWxH	Length x Width x Height
MAP	Maximum A Posteriori
mar	MARker
MAT-MI	Magneto-Acoustic Tomography with Magnetic Induction
max	MAXimum
ME	Maxwell Equations
MF	Medium Frequency
MI	Magnetic Induction
min	MINimum
MIS	Magnetic Induction Spectroscopy
MIT	Magnetic Induction Tomography
MITS	Magnetic Induction Tomography Spectroscopy
MOSFET	Metal-Oxide-Semiconductor Field-Effect Transistor
N	Noise
NDT	Non-Destructive Testing
OAM	Optical Atomic Magnetometer
Op-Amp	OPerational AMPlifier
opt	OPTimal / OPTimized

OUT / Out / out	OUTput
p	Perpendicular
PA	Power Amplifier
PCB	Printed Circuit Board
PEP	Passive Electromagnetic Properties
PGRAD	Planar GRAD
PSF	Point Spread Function
PZFC	Planar ZFC
QMR	Quasi-Minimal Residual
Re	REal
reg	REGularized
rel	RELative
RF-OAM	Radio-Frequency OAM
RMIT	Rotational MIT
ROI	Region Of Interest
RX	Receiver
S	Sensitivity
SCR	Signal to Carrier Ratio
SD	State-Differential
SFD	State-Frequency-Differential
SMD	Surface Mount/Mounted Device
SNR	Signal to Noise Ratio
SR	Slew Rate
STD / std	STandard Deviation
SVD	Singular Value Decomposition
tar	TARget
tl	Truncation Level
tot	TOTal
TRX	TX-RX: transceiver
TSVD	Truncated Singular Value Decomposition
TTL	Transistor-Transistor-Logic
TX	Transmitter
UHF	Ultra High Frequency
var	VARiance
VHF	Very High Frequency
VLF	Very Low Frequency
ZFC	Zero Flow/Flux Coil
ZFGRAD	Zero Flow/Flux GRAD

D. Bibliography

Al-Zeibak S. and Saunders N. H.: *A feasibility study of in vivo electromagnetic imaging*. Institute of Physics, Physics in Medicine and Biology; Volume: 38, Issue: 1, Pagination: 151-160; January, 1993.

Asami K., Hanai T. and Koizumi N.: *Dielectric approach to suspensions of ellipsoidal particles covered with a shell in particular reference to biological cells*. The Japan Society of Applied Physics, Japanese Journal of Applied Physics; Volume: 19, Issue: 2, Pagination: 359-365; February, 1980.

Barai A., Watson S., Griffiths H. and Patz R.: *Magnetic induction spectroscopy: non-contact measurement of the electrical conductivity spectra of biological samples*. Institute of Physics, Measurement Science and Technology; Volume: 23, Issue: 8, Paper: 085501; August, 2012.

Biró O.: *Edge element formulations of eddy current problems*. Computer Methods in Applied Mechanics and Engineering; Volume: 169, Issue: 3-4, Pagination: 391-405; February, 1999.

Bollhöfer M. and Saad Y.: *Multilevel preconditioners constructed from inverse-based ILUs*. Society for Industrial and Applied Mathematics, Journal on Scientific Computing; Volume: 27, Issue: 5, Pagination: 1627-1650; July, 2006.

Borges A. R., de Oliveira J. E., Velez J., Tavares C., Linhares F. and Peyton A. J.: *Development of electromagnetic tomography (EMT) for industrial applications. Part 2: image reconstruction and software framework*. International Society for Industrial Process Tomography, Proceedings of the 1st World Congress on Industrial Process Tomography, Buxton, United Kingdom; Pagination: 219-225; April, 1999.

Bruckner R. and Schlaminger M.: *Impedanzspektroskopische Zellmassebestimmung in Bioreaktoren*. Biomedical project: Institute of Biomedical Engineering, Faculty of Electrical Engineering, Graz University of Technology, Austria; December, 2003.

Brunner P., Merwa R., Missner A., Rosell J., Hollaus K. and Scharfetter H.: *Reconstruction of the shape of conductivity spectra using differential multi-frequency magnetic induction tomography*. Institute of Physics, Physiological Measurement; Volume: 27, Issue: 5,

Pagination: 237-248; May, 2006.

Casañas R., Scharfetter H., Altes A. and Rosell J.: *Magnetic induction system for noninvasive measurement of susceptibility and conductivity of biological tissues*. International Society for Electrical Bioimpedance, Proceedings of the 11th International Conference on Electrical Bio-impedance, Oslo, Norway; Pagination: 623-626; June, 2001 (a).

Casañas R., Scharfetter H., Altes A., Remacha A., Sarda P., Sierra J. and Rosell J.: *In-vitro measurement of iron concentration in human hepatic tissue by magnetic induction methods*. Institute of Electrical and Electronics Engineers, Engineering in Medicine and Biology Society, Proceedings of the 23rd Annual International Conference, Istanbul, Turkey; Volume: 3, Pagination: 2971-2974; October, 2001 (b).

Casañas R., Scharfetter H., Altes A., Remacha A., Sarda P., Sierra J., Merwa R., Hollaus K. and Rosell J.: *In-vitro and in-vivo measurement of iron concentration in human hepatic tissue by magnetic induction methods*. Institute of Electrical and Electronics Engineers, Engineering in Medicine and Biology Society, Proceedings of the 25th Annual International Conference, Cancun, Mexico; Volume: 4, Pagination: 3064-3067; September, 2003.

Casañas R., Scharfetter H., Altes A., Remacha A., Sarda P., Sierra J., Merwa R., Hollaus K. and Rosell J.: *Measurement of liver iron overload by magnetic induction using a planar gradiometer: preliminary human results*. Institute of Physics, Physiological Measurement; Volume: 25, Issue: 1, Pagination: 315-323; February, 2004.

Chen Y.N., Yan M., Chen D.Y., Hamsch M., Liu H., Jin H., Vauhkonen M., Igney C. H., Kahlert J. and Wang Y.Y.: *Imaging hemorrhagic stroke with magnetic induction tomography: realistic simulation and evaluation*. Institute of Physics, Physiological Measurement; Volume: 31, Issue: 6, Pagination: 809-827; June, 2010.

Cole K. S.: *Permeability and impermeability of cell membranes for ions*. In: Permeability and the Nature of Cell Membranes (Organizer: Eric Ponder), Cold Spring Harbor Symposia on Quantitative Biology: New York; Volume: 8, Pagination: 110-122; 1940.

Cole K. S. and Cole R. H.: *Dispersion and absorption in dielectrics. I. Alternating current characteristics*. American Institute of Physics, The Journal of Chemical Physics; Volume: 9, Issue: 4, Pagination: 341-351; April, 1941.

Deans C., Marmugi L., Hussain S. and Renzoni F.: *Optical atomic magnetometry for mag-*

netic induction tomography of the heart. Proceedings of the Society of Photo-Optical Instrumentation Engineers, Photonics Europe, Quantum Optics; Volume: 9900, Paper: 99000F; April, 2016.

Debye P. J. W.: *Zur Theorie der anomalen Dispersion im Gebiete der langwelligen elektrischen Strahlung*. Verhandlungen der Deutschen Physikalischen Gesellschaft; Volume: 15, Issue: 16, Pagination: 777-793; August, 1913.

Debye P. J. W.: *Polar Molecules*. The Chemical Catalog Company, New York; 1929.

Dekdouk B., Ktistis C., Armitage D. W. and Peyton A. J.: *Assessing the feasibility of detecting a hemorrhagic type stroke using a 16 channel Magnetic Induction System*. Institute of Physics, Journal of Physics: Conference Series, International Conference on Electrical Bioimpedance; Volume: 224, Paper: 012047; May, 2010.

Fricke H.: *A mathematical treatment of the electric conductivity and capacity of disperse systems. I. The electric conductivity of a suspension of homogeneous spheroids*. American Physical Society, Physical Review; Volume: 24, Issue: 5, Pagination: 575-587; November, 1924.

Fricke H.: *A mathematical treatment of the electric conductivity and capacity of disperse systems. II. The capacity of a suspension of conducting spheroids surrounded by a nonconducting membrane for a current of low frequency*. American Physical Society, Physical Review; Volume: 26, Issue: 5, Pagination: 678-681; November, 1925.

Fricke H. and Morse S.: *The electric capacity of tumors of the breast*. American Association for Cancer Research, The Journal of Cancer Research; Volume: 10, Issue: 3, Pagination: 340-376; October, 1926.

Fricke H.: *The complex conductivity of a suspension of stratified particles of spherical or cylindrical form*. American Chemical Society, The Journal of Physical Chemistry; Volume: 59, Issue: 2, Pagination: 168-170; February, 1955.

Gabriel C., Gabriel S. and Corthout E.: *The dielectric properties of biological tissues: I. Literature survey*. Institute of Physics, Physics in Medicine and Biology; Volume: 41, Issue: 11, Pagination: 2231-2249; November, 1996 (a).

Gabriel S., Lau R. W. and Gabriel C.: *The dielectric properties of biological tissues: II.*

Measurements in the frequency range of 10 Hz to 20 GHz. Institute of Physics, Physics in Medicine and Biology; Volume: 41, Issue: 11, Pagination: 2251-2269; November, 1996 (b).

Gabriel S., Lau R. W. and Gabriel C.: *The dielectric properties of biological tissues: III. Parametric models for the dielectric spectrum of tissues*. Institute of Physics, Physics in Medicine and Biology; Volume: 41, Issue: 11, Pagination: 2271-2293; November, 1996 (c).

Gabriel C., Peyman A. and Grant E. H.: *Electrical conductivity of tissue at frequencies below 1 MHz*. Institute of Physics, Physics in Medicine and Biology; Volume: 54, Issue: 16, Pagination: 4863-4878; August, 2009.

Gersing E., Hofmann B., Kehrer G. and Pottel R.: *Modelling based on tissue structure: the example of porcine liver*. Innovation et Technologie en Biologie et Médecine; Volume: 16, Issue: 6, Pagination: 671-678; 1995.

Geselowitz D. B.: *An application of electrocardiographic lead theory to impedance plethysmography*. Institute of Electrical and Electronics Engineers, Transactions on Biomedical Engineering; Volume: BME-18, Issue: 1, Pagination: 38-41; January, 1971.

Gheorghiu E.: *The dielectric behaviour of a biological cell suspension*. Romanian Journal of Physics; Volume: 38, Pagination: 113-117; 1993.

Gheorghiu E.: *The dielectric behaviour of suspensions of spherical cells: a unitary approach*. Institute of Physics, Journal of Physics A: Mathematical and General; Volume: 27, Issue: 11, Pagination: 3883-3893; June, 1994.

Gheorghiu E.: *On the limits of ellipsoidal models when analyzing dielectric behaviour of living cells. Emphasis on red blood cells*. Annals of the New York Academy of Sciences; Volume: 873, Issue: 1, Pagination: 262-268; April, 1999.

Golub G. H., Heath M. and Wahba G.: *Generalized cross-validation as a method for choosing a good ridge parameter*. American Statistical Association, Technometrics; Volume: 21, Issue: 2, Pagination: 215-223; May, 1979.

González C. A. and Rubinsky B.: *The detection of brain oedema with frequency-dependent phase shift electromagnetic induction*. Institute of Physics, Physiological Measurement;

Volume: 27, Issue: 6, Pagination: 539-552; June, 2006.

González C. A., Villanueva C., Vera C., Flores O., Reyes R. D. and Rubinsky B.: *The detection of brain ischaemia in rats by inductive phase shift spectroscopy*. Institute of Physics, Physiological Measurement; Volume: 30, Issue: 8, Pagination: 809-819; August, 2009.

González C. A., Pérez M., Hevia N., Arámbula F., Flores O., Aguilar E., Hinojosa I., Joskowicz L. and Rubinsky B.: *Over-hydration detection in brain by magnetic induction spectroscopy*. Institute of Physics, Journal of Physics: Conference Series, International Conference on Electrical Bioimpedance; Volume: 224, Paper: 012123; May, 2010.

González C. A., Valencia J. A., Mora A., Gonzalez F., Velasco B., Porras M. A., Salgado J., Polo S. M., Hevia-Montiel N., Cordero S. and Rubinsky B.: *Volumetric electromagnetic phase-shift spectroscopy of brain edema and hematoma*. Public Library of Science, ONE; Volume: 8, Issue: 5, Paper: e63223; May, 2013.

Goss D., Mackin R. O., Crescenzo E., Tapp H. S. and Peyton A. J.: *Understanding the coupling mechanisms in high frequency EMT*. International Society for Industrial Process Tomography, Proceedings of the 3rd World Congress on Industrial Process Tomography, Banff, Canada; Pagination: 364-369; September, 2003 (a).

Goss D., Mackin R. O., Crescenzo E., Tapp H. S. and Peyton A. J.: *Development of electromagnetic inductance tomography (EMT) hardware for determining human body composition*. International Society for Industrial Process Tomography, Proceedings of the 3rd World Congress on Industrial Process Tomography, Banff, Canada; Pagination: 377-383; September, 2003 (b).

Griffiths H., Stewart W. R. and Gough W.: *Magnetic induction tomography: a measuring system for biological tissues*. Annals of the New York Academy of Sciences; Volume: 873, Issue: 1, Pagination: 335-345; April, 1999.

Griffiths H.: *Magnetic induction tomography*. Institute of Physics, Measurement Science and Technology; Volume: 12, Issue: 8, Pagination: 1126-1131; August, 2001.

Griffiths H.: *Magnetic induction tomography*. In: Electrical Impedance Tomography: Methods, History and Applications (Editor: David S. Holder), Institute of Physics Publishing: Bristol and Philadelphia; Part: 4, Chapter: 8, Pagination: 213-238; 2005.

Griffiths H., Gough W., Watson S. and Williams R. J.: *Residual capacitive coupling and the measurement of permittivity in magnetic induction tomography*. Institute of Physics, Physiological Measurement; Volume: 28, Issue: 7, Pagination: 301-311; July, 2007.

Grimnes S. and Martinsen, Ø. G.: *Bioimpedance and Bioelectricity Basics*. Academic Press, San Diego et al.; 2000.

Hanai T.: *Theory of the dielectric dispersion due to the interfacial polarization and its application to emulsions*. Colloid and Polymer Science; Volume: 171, Issue: 1, Pagination: 23-31; July, 1960.

Hansen P. C.: *Analysis of discrete ill-posed problems by means of the L-curve*. Society for Industrial and Applied Mathematics, Review; Volume: 34, Issue: 4, Pagination: 561-580; December, 1992.

Hansen P. C.: *Regularization tools: a Matlab package for analysis and solution of discrete ill-posed problems*. Numerical Algorithms; Volume: 6, Issue: 1, Pagination: 1-35; March, 1994.

Hollaus K., Magele C., Merwa R. and Scharfetter H.: *Fast calculation of the sensitivity matrix in magnetic induction tomography by tetrahedral edge finite elements and the reciprocity theorem*. Institute of Physics, Physiological Measurement; Volume: 25; Issue: 1, Pagination: 159-168; February, 2004 (a).

Hollaus K., Magele C., Merwa R. and Scharfetter H.: *Numerical simulation of the eddy current problem in magnetic induction tomography for biomedical applications by edge elements*. Institute of Electrical and Electronics Engineers, Transactions on Magnetics; Volume: 40, Issue: 2, Pagination: 623-626; March, 2004 (b).

Hu G., Li X. and He B.: *Imaging biological tissues with electrical conductivity contrast below 1 S m^{-1} by means of magnetoacoustic tomography with magnetic induction*. American Institute of Physics, Applied Physics Letters; Volume: 97, Issue: 10, Paper: 103705; September, 2010.

Hu G., Cressman E. and He B.: *Magnetoacoustic imaging of human liver tumor with magnetic induction*. American Institute of Physics, Applied Physics Letters; Volume: 98, Issue: 2, Paper: 023703; January, 2011.

Huang C.-N., Yu F.-M., Hsieh T.-C. and Chung H.-Y.: *The performance improvement of conductivity sensor via primary field compensation*. Institute of Physics, Journal of Physics: Conference Series, International Symposium on Instrumentation Science and Technology; Volume: 48, Pagination: 1346-1352; 2006.

Igney C. H., Watson S., Williams R. J., Griffiths H. and Dössel O.: *Design and performance of a planar-array MIT system with normal sensor alignment*. Institute of Physics, Physiological Measurement; Volume: 26, Issue: 2, Pagination: 263-278; April, 2005.

Issa S.: Biomedical project: Institute of Medical Engineering, Faculty of Electrical and Information Engineering, Graz University of Technology, Austria; September, 2005.

Issa S.: *16-Kanal-Multifrequenz-Transmittersystem für die Magnetische Induktions-Tomographie*. Diploma thesis: Institute of Medical Engineering, Faculty of Electrical and Information Engineering, Graz University of Technology, Austria; June, 2007.

Issa S. and Scharfetter H.: *Detection and elimination of signal errors due to unintentional movements in biomedical magnetic induction tomography spectroscopy (MITS)*. Journal of Electrical Bioimpedance; Volume: 9, Issue: 1, Pagination: 163-175; December, 2018.

Jin G., Qin M., Wang C., Guo W., Xu L., Ning X., Xu J. and Gao D.: *Experimental study on simulated cerebral edema detection with PSSMI*. In: Communication Systems and Information Technology (Lecture Notes in Electrical Engineering, Editor: Ming Ma), Springer: Berlin, Heidelberg; Volume: 100, Pagination: 361-367; 2011.

Jin G., Sun J., Qin M., Tang Q., Xu L., Ning X., Xu J., Pu X. and Chen M.: *A new method for detecting cerebral hemorrhage in rabbits by magnetic inductive phase shift*. Biosensors and Bioelectronics; Volume: 52, Pagination: 374-378; February, 2014.

Jossinet J.: *Variability of impedivity in normal and pathological breast tissue*. International Federation for Medical and Biological Engineering, Medical and Biological Engineering and Computing; Volume: 34, Issue: 5, Pagination: 346-350; September, 1996.

Jossinet J.: *The impedivity of freshly excised human breast tissue*. Institute of Physics, Physiological Measurement; Volume: 19; Issue: 1, Pagination: 61-75; February, 1998.

Jossinet J. and Schmitt M.: *A review of parameters for the bioelectrical characterization of breast tissue*. Annals of the New York Academy of Sciences; Volume: 873, Issue: 1, Pagi-

nation: 30-41; April, 1999.

Karbeyaz B. U. and Gencer N. G.: *Electrical conductivity imaging via contactless measurements: an experimental study*. Institute of Electrical and Electronics Engineers, Transactions on Medical Imaging; Volume: 22, Issue: 5, Pagination: 627-635; May, 2003.

Kaschke Components: *Product catalogue: ferrites and coilformers*. Factory for soft magnetic materials and electronic components, Goettingen, Germany; Issue: 2015, Edition: 16, Pagination: 33; 2015.

Korzhenevskii A. V. and Cherepenin V. A.: *Magnetic induction tomography*. Russian Academy of Sciences, Journal of Communications Technology and Electronics; Volume: 42, Issue: 4, Pagination: 469-474; 1997.

Korjenevsky A. V. and Cherepenin V. A.: *Progress in realization of magnetic induction tomography*. Annals of the New York Academy of Sciences; Volume: 873, Issue: 1, Pagination: 346-352; April, 1999.

Korjenevsky A., Cherepenin V. and Sapetsky S.: *Magnetic induction tomography: experimental realisation*. Institute of Physics, Physiological Measurement; Volume: 21, Issue: 1, Pagination: 89-94; February, 2000.

Korzhenevsky A. and Sapetsky S.: *Visualisation of the internal structure of extended conducting objects by magnetoinduction tomography*. Russian Academy of Sciences, Bulletin of the Russian Academy of Sciences: Physics; Volume: 65, Issue: 12, Pagination: 1945-1949; December, 2001.

Lanfermann G., Thijs J. A. J., Pinter R. and Igney C. H.: *Method and apparatus for inductively measuring the bio-impedance of a user's body*. Patent Application Publication, United States of America; Publication Number: US 2008/0194982 A1; Publication Date: 14th August, 2008.

Li G., Ma K., Sun J., Jin G., Qin M. and Feng H.: *Twenty-four-hour real-time continuous monitoring of cerebral edema in rabbits based on a noninvasive and noncontact system of magnetic induction*. Sensors; Volume: 17, Issue: 3, Paper: 537; March, 2017 (a).

Li G., Zheng X., Sun J., Ma K., Jin G., Feng H. and Qin M.: *A non-invasive non-contact continuous monitoring system of brain edema based on magnetic induction phase shift and*

computer programming. Nanoscience and Nanotechnology Letters; Volume: 9, Issue: 10, Pagination: 1470-1477; October, 2017 (b).

Li G., Chen J., Gu S., Yang J., Chen Y., Zhao S., Xu J., Bai Z., Ren J., Xu L., Chen M., Qin M. Leung K. and Sun J.: *A dual parameter synchronous monitoring system of brain edema based on the reflection and transmission characteristics of two-port test network*. Institute of Electrical and Electronics Engineers, Access; Volume: 7, Pagination: 50839-50848; April, 2019.

Liebold F., Hamsch M. and Igney C. H.: *Contact-less human vital sign monitoring with a 12 channel synchronous parallel processing magnetic impedance measurement system*. International Federation for Medical and Biological Engineering, Proceedings of 4th European Conference, Antwerp, Belgium; Volume: 22, Pagination: 1070-1073; November, 2008.

Liu R., Li Y., You F., Shi X., Fu F. and Dong X.: *Preliminary imaging results of magnetic induction tomography based on physical phantom*. Institute of Electrical and Electronics Engineers, Engineering in Medicine and Biology Society, Proceedings of the 30th Annual International Conference, Vancouver, Canada; Volume: 3, Pagination: 4559-4562; August, 2008.

Liu R., Li Y., Fu F., You F., Shi X. and Dong X.: *Time-difference imaging of magnetic induction tomography in a three-layer brain physical phantom*. Institute of Physics, Measurement Science and Technology; Volume: 25, Issue: 6, Paper: 065402; June, 2014.

Liu X., Liu Z. and Yue Y.: *Simulation research of impact of number of coils in EMT sensors on reconstructed images quality*. Sensing and Imaging; Volume: 20, Issue: 1, Paper: 27; December, 2019.

Ma L., Wei H.-Y. and Soleimani M.: *Pipelines inspection using magnetic induction tomography based on a narrowband pass filtering method*. The Electromagnetics Academy, Progress In Electromagnetics Research M; Volume: 23, Pagination: 65-78; January, 2012 (a).

Ma L., Wei H.-Y. and Soleimani M.: *Cryosurgical monitoring using electromagnetic measurements: a feasibility study for magnetic induction tomography*. Proceedings of the 13th International Conference on Biomedical Applications of Electrical Impedance Tomography, Tianjin, China; May, 2012 (b).

Ma L., Hunt A. and Soleimani M.: *Experimental evaluation of conductive flow imaging us-*

ing magnetic induction tomography. International Journal of Multiphase Flow; Volume: 72, Pagination: 198-209; June, 2015.

Ma L., Banasiak R. and Soleimani M.: *Magnetic induction tomography with high performance GPU implementation*. The Electromagnetics Academy, Progress In Electromagnetics Research B; Volume: 65, Pagination: 49-63; January, 2016.

Ma L. and Soleimani M.: *Magnetic induction tomography methods and applications: a review*. Institute of Physics, Measurement Science and Technology; Volume: 28, Issue: 7, Paper: 072001; June, 2017.

Ma L., Spagnul S. and Soleimani M.: *Metal solidification imaging process by magnetic induction tomography*. Nature: International Journal of Science, Scientific Reports; Volume: 7, Paper: 14502; November, 2017 (a).

Ma L., McCann D. and Hunt A.: *Combining magnetic induction tomography and electromagnetic velocity tomography for water continuous multiphase flows*. Institute of Electrical and Electronics Engineers, Sensors Journal; Volume: 17, Issue: 24, Pagination: 8271-8281; December, 2017 (b).

Ma L. and Soleimani M.: *Magnetic induction spectroscopy for permeability imaging*. Nature: International Journal of Science, Scientific Reports; Volume: 8, Paper: 7025; May, 2018.

Marmugi L. and Renzoni F.: *Optical magnetic induction tomography of the heart*. Nature: International Journal of Science, Scientific Reports; Volume: 6, Paper: 23962; April, 2016.

Martinsen Ø. G., Grimnes S. and Schwan H. P.: *Interface phenomena and dielectric properties of biological tissues*. In: Encyclopedia of Surface and Colloid Science (Editor: Arthur T. Hubbard), Marcel Dekker: New York; Volume: 2, Pagination: 2643-2652; July, 2002.

Matoorian N., Patel B. C. M. and Bowler A. M.: *Dental electromagnetic tomography: properties of tooth tissues*. The Institution of Engineering and Technology, Colloquium on Innovations in Instrumentation for Electrical Tomography, London, United Kingdom; Digest: 1995/099, Pagination: 3/1-3/7; May, 1995.

Merwa R., Hollaus K., Brandstätter B. and Scharfetter H.: *Numerical solution of the gen-*

eral 3D eddy current problem for magnetic induction tomography (spectroscopy). Institute of Physics, Physiological Measurement; Volume: 24, Issue: 2, Pagination: 545-554; May, 2003.

Merwa R., Hollaus K. and Scharfetter H.: *Detection of brain oedema using magnetic induction tomography: a feasibility study of the likely sensitivity and detectability*. Institute of Physics, Physiological Measurement; Volume: 25, Issue: 1, Pagination: 347-354; February, 2004.

Merwa R.: *Rekonstruktion pathologischer Strukturveränderungen im menschlichen Gehirn mit Hilfe der Magnetischen-Induktions-Tomographie*. Doctoral thesis: Institute of Medical Engineering, Faculty of Electrical and Information Engineering, Graz University of Technology, Austria; March, 2004.

Merwa R., Hollaus K., Brunner P. and Scharfetter H.: *Solution of the inverse problem of magnetic induction tomography (MIT)*. Institute of Physics, Physiological Measurement; Volume: 26, Issue: 2, Pagination: 241-250; April, 2005 (a).

Merwa R., Brunner P., Missner A., Rosell J., Hollaus K. and Scharfetter H.: *Solution of the inverse problem of magnetic induction tomography (MIT) in silicio and in vitro*. Proceedings of the 6th International Conference on Biomedical Applications of Electrical Impedance Tomography, London, United Kingdom; June, 2005 (b).

Merwa R., Brunner P., Missner A., Hollaus K. and Scharfetter H.: *Solution of the inverse problem of magnetic induction tomography (MIT) with multiple objects: analysis of detectability and statistical properties with respect to the reconstructed conducting region*. Institute of Physics, Physiological Measurement; Volume: 27, Issue: 5, Pagination: 249-259; May, 2006.

Merwa R. and Scharfetter H.: *Magnetic induction tomography: evaluation of the point spread function and analysis of resolution and image distortion*. Institute of Physics, Physiological Measurement; Volume: 28, Issue: 7, Pagination: 313-324; July, 2007 (a).

Merwa R. and Scharfetter H.: *Magnetic induction tomography: a feasibility study of brain oedema detection using a finite element human head model*. International Federation for Medical and Biological Engineering, Proceedings of the 13th International Conference on Electrical Bio-Impedance and the 8th International Conference on Biomedical Applications of Electrical Impedance Tomography, Graz, Austria; Volume: 17, Pagination: 480-483;

August-September, 2007 (b).

Merwa R. and Scharfetter H.: *Magnetic induction tomography: comparison of the image quality using different types of receivers*. Institute of Physics, Physiological Measurement; Volume: 29, Issue: 6, Pagination: 417-429; June, 2008.

Morozov V. A.: *Methods for Solving Incorrectly Posed Problems*. Springer, New York; 1984.

Mortarelli J. R.: *A generalization of the Geselowitz relationship useful in impedance plethysmographic field calculations*. Institute of Electrical and Electronics Engineers, Transactions on Biomedical Engineering; Volume: BME-27, Issue: 11, Pagination: 665-667; November, 1980.

Netz J., Forner E. and Haagemann S.: *Contactless impedance measurement by magnetic induction - a possible method for investigation of brain impedance*. Institute of Physics, Physiological Measurement; Volume: 14, Issue: 4, Pagination: 463-471; November, 1993.

Nopp P., Zhao T.-X., Brown B. H. and Wang W.: *Cardiac-related changes in lung resistivity as a function of frequency and location obtained from EITS images*. Institute of Physics, Physiological Measurement; Volume: 17, Issue: 4A, Pagination: 213-225; November, 1996.

Nopp P., Harris N. D., Zhao T.-X. and Brown B. H.: *Model for the dielectric properties of human lung tissue against frequency and air content*. International Federation for Medical and Biological Engineering, Medical and Biological Engineering and Computing; Volume: 35, Issue: 6, Pagination: 695-702; November 1997.

Pamperl H.: *Magnetische Induktionstomografie: Systemsteuerung und Datenvorverarbeitung für das Graz Mk2-System*. Master thesis: Institute of Medical Engineering, Faculty of Electrical and Information Engineering, Graz University of Technology, Austria; June, 2008.

Pan W., Yan Q., Qin M., Jin G., Sun J., Ning X., Zhuang W., Peng B. and LI G.: *Detection of cerebral hemorrhage in rabbits by time-difference magnetic inductive phase shift spectroscopy*. Public Library of Science, ONE; Volume: 10, Issue: 5, Paper: e0128127; May, 2015.

Pauly H. and Schwan H. P.: *Über die Impedanz einer Suspension von kugelförmigen Teilchen mit einer Schale. Ein Modell für das dielektrische Verhalten von Zellsuspensionen und von Proteinlösungen*. Zeitschrift für Naturforschung B; Volume: 14b, Issue: 2, Pagination: 125-131; February, 1959.

Pethig R.: *Dielectric and Electronic Properties of Biological Materials*. Wiley, Chichester; 1979.

Pethig R. and Kell D. B.: *The passive electrical properties of biological systems: their significance in physiology, biophysics and biotechnology*. Institute of Physics, Physics in Medicine and Biology; Volume: 32, Issue: 8, Pagination: 933-970; August, 1987.

Peyton A. J., Yu Z. Z., Lyon G., Al-Zeibak S., Ferreira J., Velez J., Linhares F., Borges A. R., Xiong H. L., Saunders N. H. and Beck M. S.: *An overview of electromagnetic inductance tomography: description of three different systems*. Institute of Physics, Measurement Science and Technology; Volume: 7, Issue: 3, Pagination: 261-271; March, 1996.

Peyton A. J., Beck M. S., Borges A. R., de Oliveira J. E., Lyon G. M., Yu Z. Z., Brown M. W. and Ferrerra J.: *Development of electromagnetic tomography (EMT) for industrial applications. Part 1: sensor design and instrumentation*. International Society for Industrial Process Tomography, Proceedings of the 1st World Congress on Industrial Process Tomography, Buxton, United Kingdom; Pagination: 306-312; April, 1999.

Riedel C. H., Golombeck M. A., von Saint-George M. and Dössel O.: *Data acquisition system for contact-free conductivity measurement of biological tissue*. International Federation for Medical and Biological Engineering, Proceedings of the 2nd European Conference, Vienna, Austria; Volume: 3, Issue: 1, Pagination: 86-87; December, 2002.

Riedel C. H. and Dössel O.: *Planar system for magnetic induction impedance measurement*. Proceedings of the 4th International Conference on Biomedical Applications of Electrical Impedance Tomography, Manchester, United Kingdom; Pagination: 32; April, 2003.

Riedel C. H., Keppelen M., Nani S., Merges R. D. and Dössel O.: *Planar system for magnetic induction conductivity measurement using a sensor matrix*. Institute of Physics, Physiological Measurement; Volume: 25, Issue: 1, Pagination: 403-411; February, 2004.

Rosell J., Casañas R. and Scharfetter H.: *Sensitivity maps and system requirements for magnetic induction tomography using a planar gradiometer*. Institute of Physics, Physio-

logical Measurement; Volume: 22, Issue: 1, Pagination: 121-30; February, 2001.

Rosell-Ferrer J., Merwa R., Brunner P. and Scharfetter H.: *A multifrequency magnetic induction tomography system using planar gradiometers: data collection and calibration.* Institute of Physics, Physiological Measurement; Volume: 27, Issue: 5, Pagination: 271-280; May, 2006.

Schäfer M.: *Die dielektrischen Eigenschaften ischämischer Leber- und Nierenproben im Frequenzbereich von 0,3 MHz bis 3000 MHz.* Doctoral thesis: Third Institute of Physics - Biophysics, Faculty of Physics, Georg-August University, Göttingen, Germany; 1991.

Schäfer M., Kirlum H. J., Schlegel C. and Gebhard M. M.: *Dielectric properties of skeletal muscle during ischemia in the frequency range from 50 Hz to 200 MHz.* Annals of the New York Academy of Sciences; Volume: 873, Issue: 1, Pagination: 59-64; April, 1999.

Scharfetter H., Ninaus W., Puswald B., Petrova G. I., Kovachev D. and Hutten H.: *Inductively coupled wideband transceiver for bioimpedance spectroscopy (IBIS).* Annals of the New York Academy of Sciences; Volume: 873, Issue: 1, Pagination: 322-334; April, 1999.

Scharfetter H.: *Structural modeling for impedance-based non-invasive diagnostic methods.* Thesis for the habilitation: Institute of Biomedical Engineering, Faculty of Electrical Engineering, Graz University of Technology, Austria; November, 1999.

Scharfetter H., Lackner H. K. and Rosell J.: *Magnetic induction tomography: hardware for multi-frequency measurements in biological tissues.* Institute of Physics, Physiological Measurement; Volume: 22, Issue: 1, Pagination: 131-146; February, 2001 (a).

Scharfetter H., Casañas R. and Rosell J.: *Systematic measurement errors in multi-frequency magnetic induction tomography (MIT).* International Society for Electrical Bioimpedance, Proceedings of the 11th International Conference on Electrical Bio-impedance, Oslo, Norway; Pagination: 415-419; June, 2001 (b).

Scharfetter H., Riu P., Populo M. and Rosell J.: *Sensitivity maps for low-contrast perturbations within conducting background in magnetic induction tomography.* Institute of Physics, Physiological Measurement; Volume: 23, Issue: 1, Pagination: 195-202; February, 2002 (a).

Scharfetter H., Casañas R., Merwa R. and Rosell J.: *Magnetic induction spectroscopy of*

biological tissue with a conducting background: experimental demonstration within the β-dispersion. International Federation for Medical and Biological Engineering, Proceedings of the 2nd European Conference, Vienna, Austria; Volume: 3, Issue: 1, Pagination: 88-89; December, 2002 (b).

Scharfetter H., Casañas R. and Rosell J.: *Biological tissue characterization by magnetic induction spectroscopy (MIS): requirements and limitations*. Institute of Electrical and Electronics Engineers, Transactions on Biomedical Engineering; Volume: 50, Issue: 7, Pagination: 870-880; July, 2003.

Scharfetter H., Rauchenzauner S., Merwa R., Biró O. and Hollaus K.: *Planar gradiometer for magnetic induction tomography (MIT): theoretical and experimental sensitivity maps for a low-contrast phantom*. Institute of Physics, Physiological Measurement; Volume: 25, Issue: 1, Pagination: 325-333; February, 2004.

Scharfetter H., Merwa R. and Pilz K.: *A new type of gradiometer for the receiving circuit of magnetic induction tomography (MIT)*. Institute of Physics, Physiological Measurement; Volume: 26, Issue: 2, Pagination: 307-318; April, 2005.

Scharfetter H.: *Systematic errors in frequency-differential imaging with magnetic induction tomography*. Proceedings of the 6th International Conference on Biomedical Applications of Electrical Impedance Tomography, London, United Kingdom; June, 2005.

Scharfetter H., Brunner P. and Merwa R.: *Magnetic induction tomography: single-step solution of the 3-D inverse problem for differential image reconstruction*. Institute for Scientific Computing and Information, International Journal of Information and Systems Sciences; Volume: 2, Issue: 4, Pagination: 585-606; 2006 (a).

Scharfetter H., Hollaus K., Rosell-Ferrer J. and Merwa R.: *Single-step 3-D image reconstruction in magnetic induction tomography: theoretical limits of spatial resolution and contrast to noise ratio*. Annals of Biomedical Engineering; Volume: 34, Issue: 11, Pagination: 1786-1798; November, 2006 (b).

Scharfetter H.: *Correction of systematic errors in frequency differential magnetic induction tomography*. International Federation for Medical and Biological Engineering, Proceedings of the 13th International Conference on Electrical Bio-Impedance and the 8th International Conference on Biomedical Applications of Electrical Impedance Tomography, Graz, Austria; Volume: 17, Pagination: 476-479; August-September, 2007.

Scharfetter H., Köstinger A. and Issa S.: *Spectroscopic 16 channel magnetic induction tomograph: the new Graz MIT system*. International Federation for Medical and Biological Engineering, Proceedings of the 13th International Conference on Electrical Bio-Impedance and the 8th International Conference on Biomedical Applications of Electrical Impedance Tomography, Graz, Austria; Volume: 17, Pagination: 452-455; August-September, 2007.

Scharfetter H., Köstinger A. and Issa S.: *Hardware for quasi-single-shot multifrequency magnetic induction tomography (MIT): the Graz Mk2 system*. Institute of Physics, Physiological Measurement; Volume: 29, Issue: 6, Pagination: 431-443; June, 2008.

Scharfetter H. and Issa S.: *Reduction of low-frequency noise in magnetic induction tomography systems*. International Federation for Medical and Biological Engineering, Proceedings of 4th European Conference, Antwerp, Belgium; Volume: 22, Pagination: 752-755; November, 2008.

Scharfetter H., Issa S. and Gürsoy D.: *Image reconstruction in magnetic induction tomography without using a phase reference channel*. Proceedings of the 10th Conference on Biomedical Applications of Electrical Impedance Tomography, Manchester, United Kingdom; June, 2009.

Scharfetter H., Issa S. and Gürsoy D.: *Tracking of object movements for artefact suppression in magnetic induction tomography (MIT)*. Institute of Physics, Journal of Physics: Conference Series, International Conference on Electrical Bioimpedance; Volume: 224, Paper: 012040; May, 2010.

Schober G.: *Magnetische Induktionstomographie mit Hybrid-Sensoren*. Diploma thesis: Institute of Medical Engineering, Faculty of Electrical and Information Engineering, Graz University of Technology, Austria; February, 2011.

Schöberl J.: *NETGEN An advancing front 2D/3D-mesh generator based on abstract rules*. Computing and Visualization in Science; Volume: 1, Issue: 1, Pagination: 41-52; July, 1997.

Schwan H. P.: *Electrical properties of tissue and cell suspensions*. In: Advances in Biological and Medical Physics (Editors: Lawrence J. H. and Tobias C. A.), Academic Press: New York; Volume: 5, Pagination: 147-209; February, 1957.

Schwan H. P.: *Electrical properties of tissues and cell suspensions: mechanisms and mod-*

els. Institute of Electrical and Electronics Engineers, Engineering in Medicine and Biology Society, Proceedings of the 16th Annual International Conference, Baltimore, United States of America; Volume: 1, Pagination: A70-A71; November, 1994.

Sun J., Jin G., Qin M.X., Wan Z.B., Wang J.B., Wang C., Guo W.Y., Xu L., Ning X., Xu J., Pu X.J., Chen M.S. and Zhao H.M.: *Detection of acute cerebral hemorrhage in rabbits by magnetic induction*. Brazilian Journal of Medical and Biological Research; Volume: 47, Issue: 2, Pagination: 144-150; February, 2014.

Tapp H. S. and Peyton A. J.: *A state of the art review of electromagnetic tomography*. International Society for Industrial Process Tomography, Proceedings of the 3rd World Congress on Industrial Process Tomography, Banff, Canada; Pagination: 340-346; September, 2003.

Tapp H. S., Goss D., Mackin R. O., Crescenzo E., Wan-Daud W. A., Ktistis C. and Peyton A. J.: *A combined digital camera-EMT system to measure human body composition*. International Society for Industrial Process Tomography, Proceedings of the 3rd World Congress on Industrial Process Tomography, Banff, Canada; Pagination: 384-389; September, 2003.

Tarjan P. P. and McFee R.: *Electrodeless measurements of the effective resistivity of the human torso and head by magnetic induction*. Institute of Electrical and Electronics Engineers, Transactions on Biomedical Engineering; Volume: 15, Issue: 4, Pagination: 266-278; October, 1968.

Trakic A., Eskandarnia N., Li B. K., Weber E., Wang H. and Crozier S.: *Rotational Magnetic induction tomography*. Institute of Physics, Measurement Science and Technology; Volume: 23, Issue: 2, Paper: 025402; February, 2012.

Űlker B. and Gencer N. G.: *Implementation of a data acquisition system for contactless conductivity imaging*. Institute of Electrical and Electronics Engineers, Engineering in Medicine and Biology Magazine; Volume: 21, Issue: 5, Pagination: 152-155; September-October, 2002.

Vauhkonen M., Hamsch M. and Igney C. H.: *A measurement system and image reconstruction in magnetic induction tomography*. Institute of Physics, Physiological Measurement; Volume: 29, Issue: 6, Pagination: 445-454; June, 2008.

Wagner K. W.: *Erklärung der dielektrischen Nachwirkungsvorgänge auf Grund Maxwell-scher Vorstellungen*. Archiv für Elektrotechnik, Mitteilung aus der Physikalisch-Technischen Reichsanstalt; Volume: 2, Issue: 9, Pagination: 371-387; 1914.

Watson S., Williams R. J., Griffiths H., Gough W. and Morris A.: *A transceiver for direct phase measurement magnetic induction tomography*. Institute of Electrical and Electronics Engineers, Engineering in Medicine and Biology Society, Proceedings of the 23rd Annual International Conference, Istanbul, Turkey; Volume: 4, Pagination: 3182-3184; October, 2001.

Watson S., Williams R. J., Griffiths H., Gough W. and Morris A.: *Frequency downconversion and phase noise in MIT*. Institute of Physics, Physiological Measurement; Volume: 23, Issue: 1, Pagination: 189-194; February, 2002 (a).

Watson S., Williams R. J., Morris A., Gough W. and Griffiths H.: *The Cardiff magnetic induction tomography system*. International Federation for Medical and Biological Engineering, Proceedings of the 2nd European Conference, Vienna, Austria; Volume: 3, Issue: 1, Pagination: 116-117; December, 2002 (b).

Watson S., Williams R. J., Griffiths H., Gough W. and Morris A.: *Magnetic induction tomography: phase versus vector-voltmeter measurement techniques*. Institute of Physics, Physiological Measurement; Volume: 24, Issue: 2, Pagination: 555-564; May, 2003.

Watson S., Morris A., Williams R. J., Griffiths H. and Gough W.: *A primary field compensation scheme for planar array magnetic induction tomography*. Institute of Physics, Physiological Measurement; Volume: 25, Issue: 5, Pagination: 271-279; February, 2004.

Watson S., Igney C. H., Dössel O., Williams R. J. and Griffiths H.: *A comparison of sensors for minimizing the primary signal in planar-array magnetic induction tomography*. Institute of Physics, Physiological Measurement; Volume: 26, Issue: 2, Pagination: 319-331; April, 2005.

Watson S., Williams R. J., Gough W. and Griffiths H.: *A magnetic induction tomography system for samples with conductivities below 10 S m^{-1}*. Institute of Physics, Measurement Science and Technology; Volume: 19, Issue: 4, Paper: 045501; April, 2008.

Wei H.-Y., Ma L. and Soleimani M.: *Volumetric magnetic induction tomography*. Institute of Physics, Measurement Science and Technology; Volume: 23, Issue: 5, Paper: 055401;

May, 2012.

Wei H.-Y. and Soleimani M.: *Hardware and software design for a National Instrument-based magnetic induction tomography system for prospective biomedical applications*. Institute of Physics, Physiological Measurement; Volume: 33, Issue: 5, Pagination: 863-879; May, 2012 (a).

Wei H.-Y. and Soleimani M.: *Two-phase low conductivity flow imaging using magnetic induction tomography*. The Electromagnetics Academy, Progress In Electromagnetics Research; Volume: 131, Pagination: 99-115; September, 2012 (b).

Wei H.-Y. and Soleimani M.: *Theoretical and experimental evaluation of rotational magnetic induction tomography*. Institute of Electrical and Electronics Engineers, Transactions on Instrumentation and Measurement; Volume: 61, Issue: 12, Pagination: 3324-3331; December, 2012 (c).

Wei H.-Y. and Soleimani M.: *Electromagnetic tomography for medical and industrial applications: challenges and opportunities*. Institute of Electrical and Electronics Engineers, Proceedings; Volume: 101, Issue: 3, Pagination: 559-565; March, 2013.

Williams R. A. and Beck M. S. (Editors): *Process Tomography Principles, Techniques and Applications*. Butterworth-Heinemann, Oxford; 1995.

Xiang J., Dong Y., Zhang M. and Li Y.: *Design of a magnetic induction tomography system by gradiometer coils for conductive fluid imaging*. Institute of Electrical and Electronics Engineers, Access; Volume: 7, Pagination: 56733-56744; May, 2019.

Xiao Z., Tan C. and Dong F.: *Effect of inter-tissue inductive coupling on multi-frequency imaging of intracranial hemorrhage by magnetic induction tomography*. Institute of Physics, Measurement Science and Technology; Volume: 28, Issue: 8, Paper: 084001; August, 2017.

Xiao Z., Tan C. and Dong F.: *Multi-frequency difference method for intracranial hemorrhage detection by magnetic induction tomography*. Institute of Physics, Physiological Measurement; Volume: 39, Issue: 5, Paper: 055006; May, 2018.

Xiao Z., Tan C. and Dong F.: *3-D hemorrhage imaging by cambered magnetic induction tomography*. Institute of Electrical and Electronics Engineers, Transactions on Instrumen-

tation and Measurement; Volume: 68, Issue: 7, Pagination: 2460-2468; July, 2019.

Xu Z., He W., He C., Zhang Z. and Liu Z.: *Measurement system of biological tissue magnetic induction tomography*. Institute of Electrical and Electronics Engineers, Proceedings of the Biannual World Automation Congress, Hawaii, United States of America; September-October, 2008.

Xu Z., Luo H., He W., He C., Song X. and Zhang Z.: *A multi-channel magnetic induction tomography measurement system for human brain model imaging*. Institute of Physics, Physiological Measurement; Volume: 30, Issue: 6, Pagination: 175-186; June, 2009.

Yan Q., Jin G., Ma K., Qin M., Zhuang W. and Sun J.: *Magnetic inductive phase shift: a new method to differentiate hemorrhagic stroke from ischemic stroke on rabbit*. BioMed Central, BioMedical Engineering Online; Volume: 16, Issue: 1, Paper: 63; December, 2017.

Yu Z. Z., Peyton A. J., Conway W. F., Xu L. A. and Beck M. S.: *Imaging system based on electromagnetic tomography (EMT)*. The Institution of Engineering and Technology, Electronics Letters; Volume: 29, Issue: 7, Pagination: 625-626; April, 1993.

Yu Z. Z., Peyton A. J. and Beck M. S.: *Electromagnetic tomography (EMT), Part I: Design of a sensor and a system with a parallel excitation field*. Proceedings of the 3rd European Concerted Action on Process Tomography, Oporto, Portugal; Pagination: 147-154; March, 1994.

Yu Z. Z., Peyton A. J., Xu L. A. and Beck M. S.: *Electromagnetic inductance tomography (EMT): sensor, electronics and image reconstruction algorithm for a system with a rotatable parallel excitation field*. The Institution of Engineering and Technology, Proceedings - Science, Measurement and Technology; Volume: 145, Issue: 1, Pagination: 20-25; January, 1998.

Yu Z. Z. and Peyton A. J.: *Development of sensor arrays for electromagnetic inductive tomography: compensation of large background signal values*. Transactions of the Institute of Measurement and Control; Volume: 20, Issue: 4, Pagination: 195-202; October, 1998.

Zhang M., Ma L., and Soleimani M.: *Magnetic induction tomography guided electrical capacitance tomography imaging with grounded conductors*. Measurement; Volume: 53, Pagination: 171-181; July, 2014.

Zhang M., Ma L., and Soleimani M.: *Dual modality ECT-MIT multi-phase flow imaging*. Flow Measurement and Instrumentation; Volume: 46, Issue: B, Pagination: 240-254; December, 2015.

Zhao S., Li G., Gu S., Ren J., Chen J., Xu L., Chen M., Yang J., Leung K. and Sun J.: *An experimental study of relationship between magnetic induction phase shift and brain parenchyma volume with brain edema in traumatic brain injury*. Institute of Electrical and Electronics Engineers, Access; Volume: 7, Pagination: 20974-20983; February, 2019.

Zolgharni M., Ledger P. D., Armitage D. W., Holder D. S. and Griffiths H.: *Imaging cerebral haemorrhage with magnetic induction tomography: Numerical modelling*. Institute of Physics, Physiological Measurement; Volume: 30, Issue: 6, Pagination: 187-200; June, 2009 (a).

Zolgharni M., Ledger P. D. and Griffiths H.: *Forward modelling of magnetic induction tomography: a sensitivity study for detecting haemorrhagic cerebral stroke*. International Federation for Medical and Biological Engineering, Medical and Biological Engineering and Computing; Volume: 47, Issue: 12, Pagination: 1301-1313; December, 2009 (b).

Zolgharni M., Griffiths H. and Ledger P. D.: *Frequency-difference MIT imaging of cerebral haemorrhage with a hemispherical coil array: numerical modelling*. Institute of Physics, Physiological Measurement; Volume: 31, Issue: 8, Pagination: 111-125; August, 2010.

E. Figures

F.   Tables